Dissertation
submitted to the
Combined Faculty of Natural Sciences and Mathematics
of the Ruperto Carola University Heidelberg, Germany
for the degree of
Doctor of Natural Sciences

Presented by
M.Sc. Manuel Lera-Ramírez
Born in: Zaragoza, Spain
Oral examination: 07.12.2020

Effects of motors, crosslinkers and microtubule dynamics on the sliding and stabilisation of antiparallel microtubule overlaps

Referees:
Prof. Dr. Michael Knop
Prof. Dr. Ulrich Schwarz

Acknowledgements

First and foremost, I thank François Nédélec and Phong Tran for their supervision. I would like to thank François for accepting me in his group even though I was not coming from a theoretical background, and for giving me the time to learn and adapt. Thank you also for staying responsive despite the distance, even willing to help me debug my Cytosim code. I would like to thank Phong for welcoming me in his group from the beginning. I really appreciate his scientific enthusiasm, but I am especially grateful for his availability and unconditional support when I would come to talk to him about experiments not working. Feeling that someone believes in you makes a real difference those times.

I would like to also thank my thesis committee members, Ulrich Schwarz and Michael Knop, for their support and feedback during these years. I want to also express my gratitude to Ursula Kummer and Alba Diz-Muñoz, for taking part in the jury of my defense. I was extremely lucky to cross scientific paths with Thomas Surrey and Jonathon Hannabuss, a lot of what is written here would not have happened without meeting them. Finally, a special mention to the kind souls in administrative positions that have dealt with my too often last minute requests: Aurelie, Anette, Elodie, Edwige, Adele, Didier ... You shine a light on this world.

During these four years I have learnt a lot from all of my colleagues. To Serge, for being my go-to theoretician all these years, and eventually becoming my go-to friend. To Ana, for almost literally taking me by the hand through the lab, and for always finding the time to help me out when I did not know how to do something.

Thanks to Lara, for the discussions, but also for helping me putting things in perspective in my indecision moments. To Federica, for letting me pilfer her buffers and always giving a heads-up on LIDL offers. To Natalia and Sandra, for making Heidelberg feel like home for the brief time I was there. To Sergio, for being so kind and available.

Aastha, of course, deserves her own thanking section. The *fil rouge* of this unusual academic experience. For welcoming me in Heidelberg, becoming such a dear friend, and for being an island of home in those early months when I moved to Paris and things were uncertain.

I am grateful for all the friends who supported me outside of work, especially the Colochos, Alberto, Olga, Luis, Dani, Konstantin, Corentin, who throughout the years have managed to cherish and cryogenize those better parts of our lives that just come back to life when we meet.

Special gratitude goes to my parents, uncles and aunts, my cousins, my sister and Luci for their presence during these years, and all the ones before, where I always felt loved and supported.

And to Ludo, for being always there, in the bad times and the cute times, believing in me, and showing it.

Gracias (...)
Porque entre tanto rigor
y habiendo perdido tanto,
no perdí mi amor al canto
ni mi voz como cantor.

— José Hernández

Summary

The mitotic spindle is a bipolar structure that segregates the chromosomes during mitosis. The main components of the spindle are microtubules: polymers that can grow and shrink at their ends. Microtubule length and spatio-temporal organisation are regulated by proteins that can crosslink microtubules, slide them with respect to each other, and affect their polymerization dynamics.

During anaphase, the spindle elongates to separate the two chromosome masses into the daughter cells. This is driven by the simultaneous sliding and growth of microtubules organised into antiparallel bundles. Since microtubule growth increases overlap length, and sliding decreases it, they have to be coordinated to maintain the microtubule overlap. Importantly, diffusible crosslinkers can slow down microtubule sliding *in vitro*, leading to the formation of stable overlaps that resemble those of the spindle. Two important questions remain unanswered to understand these processes: 1. How do diffusible crosslinkers work as brakes against microtubule sliding to form stable overlaps? 2. How are microtubule dynamics regulated in cells to maintain overlaps while sliding?

In the first part of this thesis, we produced a continuous theory that explains how diffusible crosslinkers affect sliding by molecular motors and produce stable overlaps. We verified the validity of this approach by comparing the theory with computer simulations containing individual motors, crosslinkers and microtubules. Our findings suggest that braking by diffusible crosslinkers results from the drag associated to their diffusive tails, as previously proposed. However, we find that occupancy of binding sites in the microtubule lattice plays an important role in this process. In addition, we propose a mechanism by which diffusible crosslinkers can coordinate sliding and microtubule growth. Finally, we apply this theory to an *in vitro* setup containing dynamic microtubules, diffusive crosslinkers and molecular motors. Such system can self organise into bundles that resemble anaphase spindles. Our theory can explain why a complex of motor and diffusive crosslinker can produce sliding, and drive the system to a state in which all the lattice sites are occupied by crosslinkers. It predicts that in overlaps which are kept at very high crosslinker density by the action of motors, crosslinker unbinding drives the sliding of microtubules at a much slower speed than motor sliding, and this prediction is matched by the experimental data.

In the second part, we studied anaphase microtubule dynamics in fission yeast. In this organism, no microtubule nucleation occurs during anaphase, so rescues are required to maintain the microtubule overlap of the spindle. Since not all microtubules that undergo catastrophe are rescued, the number of microtubules decreases during anaphase. We found that, as anaphase progresses, microtubule growth speed decreases and rescue rate increases. Our data supports a model in which this is mediated by the progressive enrichment of the rescue factor Cls1 on the spindle, which increases microtubule stability in time, and prevents the collapse of spindles at late anaphase, when the number of microtubules is around 4. Additionally, we found that the organisation of rescues that results from the recruitment of Cls1 to the midzone by the microtubule crosslinker Ase1 ensures the maintenance of microtubule overlap without the need for feedback between microtubule growth and sliding. Finally, we studied how microtubule dynamics change with cell size, and with deletion of kinesin-6 klp9, the main driver of microtubule sliding during anaphase. We found that klp9 deletion increases rescue rate, and that cell size increases the duration of microtubule growth events and decreases the rate at which microtubules are lost.

Zusammenfassung

Der Spindelapparat ist eine bipolare Struktur deren Funktion darin besteht den Zellkern in zwei identische Tocherkerne aufzuteilen. Hauptbestandteil des Spindelapparats sind Mikrotubuli, dynamische Polymere, welche an beiden Enden polymerisieren und depolymerisieren können. Die Länge sowie die räumliche und zeitliche Organisation von Mikrotubuli wird von Proteinen reguliert, welche Mikrotubuli vernetzen, gegeneinander verschieben und deren Polymerisation und Depolymerisation beeinflussen.

Während der mitotischen Phase Anaphase, werden die zwei Spindelpole auseinandergeschoben um die zwei Tocherkerne voneinander zu trennen. Dieser Prozess hängt davon ab, dass antiparallel überlappende Mikrotubuli (polare Mikrotubuli) gegeneinander verschoben werden und gleichzeitig wachsen. Die Polymerisation und das Verschieben muss dabei präzise koordiniert werden um die überlappenden Mikrotubuli während der Spindelausdehnung zu erhalten. Zwei wichtige Fragen, welche es ermöglichen diesen Prozess zu verstehen, sind noch immer offen: 1. Wie können diffusionsfähige, Mikrotubuli vernetzende Proteine das Auseinanderscheiben von Mikrotubuli bremsen? 2. Wie wird die Polymerisation und Depolymerisation von polaren Mikrotubuli reguliert?

Im ersten Teil meiner Doktorarbeit haben wir ein Model entwickelt, welches die Formation einer stabilen Region antiparallel überlappender Mikrotubuli und den bremsenden Effekt diffusionsfähiger Vernetzer auf das durch Motorproteine vemittelte Auseinanderschieben von Mikrotubuli erklärt. Dieses Model haben wir durch Computersimulationen mit einzelnen Motorproteinen, Vernetzern und Mikrotubuli verifiziert. Unsere Ergbenisse weisen darauf hin, dass, wie zuvor beschrieben, die von diffusionsfähigen Vernetzern generierte Bremskräfte von dem Wiederstand der diffusiven Schwanzdomänen stammen. Wir stellen jedoch darüeber hinaus fest, dass die Belegung der Bindungsstellen entlang der Mikrotubuli eine wichtige Rolle in diesem Prozess spielt. Gleichzeitig kann dies erklären warum das Auseinanderschieben in Gegenwart von diffusionsfähigen Vernetzern unabhängig von der Länge überlappender Mikrotubuli ist. Diese beiden Beobachtungen konnten durch frühere Theorien nicht in Einklang gebracht werden. Darüber hinaus schlagen wir einen Mechanismus vor durch welchen diffusionsfähige Vernetzer das Auseinanderschieben und Wachsen von Mikrotubuli koordinieren können. Schließlich verwenden wir die Theorie zur Erklärung der Ergebnisse von in vitro Experimenten mit dynamischen Miktrotubuli, diffusionsfähigen Vernetzern und molekularen Motorproteinen. Ein solches System erlaubt die selbstorganisierende Formation von Mikrotubulibündeln, wie sie in dem Spindelapparat während der Anaphase zu finden sind. Unsere Theorie kann erklären wie ein Komplex aus Motorproteinen und diffusionsfähigen Vernetzern das Auseinanderschieben von Mikrotubuli gewährleisten kann und wie ein Zustand erreicht wird in dem alle Bindungsstellen durch Vernetzer belegt sind. Das Model besagt, dass das Loslösen von Vernetzern von antiparallel überlappenden Mikrotubuli ihr Auseinanderschieben mit einer Geschwindigkeit reguliert, welche wesentlich geringer ist im Vergleich zu der Geschwindigkeit des durch Motorprotein vermittelte Auseinanderschiebens von Mikrotubuli. Diese Prognose wird durch die experimentellen Daten belegt.

Der zweite Teil meiner Arbeit widmet sich der experimentellen Studie der Polymerisations und Depolymerisationsdynamiken von Mikrotubuli während der Anaphase in Schizosaccharomyces pombe. In diesem Organismus findet keine Neubildung von Mikrotubuli während der Anaphase statt. Daher muss die Depolymerisierung von Mikrotubuli streng geguliert werden um antiparallel überlappende Mikrotubuli in dem Spindelapparat zu erhalten. Da trotzdem ein Teil der Mikrotubuli vollständig depolymerisieren, wird

im Verlauf der Anaphase die Anzahl an in dem Spindelapparat enthaltenen Mikrotubuli verringert. Wir haben herausgefunden, dass sich mit fortschreitender Anaphase, die Wachstumsgeschwindigkeit der Mikrotubuli verringert und sich die Rate erhöht mit welcher depolymerisierende Mikrotubuli wieder in eine Phase der Polymerisierung eintreten. Dies wird vermittelt durch eine progressive Anreicherung des Proteins Cls1 auf dem Spindelapparat, was mit der Zeit zu einer erhöhten Stabilität der Mikrotubuli führt und einen Zusammenbruch des Spindelapparats gegen Ende der Anaphase, wenn nur noch vier Mikrotubuli im Spindelapparat enthalten sind, verhindert. Außerdem haben wir herausgefunden, dass Cls1, welches von Ase1 zum Spindelapparat gebracht wird, den Erhalt antiparallel überlappenden Mikrotubuli gewährleistet, ohne dass eine Koordination zwischen Auseinanderschieben und Polymerisation der Mikrotubuli nötig ist. Abschließend haben wir den Einfluss der Zellgröße als auch der Abwesenheit des Motorproteins Klp9 (Kinesin-6 Familie), welches für das Auseinanderschieben der Mikrotubuli verantworklich ist, auf die Polymerisation und Depolymerisation der Mikrotubuli untersucht. In Abwesenheit von Klp9 ist die Rate der depolymerisierenden Mikrotubuli welche wieder in einer Phase der Polymerisierung eintreten erhöht. Mit Steigerung der Zellgröße verlängern sich Phasen der Polymerisation und verringert sich die Rate mit welcher Mikrotubuli vollständig depolymerisieren.

Contents

1 Introduction **7**

1 Cells: the basic units of life 7
1.1 The cell cycle 7
1.2 Mitosis 7
2 The microtubule cytoskeleton 8
2.1 Microtubules are polar polymers composed of tubulin heterodimers 8
2.2 Microtubules undergo dynamic instability 10
2.3 Microtubules in mitosis 12
3 Microtubule molecular motors 14
3.1 Motors are molecular machines that walk on microtubules 15
3.2 *In vitro* experiments with molecular motors 15
4 Non-motor Microtubule Associated Proteins 17
4.1 End binding proteins 18
4.2 CLIPs 18
4.3 TOG proteins 19
4.4 PRC1/Ase1/MAP65 family 22
5 Fission yeast as a model system
to study microtubules 28
5.1 Microtubules in interphase 29
5.2 Microtubules in mitosis 30
6 Modelling of the mitotic spindle 35
6.1 Metaphase models 35
6.2 Anaphase models 41

2 Theory of antiparallel microtubule overlap stabilization by motors and diffusible crosslinkers **43**

1 Introduction 43
2 Part 1: Development of the theory 45
2.1 Assumptions 45
2.2 Results 47
3 Part 2: Application of the theory to an *in vitro* system 58
3.1 Experimental results 58
3.2 Assumptions 61
3.3 Computational results 63
4 Stochastic Simulation Methods 66
5 Discussion 68

3 Microtubule dynamics in fission yeast Anaphase B **74**
1 Introduction 74
2 Results 76
3 Materials and Methods 90
3.1 Strains and imaging 90
3.2 Image and data analysis 92
4 Discussion 96
5 Supplementary figures and tables 103

4 Bibliography **110**

Acronyms

γ-TuC γ-tubulin complex. 29, 30, 37

γ-TuRC γ-tubulin ring complex. 8, 29

ATP Adenosine triphosphate. 14, 15

CH Calponin Homology. 18

CPC Chromosome Passenger Complex. 34

DNA deoxyribonucleic acid. 7

EB End binding. 18, 19

FRAP Fluorescence Recovery after Photobleaching. 19, 35, 58, 72, 75

GDP Guanosine diphosphate. 8, 10, 11

GTP Guanosine triphosphate. 8–12, 18

iMTOC interphase Microtubule Organising Centers. 29, 30

MAP Microtubule Associated Protein. 7, 10, 14, 16, 17, 21, 22, 24, 28, 30, 31, 33, 34, 74, 75, 80, 96, 97

MTOC Microtubule Organising Center. 12–14

SAC Spindle Assembly Checkpoint. 8, 14, 31

SPB Spindle Pole Body. 12–14, 29, 30, 35, 40, 75, 78, 79

SR-SIM Super Resolution Structured Illumination Microscopy. 77, 97

List of Figures

1.1 **Microtubule assembly** . . . 9
1.2 **Single protofilament models** . . . 10
1.3 **Microtubule roles in mitosis** . . . 13
1.4 **The kinesin superfamily** . . . 15
1.5 ***In vitro* assay arrangements** . . . 17
1.6 **Domain organisation in TOG proteins** . . . 20
1.7 **Ase1 and PRC1 *in vivo*** . . . 23
1.8 **Ase1 *in vitro* experiments** . . . 25
1.9 **PRC1 *in vitro* experiments** . . . 27
1.10 **Ase1 modelling** . . . 29
1.11 **Microtubules in fission yeast interphase** . . . 30
1.12 **Kinetochore attachments** . . . 32
1.13 **Anaphase B in fission yeast** . . . 33
1.14 **Force balance model** . . . 36
1.15 ***Xenopus* egg extract spindles** . . . 39

2.1 **Schematics of the modelled systems** . . . 48
2.2 **Systems A&B, bivalent motor and diffusible or non-diffusible crosslinkers** . . . 50
2.3 **Systems C&D, sliding by diffusible motors** . . . 53
2.4 **Entropic expansion of compressed overlaps** . . . 55
2.5 **Steady state overlaps length and entropic forces** . . . 57
2.6 **Self-Organization of Minimal Anaphase Midzone Bundles** . . . 59
2.7 **Overlap length correlations** . . . 60
2.8 **Components of the computational model.** . . . 62
2.9 **Sliding by the PRC1/KIF4A complex** . . . 64
2.10 **Simulation results** . . . 65
2.11 **Friction generated by diffusible crosslinkers** . . . 69

3.1 **Anaphase B in fission yeast** . . . 75
3.2 **Simultaneous measurement of spindle and midzone length allows inference of microtubule number during anaphase B** . . . 77
3.3 **Microtubule dynamics change as anaphase progresses** . . . 78
3.4 **Ase1 organises spindle rescues and affects microtubule dynamics** . . . 81
3.5 **Cls1 modifies microtubule dynamics in a dose dependent manner** . . . 83
3.6 **Cls1 density and rescue rate increase with anaphase progression** . . . 85
3.7 **Klp9 deletion increases rescue rate** . . . 87
3.8 **Bigger cells recruit more Cls1 and have higher rescue rates** . . . 89
3.9 **Progressive increase in microtubule stability prevents spindle collapse** 91

3.10 **Measurements of intensity** 93
3.11 **Estimating microtubule number from spindle and midzone length** . . 95
3.12 **Phenomenological model** 100
S1 **Our method for inferring number of microtubules only works for anaphase** 103
S2 **Metaphase kymograph** 103
S3 **Distribution of the duration of microtubule growth events** 104
S4 **Ase1 organises spindle rescues and affects microtubule dynamics** . . . 105
S5 **Overexpression of Cls1 from induced P41nmt1 produces ectopic cytoplasmic bundles during mitosis** 106
S6 **Comparison of microtubule dynamics in cells expressing GFP-mal3 from uninduced P1nmt1 and induced P41nmt1** 107

List of Tables

2.1 **Microtubule binding heads** 47
2.2 **Parameters of simulations** 51
2.3 **Parameters of simulations** 67

S1 **Strain list** 108
S2 **Oligonucleotides** 109
S3 **Strains in figures** 109

Chapter 1

Introduction

1 Cells: the basic units of life

Cells are the building units of living organisms. Bacteria , Archaea, and Eukaryotes are all constituted by cells, which are made of biomolecules such as lipids, proteins, carbohydrates and nucleic acids. Despite the diversity of cells, all of them share certain common features: They are separated from their surrounding media by a lipid membrane, they can sense their environment and interact with it, and they are generated by an event called cell division, a stage of the process known as cell cycle.

1.1 The cell cycle

The cell cycle of a dividing cell is segmented into interphase and cell division.

Interphase is in turn divided into three phases: G1, in which cells grow and multiply their components, S phase, in which their deoxyribonucleic acid (DNA) is replicated, and G2, in which cells keep growing and also check for errors in the replication of DNA prior to proceeding into cell division.

In eukaryotes, have to modes of division: mitosis and meiosis. In mitosis, one mother cell produces two daughter cells with the same chromosomes as the mother. In meiosis, two consecutive divisions follow a single round of DNA replication, such that the resulting four cells have half of the genetic information of the mother. Some organisms can proliferate through mitosis, like unicellular organisms, and some plants and invertebrates. In multicellular organisms, mitosis is required for growth. Meiosis generates haploid gametes that take part in sexual reproduction, or spores that can develop into a new organism [7].

Since all cells are formed by cell division, the ability to reliably segregate the genetic material is essential for living organisms. Errors in chromosome segregation can lead to aneuploidy, which can cause cancer, cell death or development problems [70, 183].

1.2 Mitosis

Mitosis requires a precise spatio-temporal organisation of cell components. The orchestrating machinery that ensures this is the mitotic spindle. It is composed of polar filamentous polymers called microtubules, which can grow and shrink at their ends. Their polymerisation, spatial organisation and physical properties are regulated by proteins known as Microtubule Associated Proteins (MAPs), which can bind to one or more microtubules

and influence their behaviour [2, 174, 7]. Mitosis can be separated into different phases: prophase, metaphase, anaphase and telophase (Fig. 1.3).

During prophase, the genetic material is condensed into chromosomes by a filamentous structure called mitotic spindle, which is assembled *de novo*. The mitotic spindle is a symmetrical structure with two poles from which fibers called microtubules emanate [7]. These fibers can attach to chromosomes, and during metaphase, the spindle ensures that sister chromatids, which are linked by proteins called cohesins, face opposing sides of the cell. Cells have a signalling machinery called Spindle Assembly Checkpoint (SAC), which verifies that spindle bipolarity and chromosome biorientation are met before chromosomes are segregated. Once the SAC is satisfied, cells proceed to anaphase [142]. During this phase, two processes occur either simultaneously or subsequently depending on the organism: Anaphase A (movement of chromosomes from the spindle center to the spindle poles), and Anaphase B (separation of spindle poles). After this, during Telophase, chromosomes de-condensate, and finally during Cytokinesis, a new physical barrier between the two daughter cells is generated [7].

We can distinguish two kinds of mitosis depending on whether the nuclear envelope breaks (open mitosis) or not (closed mitosis) in the process. This has important consequences, because in closed mitosis the compartmentalization between nucleus and cytoplasm is kept, but not in open mitosis [47].

2 The microtubule cytoskeleton

2.1 Microtubules are polar polymers composed of tubulin heterodimers

Microtubules are polar filaments. They are made of heterodimers of α-tubulin and β-tubulin (Fig. 1.1A, left), which are protein homologs with sequence identity of approximately 40% [31]. Both α and β tubulin bind to Guanosine triphosphate (GTP). In addition, β subunits can hydrolize GTP into Guanosine diphosphate (GDP).

Tubulin heterodimers (8 nm length) associate longitudinally to form the so-called protofilaments. Lateral contacts between protofilaments allow the formation of a characteristic tubular structure known as microtubule (Fig. 1.1A, center and right) [149, 148]. *In vitro*, protofilament number varies. In cells, except for some known exceptions (*C. elegans* microtubules, cilia microtubules, etc.), the typical number of protofilaments is 13 [55]. This arrangement produces a hollow tube with a diameter of 25 nm. In a 13 protofilament microtubule, the contacts between pairs of neighbouring protofilaments are mediated by α-α and β-β contacts, except for a pair of protofilaments, in which the lateral contacts are α-β. This contact between neighbouring protofilaments is called the 'seam'(Fig. 1.1A, right).

In vitro, spontaneous nucleation of microtubules is only observed at high concentrations of tubulin dimers, and it involves the formation of energetically unfavourable oligomers [112, 37]. Once a sufficiently big oligomer is formed, assembly becomes easier and the microtubule elongates rapidly (Fig. 1.1C, blue line). This kinetic barrier prevents spontaneous nucleation in cells. *In vivo*, microtubules are nucleated by the γ-tubulin ring complex (γ-TuRC) or some of its analogues, which provide a template-like structure from which the microtubule can grow [109]. Cells regulate the localization and activation of γ-TuRC so that nucleation events are controlled in space and time [109].

Microtubules are rigid at the cellular scale, as their persistent length is ~5.2 mm. This means that they can exert picoNewton-range pushing forces without bending [71].

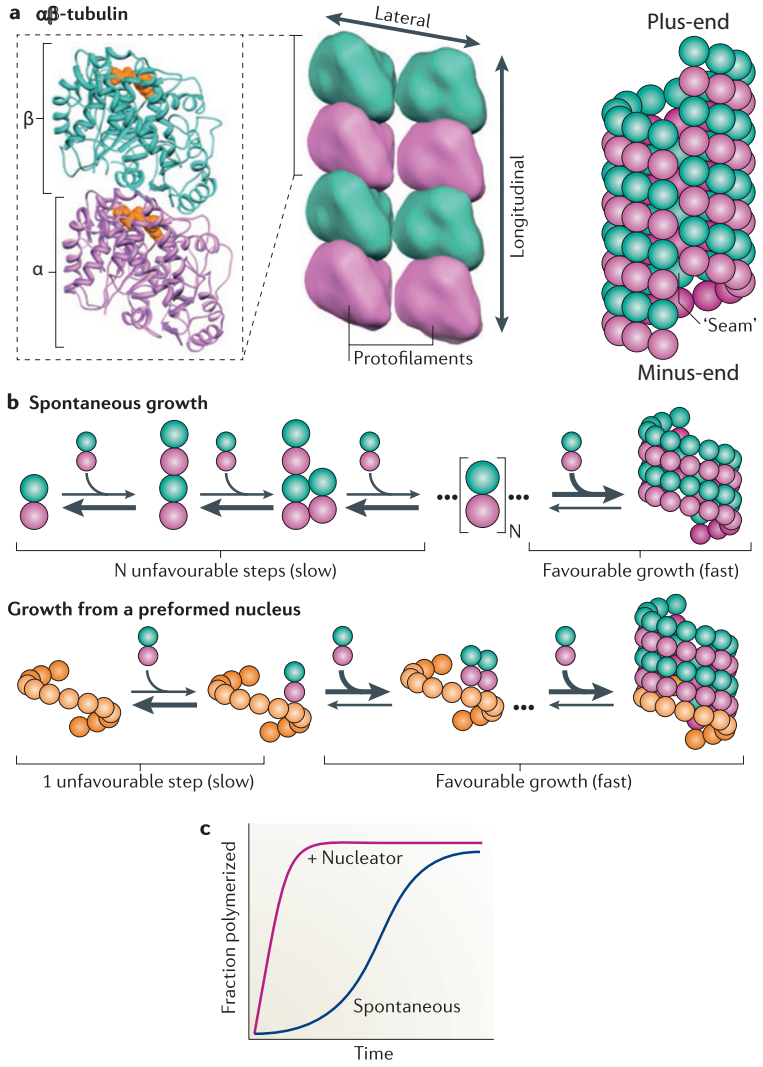

Figure 1.1: Microtubule assembly

A) The α-tubulin - β-tubulin heterodimer is the fundamental repeating subunit of microtubules. When bound to GTP (in orange), heterodimers are connected through longitudinal contacts (mediated by GTP), and form protofilaments. Lateral contacts between neighbouring α-α and β-β subunits connect protofilaments laterally allowing the formation of a hollow tubule. In microtubules composed of 13 protofilaments, a lateral interaction between α-β subunits constitutes the so-called 'seam'. **B)** Spontaneous microtubule nucleation *in vitro* is a two-phase process. Slow formation of early assembly intermediates, followed by a fast elongation phase. In the first step, disassembly dominates. However, as lateral contacts are formed between protofilaments, assembly dominates and the microtubule grows. **C)** In bulk assembly assays, the presence of a nucleator causes rapid microtubule polymerization, bypassing the lag phase observed during spontaneous growth. *Reproduced with permission from [109].*

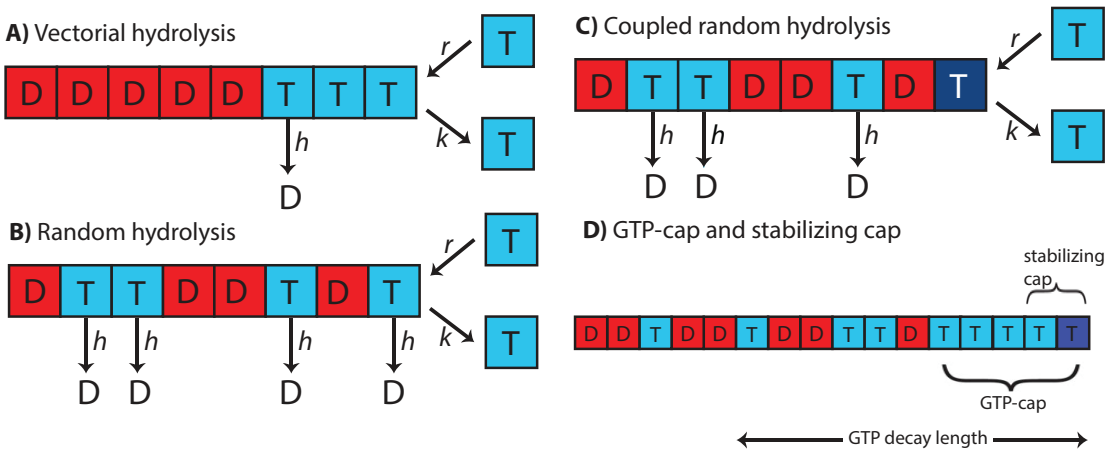

Figure 1.2: Single protofilament models

A) Vectorial hydrolysis, where hydrolysis occurs only at the GDP/GTP-tubulin interface. **B)** Random hydrolysis, in which at any time, each GTP-tubulin dimer in the microtubule has the same probability of hydrolyzing. **C)** Coupled-random hydrolysis, in which the hydrolysis occurs randomly except for the terminal dimer, which cannot hydrolyze. **D)** The distinction between the stabilizing cap, the GTP-cap (the length of uninterrupted GTP-tubulin at the end), and the GTP-tubulin decay length, over which the fraction of GTP-tubulin drops e-fold. *Reproduced with permission from [20].*

2.2 Microtubules undergo dynamic instability

In vitro, microtubules can grow or shrink by addition or removal of subunits at both of their ends, which are termed minus end (α-tubulin exposed) and plus end (β-tubulin exposed), shown in Fig. 1.1. However, most of the events occur at the plus end, so from now on we will focus only on the plus end.

Microtubules undergo dynamic instability, which involves switching between two states of persistent growth and shrinkage. Transition from a growth state to a shrinking state is called catastrophe, and transition from a shrinking state to a growing state is called rescue [137]. In cells, microtubule dynamics are regulated by different MAPs.

In vitro, growth speed of the microtubule increases linearly with tubulin concentration, suggesting that the process is governed by the rate of binding of tubulin monomers from solution to the tip of the growing microtubule (r in Fig. 1.2A) [204]. Shrinkage speed is independent of tubulin concentration, suggesting that this process is governed by a constant unbinding rate of the tubulin dimers from the microtubule tip (k in Fig. 1.2A) [204]. Rescues are very rarely observed in the absence of MAPs [204], and little is known about the mechanism that causes them. On the contrary, microtubule catastrophe has been extensively studied, and several models to explain this process have been proposed [20, 27, 154, 88, 57].

The GTP-cap

It is well established that the switch from growth to shrinkage is caused by the loss of the so-called GTP-cap [93]. Because only GTP-tubulin dimers bind at the tip of the microtubule, and GTP bound to β-tubulin only becomes hydrolysable when the dimer is incorporated into the lattice, the tip of the microtubule is enriched in GTP-subunits [167]. Since the unbinding rate of GDP-tubulin at the tip of the microtubule is very high, exposure

of GDP-bound subunits at the tip triggers a catastrophe event [203]. Some of the early evidence supporting the involvement of the GTP-cap came from experiments showing that microtubules grown in the presence of a non-hydrolysable analogue of GTP, GMPCPP, do not undergo catastrophe [93]. Furthermore, severing of microtubules using a laser, immediately causes new plus ends to shrink [203]. Finally, removing tubulin from solution when microtubules are growing results in a catastrophe within few seconds, much faster than the catastrophe time observed when microtubules grow [201, 205], suggesting that the size of the GTP-cap is small and does not scale linearly with tubulin concentration or growth speed.

Although the role of the GTP-cap in the catastrophe process is well established, the molecular mechanism of the switching from growth to shrinkage is still under debate. Experimental measurements have shown that catastrophe rate decreases moderately with concentration of soluble tubulin, and that catastrophe rate increases with microtubule age [204, 66]. This suggests that catastrophe is not a random event with a constant probability. Distributions of catastrophe times fit well with a gamma distribution with n=3, which is characteristic of a process in which 3 independent events have to occur before a catastrophe is triggered [66].

Models of microtubule growth and catastrophe

The different theoretical models that attempt to explain this process differ mostly in two points: how hydrolysis happens, and how catastrophe is defined. In addition, some models treat the microtubule as a single protofilament, neglecting the contribution of lateral interactions, and some models consider the ensemble of protofilaments, at the expense of higher complexity. Because of their simplicity, we will focus on single protofilament models.

The simplest proposed mechanisms for hydrolysis in single protofilament models are: Vectorial hydrolysis, where hydrolysis only happens at the GDP-GTP interface with a constant rate [88] (Fig. 1.2A, B), and random hydrolysis, where hydrolysis can happen anywhere in the lattice with a constant rate [27, 154]. More complicated models in which the hydrolysis rate depends on the state of neighbouring dimers have also been proposed [57].

In the vectorial model [88], catastrophe occurs when the tip dimer is in the GDP state. Then, the microtubule fully depolymerises, since GDP subunits have a very high dissociation rate. The problem with this model is that, for a bound-length regime to exist, the GDP-GTP boundary (Fig. 1.2A) has to reach the growing tip to trigger a catastrophe. This becomes almost impossible at high concentrations of tubulin, where the microtubule grows much faster than the boundary moves, so these models cannot accommodate the wide range of concentrations in which dynamic instability is observed.

In the random hydrolysis model, predictions best fit the experimental observations under the assumption that catastrophe happens when the two terminal dimers are in GDP state[27, 154]. These models reproduce well the average catastrophe rate across different concentrations [204], and the catastrophe time after dilution [201, 205]. However, catastrophe at a given tubulin concentration still remains a single-step process, and catastrophe times are exponentially distributed, contradicting the experimental evidence [66]. In addition, since hydrolysis is random, these models predict that stochastically, a shrinking protofilament may encounter a GTP-bound dimer, and this would result in a rescue. In [27], the authors propose a mechanism that could explain why this does not

happen: hydrolysis of GTP may increase as dimers become more embedded in the lattice, making it unlikely to keep GTP-bound dimers inside the lattice.

It is clear however, that the age dependent catastrophe observed experimentally requires the model to either treat catastrophe as a multiple step process, or define a continuous parameter that changes with microtubule age and increases catastrophe rate. In [20], the authors propose a single protofilament model in which the terminal dimer cannot be hydrolysed, and the hydrolysis rate is constant for the rest of the tubulin dimers (Fig. 1.2C). They define catastrophe as a 3-step process in which each "step" is a permanent modification of a protofilament, which happens when the last subunit is in the GDP state. In this model, since GTP hydrolysis cannot occur at the last position, this happens when the tip-bound GTP-dimer unbinds and the previous subunit has already been hydrolysed. They propose that after this event, the protofilament either stops growing, or the incorporated subunits are quickly hydrolysed but remain in the lattice because they can establish lateral contacts with neighbouring filaments. To explain why the stochastic encounter of a shrinking protofilament end with a GTP-bound dimer does not trigger a rescue, they make a distinction between stabilizing cap (which prevents catastrophe) and GTP-cap (which represents the decay length of GTP hydrolysis, Fig. 1.2D).

For the single protofilament, the predictions of this last model are similar to [27, 154], previously described. This suggests that combination of a single protofilament model with accumulation of lattice defects [41] might be a way to capture the observed behaviour.

2.3 Microtubules in mitosis

Microtubules are the main components of the mitotic spindle. Most spindles have two Microtubule Organising Centers (MTOCs) located at their poles, from which microtubules emanate. These are called centrosomes in animal cells and SPBs (Spindle Pole Bodies) in yeast cells. SPBs are embedded in the nuclear envelope, which does not break apart during closed mitosis (Fig. 1.3). These structures are located at spindle poles where they promote microtubule nucleation. We can distinguish mainly three types of microtubules in the spindle:

Astral microtubules (Fig. 1.3, grey) are connected to the MTOC at their minus ends and grow outwards, where they can establish contact with the cortex. These microtubules have important roles in spindle positioning and orientation in both unicellular and multicellular organisms: In budding yeast, astral microtubules contact the cell cortex, where dynein pulls from the microtubules to bring the spindle to the bud neck [140]. In animal development, astral microtubules establish contacts with the cell cortex to control the orientation and positioning of the spindle, which are important for tissue morphogenesis and differentiation [36]. In certain organisms, like *C. elegans*, they contribute to spindle pole separation during anaphase [83].

Kinetochore microtubules (Fig. 1.3, green) connect kinetochores to spindle poles. Their minus ends face the centrosome, and plus ends make contacts with kinetochores. The number of microtubules connecting a kinetochore to the pole varies between species: In budding yeast, single microtubules bridge kinetochores directly to the spindle pole [212], in fission yeast, 2-4 microtubules spanning this distance are observed [51]. In HeLa cells, the number of microtubules contacting kinetochores is around 17 [209]. During spindle formation in prophase and metaphase, microtubules are involved in the so-called search and capture process: certain microtubules from each spindle pole sequentially establish long-lived contacts with kinetochores, leading to chromosome biorientation and

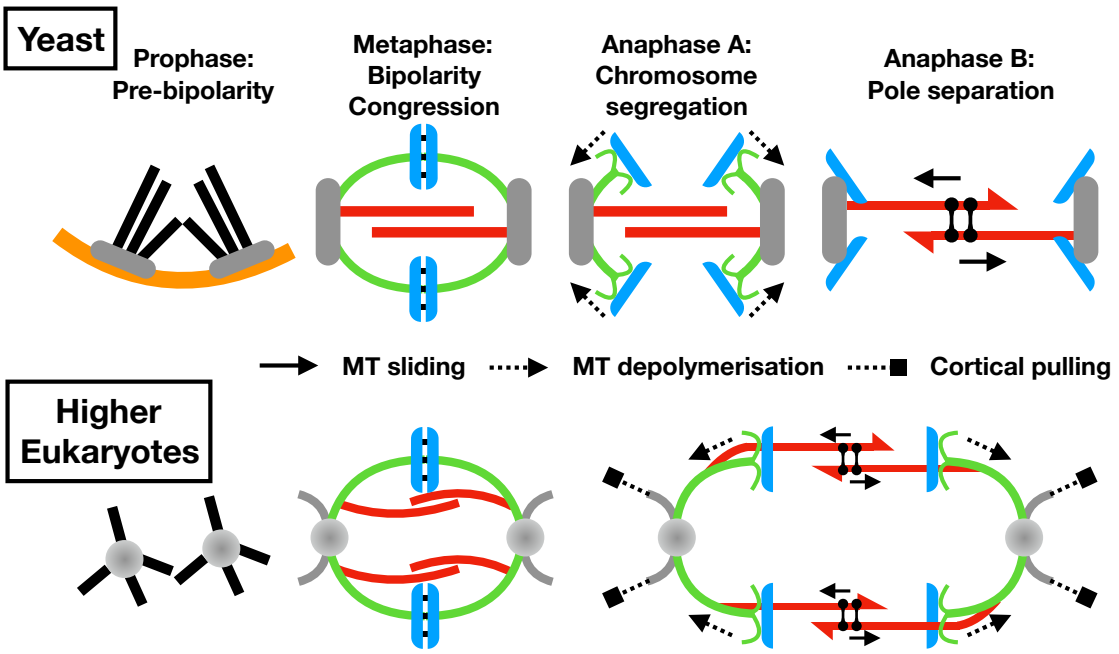

Figure 1.3: Microtubule roles in mitosis

Cartoon depicting mitotic phases in yeast's closed mitosis (top) and in higher eukaryotes open mitosis (bottom). Chromosomes are depicted in blue, and cohesin linking them is shown as black lines. Kinetochore microtubules are shown in green, interpolar microtubules in red and astral microtubules (bottom) in grey. SPBs are shown as grey capsules on top, and centrosomes as grey circles in the bottom. Yeast nuclear envelope is shown in orange on top.
In prophase, microtubules are nucleated from MTOCs, which are SPBs embedded in the nuclear envelope in yeast (top), or centrosomes in higher eukaryotes (bottom), but spindle poles are not separated. In metaphase, the spindle reaches bipolarity, where sister chromatids linked by cohesin (black lines) face opposite sides of the spindle and are connected to spindle poles through kinetochore microtubules. In yeast, anaphase A (movement of the chromosomes from the center to the poles) is driven by depolymerisation of kinetochore microtubules at their plus end. Anaphase B, which involves pole separation once chromosomes are already at the poles occurs subsequently and is mediated by motor sliding of interpolar microtubules. In higher eukaryotes, all anaphase processes occur simultaneously, and involve the mechanisms mentioned previously. In addition, cortical pulling of astral microtubules drives pole separation in *C. elegans*, and is involved in spindle positioning and orientation.

formation of a bipolar spindle (Fig. 1.3). Originally, chromosome capture was proposed to be exclusively driven by the random exploration of space by the dynamic plus ends of microtubules emanating from MTOCs [104]. It was later shown that this mechanism alone would take too long [214]. Over the years multiple mechanisms that assist this process have been discovered, which involve the cooperation of molecular motors and/or the nucleation of microtubules in the vicinity of kinetochores [84]. Biorientation inhibits SAC signalling and allows transition into anaphase [142].

Kinetochore microtubules also play a role in Anaphase A (Fig. 1.3), where the disassembly of microtubules coupled to kinetochores moves chromosomes towards spindle poles [9]. In yeast, disassembly occurs only at the plus end, while in higher eukaryotes [62, 29] minus ends are also dynamic and produce the so-called poleward flux [125, 103].

Interpolar microtubules (Fig. 1.3, red) have their plus ends at the spindle center, where they form antiparallel connections with microtubules coming from the opposite pole. In yeast, their minus ends are linked to the SPB, the equivalent of the mammalian centrosome [51]. In HeLa, *C. elegans* and PtK1 cells, the minus ends of interpolar microtubules are either linked to kinetochore fibers [128, 220], forming so-called bridging fibers [159], or (at least during anaphase) in the vicinity of chromosomes [220].

Once chromosome segregation in Anaphase A has started, interpolar microtubules maintain the physical link between spindle poles (Fig. 1.3). They drive the separation of chromosomes through antiparallel sliding mediated by molecular motors Fig. 1.3 [60, 220]. The overlap of antiparallel microtubules at the anaphase spindle midzone is also known as central spindle. In fission yeast, motor sliding at the midzone is the driver of pole separation during anaphase B [103]. The same is true for HeLa cells, where simultaneous depletion of motors involved in interpolar microtubule sliding has shown to completely inhibit chromosome segregation [202]. Similarly, laser ablation of the midzone in fission yeast [103], Hela or *C. elegans* [220] results in the arrest of chromosome separation.

In all these systems, the overlap of interpolar microtubules persists while microtubules slide apart, which requires a coordination of microtubule growth and sliding: if sliding would be faster than microtubule growth, spindles would break, and this is observed when either the organization of the midzone [216, 120] or the microtubule dynamics [222, 21] are perturbed. The process of establishment and maintenance of antiparallel microtubule arrays is therefore a core feature of mitosis.

3 Microtubule molecular motors

Microtubule molecular motors are a subset of MAPs that transform the chemical energy of Adenosine triphosphate (ATP) hydrolysis into mechanical energy, and move with a given polarity along microtubules. They belong to two main protein superfamilies: Dyneins, which all move towards the minus end of the microtubules, and kinesins, for which most of the members move preferentially towards the plus ends of microtubules, except for the kinesin-14 family. Due to their ability to move directionally, microtubule molecular motors are involved in many cellular processes: transport of vesicles and organelles, regulation of microtubule dynamics, and relative sliding of microtubules. In this study, both experimental and theoretical work focuses on different kinesins. In the next section we will focus on kinesins and their roles in microtubule dynamics and sliding.

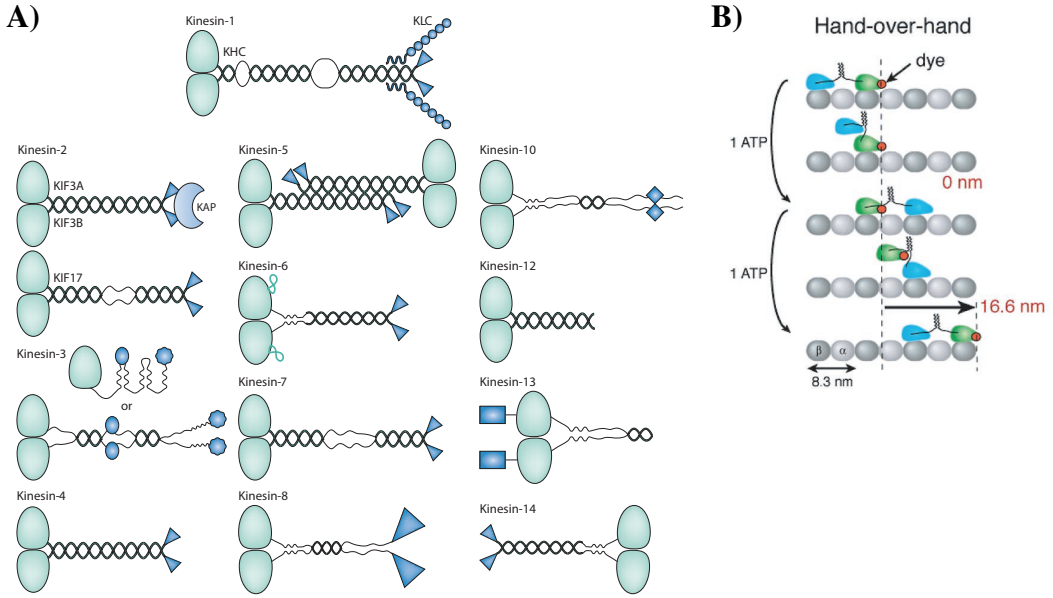

Figure 1.4: The kinesin superfamily

A) The figure depicts how the domains of kinesins are arranged in the different families. Heads are shown as light green egg-like shapes, stalks as dark green helices, globular tail domains are drawn in dark blue with different shapes. **B)** Hand-over-hand mechanism of kinesin walk explained in the main text. *Reproduced with permission from [197, 219].*

3.1 Motors are molecular machines that walk on microtubules

The structure of kinesin superfamily proteins is divided into several domains (Fig. 1.4A): The head domain contains the ATP binding catalytic site as well as the microtubule binding site [153]. The neck domain is the most characteristic part of a kinesin family [195], and is highly conserved within the family, but variable across families. The stalk domain is an α-helix coiled-coil domain that allows homo or hetero dimerisation of two kinesin molecules [197]. In addition, kinesins can also have a globular tail domain that interacts with cargo, or binds regulatory or adaptor proteins [153]. Most kinesins form dimers (kinesin-4, 6, 7, 8, 10, 12, 13, 14). Kinesin-3 exists both as dimer and monomer. Kinesin-5 and some kinesin-6 family members form homotetramers [197]. Homotetrameric kinesins and certain dimeric kinesins like kinesin-14, can bind to two microtubules at the same time. This behaviour is known as crosslinking and it can produce the relative sliding of microtubules if they are oriented in an antiparallel fashion (Fig. 1.5C)[197].

Most kinesin molecules step along microtubules with a "hand over hand mechanism" [219]. Both heads take 16 nm steps alternatively. Each step results in an 8 nm displacement of the center of mass of the molecule (Fig. 1.4B). This mechanism involves coordination of the biochemical cycles of both heads: The front head remains attached while the rear head detaches [219].

3.2 *In vitro* experiments with molecular motors

A lot of what we know about molecular motors comes from *in vitro* experiments with purified motor proteins. For the sake of this thesis, we can distinguish mainly three different types of assays:

1. Single motor experiments (Fig. 1.5A), where the movement of a single motor on a microtubule is observed. Typically, the experimental setup consists of a micrometer-sized bead coated with molecular motors. The motors can bind to a single filament and the motion of the bead is monitored via a microscope. Furthermore, the bead can be immobilised by an optical trap or by direct physical attachment to exert and measure force on the microtubule.

2. Gliding assays (Fig. 1.5B), where the surface of a coverslip is coated with motors. Filaments from solution can land on the surface and bind to multiple motors, which by walking towards one end of the microtubule, displace the microtubule with respect to the coverslip in the opposite direction.

3. Sliding assays (Fig. 1.5C, D), where a microtubule immobilized on the surface of a coverslip is crosslinked by motors or other MAPs to a free microtubule. Depending on the relative orientation of the microtubules, which is primarily either antiparallel or parallel, crosslinking motors can produce sliding of microtubules.

Force and molecular motors

How the velocity of molecular motors is affected by an opposing force was originally addressed in [135]. In this work, the authors used a setup similar to the one depicted in Fig. 1.5A and showed that the speed at which a single kinesin-1 molecule moves against a load decreases roughly linearly. The motor stops moving when the load against it is equal to the so-called stall force. For kinesin-1 in the conditions tested in the experiment, the stall force was around 5.4 pN.

Ensembles of molecular motors can cooperatively exert forces on microtubules. This also applies for tetrameric motors crosslinking antiparallel filaments, like kinesin-5, for which ensembles of motors produce a force that increases linearly with the number of motors [177]. The force per motor in these ensembles is ~1.3 pN, which is very close to the ~1.5 pN stall force measured for individual motors on single microtubules.

Some motors influence microtubule dynamics

Some plus end directed motors affect microtubule dynamics *in vitro* by binding along the length of the microtubule and moving towards the plus end, where they accumulate and affect the polymerization. Some examples are:

- Kinesin-4, which moves to the plus-end and suppresses growth and shrinkage [16].
- Kinesin-8, which increases catastrophe rate [66]. Some kinesin-8 molecules can also act as depolymerases [78].
- Kinesin-5, on the other hand, has been shown to promote microtubule growth *in vitro* [40].

In vivo, plus-end directed kinesins can bring other factors to the plus-end to control microtubule dynamics. For example, in fission yeast, Tea2/kinesin-7 associates with three other MAPs (Mal3/EB1, Tip1/CLIP170 and Alp14/XMAP215) to promote microtubule growth and suppress catastrophe, while kinesin-8 associates with Mcp1 to promote microtubule catastrophe [134].

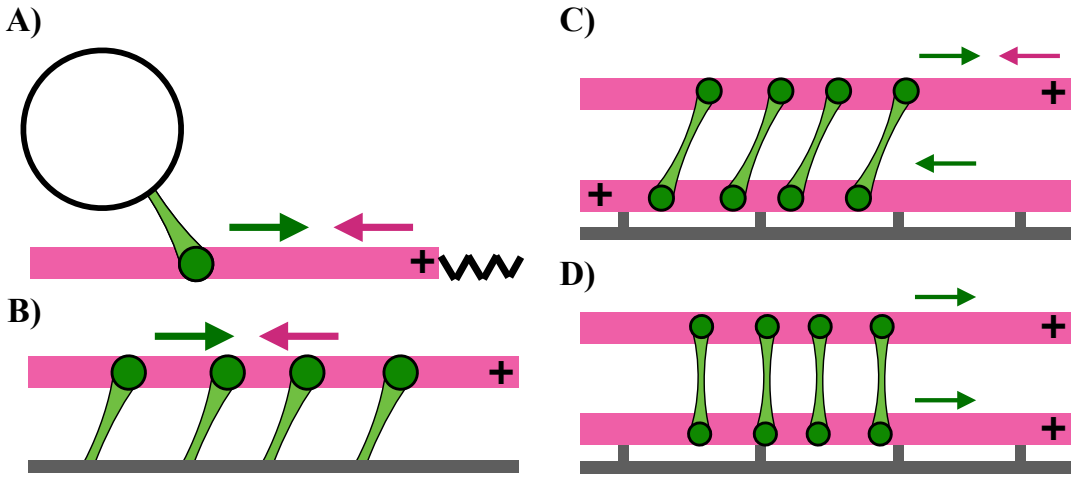

Figure 1.5: *In vitro* assay arrangements

Plus sign denotes the plus-end of the microtubule (pink). Plus end directed motors are shown in green. Green arrows indicate the direction of movement of motor heads, pink arrows indicate movement of microtubules. Gray lines represent the coverslip. Small links between the coverslip and the microtubule represent surface anchoring of microtubules. **A)** Cartoon depicting the experimental setup of a single motor experiment. A bead coated with molecular motors is placed close to a microtubule. Motors on the surface of the bead can bind to the microtubule and move towards its plus end. In addition, an elastic element (either a physical tether or an optical trap, shown as a spring on the right) can be attached to the microtubule to measure or exert force. This setup is similar to the one used in [135]. **B)** Cartoon depicting a gliding assay, in which motors have been immobilised on the surface of a coverslip. Motors that are anchored to the surface step towards the plus end of the microtubule, displacing it in the opposite direction. **C)** Cartoon depicting a sliding assay in which microtubules are crosslinked antiparallelly. In this arrangement, the two motor heads of each motor move in opposite directions, which generates an internal tension in the motor that is transmitted to the microtubules. Since the bottom microtubule is anchored to the surface, only the top microtubule moves. **D)** Cartoon depicting a sliding assay in which microtubules are crosslinked parallelly. In this arrangement, both motor heads move in the same direction, which causes motors to move towards the plus end of microtubules, but does not produce sliding.

In vivo, motor functions are controlled, as their activity and cellular localisation can be regulated [60, 194]. The functions of several motors involved in mitosis and interphase are detailed in section 5 and section 6.

4 Non-motor Microtubule Associated Proteins

Non-motor MAPs bind to microtubules. They may affect their physical properties, change microtubule dynamics, crosslink or sever them, etc. Here we present a list of the MAPs that are most relevant for this study.

4.1 End binding proteins

End binding (EB) proteins bind to GTP tubulin dimers incorporated into microtubules near their growing tips [167]. Therefore, when fluorophore-tagged versions of EB proteins are imaged on growing microtubules, they are seen as fluorescent comets that track growing microtubule tips. The signal of EB is maximum at the tip and decays with length, following the GTP tubulin levels on the microtubule [167]. Furthermore, the dwell time of EB molecules is higher at the tip, where there is more GTP tubulin. Shrinking microtubule tips are not tracked by EB proteins because they do not contain GTP tubulin.

In mammals, we can find three EB proteins: EB1, EB2 and EB3. EB1, and EB2 exist in two isoforms. In fission yeast, only one EB is present, Mal3, which is a homologue of EB1. EBs are usually dimers that contain two conserved domains bridged by a non-conserved linker sequence [75]. The N-terminal domain is a Calponin Homology (CH) domain that is necessary and sufficient for end tracking [110]. The C-terminal domain has a coiled-coil domain involved in dimerisation and interaction with EB partners through a unique domain called End Binding Homology Domain [2].

In vitro, addition of EB proteins has been shown to have various effects depending on the protein homologue and the experimental conditions. Fission yeast's Mal3 promotes formation of 13 protofilament microtubules [49], but seems to not have an effect on the growth speed of microtubules nor the catastrophe rate. Instead, it reduces shrinking speed and promotes rescues [101]. Mammalian EB1 has been shown to promote the formation of 13 protofilament microtubules, like yeast Mal3, but it increases growth velocity and promotes both catastrophe and rescue [199]. EB3 also increases growth speed and decreases catastrophe rate *in vitro* [110]. The different effects on microtubule dynamics may come from the experimental conditions and may not necessarily reflect differences between the EB homologues. In fact, a recent study showed that salt concentrations can shift the localization of EBs from mostly at the tip to all along the lattice, and that this effect is different depending on the tubulin that is used, and the EB homologue [200]. In any case, EB function *in vivo* often involves the recruitment of additional factors to the tip of the microtubules, so these differences might not even be relevant in the cellular context.

Since EB deletion or depletion often changes microtubule dynamics and/or prevents the recruitment of important factors, mitotic phenotypes are observed when EB function is impaired. In yeast [72], Mal3 deletion causes a lagging chromosome phenotype. In *Drosophila* and *Dictyostelium* EB1 is required for proper formation and position of the mitotic spindle [165, 162]. In mammalian cells, EB1 interacts with the protein adenomatous polyposis coli, and depletion of either protein results in the loss of astral microtubules and consequent mispositioning of the spindle, as well as defects in chromosome alignment [76].

4.2 CLIPs

CLIP proteins track microtubule growing ends through interaction with EBs [14]. Aromatic residues at the C-term of α-tubulin are also necessary for the recruitment of mammalian CLIP-170 [14] and yeast homologues [32, 11]. In the case of yeast, they additionally require the activity of kinesin-7 to bring CLIPs to plus ends of microtubules both *in vivo* [34] and *in vitro* [15]. CLIPs have an N-terminal CAP-Gly domain, through which they can interact with EBs, a central coiled coil domain that allows dimerisation, and a C-terminal Zinc finger region that can bind to the CAP-Gly domain and keep the protein in a self-inhibited state.

Budding yeast's Bik1, was shown to increase catastrophe activity *in vitro* [18], but

no effect was seen for human CLIP-170 [52]. Similarly to EBs, CLIPs perform their functions by recruiting and influencing the activity of other factors *in vivo*. For example, fission yeast CLIP Tip1 regulates the levels of XMAP125-like protein Alp14 at the tip of microtubules and prevents catastrophe mediated by kinesin-8 and its partner Mcp1 [147]. This is extended in subsection 5.1.

4.3 TOG proteins

TOG proteins are divided in two families: XMAP125/Dis1 and CLASP. Both families have TOG domains at their N-terminus. XMAP125/Dis1 family proteins have 2 domains and are dimeric (Alp14, Dis1, Stu2) in yeast [4]. In higher eukaryotes, they are monomeric, but have more TOG domains: worms have 3 (Zyg9), and flies, plants and mammals have 5 (Dm MSPS, Xl XMAP215, Hs ch-TOG) (Fig. 1.6A) [4]. CLASP family proteins have TOG domains that are weakly related to those in XMAP215/Dis1 family, and their numbers also vary between species (Fig. 1.6B) [4].

TOG domains in both families can bind to soluble tubulin dimers (Fig. 1.6C, D) [5, 25]. TOG domains do not mediate the interactions of XMAP215 nor CLASP with the microtubule lattice [5, 69].

XMAP215/Dis1 family

Members of the XMAP215/Dis1 family bear 2-5 TOG domains [63]. *In vitro*, they localise to the plus ends of microtubules and increase microtubule growth and shrinkage speed by catalysing polymerisation/depolymerisation reaction [25].

In vivo, the effects of loss of function of XMAP215 on microtubule dynamics differ between species. In *Xenopus* egg extract, XMAP215 also increases microtubule growth speed [64]. In *Drosophila* interphase and HeLa mitosis, depletion of XMAP215 has no effect on growth speed, but microtubule turnover measured by Fluorescence Recovery after Photobleaching (FRAP) is reduced [24, 35], suggesting perhaps a decrease in catastrophe and nucleation. In fission yeast interphase, deletion of Alp14 does not affect catastrophe, but decreases growth rate [92]. In budding yeast, Stu2 is an essential gene, so its effect on microtubule dynamics has only been studied in mutants expressing lower levels of protein, which only had minor effects on speeds and catastrophe rates [215]. In these studies, even when growth speed was not affected, microtubules exhibited periods of pause with no growth or shrinkage. These are never observed in wild type [161].

During mitosis, XMAP215 proteins are also involved in microtubule nucleation: In fission yeast, and *Xenopus* egg extracts XMAP215 acts as a nucleation factor associated with γ-tubulin through a domain that is different from the one involved in plus-end tracking [56, 186]. Perhaps one of the most striking observations comes from budding yeast [106], where Stu2 was shown to nucleate microtubules from unattached kinetochores. This process was independent of γ-tubulin, and could be induced by targeting Stu2 to another position on the chromosome.

Fission yeast is a particular case in that it has two XMAP215 homologues, Dis1 and Alp14. While Alp14 has a clear role in microtubule dynamics in interphase [6], the only effect reported on microtubule dynamics *in vivo* in dis1 deletion, is a 30% increase of interphase microtubules shrinking speed [168].

In vitro, Dis1 alone localises to growing microtubule plus ends and promotes microtubule growth. This effect is enhanced by the presence of Mal3 /EB1 [131]. However, *in vivo*, Dis1

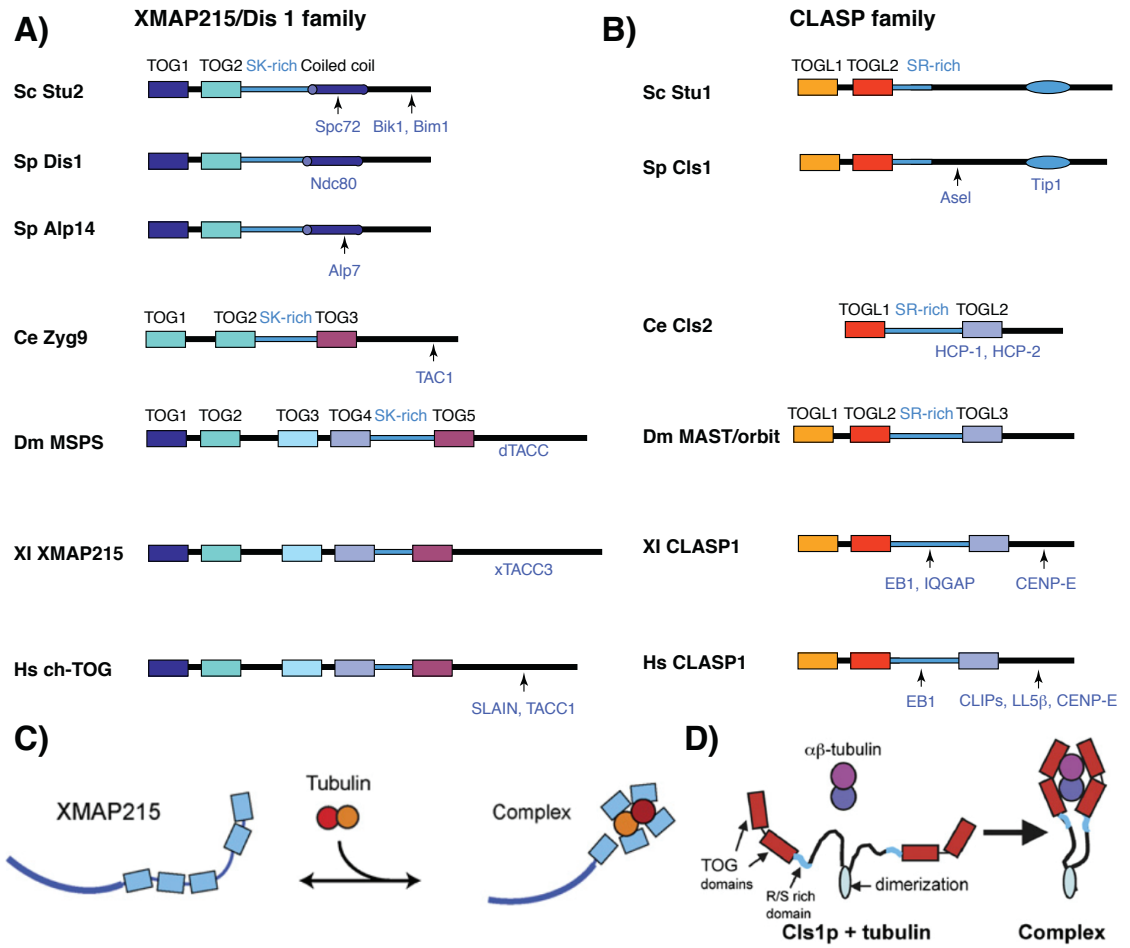

Figure 1.6: Domain organisation in TOG proteins

A) XMAP215/Dis1 proteins contain conserved TOG domains and an SK-rich domain. Domain organization of yeast orthologs *S. cerevisae* Stu2, *S.pombe* Dis1 and Alp-14 with two TOG domains, *C. elegans* Zyg9 with three and *D. melanogaster* MSPS, *Xenopus laevis* XMAP215 and human ch-TOG with five. All molecules contain regions with stretches of sequences rich in serine, glycine and lysine (SK-rich domains). TOG domains are colored on the basis of the conserved phylogenetic classes from sequence alignments: TOG1 class, blue; TOG2 class, cyan; TOG3 class, sky blue; TOG4 class, purple; TOG5 class, maroon. Protein binding partners (blue) are shown below each protein, with arrows denoting approximate binding sites. An absence of an arrow denotes an interaction in which binding domains have not been mapped. **B)** CLASP proteins contain conserved TOG-Like (TOGL) domains and SR-rich domains. Similar to (A), domain organization of *S. cerevisae* Stu1 and *S. pombe* Cls1 with two TOGL domains, *C. elegans* Cls2 with two TOGL domains and D. *melanogaster* MAST/orbit, human and *X. laevis* CLASP1 with three TOGL domains. All molecules contain regions with stretches of sequences rich in serine, proline and arginine (SR-rich domains). TOGL domains are colored on the basis of the conserved phylogenetic classes from sequence alignments: TOGL1 class, orange; TOGL2 clas, red; TOGL3 class, purple. Protein binding partners (blue) described in the text are shown below each protein with arrows denoting approximate binding sites based on studies described in the text. The absence of an arrow denotes an interaction in which the interacting domain has not been mapped. **C)** XMAP215 can associate with a tubulin dimer in solution. **D)** Cls1 dimers can associate with tubulin dimers in solution. *Reproduced with permission from [4, 5, 25].*

does not track growing plus ends. In interphase, it localizes to microtubule overlaps where it has been shown to act as a microtubule bundler, with higher affinity for parallel overlaps [168]. Dis1 localization during mitosis is very particular [8]: in metaphase, it localizes to kinetochores independently of phosphorylation by Cdc2/Cdk1. Once chromosomes are segregated in Anaphase A, dephosphorylation by an unidentified phosphatase causes its release from kinetochores, and Dis1 decorates the parallel overlap of microtubules at the spindle edges, consistent with its proposed function as crosslinker of parallel microtubules [168].

In interphase, deletion of dis1 has minor effects on the organization of microtubule bundles [168]. In mitosis, however, deletion of dis1 causes problems in kinetochore attachment and spindle bipolarity, delays metaphase to anaphase transition and causes chromosome missegregation [8]. This function of Dis1 is mediated by its interaction with Ndc80 complex, that links microtubules with kinetochores [91]. Presumably Dis1 affects microtubule dynamics at the plus ends of microtubules associated with the kinetochore, but this has not yet been shown.

In interphase, Alp14 localizes to plus ends of growing microtubules and promotes microtubule growth [147]. During mitosis, Alp14 promotes microtubule nucleation [56] and is recruited to the kinetochore by Ndc80 through a domain different from Dis1 [184]. Unlike dis1 deletion, alp14 deletion does not impact kinetochore attachment and bipolar spindle formation, but it reduces the occurrence of amphitelic attachments (each sister kinetochore is correctly attached to a different pole, see Fig. 1.12), increases metaphase duration, and causes chromosome missegregation [184]. Interestingly, overexpression of Alp14 prevents microtubule formation, presumably through sequestering soluble tubulin through its TOG domain [6].

CLASP family

Mammalian CLASP family members have been shown to track microtubule plus ends *in vitro* through interaction with EB1. They reduce microtubule growth speed, suppress catastrophes, and increase rescue rate [1]. Mammalian CLASP also suppresses catastrophes induced by drugs, MAPs, and physical barriers [1]. In the absence of EB1, it does not bind to the plus end and does not reduce catastrophe rate. However, it still reduces the growth speed and promotes rescue, suggesting that these activities are independent of its plus-end tracking activity [1].

Insect CLASP *in vitro* had similar effects. Presence of CLASP alone was enough to suppress catastrophe completely, even if it did not localise to the tip, and it also decreased the microtubule elongation speed [141]. Positions where shrinking microtubules would be rescued or where pauses would occur were not random, and instead corresponded to sites with higher CLASP intensity [141].

In vivo, mammalian [90] and insect [178] CLASP localize to plus ends of microtubules. In the case of mammalian, this was shown to occur through an EB1 binding domain, like *in vitro* [90]. During metaphase, CLASP localizes to kinetochores [156] and its function is important for the establishment of a normal bipolar spindle. Loss of CLASP activity produces the formation of smaller or monopolar spindles [116, 82, 156]. During anaphase, CLASP localizes to the central spindle through its interaction with the antiparallel crosslinker PRC1 [118, 107]. Depletion of CLASP leads to the depolymerisation of the central spindle and chromosome segregation defects [82, 107, 156]. In interphase, CLASP localizes to the tips of microtubules, and depletion of CLASP results in faster growth speed

and higher rate of catastrophe [136, 178].

Fission yeast Cls1 (also called Peg1) showed different behaviour from insect and mammalian CLASP *in vitro* [5]. It did not track plus ends, but this was not tested in the presence of EB1. However, Cls1 does not track plus ends *in vivo* either, where EB1 is present [21]. Cls1 reduced the frequency of catastrophes and promoted rescues only at positions where Cls1 accumulation was observed. In these conditions, Cls1 bound to the microtubule lattice and stayed bound in the same position for several minutes, suggesting that Cls1 does not diffuse on the surface of microtubules. Furthermore, the authors could observe the binding of labelled tubulin on Cls1 puncta, where it stayed bound for 3-4 minutes. They showed that TOG recruitment of soluble tubulin to Cls1 molecules associated with the lattice was required for rescues to occur. Additionally, growth rate of microtubules increased linearly with Cls1 concentration, as opposed to the effect observed in mammalian and insect proteins, where CLASP reduced growing speed [1, 141]. It should be noted however, that in this study the concentration of tubulin used was 3x and 4x lower than in insect and mammalian CLASP studies [141, 1].

In fission yeast, Cls1 does not localize to microtubule plus ends. It is found instead in antiparallel overlaps of microtubules both in interphase and mitosis, and to pre-anaphase kinetochores [21]. Its recruitment to antiparallel overlaps depends on its interaction with Ase1/PRC1 [21]. Mitotic phenotypes of Cls1 (tested with a Cls1 thermosensitive mutant, since Cls1 is an essential gene) resemble the ones mentioned, namely shorter or monopolar metaphase spindle and complete depolymerisation of microtubules at anaphase transition due to lack of rescues [21]. In interphase, Cls1 does not affect microtubule growth or shrinkage speeds, and it was shown to promote rescue of microtubules in interphase bundles [21]. Cells overexpressing Cls1 have very stable microtubules that do not depolymerise. Some undergo dynamic instability at their most distal ends, but others do not grow or shrink at all [21].

4.4 PRC1/Ase1/MAP65 family

Proteins of the MAP65/Ase1/PRC1 family, also known as diffusible crosslinkers, are involved in the formation and stabilisation of antiparallel microtubule arrays, where they can then recruit molecular motors [151], or other MAPs [21]. They contain an N-terminal coiled coil domain for antiparallel homodimerisation, a globular microtubule binding domain with a spectrin motif trough which interaction with microtubules is established, and a C-terminal unstructured tail that enhances microtubule interaction [180]. All the members of this family seem to share the following features:

- They form homodimers [176].
- They can crosslink microtubules, preferentially in an antiparallel configuration [99].
- *In vitro*, they can diffuse on microtubules, both when only one of the molecules of the dimer is bound, and when both are bound. As a result, they behave as viscous breaks when they crosslink microtubules [114, 22, 98].
- Their localization and activity are regulated during the cell cycle by phosphorylation/dephosphorylation, this regulation is important for their function [60, 225].
- They serve as recruiting hubs, targeting their binding partners specifically to antiparallel overlaps [151, 21, 206].

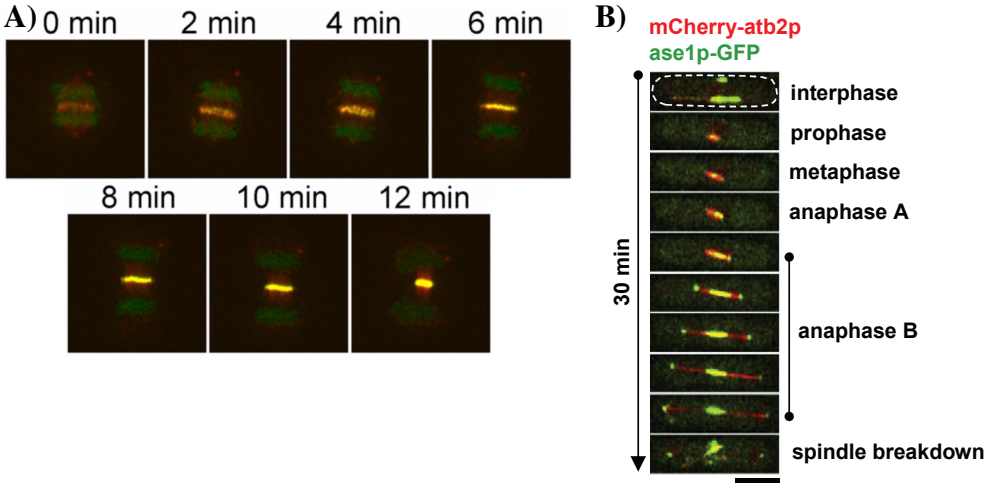

Figure 1.7: Ase1 and PRC1 *in vivo*

A) Time lapse images of mitosis in HeLa cells stably expressing eGFP-KIF4A(green) and mCherry-PRC1(red). Note the colocalisation of the signals and the progressive narrowing of the central spindle as anaphase progresses. **B)** Time-lapse images of fission yeast cells expressing mCherry-atb2p (red) and ase1p-GFP(green) in interphase, and through different phases of mitosis. Ase1p stabilises the spindle midzone throughout anaphase B. *Reproduced with permission from [151, 60].*

- It has also been shown that MAP65 and Ase1 can reduce the rigidity of both single microtubules and microtubule bundles *in vitro* [160], but no biological function has been related to this property so far.

In mammalian and insect cells, research on PRC1 has focused mostly on its roles in mitosis. Its localisation and properties are changed during the cell cycle: In HeLa, PRC1 is sequestered in the nucleus during interphase, where it cannot interact with microtubules [139]. In early mitosis, phosphorylation by Cdk1 keeps PRC1 in a state of low microtubule affinity [225]. When transitioning to anaphase, the dephosphorylation of PRC1 results in an increase in affinity and reduced turnover [94, 10]. During metaphase, it has recently been reported to locate to bridging fibers, microtubule bundles that emanate from kinetochore fibers and form antiparallel bridges between them [159, 94] (Fig. 1.3). These structures have not been extensively studied, but they play a role in maintaining the inter-kinetochore distance and influence the shape of the metaphase spindle [159, 94].

PRC1 is known mostly for its role in the organisation of the central spindle or midzone during anaphase. In mammals and insects, PRC1 localizes to the antiparallel overlap in the midzone. As anaphase progresses, the overlap narrows in width and length and an increase of PRC1 intensity is observed (Fig. 1.7A) [224, 198]. PRC1 recruits Kinesin-4 to the overlap, which slides microtubules and suppresses microtubule dynamics at the plus ends [224, 206]. Interestingly, in HeLa cells depletion of Kinesin-4 KIF4A and depletion of PRC1 have the same effect: They prevent the narrowing of the central spindle into a compact structure and result in aberrant cytokinesis [224]. Similar results are observed in *Drosophila* [46].

In fission yeast, the role of Ase1 (PRC1 analogue) is described both in interphase and mitosis. During interphase, it is involved in the formation of antiparallel overlaps in the interphase microtubule arrays [120, 216]. In addition, it recruits Cls1 to these overlaps to ensure rescues of microtubules [21], described in detail in subsection 5.1.

During mitosis, it is recruited to the spindle at metaphase, where its absence results in

the formation of shorter spindles, likely because of a failure to recruit Cls1 and stabilize microtubules [21, 53]. In anaphase, it organises the midzone: deletion of Ase1 disrupts the arrangement of the microtubules and reduces Cls1 recruitment, which can result in spindle breaking [120, 216, 21]. Turnover of Ase1 is decreased dramatically in anaphase in comparison to metaphase [60], like in mammals [10]. These functions and its coordination with other proteins are extended in subsection 5.2.

In vitro work on PRC1/Ase1 has been key in our understanding of the spindle midzone. In particular, the work was aimed at answering the question of how motors and MAPs form overlaps that are maintained over the course of several minutes during anaphase. Motivation to explore diffusive crosslinkers came from the observation that ensembles of plus and minus end directed motors alone could not form stable overlaps *in vitro* [86, 196], as predicted previously by computer simulations [144]. In the next sections, we describe in more detail some *in vitro* work that was foundational in our understanding of antiparallel overlaps.

In vitro studies on Ase1

Pioneering *in vitro* studies showed that Ase1 bundled antiparallel microtubules specifically [95], demonstrating that this was an inherent property of the molecule and did not require other factors. It was also observed that Ase1 diffused on single microtubules and microtubule overlaps [99].

In the absence of motors, microtubules crosslinked by Ase1 diffuse with respect to one another (Fig. 1.8A) [114]. During motor-driven sliding by weak kinesin-14 motors, presence of Ase1 in the overlap slows down sliding speed [22, 114]. When microtubules fully overlap (a short microtubule moves along a fixed long microtubule), Ase1 accumulates at the rear of the moving microtubule due to diffusion. When the short microtubule slides past the end of the long microtubule, overlap shrinks but Ase1 is retained in the overlap. This increases Ase1 density and results in the stabilization of the overlap (Fig. 1.8B) [22, 114].

When reducing the overlap of Ase1 crosslinked microtubules with flow or a piezo stage, Ase1 accumulates in the shrinking overlap, and eventually generates an opposing force, stabilising the overlap (Fig. 1.8C, left) [22, 114]. The magnitude of this force is at most ~4 pN (Fig. 1.8C, right). Furthermore, when the force is released, the microtubule slides back and the overlap expands. The speed of expansion is higher for shorter overlaps, which contain less crosslinkers (Fig. 1.8D). This effect is driven by entropic forces resulting from restricting the bound molecules to fewer binding sites as the overlaps shortens [114].

A puzzling observation from the experiments in [22, 114] is that, without external force, residence time of individual Ase1 molecules in the overlap was around one minute. However, when the overlaps were compressed, Ase1 remained bound for more than 15 minutes without significant changes in intensity, even when soluble Ase1 was flushed from the chamber. Maybe this goes along with the observation of [99] that Ase1 can oligomerise. However, in [99] oligomerisation resulted in the formation of puncta of Ase1 that could be seen in the microscope. Such puncta were not reported in [22, 114]. This higher residence time is a key requirement for the observed increase in density in shrinking overlaps. If the turnover remained as fast as when force was absent, unbinding of Ase1 would prevent the strong accumulation that is observed experimentally when overlaps are compressed.

In [98], the authors showed that Ase1 could counteract the sliding of tetrameric kinesin-6 Klp9 from yeast (Fig. 1.8F), showing that this braking effect is not restricted to motors

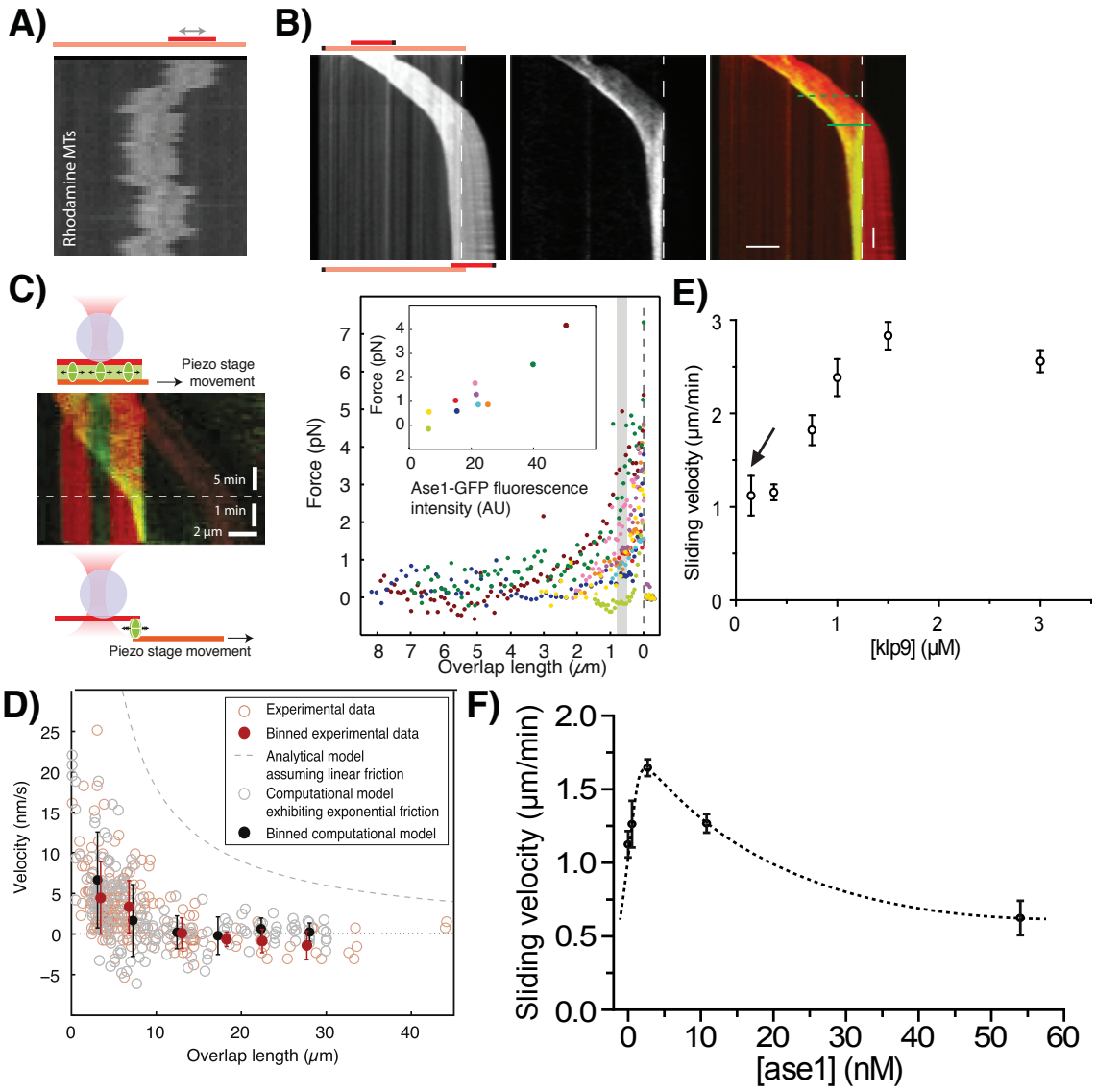

Figure 1.8: Ase1 *in vitro* experiments

A) From [22]. One-dimensional diffusion of a transport microtubule relative to an immobilized template microtubule at low Ase1-GFP concentration. **B)** From [22]. Same system as in (A), adding kinesin-14 motors that cause sliding. Note the accumulation of Ase1-GFP at overlap edges as the overlap between microtubule decreases. **C)** From [114]. Left: Typical multichannel kymograph showing the movement of the dimly labeled template microtubule (driven by the movement of the piezo stage) relative to the trapped, brightly labeled transport microtubule in the absence of free Ase1-GFP in solution. The density of Ase1-GFP increased in the shortening overlap. The region with enhanced localization of Ase1-GFP signal corresponds to the microtubule overlap. Right: Equilibrium bead displacements, corresponding to the steady-state forces induced by the confined Ase1-GFP in the overlaps, as function of overlap length. The inset shows the measured forces as function of Ase1-GFP fluorescence intensity in the overlap averaged for overlaps with lengths between 0.6 and 0.8 μm (denoted by the gray box in the main panel; same color-coding of measurements). **D)** From [114]. Averaged velocities of Ase1-GFP induced microtubule sliding as function of overlap length. Shown are experimental data (red open circles), results from the analytical model (gray dashed line, assuming a constant number of Ase1-GFP in the overlap), as well as results from the computational model (gray open circles, total of 24 simulation runs). ... (continues next page)

(legend from Fig. 1.8) ... In the computational model, the initial number of crosslinkers n0 and initial overlap lengths L0 were chosen from the experimentally observed range of n0 = 10, 20, 50, and L0 randomly between 0.1 and 30 μm, respectively. The overlaps were allowed to expand for at least 15 min. Solid red and black circles represent the binned averages (±SD) of the experimental data and the computational model, respectively. Data points (overlap lengths ranging from 0 to 30 μm) were binned in six equidistant bins with a width of 5 μm. **E)** From [98]. Sliding velocity of unidirectionally moving transport microtubules for different Klp9 concentrations. Error bars indicate SE. Arrow denotes the concentration of Klp9 that was used in (F). **F)** From [98]. Sliding velocity of unidirectional transport microtubules at increasing Ase1 concentrations. Klp9 concentration was 150 nM. Error bars indicate SE.
Reproduced with permission from [22, 114, 98].

---

with diffusive domains like Kinesin-14, which are less efficient in force generation [124]. However, the interpretation of these experiments is not straightforward. The concentration of motor used in combination with Ase1 was below the concentration at which the motor alone would slide the microtubules at its maximum speed (Fig. 1.8E, arrow). Interestingly, in these conditions, low concentrations of Ase1 were shown to increase Klp9 sliding efficiency. Further characterisation of Klp9 biochemical properties and its behaviour in the presence of Ase1 would be useful to understand the roles of these proteins, as they work closely together in anaphase (see subsection 5.2).

In vitro studies on PRC1

The study that most resembles the previously described Ase1 experiments, using human PRC1 instead, is [180]. The authors used a similar approach as in [22, 114], and studied the influence of PRC1 on sliding by molecular motors. However, in this case they used tetrameric kinesin-5, which is known to be able to generate forces in the pN scale [177], higher than kinesin-14 [124]. In this setup, PRC1 presence did not have much impact on microtubule sliding by Kinesin-5: When PRC1 was in an excess of 25:1 in the overlap, sliding speed was only reduced by half. It must be noted however that in the conditions of the study, reducing the overlap did not result in the retention of crosslinked PRC1 in the overlap, unlike in [22, 114], so the effect of an increase in density in a shrinking overlap on Kinesin-5 sliding has not yet been tested.

Most of the *in vitro* studies on PRC1 have focused on its role in combination with kinesin-4, which directly binds PRC1. The setups used have varied and addressed different consequences of this interaction. In [16] the authors used immobilised microtubule seeds, PRC1 and kinesin-4. In their assay, microtubules are nucleated from the immobilised seeds and as they grow, they make contact and form antiparallel overlaps with other growing microtubules through PRC1 crosslinking (Fig. 1.9A). Purified PRC1, like Ase1, binds preferentially to antiparallel overlaps, and PRC1 recruits kinesin-4 to the overlap by physical interaction [16]. There, kinesin-4 moves towards the plus end of the microtubules, where it stops microtubule growth[16]. Since kinesin-4 molecules bind all along the overlap and move towards the plus end, the amount of kinesin-4 that reaches the plus end and suppresses microtubule growth increases with overlap length. Therefore, the overlap grows until it reaches a length where kinesin-4 recruitment fully suppresses microtubule growth [16]. This mechanism allows for the formation of stable overlaps of defined length for a

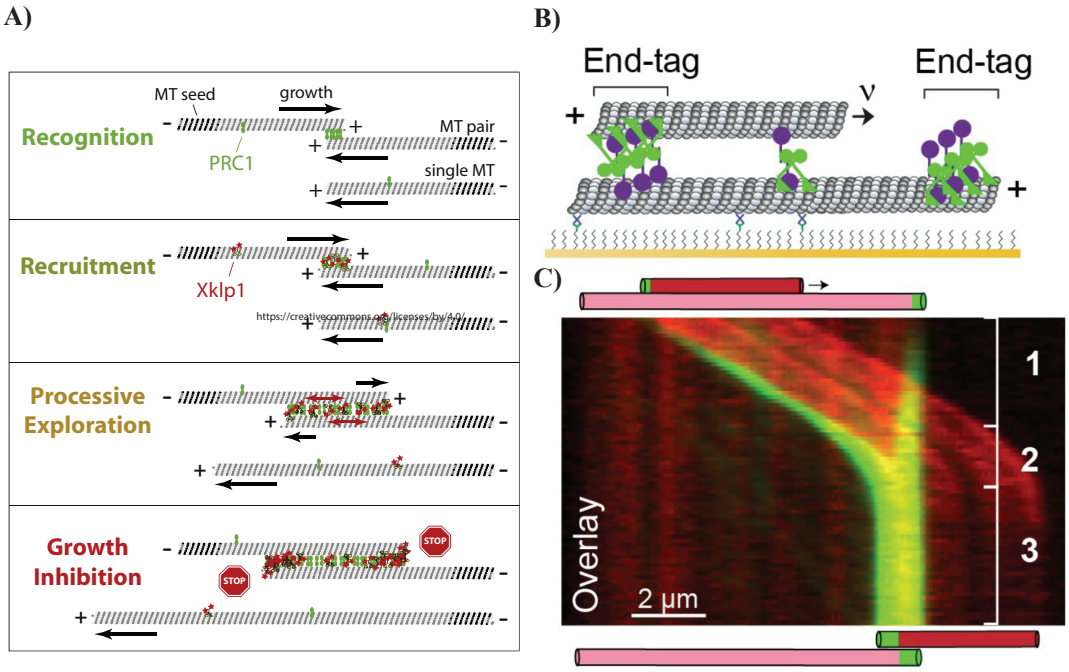

Figure 1.9: PRC1 *in vitro* experiments

A) Summary of the results in [16]. Microtubules grown from stabilised seeds make contact and get crosslinked by PRC1 (green). Kinesin-4 (Xklp1, red) is recruited to the overlap by PRC1 in a length-dependent manner and moves towards microtubule plus ends, where it inhibits microtubule growth. As overlap grows, more kinesin-4 is recruited until growth is completely suppressed. **B)** Cartoon representing the experiments in [211]. PRC1 (purple) crosslinks microtubules antiparallelly and recruits kinesin-4 (green). PRC1/kinesin-4 drive sliding of microtubules and accumulate at the plus ends of microtubules forming end tags. **C)** Kymograph of an experiment as described in (B). *Reproduced with permission from [16] and under the CC BY 4.0 terms from [211].*

given concentration of motor in solution (Fig. 1.9A) [16]. On single stabilised microtubules kinesin-4 and PRC1 accumulate at plus-ends, forming the so-called end tags [179]. This accumulation increases linearly with the length of microtubules, suggesting that kinesin-4 binds to PRC1 all along the microtubule, transports PRC1 to the tip. In microtubule overlaps [211], PRC1 and kinesin-4 together can produce sliding. This is an important point because kinesin-4 is dimeric and on its own it does not crosslink microtubules, so it cannot produce sliding. However, through interaction with PRC1, it forms a complex that is able to crosslink and slide microtubules. Interestingly, kinesin-4 and PRC1 also accumulate at the plus end of microtubules as they slide (Fig. 1.9B, C). Similarly to kinesin-14 in combination with Ase1, microtubules slide until a high density of PRC prevents further sliding. These two activities (sliding and growth suppression) make the PRC1/kinesin-4 system a suitable candidate to reproduce the anaphase central spindle behaviour *in vitro*: sliding while keeping an overlap that lasts several minutes. However, these two activities have not been tested simultaneously before.

Modelling of diffusible crosslinkers

Mathematical modelling has been used to analyse the observed *in vitro* phenomenology, namely the ability of diffusible crosslinkers to act as a brake against motor sliding, form stable overlaps, and produce forces that expand microtubule overlaps.

In [114], the authors proposed a model to explain the expansion forces observed when reducing overlap length while retaining crosslinkers. This force is the result of decreasing the entropy by constraining the same number of molecules to fewer binding sites. Calling a the lattice size of the microtubule (8 nm in the microtubule), and ρ_c the occupancy of sites of the lattice, the entropic force is $-(k_BT/a)\log(1-\rho_c)$. Hence, for an occupancy of 0.99, the force is around 2 pN. This is consistent with the observed maximum forces measured in the overlaps in [114], which were ~4 pN. To model the resistance to sliding, the authors proposed that the diffusive nature of crosslinker molecules allows them to act as viscous brakes, and we can thus associate a viscous drag to each crosslinker. In such a model, the drag exerted by diffusive crosslinkers would increase linearly with the number of crosslinkers. However, combining this drag with entropic forces predicted higher expansion speeds that the ones observed experimentally (Fig. 1.8D, dashed line on top).

To explain this effect, the authors turned to computer simulations, in which they accounted for the discrete nature of the microtubule lattice. In the simulations, the effective drag increased exponentially with the number of crosslinkers, and predictions of the model matched the experiment (Fig. 1.8D, black dots). It is important to understand the assumptions that produce this behaviour: Diffusive crosslinkers are modelled as two heads that can independently hop between adjacent sites on the microtubule lattice, connected by an elastic linker (Fig. 1.10). The stiffness of the linker affects the rates at which the molecule hops between adjacent sites. This is described in detail in chapter 2, but Fig. 1.10 provides a graphical representation of the elements of the model. We can qualitatively see that, as the linker becomes stiffer, the energy penalty of displacing microtubules with respect to each other increases. To estimate the stiffness value, the authors used the fact that diffusion rate of crosslinkers is different on single microtubules (~0.1 $\mu m^2/s$) than on microtubule overlaps (~0.01 $\mu m^2/s$). Given their assumptions of the rates, this requires a stiffness of ~400 pN/μm. The force associated with the displacement of one lattice site is then around 3 pN, which is significantly bigger than the typical thermal forces at that length scale $k_BT/a \simeq 0.5$pN. Due to the high stiffness, overlap microtubules would adopt positions in which their lattice sites are aligned. Any off-register configuration is unlikely. In this regime, the rate of transition from an aligned position to an adjacent one decreases exponentially with the number of crosslinkers.

In [97], the authors proposed a particle-based stochastic model to solve the steady state of a system composed of strong motors like kinesin-5 and diffusible crosslinkers. Their numerical results predicted formation of overlaps by a mechanism in which crosslinkers at the edges of the overlap oppose a higher resistance than in the body because microtubule ends act as diffusion barriers for crosslinkers. In this way, crosslinker-driven forces are length independent, since they only happen at the edges, while motor forces scale linearly with microtubule length. In this model, while the steady state is well explored, the friction produced by crosslinkers is not addressed.

5 Fission yeast as a model system to study microtubules

Fission yeast has been the model organism of choice for many researchers who study microtubules and MAPs. One of the biggest advantages is that genetic tools available to delete, tag or modify genes are simple compared to higher eukaryotes. Additionally, the microtubule cytoskeleton organization is less complex, and is composed of very few microtubules.

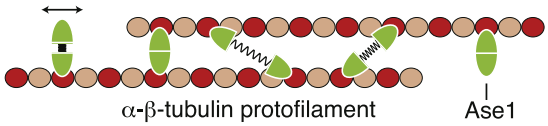

Figure 1.10: Ase1 modelling
Cartoon of the modelling framework used for diffusible crosslinkers in [114]. Ase1 is modelled as two heads that can independently bind to two microtubules and are connected by an elastic linker that affects the rate at which they hop between neighbouring sites.
Reproduced with permission from [114]

5.1 Microtubules in interphase

In interphase, microtubules are organised into three to four antiparallel bundles that overlap neir their minus end and are attached to the nucleus (Fig. 1.11) [192]. These overlaps are linked to interphase Microtubule Organising Centers (iMTOC), and one of them coincides with the SPB. During a typical growth event, microtubules grow at a speed of around ~2.3 µm/min for ~3 minutes [172], which allows them to reach the cell ends (typical length of a cell is 7 µm after cytokinesis, and 14 µm at mitosis onset [158]). When they grow, the cell boundaries constrain their orientation, so the bundles are aligned with the cell axis. When microtubules contact cell tips, they transmit forces that push the nucleus (Fig. 1.11). Such forces pushing at both cell tips keep the nucleus at the cell center, which ultimately determines the position of cytokinesis [192]. When microtubules touch the cell surface, they deliver factors that control polarised growth [38]. As a consequence, mutations that decrease the length reached during a growth event can have an effect on cell shape. This helped identify these genes in early genetic screens that looked for cell shape changes, which ultimately showed that some of the mutations affected microtubule dynamics [129, 13].

This organisation of microtubules requires the activities of multiple proteins (Fig. 1.11):

- Sad1-Kms2 anchor iMTOCs to the nuclear membrane, which in turn recruit γ-tubulin complex (γ-TuC), yeast homologue of γ-TuRC, and its activators, Mto1 and Mto2, to nucleate microtubule directly at the iMTOC [45].
- The antiparallel crosslinker Ase1 ensures that microtubules at the iMTOC are arranged with their plus ends facing outward [120, 216].
- In addition, nucleating complexes can land on pre-existing microtubules, get crosslinked antiparallelly by Ase1, and be transported to the iMTOC at the cell center by the kinesin-14 Klp2, which is specifically recruited to the plus end of the new microtubule by Mal3 [95].

Microtubule dynamics in interphase are regulated by two antagonistic sets of proteins that are targeted to the plus end by motor activity (Fig. 1.11). On the one hand, the complex of Tea2/Tip1/Mal3/Alp14 promotes microtubule growth and prevents catastrophe, while the Klp5/Klp6/Mcp1 complex promotes catastrophe [134]. Tea2 is a Kinesin-7 protein that moves towards the plus end. Its motor activity and the presence of Mal3 at the microtubule plus end are required to recruit Tip1 (CLIP170) at the plus ends [33]. This protein complex recruits Alp14 (XMAP215), which promotes growth and prevents catastrophe [147]. Interestingly, the accumulation of this complex at the plus end is not

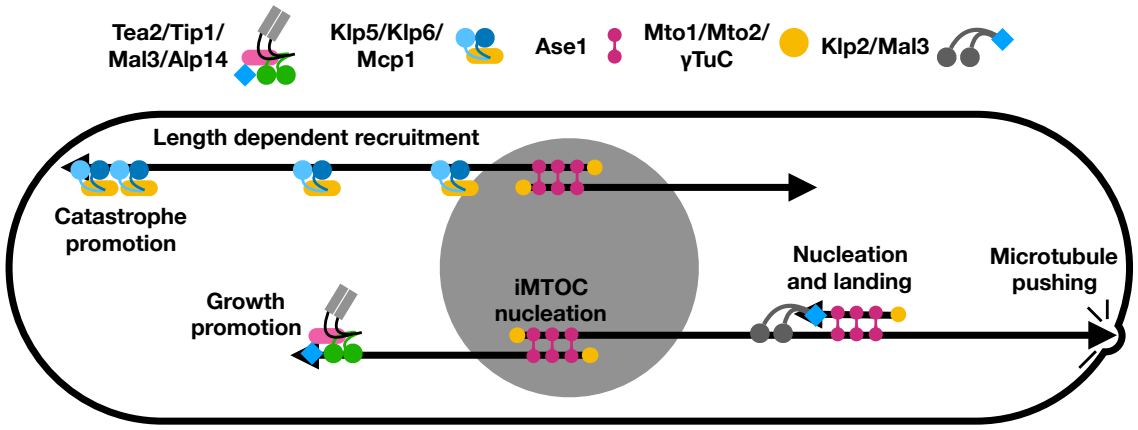

Figure 1.11: Microtubules in fission yeast interphase
Cartoon depicting the roles of microtubules and MAPs mentioned in section 5

length-dependent [134], perhaps because of high turnover of the proteins. In contrast, the complex composed of a heterodimer of Klp5/Klp6 (both kinesin-8) and Mcp1, is recruited along the microtubule and accumulates at the plus end in a length dependent manner, eventually displacing the Tea2/Tip1/Mal3/Alp14 complex and triggering a catastrophe [223, 134]. Microtubule rescues happen at the iMTOC, where Ase1 recruits Cls1 to promote rescue [21].

5.2 Microtubules in mitosis

Fission yeast undergoes closed mitosis (the nuclear envelope does not break down), which in the literature is typically divided into three phases that can be followed by the spindle length / SPB separation: prometaphase, metaphase/anaphase A, and anaphase B [143]. Prometaphase comprises the establishment of bipolarity and the initial elongation of the spindle . In metaphase, chromosomes biorient while the spindle elongates at a very slow speed. When Anaphase A is triggered, chromosome are segregated. Finally, during anaphase B, the spindle elongates dramatically from a length of approximately 2.5 µm to ~12 µm [] (Fig. 1.3).

Prometaphase

In prometaphase, the duplicated SPBs, which only face the cytoplasm during interphase, are inserted in the nuclear envelope [19] in a process known as fenestration [96]. Once inserted, they recruit γ-TuC [58] and Alp14 [56] on their nuclear side to promote microtubule nucleation. Nucleated microtubules have their minus ends anchored to the SPB [50]. Soon after prometaphase onset, microtubules emanating from both SPBs establish contact, crosslink antiparallelly and through microtubule sliding by kinesin-5, promote spindle bipolarity (Fig. 1.3). Consistent with this idea, Cut7 thermosensitive mutants (cut7 is an essential gene) form monopolar spindles, that fail to separate SPBs and stablish bipolarity. However, strains containing a double deletion of kinesin-5 cut7 and kinesin-14 pkl1 are viable, and assemble bipolar spindles, although significantly shorter than both wt and pkl1Δ strains [164]. This suggests that in the absence of Cut7, Pkl1 motors, which localise to the SPBs, prevent the separation of spindle poles.

It is worth mentioning that the requirements to establish spindle bipolarity are different in meiosis and mitosis. For example, cut7Δpkl1Δ mutants, which can achieve bipolarity normally in mitosis, fail to do so in meiosis. Both deletion of the other kinesin-14 gene klp2 or treatment with MBC, which perturbs microtubule dynamics, increase the rate at which cells manage to assemble bipolar spindles. This means that kinesin-14 molecules have distinct roles in meiosis and mitosis, and that microtubule dynamics are also important for the establishment of bipolarity [121].

Metaphase

After achieving bipolarity, the spindle elongates and reaches a length of approximately $2m$. During metaphase, spindle elongation is minimal and the tension between sister chromatids is matched by the motor forces exerted by Cut7 in the midzone [127] (Fig. 1.3). Sister chromatids linked by cohesin behave like an elastic linker, such that when motor forces from the midzone are transmitted to kinetochores through kinetochore fibers, the linker stretches and produces a counter acting force [44]. Forces on kinetochores also have an effect on dynamics of the attached microtubules. Their plus ends are linked to kinetochores by the Ndc80 complex, which recruits other MAPs, like Dis1, Alp14/Alp7 and Klp5/Klp6 [185, 91, 184]. *In vitro* experiments have shown that when a microtubule depolymerises and is pulled away from the kinetochore surface, kinetochore proteins reduce shrinking speed and promote rescue [59]. Importantly, applying a force to pull the microtubule away from the kinetochore enhances this effect, and further reduces shrinking speed and promotes rescue [59]. Therefore, tension applied on kinetochores directly promotes growth of kinetochore fibers. How the coordination of individual kinetochore proteins and MAPs produces these effects on microtubule dynamics is not completely understood. This mechanism is conserved in kinetochore attachments across eukaryotes, although the proteins involved differ between organisms [213, 127].

Mechanical and biochemical properties of kinetochores promote the formation of amphitelic attachments (all the attachments of one kinetochore are linked to the same pole, while all the attachments of the sister kinetochore are linked to the opposite pole, Fig. 1.12A).

1. Firstly, the SAC prevents transition to anaphase when kinetochores are unattached [77].

2. In addition, kinetochore attachments are stabilised under tension. This makes amphitelic and merotelic attachments (Fig. 1.12A, D), which are connected to both poles, more stable, since kinetochore microtubules from opposing poles keep the centromere in tension. In contrast, monotelic or syntelic attachments (Fig. 1.12B, C), in which all the attachments are connected to a single pole, are not under tension, and microtubules detach from kinetochores at a higher rate [3].

3. Finally, a biochemical mechanism promotes the transition from merotelic to amphitelic: Phosphorylation by Aurora B promotes detachment, and its activity is highest at the centromere equator. This gradient of Aurora B activity promotes the detachment of merotelic attachments, which are positioned closer to the centromere equator, since pulling forces on the kinetochore come from both sides (Fig. 1.12E) [182, 42, 108].

The combination of all these mechanisms promotes proper orientation before transitioning to anaphase. Besides promoting the correct attachment and orientation of kinetochores,

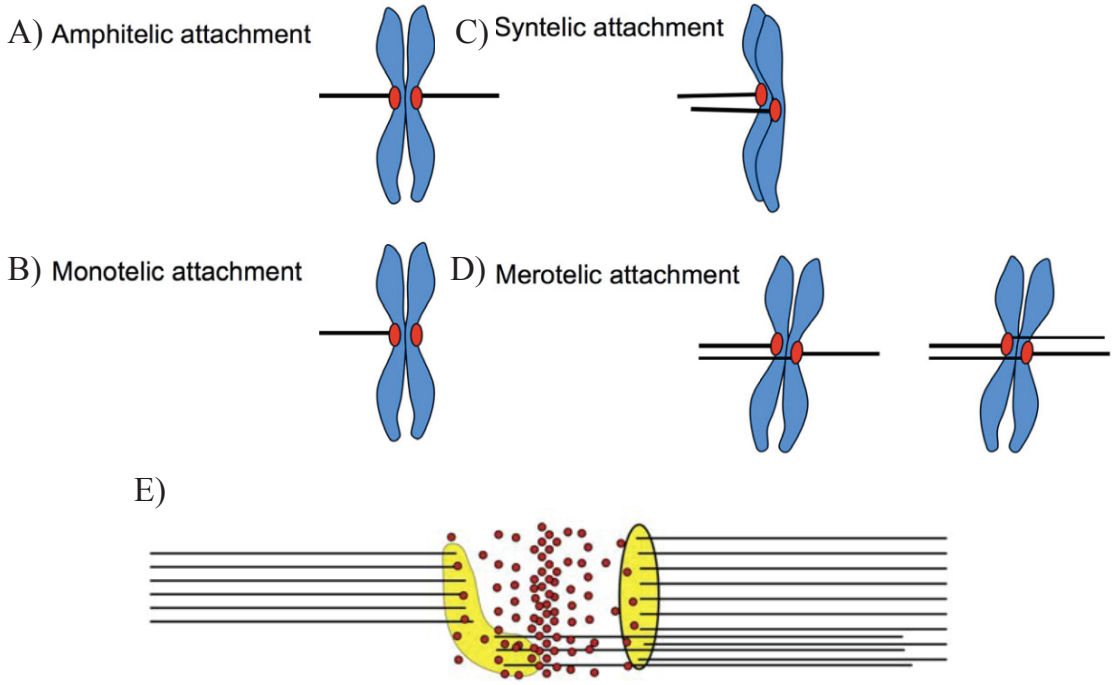

Figure 1.12: Kinetochore attachments

A) In amphitelic attachment, the sister kinetochores are correctly connected to microtubules from opposite poles, resulting in a bioriented chromosome. **B)** In a monotelic attachment, only one of the sister chromatids is connected to a spindle pole: the chromosome is mono-oriented. **C)** In a syntelic attachment, both sister kinetochores are attached to a single spindle pole, and the chromosome is mono-oriented. **D)** In a merotelic attachment, usually one or, rarely, both sister kinetochores are connected to both poles instead of one. Chromosomes are bioriented in merotelic attachments. **E)** Merotelic attachments are closer to the centromere equator, where Aurora B is the highest, and promotes their detachment.
Reproduced with permission from [79, 42].

forces generated by microtubule depolymerisation at kinetochores promote the oscillation of chromosomes and their congression to the cell equator prior to anaphase A [127]. Despite all this, merotelic attachments can still be present at anaphase onset, but the frequency is very small. These events are known as "lagging chromosome" [44].

Anaphase A

At anaphase A, the link between sister kinetochores through cohesins is degraded [157], and microtubule depolymerisation of kinetochore fibers drives the movement of chromosomes from the equator towards spindle poles [44]. Interestingly, since microtubule growth at kinetochores is affected by tension as detailed above, cohesin degradation alone triggers the depolymerisation of kinetochore microtubules which segregate chromosomes to the poles.

Rare merotelic attachments are evidenced at this stage (lagging chromosomes), because sister chromatids do not initially segregate and remain at the spindle equator. These errors can be resolved in anaphase B [127].

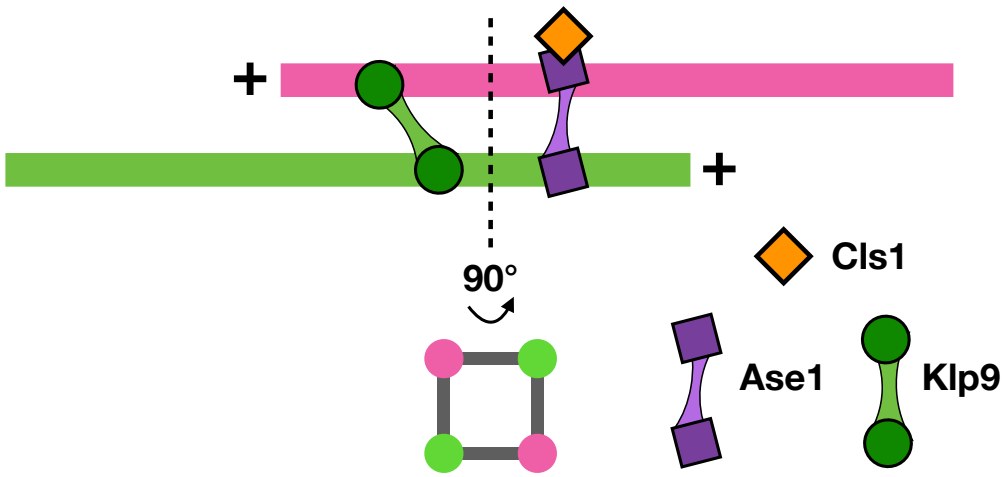

Figure 1.13: Anaphase B in fission yeast
Cartoon depicting the three main players involved in spindle elongation (Klp9, green), midzone organisation (Ase1, purple), and microtubule rescue (Cls1, orange) during anaphase B. Klp9 produces the relative sliding of antiparallel microtubules by walking to their plus ends. Ase1 ensures the formation of a midzone in which the microtubules are organised in an antiparallel square lattice. By allowing microtubules to only be crosslinked to antiparallel neighbours, a square lattice spontaneously forms (see rotated view). Cls1 is recruited to the midzone by Ase1, where it promotes rescues of shrinking microtubules.

Anaphase B

During Anaphase B, the spindle elongates dramatically from 2.5 µm to 12 µm. The switch to Anaphase B requires dephosphorylation of Cdk1 substrates by phosphatases [166, 60]. Tetrameric kinesin-6 Klp9 is dephosphorylated at anaphase onset and recruited to the midzone, where it drives microtubule sliding, and thus spindle elongation. Ase1 is also dephosphorylated, resulting in a dramatic decrease of the turnover of the protein at the midzone [60]. Ase1 in turn recruits Cls1 to the midzone, which is required for microtubule rescue: in its absence, interpolar microtubules fully depolymerise at anaphase onset due to lack of rescues [21]. The known activities of these three players (Klp9, Ase1 and Cls1) allow us to produce a minimal model to explain how elongation of the spindle during Anaphase B takes place (Fig. 1.13).

Spindles elongate at a constant speed during anaphase B, driven by antiparallel sliding by Klp9. Klp9 deletion results in slower spindle elongation [60], while overexpression of Klp9 increases sliding speed [111]. In addition, sliding is faster in bigger cells, but this scaling is suppressed if Klp9 is not present, which ultimately suggests that the total levels of Klp9 determine the sliding speed of anaphase B [111]. It is not clear why an increased number of motors at this stage would result in faster elongation, or whether sliding speed in the wild type condition is force limited. Forces opposing sliding by motors could either come from MAPs bound to the overlap, or forces acting on spindle poles. Forces at spindle poles required for nuclear deformation or viscous forces generated by the extension of the nucleus are predicted to be small compared to typical motor-generated forces [208]. In addition, theoretical calculations based on the physical properties of microtubules *in vitro* predict that late spindles present in cells would buckle under compressive forces of ~15 pN [208]. However, in wild type cells, spindles only buckle when the poles reach the edges of the cell, which would suggest that forces on poles are small. This

makes crosslinking proteins at the midzone a more promising candidate to act as brakes. Nevertheless, deletion of multiple MAP candidates that could act as brakes against sliding in the midzone, including Cut7 and Ase1, does not affect the sliding speed [111]. To my knowledge, the only study to find a counter acting force that slows down sliding speed of interpolar microtubules is [44], where the authors used a cohesin mutant that promotes the formation of merotelic attachments. They observed that the speed of spindle elongation decreased linearly with the number of kinetochores with merotelic attachments, suggesting that the force exerted at the poles by the kinetochore fibers counteracts the force of sliding motors. It should to be noted that merotelic attachments in anaphase B are extremely rare and cannot account for the wild type midzone sliding speed. Ultimately, biochemical characterisation of sliding by Klp9, which is lacking at the moment, might shed light on how this motor sets sliding speed of interpolar microtubules.

Besides the role on interpolar microtubule sliding, dephosphorylation of Klp9 at anaphase onset is required for the translocation of the Chromosome Passenger Complex (CPC) from centromeres to the spindle midzone in the metaphase to anaphase transition [133]. When Klp9 is deleted or its dephosphorylation is prevented, CPC components like Aurora B localise along the whole spindle rather than being constrained to the midzone. This has no consequence for chromosome segregation, but delays metaphase to anaphase transition due to a delayed activation of the Anaphase Promoting Complex [133] and makes total anaphase duration longer [111]. This is a conserved property of kinesin-6 proteins that is also observed in mammalian cells, where CPC translocation from centromere to central spindle mediated by kinesin-6 is important for mitotic timing [105].

Due to its biophysical characteristics described in detail in subsection 4.4, Ase1 maintains the structure of the midzone through antiparallel crosslinking of microtubules at the midzone [216, 120]. By allowing microtubules to only be crosslinked to antiparallel neighbours, a square lattice spontaneously forms (Fig. 1.13 [208, 51]). Deletion of Ase1 disrupts the formation of the midzone: tubulin signal in ase1Δ mutants no longer shows the typical intensity pattern with higher signal in the center, where microtubules overlap, and lower signal at the edges, where there is no overlap [120]. In addition, spindles in ase1 deleted cells disassemble at a shorter length than wild type spindles, suggesting that spindle poles lose contact because antiparallel connections are lost [120, 216]. In rare occasions, some anaphase spindles collapse at early stages and two halves of a broken spindle can be observed [120]. Because of its roles in spindle structure, Ase1 function is important to keep genome integrity and support faithful chromosome segregation [216]. At anaphase onset, Ase1 is dephosphorylated, which drastically decreases its turnover. Ase1 recruits Cls1 to the spindle midzone [21], where it can promote microtubule rescue [169].

As explained above, the functions of the main players involved in anaphase spindle elongation are well characterised. However, a fundamental gap still remains in the picture, and that is microtubule dynamics. To ensure the persistent elongation of the spindle, a permanent connection between spindle poles has to be maintained. This necessarily involves a coordination between sliding and microtubule dynamics. However, we do not know how anaphase MAPs regulate microtubule dynamics beyond the fact that Cls1 is required for microtubule rescue. In the case of yeast, individual microtubule dynamics in the spindle have never been measured, except at the end of anaphase, where the spindle has only ~4 microtubules and labelled tubulin allows for visualization of microtubule dynamics in a kymograph [169]. In higher eukaryotes, where microtubules are more sparsely distributed in space during metaphase, growth and duration of events have been measured in metaphase using EB1 [161] or tubulin signal [113]. However, in the central spindle,

microtubule density is very high and individual microtubules have not been observed yet. We know from FRAP studies that no nucleation of microtubules happens during fission yeast anaphase B [125, 103], which means that the spindle can only lose microtubules as anaphase progresses. This is supported by electron microscopy studies [51, 208]: as spindle elongates, the number of microtubules progressively decreases. Interestingly, the total polymerised length of microtubule reaches a maximum value that is kept roughly constant during anaphase B, which suggests that total tubulin amounts might be limited [208]. Therefore, the characterisation of microtubule dynamics in anaphase remains a key challenge to improve our understanding of the mitotic spindle.

6 Modelling of the mitotic spindle

6.1 Metaphase models

Most of the modelling work of the spindle has focused on two aspects of metaphase: chromosome capture and biorentation, and the establishment of a steady state overlap length. Models of fission yeast and higher eukaryote spindles are different because of the mechanisms at play: In yeast, minus ends are not dynamic and are anchored to the spindle pole [51, 103]. In higher eukaryotes, minus end directed motors are required to cluster microtubule ends and form poles [30], and depolymerisation of microtubules occurs at the minus ends by kinesin-13 (fission yeasts does not have kinesin-13 homologues) [73]. In addition, microtubule nucleation in yeast occurs exclusively at the SPB [58] , while in higher eukaryotes nucleation can occur not only on centrosomes [113], but also around chromosomes [26] and on pre-existing microtubules [186]. Kinetochores of higher eukaryotes are more complex than those of yeast, and contain motor proteins that exert forces on kinetochore microtubules [61].

In the two following sections we present a summary of force balance models and microtubule flux models. These two models have been used to explain how the spindle maintains a steady state length during metaphase. Force balance models propose that this results from an equilibrium of inward and outward forces [171, 213, 127], while in microtubule flux models, nucleation, transport of microtubules and depolymerisation can explain the shape and length of the spindle [26, 123, 161]. Spindles of various scales present characteristics of each model to different extents. Small metaphase spindles of *S. Pombe* (~2 µm) have no microtubule flux [103], and are explained by force balance models [127], while large meiotic *X. laevis* spindles (~30 µm), where microtubule flux occurs across the spindle length, and there are no centrosomes to couple interpolar microtubule pushing and kinetochore tension are well characterised by microtubule flux models [26, 161, 123, 30]. In between, spindles exhibit characteristics of both models. For example, *Drosophila* S2 cells show mechanical coupling of interpolar microtubules and kinetochore fibers through centrosomes, but also display poleward flux [73].

Force balance models

Many of the metaphase models fall under the category of force balance models (Fig. 1.14). The term was first used to explain the antagonistic functions of plus-end directed kinesin-5 and minus end directed kinesin-14. Deletion of all kinesin-5 isoforms is lethal in budding yeast, where it leads to the formation of monopolar spindles. However, deletion of both kinesin-5 isoforms and kinesin-14 is viable [171]. This suggested these motors had

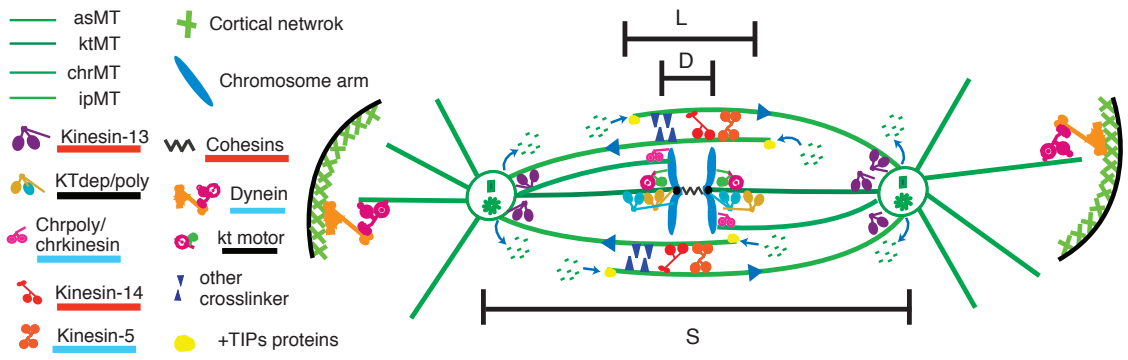

Figure 1.14: Force balance model

Cartoon depicting the different agents that take part in the force balance model. Components that exert only inward forces that reduce spindle length are underlined in red. Components that exert only outward forces that increase spindle length are underlined in blue. Components which can exert both are underlined in black. *L* represents overlap length, *D* inter-kinetochore distance, and *S* spindle length.

Reproduced from [213] under the CC BY 4.0 terms.

antagonistic effect, and it was proposed that the spindle length would be the result of a balance of outward forces in the overlaps, where kinesin-14 forces counteracted kinesin-5 forces, against inward forces coming from kinetochores.

Later experiments showed that overexpression of kinesin-14 decreased spindle length, and overexpression of kinesin-5 increased spindle length, even leading to spindle disruption by sliding [170]. This raised the possibility that both kinesins would act against each other on interpolar microtubules in a "tug of war" that would set spindle length. It was eventually shown that this is not the case: deletion of kinesin-14 decreases spindle length in budding yeast and fission yeast [87, 181], and biochemical experiments with purified kinesins have shown that kinesin-5 is several orders of magnitude stronger than kinesin-14 [86]. It seems then that kinesin-14 prevents the "snap" into bipolarity of the spindle in the absence of kinesin-5 rather than counteracting its outward force in the wild type scenario.

As more metaphase specific functions of motors were discovered, new modules of the force balance model emerged (Fig. 1.14) [213]: Inward forces originated at kinetochores can be driven by plus end depolymerisation, or minus-end directed motors bound to the kinetochore. Inward forces originated in interpolar microtubules come from depolymerisation of microtubules at their minus ends at the pole, and minus end directed motors at the spindle midzone. In addition, elastic inward forces come from the stretching of the centromere, which behaves like an elastic linker. Outward forces can come from plus-end directed motors located at the interpolar microtubules, kinetochores and surface of chromosomes, by polymerisation of microtubules attached to the kinetochore, and by pulling on astral microtubules by cortical dynein.

Mathematical formulations of force balance models were initially designed to describe pole separation in Anaphase B [28] or chromosome oscillations during metaphase [43] in *Drosophila* S2 cells, and were not intended to predict metaphase steady state length. Eventually a force balance model that accounted for force magnitude and sequential activation / inactivation of the modules in (Fig. 1.14) was used to explain the progression of spindle length in time during mitosis [213]. It is important to notice that the steady states generated by this model are not stable: perturbations in either pulling or pushing forces

drive the system away from steady state without mechanisms that would bring it back. This had been noticed previously [73], where the authors acknowledged that in such framework no stable steady state can be formed unless an extra assumption is added, for instance that the depolymerisation and sliding velocity of interpolar microtubules match. In addition, changing the protein levels of factors controlling microtubule dynamics changes spindle length significantly, while depletion of dynein, kinesin-14 or kinesin-5 on S2 cells only has minor effects. Kinesin-5 has an "all or nothing effect": below a given amount, spindles stay monopolar, but above that threshold increasing amounts have no effect on the length [73]. All these observations suggest that microtubule dynamics play a key role in setting metaphase spindle length.

In fission yeast, the trajectory of force balance models was similar: originally they were used to describe chromosome segregation during Anaphase A, and the effect that lagging chromosomes would have on spindle elongation in Anaphase B [44]. Eventually, the model was extended to explain the formation of metaphase spindles in [127]. A key mechanism was added to the model to allow the formation of stable steady states: a kinetochore force that increases with the length of kinetochore microtubules. This is produced by the combination of two mechanisms that influence microtubule dynamics:

1. The activity of kinesin-8, which triggers catastrophe in a length-dependent manner by being recruited along the microtubule and moving towards the plus-end (Fig. 1.11)[190].

2. The increase of rescue rate of kinetochore microtubules produced by forces pulling on them [59].

For a given force pulling the kinetochore microtubule away from the kinetochore, a steady state kinetochore microtubule length is reached when the force dependent rescue rate is matched by the length dependent catastrophe rate [127]. In this scenario, kinesin-5 outward forces push poles apart, which in turn exert a force on kinetochore fibers, promoting rescue, and resulting in their net elongation. Eventually, kinetochore microtubules reach a length where the catastrophe due to recruitment of kinesin-8 is such that kinetochore fibers no longer elongate. Then, a steady state is reached where midzone forces are matched by centromere tension [127]. This mechanism provides an explanation of why affecting microtubule dynamics can have a strong effect on spindle length, by changing the length of kinetochore microtubules [73], and is also compatible with spindle length increasing with higher amounts of kinesin-5 [170] in yeast. Strikingly, length dependent catastrophe of kinetochore microtubules in budding yeast is controlled by kinesin-5 and not kinesin-8 [65], suggesting that these two species have developed different mechanisms to regulate spindle length.

Other kinesin-5 functions that may influence the spindle in fission yeast are in general overlooked. Longer spindles have longer interpolar microtubules, which means that kinesin-5, in addition to generating force, may also promote the elongation of interpolar microtubules, which often span the whole spindle [115, 50, 208]. Kinesin-5 has been shown to promote microtubule polymerisation *in vitro* [40], so this function might operate as well *in vivo*. In addition, kinesin-14 and kinesin-5 bind to γ-TuC in fission yeast, inhibiting and promoting nucleation respectively, which suggests extra roles of kinesin-5 in metaphase [152]. Along these lines, in *Xenopus*, *Drosophila*, and yeast, kinesin-5 localises mostly at the poles, and the minimum signal is at the center of the spindle, where most microtubule overlap is found [194, 221, 39]. All these data suggest that kinesin-5 might have important functions other than sliding.

Microtubule flux models

Microtubule flux models are commonly used to describe meiotic spindles formed in *Xenopus* egg extracts [26, 123, 161, 30]. In these spindles, the effects of microtubule dynamics on spindle length have been extensively studied. This is because elegant laser ablation techniques have allowed to measure position and length distributions of microtubules that can be compared with model predictions [26, 48]. In this system, spindles are very big (~ 30 µm), microtubules are nucleated around chromosomes and are transported towards spindle poles by kinesin-5 motors that crosslink microtubules antiparallelly (Fig. 1.15A) [138]. In addition, microtubules can be nucleated on the surface of pre-existing microtubules [48], and are depolymerised at the spindle poles by kinesin-13 and katanin [123]. Importantly, *X. laevis* spindles of length similar to wild type spindle length can assemble in the absence of chromosomes [80]. This undermines contribution of kinetochore fibers in setting the spindle length.

Changing the growth of microtubules by modifying the concentration of XMAP215, or introducing mutations that affect its activity, revealed a direct proportionality between spindle length and individual microtubule growth speed [161]. This was explained by using a simple mass balance model, in which tubulin is incorporated mainly at the center of the spindle, where chromatin promotes microtubule nucleation, and microtubule growth results in movement of the minus ends towards the poles. Assuming a constant catastrophe rate, an increase in the spindle growth rate yields a longer spindle. This simple model could account for the morphology of the spindle as well as the spindle length dependency on growth speed of individual microtubules. However, a more detailed description of the system components, requires microtubules to be transported towards the poles of the spindle by kinesin-5 motors, which are significantly slower than microtubule growth [122]. Briefly, increasing microtubule growth speed above kinesin-5 walking speed cannot have an effect on how fast the minus end of a microtubule is transported towards the pole, and cannot affect spindle length (unless the microtubule grows against an obstacle, which is not generally the case, see section below). In this scenario, longer lifetimes or higher nucleation of microtubules would increase spindle length by increasing the number of minus ends reaching a given distance away from the equator, but growing speed should have no effect. Recent experiments have shown that XMAP215 is a microtubule nucleator, so perhaps the effects observed on spindle length might be a result of its nucleating activity [186]. In line with this possibility, mutations in XMAP215 that change its effect on growth speed, also affect its nucleation activity. It would be interesting to dissect these two contributions of XMAP215 on spindle length in the future.

An alternative mass balance model that reconciles these observations is the slide and cluster model [30], which proposes that microtubules are nucleated at the center of the spindle, catastrophe is independent of microtubule position, and microtubules are transported towards the poles by kinesin-5. It was shown that distributions of positions and lengths of microtubules in the spindle, and therefore spindle length, are consistent with this model [26]. Kinesin-5 alone can produce a bipolar spindle in such model, but for spindle poles to be focused, an extra factor is required [122]. This is promoted by higher microtubule depolymerisation by katanin at the poles [123] and by minus end clustering by dynein motors that operate on parallel microtubules [30]. The microtubule flux speed is comparable to kinesin-5 unloaded speed [100, 217], which suggests that motors are not force-limited in this system. Velocity only decays at the poles, where dynein clustering of minus ends of parallel microtubules counteracts antiparallel sliding [30].

A very interesting observation is that egg extract from the *X. laevis* close relative *X.*

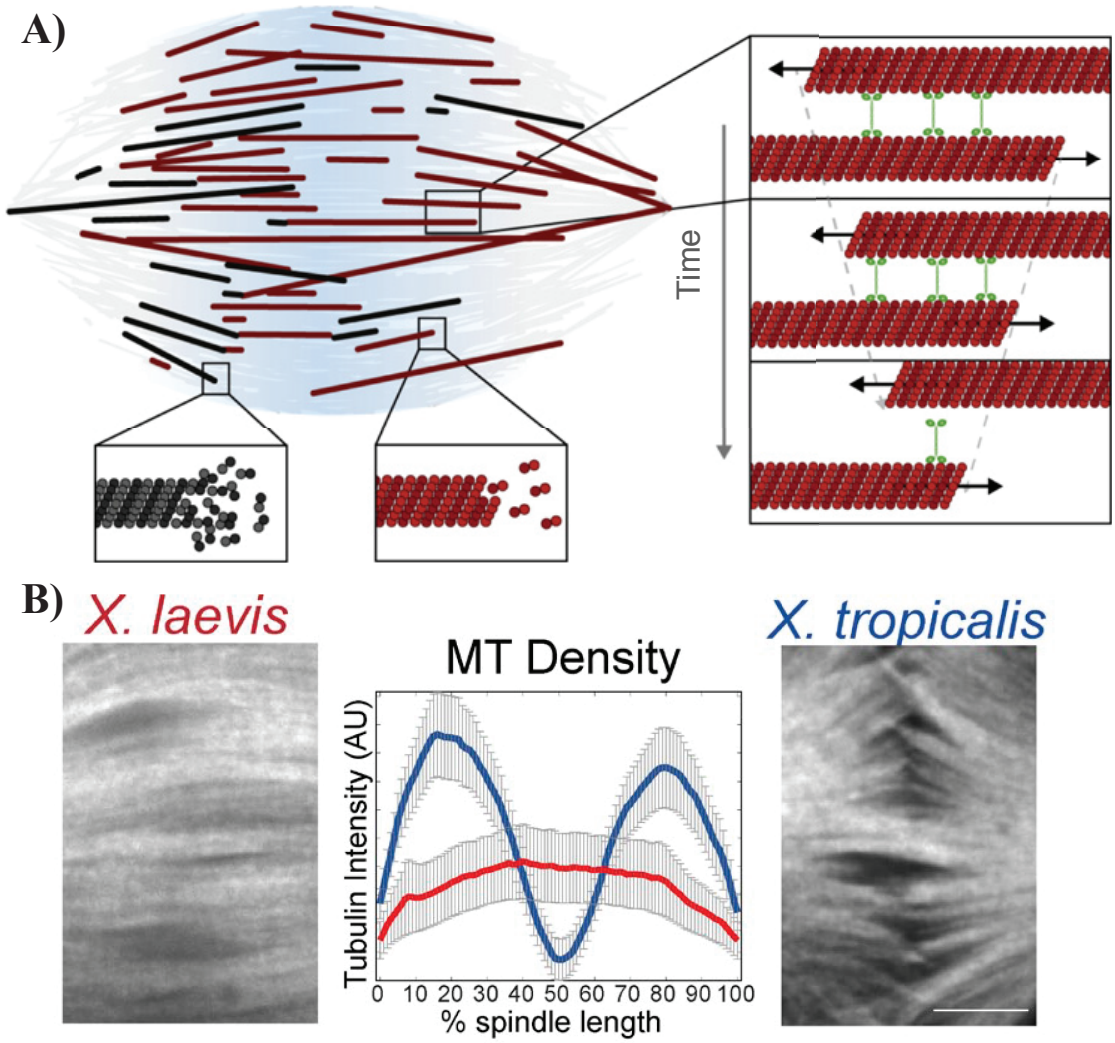

Figure 1.15: *Xenopus* egg extract spindles

A) Model of metaphase spindle of *X. laevis*, from [26] in which microtubules are nucleated at the equator by chromatin (light blue), then microtubules are transported towards spindle poles by antiparallel sliding of kinesin-5 (tetrameric motor shown in green on the inset at the right). **B)** Spindle architectures in egg extracts of *X. laevis* (left, red curve), and *X. tropicalis*, (right, blue curve). Note that *laevis* spindles have many interpolar microtubules and therefore highest intensity at the center of the spindle, while *tropicalis* spindles have barely any signal at the equator. *Reproduced with permission from [26, 85]*

tropicalis generates very different spindles, in which almost no interpolar microtubules are observed, and nucleation from chromatin is not necessary for spindle formation (Fig. 1.15B) [85]. These spindles are also shorter than those of *X. laevis*, around 20 µm. Most importantly, this behaviour is dependent on the protein TPX2, which shifts the localization of Eg5 from interpolar microtubules to poles. *X. laevis* extracts in which excess TPX2 is added, form spindles that look like those of *X. tropicalis* [85]. In both organisms, spindle length can be increased by suppressing the depolymerase activity of katanin at the poles. However, the effect is more severe in the case of *X. tropicalis*, where kinetochore fibers extend beyond the focused spindle poles [123]. It seems that the activity of TPX2 switches spindles from a mode in which their length depends on microtubule nucleation and flux to a mode in which the length is determined by the length of kinetochore fibers.

Other models

Computational models have been proposed in which spindle poles are treated as asters that nucleate dynamic microtubules. Those asters move in space due to microtubule pushing on cell boundaries and on the surface of chromosomes. They have been used to explain why in *C. elegans* metaphase spindle length increases with cell size, while spindle assembly timing remains constant [113]. In this system, microtubule growth speed increases with cell size. Simulating the spindle poles as two asters of dynamic microtubules in a confined cell volume, where a surface representing the chromosomes is placed in the center, causes the asters to separate from the chromosomes. The velocity of this process increases with growth speed of microtubules, but the time it takes to reach spindle length steady state is independent of cell size. A similar approach was used in [74], where the authors found that the tendency of polyploid cells to form multipolar spindles could be explained by chromosomes acting as physical barriers that prevent multiple spindle poles to make contact and cluster through kinesin-14 activity. These models are highly specific to the mentioned processes, however they capture most of the phenomenology using a simple model with few parameters.

In recent years, computational models that specifically simulate spindle components have been produced, and yield similar results as the simplified versions of force balance models [17, 54]. These models have the potential to be extremely powerful, since they simulate molecular motors, filaments, SPBs, etc. Therefore, experimental perturbations that affect only certain components of the system could be explicitly simulated. These computational models are likewise limited by the high number of parameters required to simulate those systems. The parameter space is very large, and key parameters are often not measurable experimentally due to technical limitations: microtubule nucleation rate, rescue rate, motor binding rates, and certain parameters of microtubule dynamics.

In summary, multiple models have been used to model metaphase spindles. Some of them are targeted at specifics aspects of it, like pole clustering [74], or a particular organism [17, 54] while others are more abstract and provide a general framework [213]. The large *Xenopus* spindle length seems to be governed by kinesin-5 flux and nucleation of microtubules and not by force [26], while in the small spindles of yeast, where certain microtubules span the whole spindle, kinesin-5 forces separate spindle poles, which pull on kinetochores elongating the k-fibers, until a force balance is reached [127]. Ultimately, all spindles are assembled for the same purpose: to organise the chromosomes along

a symmetric structure that will segregate them equally to two daughter cells. Despite the differences in size and organisation, kinesin-5 depletion effects on all organisms are remarkably similar, producing monopolar spindles. This suggests that conserved mechanisms operate across all scales and that sliding of antiparallel microtubules by molecular motors is a fundamental requirement for achieving spindle bipolarity.

6.2 Anaphase models

Anaphase has received considerably less attention than metaphase in terms of modelling. The same force balance models described above were used to model chromosome segregation in Anaphase A. Once the elastic linker between kinetochores is removed so is the tension on kinetochores. Therefore, rescues of kinetochore fibers are prevented, and they depolymerise. Shrinking plus ends then bring chromosomes to the poles. Hence, the same mechanism that causes oscillations of linked kinetochores in metaphase is responsible for chromosome segregation in Anaphase A, once cohesin is removed [213, 68].

As mentioned above, the foundational model that became the metaphase force balance model [28] was initially conceived to explain anaphase B in *Drosophila* S cells, and proposed that motors in the interpolar overlap drive the separation of poles. The authors argued that for the drag forces required to displace the poles, motors would not be force-limited, and the spindle would slide at a constant speed, as observed experimentally. They noted that microtubule dynamics were important for the maintenance of the overlap to sustain sliding, since no nucleation happens in Anaphase B. In [44], a similar model was used for fission yeast to explain why the presence of merotelic attachments that persist in anaphase B would slow down spindle elongation. In that scenario, forces coming from the merotelic attachment slow down spindle elongation by stalling kinesin-6 sliding of interpolar microtubules.

A very special case is the Anaphase B of *C. Elegans*, where cortical pulling has an important role in pole separation. In this system, centrosomes are connected to the cortex, where dynein exerts pulling forces that move poles away from each other. Due to the geometry of the embryo, at anaphase onset the sum of forces drives a net displacement of the centrosomes towards the cell poles. As centrosomes move apart, the total force decreases and eventually a balance between pulling and pushing is reached, and length remains constant. This geometrical effect results in a scaling of the final anaphase pole to pole distance with cell size [83]. Interestingly, the spindle elongation velocity also increases with cell size [83]. This was explained by an increase in the number of force generators at the cortex in bigger cells, that would increase the speed at which the steady state is reached. At this point, it is important to make a distinction between pole separation and chromosome segregation. In yeast, where Anaphase A occurs prior to Anaphase B, these measurements are equivalent (Fig. 1.3, top right). However, in open mitosis, the distance between the two masses of chromosomes that are being segregated does not necessarily correlate with pole segregation (Fig. 1.3, bottom right). This was recently addressed in [220], where the authors showed that disrupting cortical pulling only weakly impacts chromosome segregation speed, while laser ablation of interpolar microtubules stops chromosome segregation completely, suggesting that cortical forces are involved in centrosome/pole separation but not chromosome segregation. In summary, *C. elegans* chromosomes are segregated at the speed of microtubule sliding at the central spindle, but centrosomes are separated faster by cortical pulling.

In anaphase B, the challenge remains to understand what mechanisms allow for the

maintenance of microtubule overlaps that sustain sliding. This feature is common to anaphase in all organisms, and cannot be understood without measuring microtubule dynamics.

Chapter 2

Theory of antiparallel microtubule overlap stabilization by motors and diffusible crosslinkers

The results presented in this chapter were previously published in [117] and [81].

Data and analysis from [117] were generated by myself. The original text was written by myself. Figures, assumptions and methods are reproduced from the original text under the CC BY 4.0 terms.

Experimental data acquisition and analysis from [81] were performed by J. Hannabuss, N. I. Cade and J. Fourniol from T. Surrey's lab (Francis Crick institute). The part of the text concerning simulations was written by myself. Figures, assumptions and methods are reproduced from the article under the CC BY 4.0 terms.

1 Introduction

Microtubule bundles are found across different structures in cells: mitotic spindles [208], dendrites [218], marginal bands of blood platelets [130], etc. Microtubules in such structures can be arranged in triangular, square [208] or hexagonal lattices [188]. The organisation of these bundles depends on crosslinking proteins that mechanically bridge neighbouring microtubules. Crosslinkers can have a preference for microtubules oriented in the same direction [168] or in opposite directions [208]. Molecular motors also crosslink microtubules and slide them with respect to each other, and crosslinkers can act like brakes against motor sliding [22, 114].

As explained in chapter 1 subsection 2.3, interplay between motors and crosslinkers is of vital importance during anaphase B. In some organisms, once sister chromatid cohesion is removed, the only connections left between the spindle poles are the interpolar microtubules (Fig. 1.3) [175], which interdigitate at the cell equator forming an antiparallel square lattice known as central spindle or midzone, organised by crosslinkers and motors [120, 224]. Motor sliding at the midzone leads to the elongation of the spindle, and drives separation of the genetic material into the two daughter cells [220, 103]. Since midzone overlap persists during this process, polymerisation at plus ends and sliding must be coordinated. How this coordination happens remains an open question.

Requirements to form stable antiparallel overlaps have been studied *in vitro* using non dynamic microtubules, motors and crosslinkers. A pair of antiparallel microtubules bridged by diffusible crosslinkers of the MAP65/PRC1/Ase1 family is sufficient to form a stable

overlap in the presence of certain motors. Kinesin-14 in combination with Ase1 [22, 114] and kinesin-4 in combination with PRC1 [211] form such stable overlaps. However, microtubules crosslinked by PRC1 and kinesin-5 motors slide apart completely [180]. These differences may be due to the properties of motors: kinesin-5 is known to be a strong motor that can produce forces in the picoNewton range in overlaps [177]. On the other hand, kinesin-14 family members like HSET and Ncd differ from other kinesins in that they have a motor head and a diffusive tail. They form asymmetric connections, with the motor and diffusive ends bound to different microtubules. Kinesin-14 motors can only exert weak sub-picoNewton forces between microtubules, even though their motor domain can reach picoNewton-range forces, suggesting that diffusive anchorage limits their force production [124]. A similar behaviour can be expected from kinesin-4 and PRC1. Kinesin-4 on its own does not crosslink microtubules, but when bound to PRC1, which can diffuse on microtubules, the complex can produce sliding [211].

Crosslinkers of the MAP65/PRC1/Ase1 family are described in chapter 1 subsection 4.4. They form homodimers that can crosslink microtubules, preferentially in an antiparallel configuration [95]. They diffuse longitudinally along single microtubules and microtubule overlaps. *In vivo*, their antiparallel crosslinking activity is required to organise the central spindle across species [120, 224]. PRC1 is also present in bridging fibers linking sister kinetochore fibers in higher eukaryotes [159]. In fission yeast, recruitment of Ase1 to the overlap of transported microtubules in interphase slows down sliding [95], and overexpression of Ase1 reduces spindle elongation velocity in anaphase [164, 111], suggesting that diffusible crosslinkers can counteract motor sliding in cells.

In vitro, diffusible crosslinkers can act like brakes and promote the formation of stable overlaps [22, 114, 211]. Interestingly, diffusive crosslinkers can also drive the expansion of overlaps *in vitro* in the absence of motors, and they have been compared to a one dimensional gas confined in the overlap [114]. This is due to the discrete nature of the microtubule lattice, where binding sites for crosslinkers are evenly spaced every 8 nm. Since only one crosslinker can bind to each lattice site, an expansive entropic force is achieved without changing the internal energy of the system. Conversely, reducing the overlap by sliding reduces the entropy and causes a counteracting force that opposes sliding, which can lead to the formation of a stable overlap [22, 114, 211].

Diffusible crosslinkers produce interesting behaviours when combined with the plus end directed motor kinesin-4. This dimeric kinesin can bind to PRC1, which enhances its recruitment to microtubules [16]. Because of its diffusive nature, PRC1 bound to kinesin-4 is transported to the plus ends of single microtubules [179]. Importantly, the motor-crosslinker complex can slide microtubule overlaps [211]. On the other hand, kinesin-4 alone, which cannot crosslink microtubules, does not produce sliding. In addition, kinesin-4 suppresses microtubule dynamics at the plus ends, preventing growth or shrinkage [16]. When PRC1 and kinesin-4 are present in overlaps of dynamic microtubules that cannot slide, the length of microtubule overlap is regulated by kinesin-4. When overlaps form, microtubules grow at their plus ends and elongate the overlap, since there is little or no kinesin-4 in the overlap. However, as the overlap grows, it recruits more kinesin-4, which processively walks to plus ends and ultimately stops growth [16]. These two activities of the PRC1/ kinesin-4 system (sliding and suppression of microtubule dynamics) have important functional consequences in cells, since they regulate the overlap length of the central spindle [224, 46], but also of antiparallel overlaps found in other structures [146]. However, these two activities have not been studied together *in vitro* so far. For extended description of the PRC1/ kinesin-4 system, see chapter 1 subsection 4.4.

Theoretical modelling has been previously used to understand the effect of diffusible crosslinkers on microtubule sliding. In the simplest scenario, they could act as viscous brakes. Each bound diffusive head would create a viscous drag, and the total drag would increase linearly with the number of crosslinkers. However, such a model does not fit the experimental observations. Instead, entropic expansion results were reproduced in computer simulations, which accounted for the discrete nature of the microtubule lattice [114]. The effective drag in the simulations increased exponentially with crosslinker number, and predictions of the model matched the experimental results. See chapter 1 subsection 4.4 and discussion, where we explain why the assumptions in [114] produce this behaviour. However, an exponential dependency of the drag on crosslinker number is incompatible with the observations from [22], in which Ase1 acted like a brake against motor sliding by kinesin-14. In those experiments, the sliding speed was independent of the microtubule overlap length, and depended only on the density of motors and crosslinkers. Since motor force increases linearly with the number of bound motors [177], it increases linearly with overlap length. If friction increased exponentially with crosslinker number, we would expect instead the drag coefficient to increase exponentially with overlap length.

A different study used a particle-based stochastic model to solve the steady state of a system composed of strong motors like kinesin-5 and diffusible crosslinkers [97]. Numerical results predicted formation of overlaps by a mechanism in which crosslinkers at the edges of the overlap oppose a higher resistance than in the body, because microtubule ends act as diffusion barriers for crosslinkers. In this way, crosslinker-driven forces are length independent, since they only happen at the edges, while motor forces scale linearly with microtubule length. In this model, braking and entropic expansion are not addressed.

In the present thesis, we aim to understand how motors and diffusible crosslinkers can be combined to form stable overlaps and how diffusible crosslinkers generate friction against motor sliding. In the first part, we study four related systems (Fig. 2.1) inspired by the mentioned *in vitro* work [22, 114, 180]. All systems are one dimensional and composed of two antiparallel microtubules. We presume a constant overlap length, and impose that microtubule growth matches sliding exactly. This will be discussed. In the four systems, motor and diffusive heads are associated to form crosslinking entities: System A is composed of crosslinkers that bind and unbind but do not diffuse on microtubules. System B is similar, but crosslinkers diffuse on microtubules and cannot detach. It is based on experiments with kinesin-5 and PRC1 [180]. System C models experiments with kinesin-14, which has a motor domain and a diffusible domain [124]. In system D we combine diffusive motors and diffusive crosslinkers, as done experimentally in [22, 114]. These systems present increasing complexity, and produce different outcomes. We initially define a common set of assumptions and then predict the sliding speed of microtubules in each system.

In the second part, we apply our theory to an *in vitro* experimental system composed of kinesin-4 and PRC1, which can produce stable overlaps that slide at the rate of crosslinker unbinding.

2 Part 1: Development of the theory

2.1 Assumptions

This section is reproduced under the CC BY 4.0 terms from [117] and was originally written by myself

The general assumptions are the same for all systems. Motor and crosslinker entities are made of two heads, binding to different microtubules. Unbound entities are uniformly distributed in space, and their heads can bind with equal rates k_b if they reach a microtubule. A bound head may unbind with constant rate k_u. If one head is attached, the other head can attach to the other microtubule if microtubules are overlapping at this position, also with rate k_b. An entity bound to two microtubules exerts an elastic force of stiffness κ and zero resting length (Fig. 2.1). At the time of second binding, the gap between the two heads (δ) is null, but if microtubules slide, a tension $f = \kappa\delta$ will build up. This tension also changes when the heads move along the microtubules. Conversely, movement of the heads along the microtubule is affected by the tension f in the associated link, differently for motors and passive heads. We consider three types of heads (Table 2.1). **Motor heads** move continuously, since we are considering situations where jamming of motors does not occur. Attached motor heads move towards the plus-end with a speed $v_m = v_0\,(1 - f/f_s)$, depending on the force against which the motor is pulling f, its unloaded speed v_0 and stall force f_s. Thus, an antagonistic force reduces motor speed linearly, as shown experimentally [135]. We define the characteristic drag coefficient of the motor head as $\gamma_m = f_s/v_0$, such that $v_m = v_0 - f/\gamma_m$. This equation determines the force-velocity relationship of the motor. We note that kinesin-14 moves towards the minus end of microtubules, but as microtubule assembly dynamics are ignored here and only one type of motor is present, we can ignore microtubule polarity as the system is unchanged by swapping 'plus' and 'minus' throughout. **Non-diffusible passive heads** do not move along microtubules, and must unbind to relocate on a filament, releasing the associated linker tension immediately. We define the effective drag coefficient of the crosslinkers as $\gamma_c = \kappa/k_u$. **Diffusible passive heads** are modelled following [114]. They bind at discrete sites on the microtubule lattice, separated by $a = 8$ nm. Passive heads can diffuse on this lattice by hopping to adjacent sites with a rate k_0. However, a crosslinker head may not move to a position that is already occupied, nor step out of the microtubule at its ends. In the absence of external force, passive heads hop equally in both directions, undergoing pure one dimensional diffusion with a coefficient $D_1 = k_0\,a^2$. When the tension f in the linker between the heads builds up, the upstream (k^+) and downstream (k^-) rates differ (Fig. 2.1). How these rates vary is not known, but thermodynamic consideration dictates that for any pair of states (a, b) with potential energies (U_a, U_b), the transition rates should satisfy detailed balance: $k_{a\to b}/k_{b\to a} = e^{\epsilon}$ with $\epsilon = (U_a - U_b)\,/k_BT$, and this is fulfilled by assuming [207]:

$$k_{a\to b} = \frac{\epsilon}{1 - e^{-\epsilon}}k_0 \quad \text{and} \quad k_{b\to a} = \frac{\epsilon}{e^{\epsilon} - 1}k_0 \tag{2.1}$$

Since $U(\delta) = \frac{1}{2}\kappa\,\delta^2$, the hopping rates to neighbouring sites as shown in Fig. 2.1B read:

$$k^+ = \frac{\alpha - \beta}{1 - e^{\beta-\alpha}}k_0 \quad \text{and} \quad k^- = \frac{\alpha + \beta}{e^{\alpha+\beta} - 1}k_0, \tag{2.2}$$

where $\alpha = a\,f/k_BT$ expresses the bias caused by force and $\beta = \kappa a^2/2k_BT$ echoes the difficulty of reaching a neighbouring binding site due to the stiffness of the linker. The diffusion rate of a crosslinker that is bound to two overlapping microtubules is defined by a, k_0 and β and the microtubule's own movements. Initially, we adopt the continuum limit that is obtained by neglecting the contribution of β. The drift speed along a microtubule, under a given force, then reads:

$$v_d = a\,(k^+ - k^-) = \frac{f}{\gamma_d}, \tag{2.3}$$

Motor		
f_s	stall force	
v_0	unloaded speed	
$v_m = v_0 - f_m/\gamma_m$	with $\gamma_m = f_s/v_0$	
Non-diffusible head		
k_u	unbinding rate	
κ	stiffness of linker	
$\gamma_c = \kappa/k_u$	effective drag coefficient	
Diffusible heads		
D_1	1D diffusion rate	
a	lattice unit length	
$v_d = f_d/\gamma_d$	with $\gamma_d = k_B T/D_1$	

Table 2.1: Microtubule binding heads
Reproduced under the CC BY 4.0 terms from [117]

with $\gamma_d = k_B T/k_0 a^2$, the characteristic drag coefficient of a diffusible head. We adopted κ = 100 pN/µm, a value for which the continuum limit is valid (see discussion). **Microtubules** are modelled as incompressible lines oriented in opposite directions. The orientation of each microtubule dictates the natural movement of attached motors. The estimated viscous drag $\gamma_{\text{fil}} \sim 3\pi\xi H/[\log(H/d) + 0.312]$ depends on the length of the microtubule H, its diameter d and the viscosity of the fluid ξ, following [189].

2.2 Results

System A: conventional motors and crosslinkers

We first model a system composed of non diffusible crosslinkers that can bind and unbind from a pair of antiparallel microtubules with constant rates k_b and k_u (Fig. 2.1A). Motors are modelled like kinesin-5 (two motor heads linked by an elastic element). Given that the overlap length does not change (see assumptions), and that the rates of binding and unbinding are constant, a steady state is reached where the average number of bound motors (m) and crosslinkers (c) does not change. This results in an average motor force F between the microtubules. This force will be matched by the total crosslinker force plus the viscous force of the fluid opposing microtubule movement. Since viscous drag of the fluid is expected to be small compared with the characteristic drag of crosslinkers for the chosen parameters (Table 2.1, Table 2.2), we can neglect its contribution. In this regime, the combined force of bound crosslinkers must match the motor force. Average force per crosslinker is then $f_d = F/c = \kappa\,\delta$, where κ is the linker stiffness and δ the average crosslinker stretch.

Microtubule sliding in this scenario happens when one crosslinker detaches from either microtubule, since the total motor force is then distributed among fewer crosslinkers. We can calculate the displacement associated with a detachment event using the balance of forces after the unbinding: $F/(c-1) = \kappa\,\delta^{\text{after}}$. The maximum displacement of the microtubule is therefore $\delta^{\text{after}} - \delta = \delta/(c-1)$. This will be the displacement if the binding

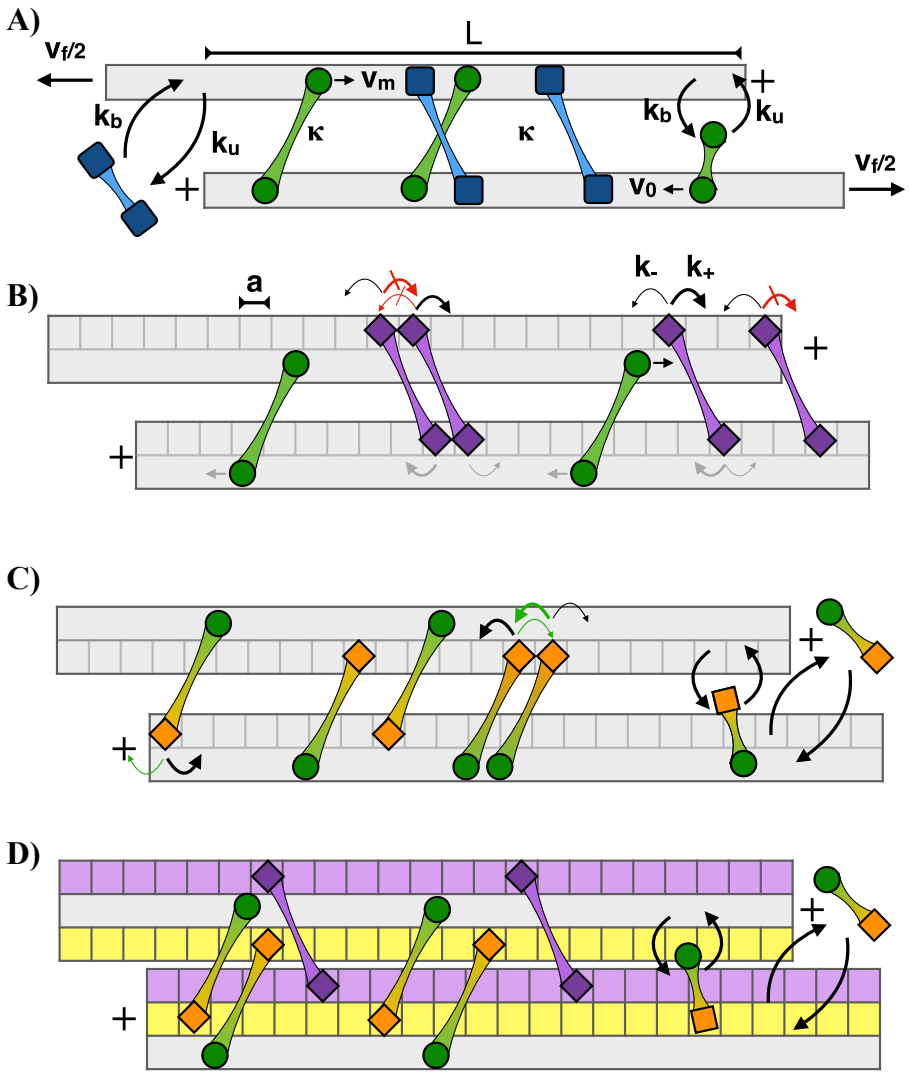

Figure 2.1: Schematics of the modelled systems

Systems containing two antiparallel microtubules, arranged with an overlap length L that is constant because microtubules grow at the required speed to compensate exactly for the sliding. **A)** In system A, microtubule sliding is determined by bivalent motors (green circular heads) and crosslinkers (blue square heads). These crosslinkers bind and unbind but do not slide along microtubules. Motor heads move actively towards the plus ends and tend to reduce the overlap. Crosslinkers resist this motion until they unbind. **B)** System B combines bivalent motors and diffusible crosslinkers (purple diamond heads). Motors and crosslinkers do not bind or unbind but may slide along microtubules. Motors create tension in the linkers that hinder their progression, while promoting the hopping of crosslinkers heads and microtubule sliding. A steady state is reached where motors and crosslinkers move on average at the same speed towards the plus end. By impairing the movements of the crosslinkers (red crossed arrows), occupancy decreases the sliding speed. **C)** System C has diffusible motors composed of a motor head (green circle) with a diffusible head (orange diamond). Tension generated by active motor movement is released by hopping of diffusible heads, and microtubule sliding. **D)** System D has diffusible motors as described in D and diffusible crosslinkers as described in B. Diffusible heads of crosslinkers (purple diamonds) interfere with other molecules of the same category but not across category.

timescale is slow enough to allow the system to reach equilibrium before another crosslinker attaches: $k_b \gamma_{\text{fil}} \ll \kappa$. This is the case for realistic parameter values. In these conditions, filaments will move on average at speed $v_{\text{fil}} = k_u \delta\, c/(c-1)$, since $2c$ heads can unbind, and the displacement of each filament after an unbinding event is $\delta/2(c-1)$.

To solve the steady state, we calculate the motor force. Processive motors can reach their stall force without detaching from the microtubule ($v_0 \kappa / f_s \gg k_u$, see Table 2.2), so we can expect them to have reached a steady state given by the force-velocity relationship $v_m/v_0 = 1 - f_m/f_s$. For m bound motors, the force per motor is given by $f_m = F/m = \kappa\delta c/m$. We substitute v_{fil} and obtain:

$$\frac{v_0}{v_{\text{fil}}} = 1 + \frac{c-1}{m}\frac{\gamma_c}{\gamma_m}. \tag{2.4}$$

Filament speed (v_{fil}/v_0) is given by the ratio of crosslinkers to motors (Fig. 2.2A), and the ratio of characteristic drags of crosslinkers and motors. Sliding velocity is twice v_{fil} and its maximum value is $2v_0$, which is expected for a motor like kinesin-5. Speed is independent of the absolute densities of crosslinkers and motors. Therefore, this system cannot form stable overlaps, since velocity of sliding ($v_{\text{fil}} > 0$) is always positive for any number of motors ($m > 0$).

System B: bivalent motors and diffusive crosslinkers

In system B, we consider diffusible crosslinkers, that do not bind or unbind for simplicity (Fig. 2.1). This setup is inspired by experiments with kinesin-5/PRC1 [180]. To represent the fact that one lattice site can only contain one crosslinker head, we define the probability for a lattice site to be occupied: $\rho_c \in [0,1]$. When overlap length changes, or one microtubule is immobile, this probability is higher at filament edges, since they act as diffusion barriers [22, 114, 211]. In our simplified system where the overlap length does not change, crosslinkers are homogeneously distributed and we can consider a uniform value of this probability $\rho_c = c\,a/L$. Then, Equation 2.3 becomes:

$$v_d = (1-\rho_c)\frac{f_d}{\gamma_d}. \tag{2.5}$$

For *in vitro* conditions, we expect the fluid drag to be negligible compared with the drag associated with diffusible crosslinkers. For a medium viscosity ξ<0.01 Pa.s, the viscous drag per unit length of microtubule is $\sim 0.015\,\text{pN.s.}\mu\text{m}^{-2}$, while the characteristic drag of a single crosslinker with D_1=0.1μm^2/s is γ_d=0.04pN.s.μm^{-1}. Therefore, we can neglect the contribution of viscous forces from solution for densities of crosslinkers above 1 crosslinker per μm. It follows then that the total force exerted by motors must be equal to the total force in the crosslinkers. For f_m and f_c being the average force per motor and crosslinker, and m, c the average number of bound motors and crosslinkers, this implies $F = m\,f_m = c\,f_d$. Due to the symmetry of the system, at steady state the average position of bound motors and crosslinkers does not change, and the speed of the heads along the microtubule matches the velocity of the filament: $v_{\text{fil}} = v_m = v_d$. Combining the motor force-velocity relationship ($v_m = v_0 - f_m/\gamma_m$) and Equation 2.5, we obtain:

$$\frac{v_0}{v_{\text{fil}}} = 1 + \frac{1}{1-\rho_c}\frac{c}{m}\frac{\gamma_d}{\gamma_m}. \tag{2.6}$$

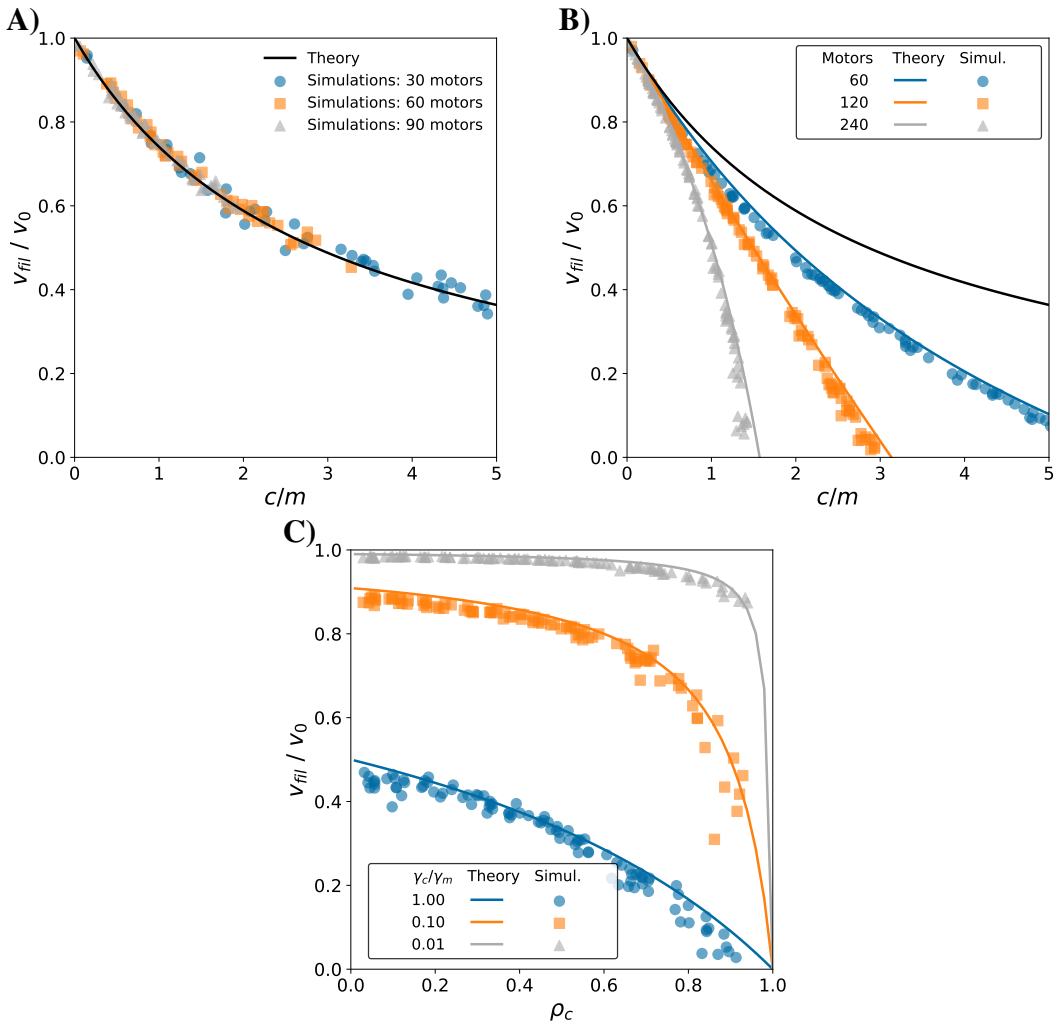

Figure 2.2: Systems A&B, bivalent motor and diffusible or non-diffusible crosslinkers
A) Steady state speed for system A as a function of the ratio of the number of crosslinkers to motors (c/m), with motors ($f_s = 6$ pN, $v_0 = 0.05$ µm/s) pulling non-diffusible crosslinkers ($\kappa = 100$ pN/µm, $k_u = 2.38$ s^{-1}), resulting in $\gamma_c/\gamma_m = 0.35$ (see Table 2.1). Dots represent the results of individual simulations containing 30 (blue circles), 60 (orange squares) or 90 (grey triangles) motors and a random number of crosslinkers (1 to 375). The line indicates Eq. 2.4. **B)** Steady state speed for system B as a function of the ratio of the number of crosslinkers to motors (c/m), with bivalent motors ($f_s = 6$ pN, $v_0 = 0.05$ µm/s) and diffusible crosslinkers ($D_1 = 10^{-4}$µm^2/s), resulting in $\gamma_d/\gamma_m = 0.35$ (see Table 2.1). Dots represent the results of individual simulations containing 60 (blue circles), 120 (orange squares), 240 (grey triangles) motors, and a random number of crosslinkers (1 to 380). Coloured lines show the corresponding predictions of Eq. 2.6. Black line represents the prediction if occupancy of the lattice is ignored ($\rho_c = 0$). Speed becomes zero when $\rho_c = 1$. **C)** Steady state sliding speed for system B as a function of the occupancy of crosslinkers (ρ_c), in simulations containing equal number of crosslinkers and motors, for three different values of crosslinker diffusion rates (D_1). Dots represent the results of individual simulations, with $D_1 = 3.5 \times 10^{-5}$ (blue discs), $D_1 = 3.5 \times 10^{-4}$ (orange squares) and $D_1 = 3.5 \times 10^{-3}$ µm^2/s (grey triangles), resulting in $\gamma_d/\gamma_m = 1; 10^{-1}$ and 10^{-2}, respectively (see Table 2.1).
These simulations included an equal amount of crosslinkers and motors, randomly chosen between 5 and 375. Since motors and crosslinkers do not unbind, the mean occupancies of crosslinkers and motors are equal. Coloured lines show the corresponding predictions of Eq. 2.6. $L = 3$µm for all the simulations on this figure, and the horizontal and vertical positions of simulation dots are calculated from the simulation results (see methods).

Common	Linker stiffness	κ	100 pN/μm
	Lattice size	a	8 nm
Rigid crosslinker	Unbinding rate	k_u	2.38 s^{-1}
	Binding rate	k_b	1 s^{-1}
Bivalent motor	Unbinding rate	k_u	†0.01 s^{-1}
	Binding rate	k_b	†0.01 s^{-1}
	Unloaded speed	v_0	0.05 μm/s
	Stall force	f_s	6 pN
Diffusive crosslinker	1D Diffusion rate	D_1	0.1 $\mu m^2/s$
Diffusive motor	Unloaded speed	v_0	0.2 μm/s
	Stall force	f_s	6 pN
	1D Diffusion rate	D_1	0.1 $\mu m^2/s$

Table 2.2: Parameters of simulations
Parameters used in the computer simulations, unless specified.
† Binding and unbinding of bivalent motors is disabled in System B.

This equation resembles Equation 2.4, but in addition v_{fil} depends on the density of crosslinkers in the overlap (Fig. 2.2B). Higher occupancy prevents crosslinkers from releasing force by diffusion, increasing the tension stored in them, which opposes sliding. In the regime where the second term dominates, speed is proportional to the number of motors, and is affected by crosslinkers through c and ρ_c. From the equation it follows that this system can only form stable overlaps when all lattice sites are occupied by crosslinkers ($\rho_c = 1, v_{\text{fil}} = 0$).

System C: Diffusible motors

Next, we consider a system of two microtubules crosslinked by diffusive motors like kinesin-14. Diffusive motors are composed of a diffusive and a motor head (Fig. 2.1C). For the diffusive head, we model a low density regime, in which the lattice is not exclusive, and multiple heads can bind to the same site. Since kinesin-14 does not accumulate at microtubule ends [22], we allow diffusive heads to unbind from the lattice by diffusion at the plus ends (Fig. 2.1C, green arrow on the left).

At steady state, each motor head moves towards the plus end of the microtubule it is attached to. Its associated diffusive head moves on average at the same speed towards the minus end of the opposite microtubule, lagging an average distance δ with respect to the motor head that pulls from it. Therefore, the average force every motor exerts on the microtubule pair is $f = \kappa\delta$. Forces of all motors add up and the movement of the filament is given by $v_{\text{fil}} = m f / \gamma_{\text{fil}}$, where γ_{fil} is the viscous drag of the solution, and m is the average number of bound motors. For the motor to reach steady state where the average distance between motor and diffusive head is conserved, velocity of the motor (v_m) and crosslinker (v_c) heads with respect to the microtubule they are attached to must satisfy $v_m - v_{\text{fil}} = v_d + v_{\text{fil}}$. From the motor force-velocity and Equation 2.3 we then derive

$v_0 - f/\gamma_m = f/\gamma_d + 2v_{\text{fil}}$ and finally:

$$\frac{v_0}{v_{\text{fil}}} = 2 + \frac{\gamma_{\text{fil}}}{m}\left(\frac{1}{\gamma_d} + \frac{1}{\gamma_m}\right) \tag{2.7}$$

This formula is comparable to the sliding speed in a gliding assay with immobilised motors: $v_0/v_{\text{fil}} = 1 + \gamma_{\text{fil}}/(m\gamma_m)$. The factor 2 represents the fact that motors that have one single motor head can only move each filament at half of their unloaded speed. Conversely tetrameric motors like kinesin-5, can slide each filament at their maximum speed (Equation 2.4, 2.6). Part of the work generated by the motor is dissipated through diffusion, so optimal force production happens when $1/\gamma_d \to 0$. This can be understood by looking at the expression of the maximum force a motor can exert (f). This happens when microtubules are immobile and no tension is dissipated through sliding:

$$\frac{f_s}{f} = 1 + \frac{f_s}{\gamma_d v_0} \tag{2.8}$$

There are two extreme behaviours predicted by this equation: If $f_s \ll v_0\gamma_d$ (the tail is hard to move for the stall force), all the force produced by the motor is transmitted to the microtubules. If $f_s \gg v_0\gamma_d$ (tail moves at the unloaded speed of the motor head), the force is $\gamma_d\, v_0$, which is independent of stall force and corresponds to the viscous force produced by dragging the diffusive tail at unloaded speed (Fig. 2.3A). For the measured parameters, we expect kinesin-14 to be in this second regime, where force generated is independent of stall force (see next paragraph). The system exhibits an intermediate behaviour between these two extremes, but the force never exceeds $\gamma_d\, v_0$ (Fig. 2.3A, dashed line).

We simulated system C with the experimentally measured parameters of kinesin-14: $v_0 \sim 0.2$ µm/s, $f_s \sim 5$ pN [124] and $D_1 \sim 0.1\mu\text{m}^2/\text{s}$[23, 150]. We recover Equation 2.7 and increasing viscosity reduces the sliding speed as anticipated (Fig. 2.3b). Since $\gamma_d = 0.04$ pN.s/µm and $\gamma_m = 25$ pN.s/µm, we have that $\gamma_d \ll \gamma_m$ and the sliding speed simplifies to $v_0/v_{\text{fil}} = 2 + \gamma_{\text{fil}}/(m\gamma_d)$, which is independent of motor stall force. From this, we predict that for microtubules of length greater than ~2µm, for which the drag of a filament is roughly proportional to its length [189], if the linear density of active motors is constant, the sliding speed is independent of the filament length, since since γ_{fil}/m is constant. This is observed experimentally [124].

System D: Diffusible motors and diffusible crosslinkers

We then add diffusible crosslinkers to system C (Fig. 2.1D). This has been realised experimentally with Ase1 and kinesin-14 Ncd [22]. In those experiments, a short microtubule is crosslinked to a long fixed microtubule by Ase1 and Ncd. The short microtubule is transported by Ncd sliding. Eventually, it reaches the end of the long microtubule, and the overlap between them shrinks. Finally, a stable overlap is formed (see Fig. 1.8B for a kymograph). During shrinkage, Ase1 is retained in the overlap, so its density increases, while Ncd density does not change. This suggest that Ncd turnover is faster than the scale of microtubule sliding and that it does not compete for binding sites with Ase1 (since a significant change in Ase1 density does not affect Ncd density).

We make corresponding assumptions, with diffusible crosslinkers that do not unbind, and diffusible motors that bind and unbind with constant rates. Crosslinkers are modelled as in System B and diffusive motors as in System C. Since experimentally they don't compete for binding sites, they are modelled on different lattices and do not interact (Fig. 2.1D).

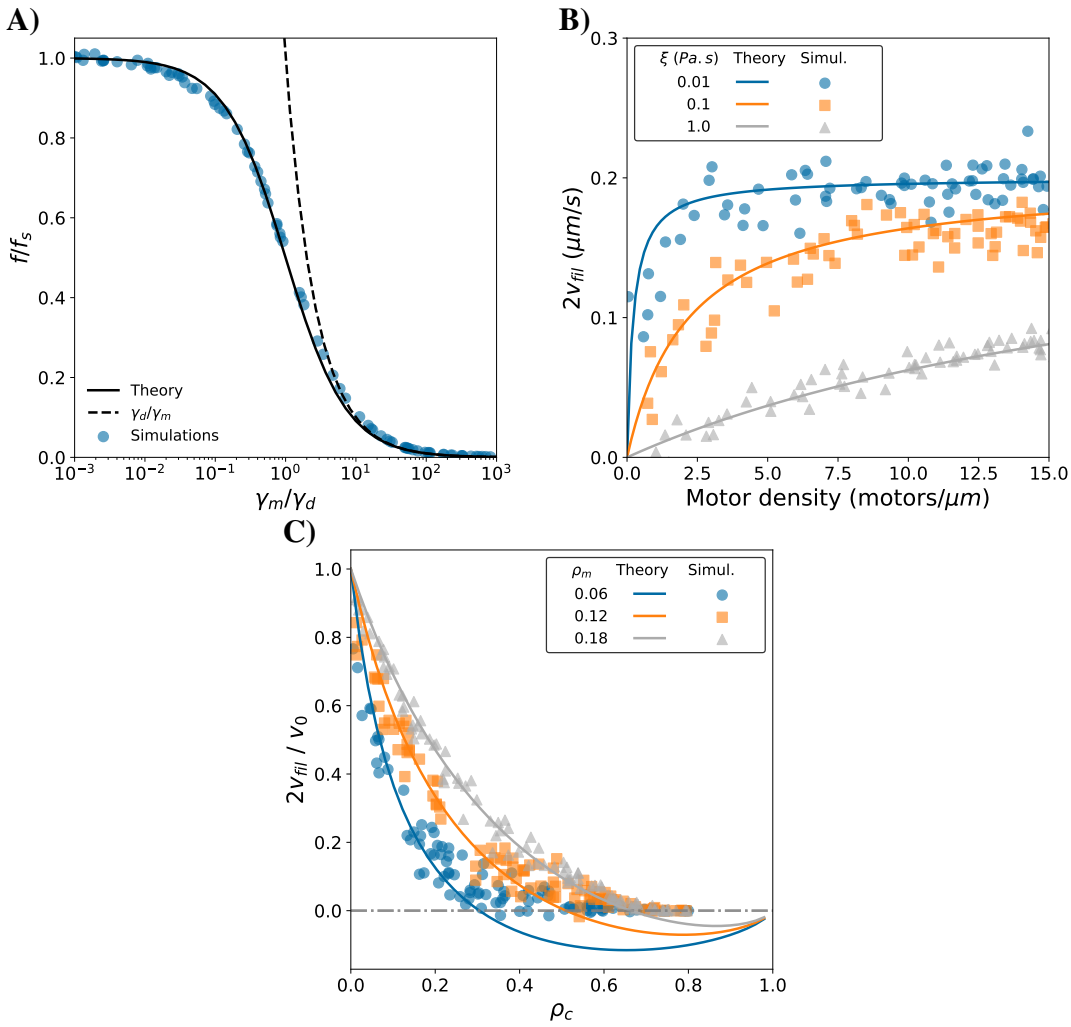

Figure 2.3: Systems C&D, sliding by diffusible motors

A) The maximum usable force of a diffusible motor is limited by the drag coefficient of its diffusible head γ_d (see Table 2.1). Dots represent the average force exerted per motor on fixed microtubules at steady state divided by motor stall force (f/f_s) as a function of the parameter γ_m/γ_d (see Table 2.1) in individual simulations with different diffusion rates of motor tail for Kinesin-14 like motors ($f_s = 6$ pN, $v_0 = 0.2$ µm/s) and $D_1 \in [10^{-7}, 1]$µm^2/s. The line represents the prediction of Eq. 2.8. The dashed line represents the upper limit γ_d/γ_m. **B)** Sliding speed for system C as a function of density of motors, with Kinesin-14 like diffusive motors ($f_s = 6$ pN, $v_0 = 0.2$ µm/s, $D_1 = 0.1$ µm^2/s), for different viscosities (ξ, in Pa.s): 0.01 (blue discs), 0.1 (orange squares) and 1 (grey triangles). Dots represent the results of individual simulations containing a random number of motors in [1, 100]. Coloured lines show the corresponding predictions of Eq. 2.7. **C)** Sliding speed for system D as a function of crosslinker occupancy (ρ_c), with diffusible motors, as in (b), and diffusible crosslinkers ($D_1 = 0.1$ µm^2/s). Dots represent the results of individual simulations with varying number of motors: 100 (blue circles, $\rho_m = 0.06$), 200 (orange squares, $\rho_m = 0.12$), 300 (grey triangles, $\rho_m = 0.18$). The number of crosslinkers is randomly chosen in [1, 300]. Coloured lines show the corresponding predictions of Eq. 2.9. Note that simulations cannot yield negative speeds because overlap is kept constant by growth. For all simulations, $L = 3$ µm. All dots are placed according to the values of the relevant quantities averaged after the system has reached steady state (see methods).

The diffusible heads from crosslinkers and motors are distinct, and we note their drag coefficients γ_d and γ_t respectively ('t' for tail of diffusive motors). As in system B, the main resistance against sliding comes from crosslinkers, so we can neglect viscous drag from the fluid. From system C, we expect kinesin-14 to generate small forces, comparable to the entropic forces from crosslinkers [114]. In this regime, the resistance from crosslinkers comes both from the entropic pressure and the drag modelled in system B. We use the formulation of entropic pressure from [114]: $P = -(k_B T/a)\log(1-\rho_c)$. Adding this term, the force balance becomes: $c\, f_d + P = m f_m$. From the relationships of speeds of heads along microtubule and sliding speed defined in system B and C: $v_{\text{fil}} = v_d$ and $v_m - v_{\text{fil}} = v_t + v_{\text{fil}}$, we use Equation 2.5 and derive:

$$v_{\text{fil}} = \left[v_0 - \frac{P}{m\,\gamma_{tm}}\right] \Big/ \left[2 + \frac{1}{1-\rho_c}\frac{c}{m}\frac{\gamma_d}{\gamma_{tm}}\right], \tag{2.9}$$

with $\frac{1}{\gamma_{tm}} = \frac{1}{\gamma_t} + \frac{1}{\gamma_m}$. The denominator is similar to Equation 2.6, and represents the resistance due to tension in the crosslinkers. The numerator represents entropic pressure. Speed increases with motor drag ($m\gamma_{tm}$), and decreases with drag from crosslinkers ($c\gamma_d$). In the crosslinker low density regime ($\rho_c \ll 1$), speed depends only on the ratio of crosslinkers to motors, as previously observed [22]. Just like in Equation 2.6, sliding speed is zero when $\rho_c = 1$. Most importantly, speed can become negative if the entropic pressure is stronger than motor forces (Fig. 2.3C). This means that stable overlaps can form for $\rho_c < 1$, unlike in System B. We can rewrite Equation 2.9 as a function of motor and crosslinker densities $\rho_m = m\,a/L$ and $\rho_c = c\,a/L$:

$$v_{\text{fil}} = \left[v_0 + \frac{k_B T\,\log(1-\rho_c)}{\rho_m\, L\,\gamma_{tm}}\right] \Big/ \left[2 + \frac{\rho_c\,\gamma_d}{(1-\rho_c)\,\rho_m\,\gamma_{tm}}\right]$$

This form highlights the fact that motor and crosslinker forces increase with overlap length L, while entropic pressure only depends on density. It also shows that at very high occupancies, where entropic expansion forces tend to infinity, the occupancy of the lattice dominates and prevents expansion, and $v_{\text{fil}} \to 0$ when $\rho_c \to 1$ (Fig. 2.3C).

$$v_{\text{fil}} \sim \frac{k_B T}{L\,\gamma_d}(1-\rho_c)\log(1-\rho_c) \tag{2.10}$$

We conclude that system D can form stable overlap for densities lower than total occupancy ($\rho_c < 1$), when the entropic pressure matches motor forces.

Entropic expansion

We next asked whether our model from system D could also explain entropic expansion in the absence of motors. Experimentally this phenomenon was studied by compressing overlaps with hydrodynamic flow, and letting overlaps expand due to entropic pressure [114]. In this scenario, crosslinker drag opposes entropic forces, and sets the expansion speed. Interestingly, in this system the expansion speed decreases with overlap length, consistent with the predictions from Equation 2.9, which predicts that crosslinker drag increases with length but entropic forces do not. We compare the predictions of our simulations and theory with the experimental data of [114], kindly provided by the authors. We simulate the system with a pair of microtubules of length 20 µm, with different initial overlap lengths. Assuming that the force used to compress the overlaps is the same in all overlaps, the density of Ase1 in them should be the same, since entropic forces only depend

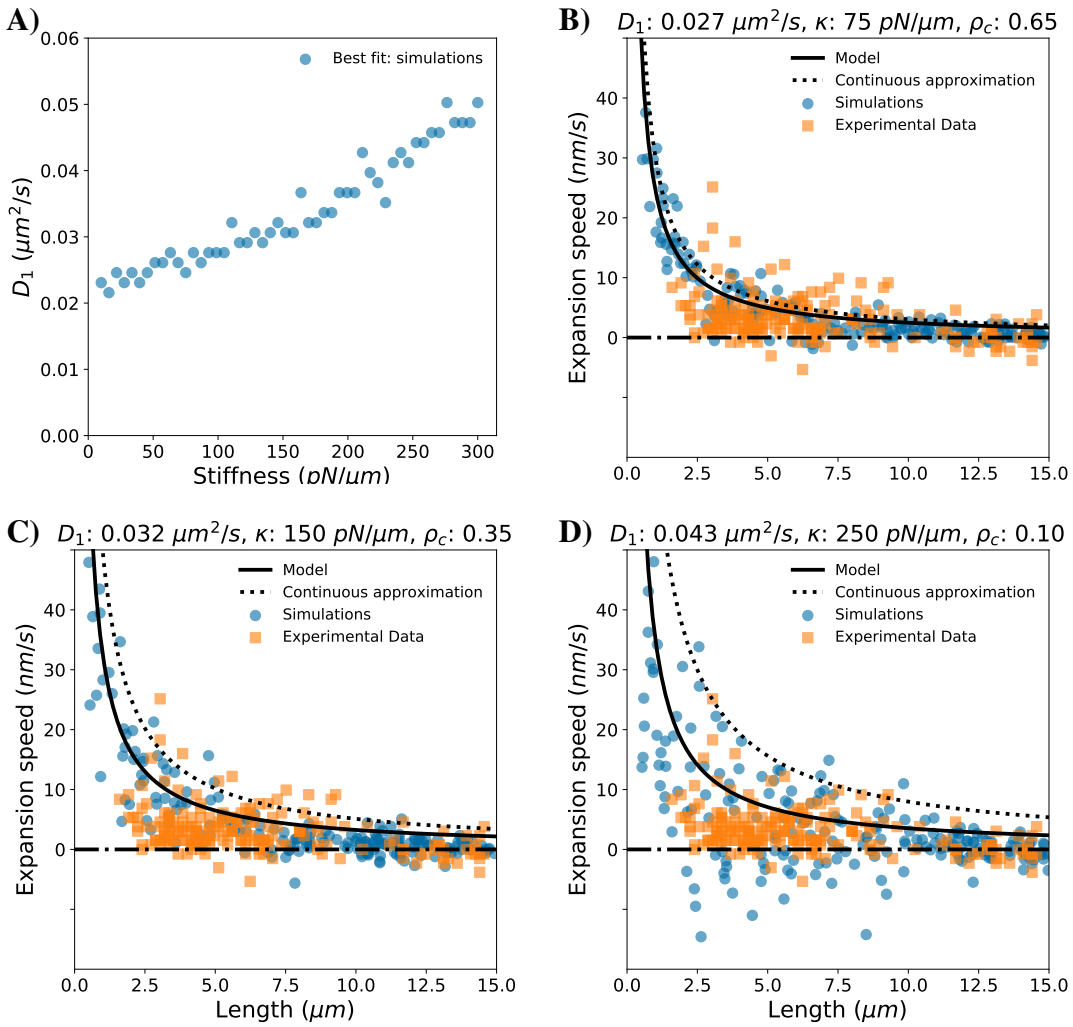

Figure 2.4: Entropic expansion of compressed overlaps

A) Pairs of diffusion rate (D_1) and stiffness (κ) that best matched the observed diffusion rate of Ase1 in overlaps. For every value of κ (from 10 to 300 pN/µm), simulations were run scanning 50 values for D_1 (from 0.011 to 0.085 µm^2/s). A dot is placed indicating the D_1 for which the simulated diffusion of 1000 crosslinkers was closest to the experimental value (0.011 µm^2/s). **B)** Expansion speed for an overlap containing diffusible crosslinkers, as described in [114]. Blue dots represent the initial speed of sliding of individual simulations (κ = 75 pN/µm, D_1 = 0.027 µm^2/s), with an initial occupancy ρ_c = 0.65. The black line represents the prediction of Eq. 2.11 with β = 0, and the dotted line indicates the result obtained without this approximation. The experimental data (orange squares) is reproduced from [114] with permission. **C)** Same as B, but with a different value of the parameters: κ = 150 pN/µm, D_1 = 0.032 µm^2/s and ρ_c = 0.35. **D)** Same as B, but with a different value of the parameters: κ = 250 pN/µm, D_1 = 0.043 µm^2/s and ρ_c = 0.1.
Reproduced from [117] under the CC BY 4.0. Experimental Data is from [114] and was provided by the authors

on density. Under these assumptions, the force per crosslinker is $f_d = \frac{P}{c}$ and using (2.2), expansion velocity can be predicted analytically:

$$v_{\text{fil}} = a\,(1-\rho_c)\left[k^+(f_d) - k^-(f_d)\right] \tag{2.11}$$

To choose the parameters to model the system, we assume that k_0 in Equation 2.2 can be different for crosslinkers that are bound with one head only and for those bound with both. This means that multiple combinations of k_0 and κ can match the observed diffusion rate of Ase1 in overlaps, 0.011 $\mu m^2/s$ (Fig. 2.4A). For such combinations, and fitting the initial density, simulations show good agreement with the experimental data (Fig. 2.4B-D). For $\kappa < 300$ pN/μm, the theory agrees with the stochastic model. For small values of stiffness, the solution neglecting β in Equation 2.11 is in good agreement with the simulations, but increasing stiffness requires accounting for the contribution of β (Fig. 2.4C-D). Multiple combinations of parameters are therefore adequate to model these results.

Steady overlaps

We next consider the scenario in which sliding results in overlap shrinkage. It has been observed experimentally that when Ase1 [22, 114] or PRC1 [211] are retained in a shrinking overlap, such that sliding results in the increase of the density of crosslinkers, stable overlaps form. However, if PRC1 turnover is fast compared to sliding, so that overlap shrinkage does not result in an increase of density, sliding continues until both microtubules are completely slid apart [180]. We model this by suppressing the growth of microtubules in system B and system D, which previously kept overlap constant. In this regime, overlaps can shrink and occupancy of crosslinkers increases (see assumptions). From Equation 2.6 we predict that strong tetrameric motors, like kinesin-5, only stop sliding when all lattice sites are occupied. In this case, the final length L is simply determined by the number of crosslinkers $L = ca$ (Fig. 2.5A). However, from Equation 2.9 we predict that weaker motors, like kinesin-14, can form stable overlaps above total compaction, where motor forces are balanced by entropic pressure:

$$-\frac{1}{L}\log\left(1-\frac{c\,a}{L}\right) = \frac{v_0\,\rho_m\,\gamma_{tm}}{k_B T} \tag{2.12}$$

We confirmed these results with simulations (Fig. 2.5B), showing that, even when their magnitude is comparable with the stall force of a single motor, entropic forces can promote the formation of stable overlaps.

Therefore, our results predict that stable overlaps can be formed in the presence of diffusible crosslinkers in two different ways. When motors forces are small, sliding speed gradually decreases as overlap shrinks, until it eventually stops when motor force is matched by entropic pressure (Fig. 2.3C). This behaviour has been observed previously for kinesin-14 and Ase1 [22] (for a kymograph, see Fig. 1.8B). However, when motor forces are strong, our theory predicts that sliding speed is mostly unaffected by overlap shrinkage until an eventual sharp transition at very high occupancies (Fig. 2.2C, grey line). This behaviour has been observed in the kinesin-4 / PRC1 system [211] (for a kymograph, see Fig. 1.9C).

We have seen that at a given density of crosslinkers, sliding velocity becomes zero. This allows for the formation of stable overlaps with non-dynamic microtubules. However, a more interesting scenario is predicted if we allow microtubules to grow at a constant speed (v_g). In such a situation, as long as the maximum sliding speed is faster than the growth

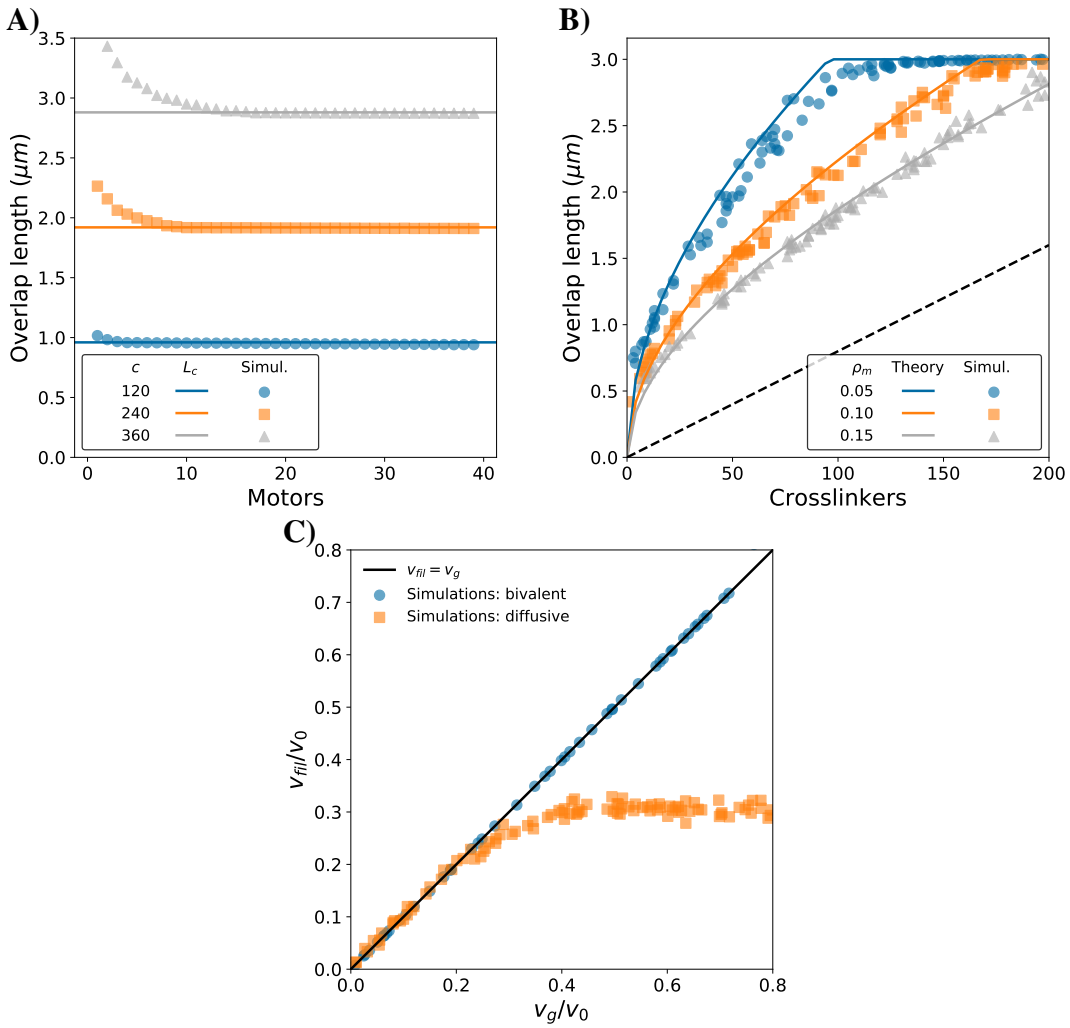

Figure 2.5: Steady state overlaps length and entropic forces

A) Steady state overlap length for system B with non-growing microtubules. Dots represent the results of individual simulations, with 1 to 40 bivalent motors (f_s = 6 pN, v_0 = 0.05 μm/s). The number of crosslinkers (D_1 = 0.1 μm^2/s) is 120 (blue discs), 240 (orange squares) and 360 (grey triangles). Coloured lines indicate total compaction. **A)** Steady state overlap length for system D with non-growing microtubules. Dots represent the results of individual simulations, with 1 to 200 crosslinkers (D_1 = 0.1 μm^2/s). The number of motors (D_1 = 0.1 μm^2/s, f_s = 6 pN) is 100 (blue discs), 200 (orange squares) and 300 (grey triangles) and v_0 = 0.2 μm/s. Coloured lines indicate Eq. 2.12, dashed line indicates the overlap length if occupancy of the lattice by crosslinkers was total (ρ_c = 1). **C)** Sliding speed for systems B (blue circles) and D (orange squares), in which microtubules grow at a constant speed v_g (x-axis). Speeds are normalised to the unloaded speed of the motor v_0. Dots represent the results of individual simulations with 150 crosslinkers and 100 motors (blue) or 300 motors and 75 crosslinkers (orange), and microtubule growth speed (in μm/s) chosen randomly in (0, 0.04). The parameters are as in A and B. The black line indicates equality between growth and sliding speeds. Note that sliding by diffusible motors stops matching growth speed once the microtubule growth speed surpasses the maximum speed of the motors (Equation 2.9 with $\rho_c \simeq 0$)

Reproduced from [117] under the CC BY 4.0

speed, a stable overlap forms in which sliding occurs at the speed of microtubule growth. This coordination happens because elongation of the microtubules decreases the density of crosslinkers in the overlap, allowing motors to sustain sliding. Indeed, we observed this coordination in our simulations both for bivalent and diffusive motors (Fig. 2.5C). We therefore predict than in a regime where growth speed is limiting, diffusible crosslinkers alone can produce the coordination of sliding and growth. This prediction is important because such coordination is a landmark of the anaphase spindle. Conversely, in a system in which crosslinker unbinding timescale is slower than sliding, motor sliding can shrink overlaps and increase crosslinker density, eventually stopping sliding. Once this point is reached, sliding will continue at the rate of crosslinker unbinding, as unbinding of crosslinkers decreases the occupancy and allows further motor sliding.

3 Part 2: Application of the theory to an *in vitro* system

3.1 Experimental results

Experimental results presented in this section were produced and analysed by J. Hannabuss and colleagues. Here we provide a brief summary of the key results that we explain with our model. For experimental and analysis methods see [81]

Tubulin, KIF4A and PRC1 self-organise into structures that resemble the anaphase central spindle

For a detailed description of the KIF4A/PRC1 system see chapter 1 subsection 4.4. In short, KIF4A (kinesin-4) is a dimeric kinesin that can bind to single microtubules, but cannot crosslink microtubules on its own [211]. However, it can bind to the microtubule crosslinker PRC1 [16]. When kinesin-4 is bound to PRC1, it transports PRC1 to the plus ends of single microtubules [179], and produces sliding of overlapping microtubules crosslinked by PRC1 [211]. The mechanism by which KIF4A/PRC1 complexes produce sliding has not been yet described. In addition, kinesin-4 suppresses microtubule dynamics at the plus ends, preventing growth and shrinkage [16]. The sliding activity of the KIF4A/PRC1 system has been previously studied with stabilised microtubules [211], while its effects on microtubule dynamics have only been studied in setups where sliding could not happen [16]. In this study, Hannabuss and colleagues first combine these two activities and study how the components of this system (tubulin, KIF4A and PRC1) self organise *in vitro*. In the conditions of the experiments, components are free to diffuse and no microtubule seeds nor microtubule stabilising agents are added.

Mixing purified PRC1, kinesin-4 KIF4A and tubulin *in vitro* leads to the spontaneous nucleation of microtubules, which are crosslinked into antiparallel bundles by PRC1 (Fig. 2.6A). These bundles are subsequently slid by KIF4A, resulting in the formation of symmetrical structures in which plus ends are focused in the overlap of the bundle, and minus ends extend outwards (Fig. 2.6A, B). Overlaps in these structures initially elongate, reaching a peak length. Then they slowly shrink in time until they reach a final overlap length (Fig. 2.6C). After overlaps reach their peak length, the total amount of KIF4A and tubulin is roughly constant, but PRC1 amount decreases at the same pace as overlap length (Fig. 2.6C). Interestingly, while FRAP experiments show turnover of KIF4A in the overlaps, PRC1 intensity does not recover at all after photobleaching (data not included, see [81]). This means that the decrease in PRC1 intensity represents a net unbinding of PRC1

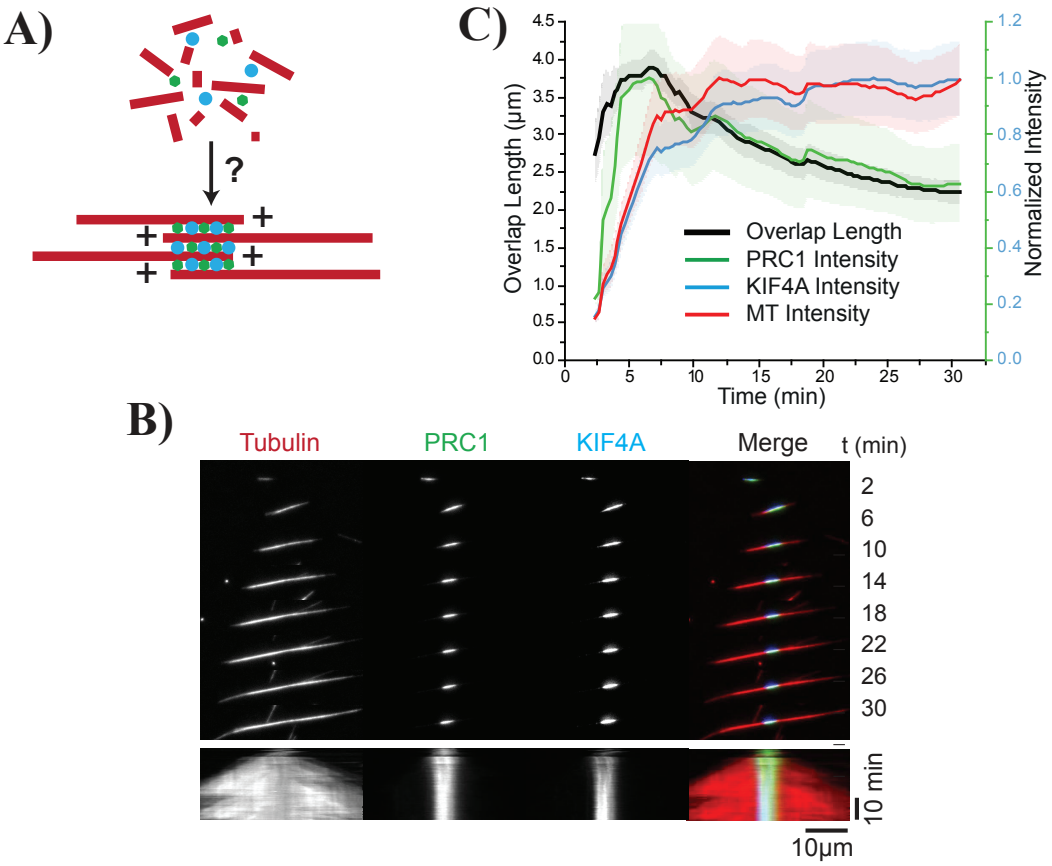

Figure 2.6: Self-Organization of Minimal Anaphase Midzone Bundles

A) Schematic of the formation of minimal anaphase midzone bundles, with tubulin in red, PRC1 in green and KIF4A in blue. **B)** Single- and triple-colour TIRF microscopy image sequences (top) and kymographs (bottom) showing PRC1 and KIF4A accumulation in the central part of the antiparallel microtubule bundle. Experiment containing 20 nM PRC1-Alexa546 (green), 50 nM KIF4A-mBFP (blue) and 12.5 µM Alexa647-tubulin (red). **C)** Mean overlap length and normalised mean total fluorescence intensity measured in the overlap region of minimal midzone bundles for Alexa647-tubulin, PRC1-Alexa546 and KIF4A-mBFP plotted as a function of time (n = 17). The shaded areas show the standard error. Protein concentrations as in (B).

from the overlap. These antiparallel bundles with plus ends at the equator (Fig. 2.6A) are reminiscent of the anaphase central spindle, which is composed of interpolar microtubules that are crosslinked antiparallelly at their plus ends [175]. Similarly to these structures, the mammalian central spindle also slowly shrinks as anaphase progresses [224], and is characterised by a low turnover of PRC1 [10].

From Fig. 2.6C, we can distinguish two phases in this experiment: (phase 1) an initial phase where microtubules grow until the overlap reaches its peak length, and (phase 2) a slow decay of overlap length, which stabilizes at a given final length. Importantly, the decrease in overlap length during phase 2 is driven exclusively by sliding, as shown by bleaching experiments (see [81]).

The peak overlap length reached during phase 1 is affected by the amounts of PRC1 and KIF4A in solution: increasing PRC1 concentration for a given concentration of KIF4A

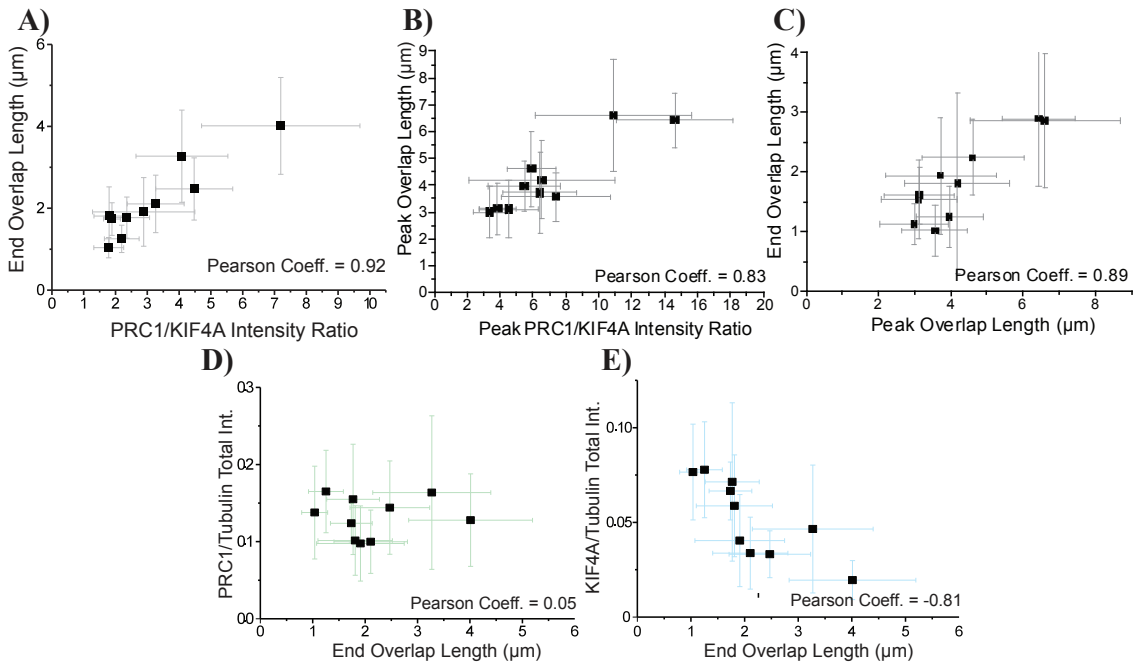

Figure 2.7: Overlap length correlations

A) Scatter plot of the mean final overlap length as a function of the mean final PRC1/KIF4A fluorescence intensity ratio. **B)** Plot of the mean peak overlap length against the mean PRC1/KIF4A intensity ratio measured in the overlap at the time of its maximum length, also demonstrating a positive correlation. **C)** The mean peak overlap length and mean final overlap length show a positive correlation. **D)** Mean PRC1/tubulin and **E)** mean KIF4A/tubulin total fluorescence intensity ratios in the overlap region, versus the mean end overlap length. Conditions: Alexa647-tubulin concentration 12.5 µM and PRC1/KIF4A concentration pairs (in nM/nM): 5/5, 5/10, 5/50, 10/5, 10/10, 10/50, 20/5, 20/10, 20/50, 50/50 (n > 93 overlaps per condition). Error bars represent standard deviation. *Reproduced under the CC BY 4.0 terms from [81]. Data acquisition and analysis were performed by J. Hannabuss and colleagues*

increases peak length. Conversely, increasing KIF4A concentration for a given PRC1 concentration reduces peak length. This data is summarised in Fig. 2.7B, which shows that peak length positively correlates with the ratio of PRC1/KIF4A measured by fluorescence signal of labelled PRC1 and KIF4A in overlaps.

This behaviour is consistent with the mechanism of overlap length regulation by KIF4A and PRC1 proposed in [16]. Initially, microtubules grow at their plus ends and elongate the overlap, since there is little or no kinesin-4 in the overlap. However, as the overlap grows, it recruits more kinesin-4, which processively walks to plus ends and ultimately stops growth. Increasing concentrations of KIF4A for a given concentration of PRC1 would stop growth earlier and result in shorter peak length. When keeping KIF4A concentration constant, higher PRC1 levels increase overlap length because in this system it is PRC1 that promotes microtubule nucleation. Therefore, increasing PRC1 concentration produces more bundles, which effectively dilutes the concentration of KIF4A per bundle.

Intriguingly, peak length strongly correlates with final length (Fig. 2.7C). This means that the ratio of peak and final overlap is roughly constant across conditions, which implies that overlaps that reach a longer peak length during phase 1 slide faster in phase 2. This is not intuitive, given that overlaps reach longer lengths in phase 1 when they recruit less KIF4A motors (Fig. 2.7B, E). This means that overlaps with lower motor density slide faster.

Additionally, the PRC1 density on overlaps is the same across all conditions (Fig. 2.7D).

In the next sections, we adapt our previous model to explain the sliding produced by KIF4A and PRC1 in phase 2 (Fig. 2.6B), and the measured correlations (Fig. 2.7). Since we think that the peak length is determined by the mechanism from [16] described above, we focus on phase 2. We model a system with microtubules that do not grow or shrink, in order to understand the correlation between peak length and final length, and why PRC1 density is the same across all conditions.

3.2 Assumptions

This section is partially reproduced under the CC BY 4.0 terms from [81] and was originally written by myself.

For modelling the PRC1/ KIF4A system we take the same assumptions as in subsection 2.1, with few modifications presented here (Fig. 2.8).

PRC1 diffusible heads are modelled on a lattice as before. Unbound entities are uniformly distributed in the space, and heads bind to the microtubule with constant rate k_b, but their detachment increases exponentially with the tension in the linker:

$$k_u = k_u^0 exp(|f_d|/f_u) \tag{2.13}$$

Where k_u^0 is the detachment rate in the absence of force, f_d is the force in the linker and f_u is a characteristic unbinding force.

KIF4A motors are composed of a single motor head. In this case, motor heads are modelled as discrete entities on a lattice of same spacing as diffusive heads. The motor lattice is exclusive, so motor heads cannot either bind or step into an occupied site. However, the lattice sites of motors are distinct from those of crosslinkers. This assumption follows experimental observations showing that kinesin-4 can move on microtubules where PRC1 density is so high that individual PRC1 molecules do not diffuse [16]. In our model, we tried two assumptions for KIF4A: either it is not allowed to fall off at microtubule plus-ends, or it falls of immediately (parameter set 3). KIF4A can associate with PRC1 from the microtubule or from solution (Fig. 2.8, 2). This interaction is represented by an elastic link between the KIF4A head, and the PRC1 linker, as described below. When it is not bound to PRC1, KIF4A moves on the lattice towards the plus end with a rate v_0/a, given by its maximum speed v_0 and the lattice spacing a. When it is bound to PRC1, the stochastic plus end stepping rate k^+ is affected by the antagonistic force in the linker ($f_m > 0$) (Fig. 2.8, 7), and follows the linear force-velocity relation that was measured for kinesin [135], where f_s is the stall force of the motor:

$$k^+ = \frac{v_0}{a}\left(1 - \frac{f_m}{f_s}\right) \tag{2.14}$$

The interaction between crosslinker and motor is modelled as follows: KIF4A can attach to PRC1 from the microtubule, when a PRC1 head and a KIF4A head are on adjacent sites of the lattice, with rate k_{am} (Fig. 2.8, 2). KIF4A can also attach from solution to PRC1 on the microtubule or to PRC1 in solution following second-order reaction kinetics with rate k_{as} (Fig. 2.8, 2). KIF4A that is bound to PRC1 can bind to microtubules as it does from solution. The interaction is represented by an elastic link between the KIF4A head, and the PRC1 linker. For simplicity, the link between KIF4A and PRC1 is at the center of the PRC1 linker. The three heads are then connected to a dragless junction by elastic linkers of equal stiffness, and the position of the junction at every time point is given by the force balance of the connected links. To calculate the force applied to each head of the

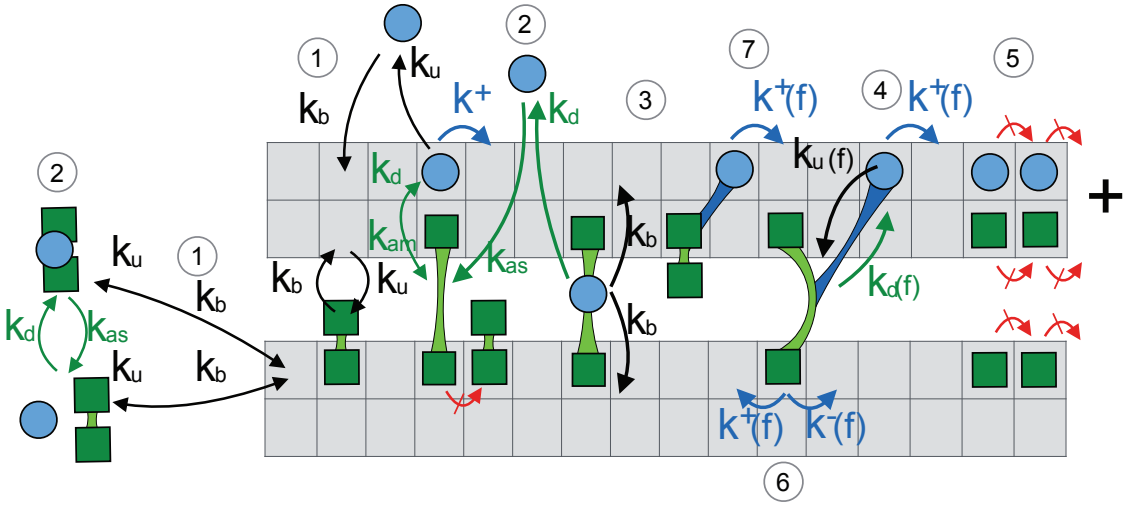

Figure 2.8: Components of the computational model.
1) KIF4A and PRC1 can bind to a microtubule from solution with constant rates (k_b) and unbind with force-dependent rates (k_u). PRC1 and KIF4A bind to different sites on the microtubule, spaced every 8 nm, that can only accommodate one molecule. The PRC1 molecules are composed of two identical heads. If one of the PRC1 heads is bound to a microtubule, the other head can bind to a second microtubule with rate k_b. **2)** KIF4A can attach to PRC1 from solution with rate k_{as}, or from adjacent sites on the microtubule with rate k_{am}, and detach with a force-dependent rate k_d. **3)** KIF4A molecules that are attached to PRC1 can bind to microtubules as they do from solution. **4)** KIF4A molecules that are attached to PRC1 molecules and bound to a microtubule can either detach from PRC1 or unbind from the microtubule with force-dependent rates (k_u, k_d). **5)** Both PRC1 and KIF4A cannot move to an occupied binding site, and do not step out of the lattice at either ends. **6)** PRC1 heads diffuse on the lattice with hopping rates (k^+, k^-), which depend on the tension in the linker to the other PRC1 head, and eventual KIF4A partner. **7)** KIF4A moves towards the plus end with a rate (k^+), affected by the force that drags the eventual PRC1 partner.

complex when all three are attached, we use the following equivalence: Let P_1, P_2 and P_3 be the positions in space of the two heads of the PRC1 molecule and the KIF4A head, and X the position of the dragless junction. If the stiffness of all linkers is the same (κ), the force balance reads:

$$0 = \kappa(P_1 - X) + \kappa(P_2 - X) + \kappa(P_3 - X) \tag{2.15}$$

$$X = 1/3(P_1 + P_2 + P_3) \tag{2.16}$$

Since P_1 is only linked to X, the force on P_1 is $\kappa(X - P_1)$. If we substitute X, we get:

$$f_1 = \kappa/3[(P_2 - P_1) + (P_3 - P_1)] \tag{2.17}$$

And similarly, for P_2 and P_3. Therefore, the situation is comparable to having the three heads linked to each other by springs of elastic constant $\kappa/3$ (Fig. 2.9A). In case only two heads of the complex are bound, the effective stiffness acting between the two heads is $\kappa/2$ (Fig. 2.9A). The force in the link between KIF4A and PRC1 affects the detachment rate of KIF4A from PRC1 and the unbinding of KIF4A from the microtubule with forces characteristic of the interaction between KIF4A and PRC1 (f_d), and KIF4A and

the microtubule (f_u) as in Equation 2.13. In the simulation we do not include the scenario in which a complex of PRC1-KIF4A is only attached to the microtubule through the KIF4A head, because experimentally KIF4A binding is strongly enhanced by the presence of PRC1; therefore, when the complex PRC1-KIF4A binds from solution, it only does so by first attaching a PRC1 head. When in a complex in which one PRC1 head is bound to the microtubule there is unbinding of that head from the microtubule, the KIF4A detaches from PRC1.

3.3 Computational results

Computational model

To understand the mechanism of long lasting overlap formation by PRC1 and KIF4A, we used a slight variation of the model proposed in section 2 (see assumptions in subsection 3.2 and Fig. 2.8). Essentially, we consider a one dimensional system composed of a pair of antiparallel microtubules that for simplicity have a constant length. PRC1 is modelled as a diffusible crosslinker, like in System B of subsection 2.2. However, in this case diffusible crosslinkers can bind with constant rate and unbind with force-dependent rates. KIF4A is modelled as a single motor head in a lattice. It steps towards the plus end, and it cannot bind nor step into an occupied site. KIF4A and PRC1 lattices are different, following the experimental observation that kinesin-4 can move on microtubules where PRC1 density is so high that individual PRC1 molecules do not diffuse [16]. In addition, KIF4A can bind to PRC1 when they are at the same lattice position on the microtubule with a constant rate, or in solution following second-order reaction kinetics. The association of KIF4A and PRC1 is represented by an elastic link joining KIF4A to the middle of the PRC1 molecule (Fig. 2.9B). On a single microtubule, KIF4A transports PRC1 towards the plus end. In an overlap, when PRC1 is bound to both microtubules, motor stepping produces a tension in the linker, which can be dissipated by either diffusion of the PRC1 bound to the opposite microtubule or by sliding of the microtubules (Fig. 2.9D). Since part of the tension is released through diffusion, there is a net displacement of the complex towards the plus end of the microtubule to which the motor is bound.

Sliding speed in the low density regime

In the low density regime, the sliding speed produced by KIF4A/PRC1 complexes at steady state can be derived from the force-velocity equations of the motor and diffusive heads, and the filament, as we did in section 2. Let us name m the motor, a the PRC1 head that is attached to the same microtubule as the motor, and b the PRC1 head attached to the opposite microtubule (Fig. 2.9B). Using the equivalence depicted in Fig. 2.9A (see assumptions), the force-velocity equations are:

$$\begin{aligned} v_m &= v_0 - \frac{f_{ma} + f_{mb}}{\gamma_m} \\ v_a &= \frac{1}{\gamma_d}\left(f_{ma} - f_{ab}\right) \\ v_b &= \frac{1}{\gamma_d}(f_{mb} + f_{ab}) \\ v_{\text{fil}} &= \frac{n}{\gamma_{\text{fil}}}\left(f_{mb} + f_{ab}\right) \end{aligned} \tag{2.18}$$

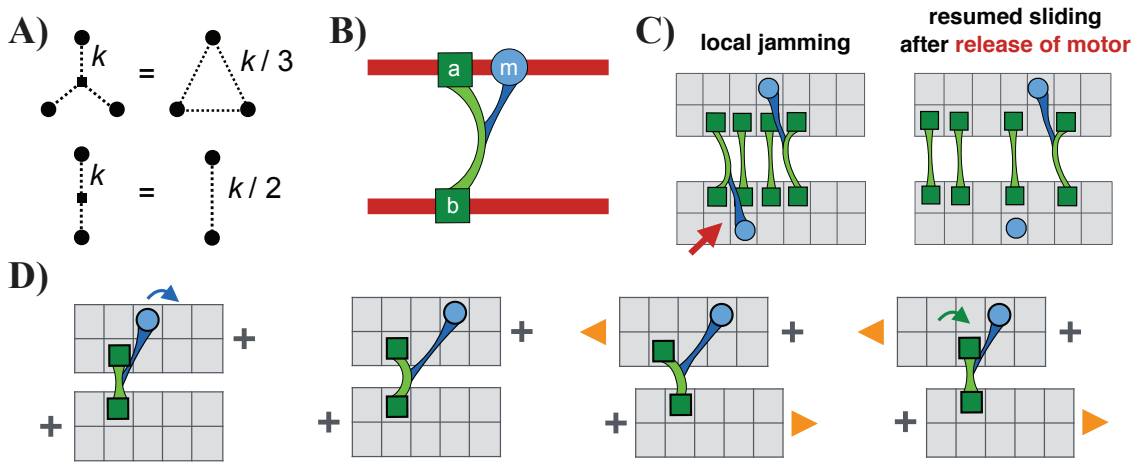

Figure 2.9: Sliding by the PRC1/KIF4A complex

A) Equivalence of different configurations of Hookean springs as described in the assumptions. **B)** Symbols used in Equation 2.18: m the motor, a the PRC1 head that is attached to the same microtubule as the motor, and b the PRC1 head attached to the opposite microtubule. **C)** Resolution of a traffic jam caused by two motors moving in opposite directions that trap PRC1 molecules between them. The resolution is due to the increase in the tension of the linker between KIF4A and PRC1, which promotes unbinding of KIF4A from PRC1. **D)** Sliding mechanism. KIF4A pulls a PRC1 molecule that is linking two microtubules, inducing strain on both PRC1 heads. The top PRC1 head releases the strain by biased diffusion towards the plus end. The bottom PRC1 head releases the strain by biased diffusion or microtubule sliding.

Where γ_d and γ_m are the characteristic drags of the diffusive and motor head, as defined in Table 2.1, γ_{fil} is the fluid drag, n is the number of bound complexes, and f_{ij} represents the projection of the force between i and j on the microtubule.

Similarly to System C in subsection 2.2, at steady state $v_m = v_a = v_b + 2v_{\text{fil}}$, and by definition of the forces we have that $f_{mb} = f_{ma} + f_{ab}$. We obtain the following expression for the filament speed:

$$\frac{v_{\text{fil}}}{v_0} = n\frac{\gamma_d\gamma_m}{2\gamma_d\gamma_{fil} + \gamma_{fil}\gamma_m + 2\gamma_d^2 n + 2\gamma_d\gamma_m n} \tag{2.19}$$

Given that for the parameters of the system we expect $\gamma_m \gg \gamma_d$, and $\gamma_m \gg \gamma_{fil}$ the expression simplifies to:

$$\frac{v_0}{v_{\text{fil}}} = 2 + \frac{\gamma_{\text{fil}}}{n\gamma_d} \tag{2.20}$$

This equation is identical to Equation 2.7 when $\gamma_m \gg \gamma_d$. The reason for this is that, since KIF4A stall force is enough to drag a PRC1 head at its maximum speed, the presence or absence of the head a in Fig. 2.9B makes no difference, and this is equivalent to System C in subsection 2.2 for the expected parameters.

PRC1/KIF4A drive microtubules to total compaction

In the more complicated scenario where PRC1 is present in the overlap both on its own and in complex with KIF4A, the drag opposing sliding comes mainly from PRC1 crosslinkers not associated with KIF4A. In addition, transient PRC1 "traffic jams" are formed when two

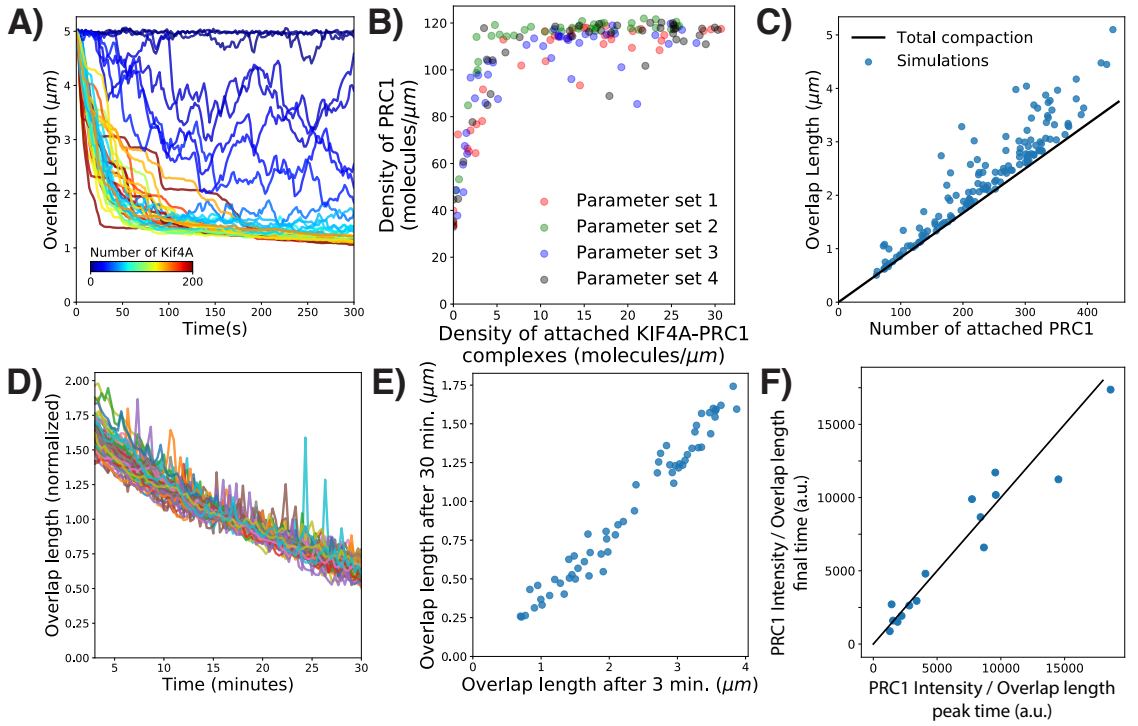

Figure 2.10: Simulation results

A) Dynamics of overlap length in simulations (MT length 5 µm, 200 PRC1, Table 2.3, set 1). Lines stand for individual simulations where the number of KIF4A varies from 0 to 200 (see color scale). **B)** PRC1 density after 300 s in simulations containing two microtubules of length 5 µm, 200 PRC1 molecules, and KIF4A molecules varying from 0 to 200, for parameters indicated in Table 2.3. Dots represent individual simulations placed as a function of the density of PRC1-KIF4A complexes in the overlap. Note that a density of 125 PRC1/µmcorresponds to full compaction. **C)** Scatter plot showing the correlation between the length of the overlap and the number of PRC1 molecules attached in the overlap after 300 s. Each dot represents one simulation (Table 2.3, set 1), but with randomized numbers of KIF4A (30-200) and PRC1 (100-600) and microtubule length (3–7 µm). The diagonal black line represents full compaction (i.e. one molecule per 8nm). **D)** Shortening of overlaps in different simulations containing 100 KIF4A molecules and between 100 and 600 PRC1 simulations (Table 2.3, set 1). In these simulations, compaction is reached earlier than 3 minutes after KIF4A addition (A), and this plot focuses on later times. Overlap length is normalised to median length for each simulation. **E)** Overlap at 3 minutes (when total compaction reached) vs. overlap at 30 minutes for data shown in (D). **F)** Comparison between the experimental ratio between PRC1 intensity and overlap length, at the time of maximal overlap (x-axis) and at final time (y-axis). Dots represent individual overlaps from the data shown in Fig. 2.6C. The diagonal indicates perfect conservation of this quantity.

complexes moving in opposite directions meet (Fig. 2.9C). These jams initially increase sliding efficiency, since PRC1 cannot diffuse, and force generated by the motor can only be dissipated by sliding. Jamming events are resolved in simulations by unbinding of the motor from PRC1 due to the increase of force in the linker between KIF4A and PRC1 (Fig. 2.9C, red arrow). Once one of the motors is released, since PRC1 diffusion rate is fast compared to motor stepping, the jamming is resolved. Eventually, as the overlap shrinks, the lattice of PRC1 becomes saturated and sliding stops at total occupancy, producing a

long lasting microtubule overlap. Therefore, sliding initially occurs at a fast speed, and suddenly slows down when total compaction is approached (Fig. 2.10A). This behaviour matches the experimental observations where pairs of microtubules in presence of PRC1 and KIF4A slide at constant speed and abruptly stop [211] (see Fig. 1.9C for a kymograph). We tried various parameters of the system. From our reference set of parameters (Table 2.3, parameter set 1), we decreased the stall force six fold (parameter set 4), we increased the turnover of binding and PRC1 interaction of KIF4A ten fold (parameter set 2), and we allowed KIF4A to step out of the microtubule at the plus ends (parameter set 3). For all conditions, we observe that PRC1 density reaches values near total compaction whenever the density of PRC1/ KIF4A complexes is higher than ~10/µm (Fig. 2.10B, Table 2.3). Total compaction is also reached for a wide range of motor and crosslinker number and initial overlap length (Fig. 2.10C). Since experimentally we observe a constant density of PRC1 in final overlaps (Fig. 2.7D), we propose that in our experimental conditions, concentrations of KIF4A and PRC1 are enough to always reach total compaction.

Our computational model therefore explains how the KIF4A/PRC1 system can form long lasting microtubule overlaps in which the PRC1 density is driven to total compaction by the action of KIF4A. We believe this total compaction occurs early on in our experiments, while overlaps are still elongating in phase 1. Later, PRC1 amount decays at the same rate as overlap length (Fig. 2.6C), suggesting that overlaps remain at total compaction as they shrink.

PRC1 unbinding drives overlap shrinking during phase 2

In phase 2, we observe that overlap length slowly decreases with similar dynamics as PRC1 unbinding (Fig. 2.6C). The value of sliding speed is at least 100 times slower than the unloaded motor speed. In our model, since KIF4A keeps overlaps at total compaction, loss of PRC1 from the overlap produces shrinkage (Fig. 2.10D). For a constant unbinding rate of PRC1, longer overlaps lose PRC1 at a higher rate than shorter overlaps. This yields a positive correlation between initial and final length in simulations (Fig. 2.10E), which matches the observed correlation between peak and final length of overlaps (Fig. 2.7C). If PRC1 is kept at total compaction throughout the shrinking phase, the ratio of PRC1 intensity to overlap length should be the same at peak and final length, and this is indeed the case (Fig. 2.10F).

We propose therefore the following model for the self organisation of this system, divided in two parts: (1) Prior to reaching peak overlap length, microtubules are bundled by PRC1 and grow at their plus ends until they reach a length at which KIF4A recruitment fully suppresses the elongation, as previously published [16]. We have not modelled this step. (2) When microtubules reach their peak overlap length, they are kept at total compaction by the action of KIF4A, and overlaps shrink as PRC1 unbinds.

4 Stochastic Simulation Methods

This section is reproduced and extended under the CC BY 4.0 terms from [117] and was originally written by myself.

We used the Open Source project Cytosim in 1D (https://gitlab.com/f.nedelec/cytosim). We extended the code to include diffusible crosslinkers, and to allow binding of motors to crosslinkers to model the binding of KIF4A to PRC1. The top (resp. bottom) microtubule is represented by an ordinate p (resp. p') and a direction $d = +1$ (resp. $d' = -1$). The

	Symbol (units)	Description	Set 1	Set 2	Set 3†	Set 4
PRC1	k_b (s^{-1})	Binding rate	0.01	-	-	-
	k_u (s^{-1})	Unbinding rate	0.001	-	-	-
	f_u (pN)	Unbinding force	6	-	-	-
	D ($\mu m^2/s$)	Diffusion rate	0.1	-	-	-
KIF4A	k_b (s^{-1})	Binding rate	0.1	1	0.1	0.1
	k_u (s^{-1})	Unbinding rate	0.1	1	0.1	0.1
	f_u (pN)	Unbinding force	6	-	-	-
	v_0 (μm/s)	Unloaded speed	0.8	-	-	-
	f_s (pN)	Stall force	6	6	6	1
Interactions	k_{as} (s^{-1} $molecule^{-1}$)	Attachment rate (solution)	$5x10^{-4}$	$5x10^{-4}$	$5x10^{-4}$	$5x10^{-4}$
	k_{am} (s^{-1})	Attachment rate (lattice)	1	10	1	1
	k_d (s^{-1})	Detachment rate	0.1	1	0.1	0.1
	f_d (pN)	Detachment force	1	-	-	-
	κ (pN/μm)	Linkers stiffness	200	-	-	-

Table 2.3: Parameters of simulations

Parameters used in the computer simulations, unless specified.
† In parameter set 3, when KIF4A tries to step beyond the plus end, it unbinds from the microtubule and is released to the unbound pool.

location of the heads are recorded by their distance from the minus-end, a.k.a the abscissa x_i, such that the position in space is $p + d\,x_i$. An array of boolean values T is used for each microtubule to represent lattice occupancy, where $T[i]$ corresponds to abscissas in $[ai, a(i+1)]$. The system is evolved using a time step of $\tau = 10^{-5}s$. Hopping to neighbouring sites are stochastic events, simulated using a random number generator: a rate R is simulated by testing $\theta < 1 - e^{-R\tau}$ at every time step. Hopping is forbidden if the lattice is occupied, and the lattice is updated at each molecular binding, unbinding or displacement. The force in a link is $\kappa\,\delta$ with $\delta = x_i - x'_i$. The movement of motors is represented by updating the abscissa: $x_i = x_i + v\,\tau$. The total force on each microtubule is calculated by summing all link forces. A Brownian dynamic approach using an overdamped Langevin equation is used to model the system, with an implicit numerical integration scheme [145]. **The steady state speeds** in Fig. 2.2 and Fig. 2.3B, C were calculated from 40s of simulated time. The sliding speed was obtained by regression of the distance between the microtubule minus ends, from 8 to 40 seconds. Steady state speed measurements in Fig. Fig. 2.5C were calculated similarly from 100s of simulated time. The fitting for bivalent motors (blue dots) was done using data from 70 to 100s, and from 40 to 100s for diffusive motor (orange squares). **The steady state force** in Fig. 2.3A was measured from 40s of simulated time. The microtubules (as shown on Fig. 2.1C), were immobilized by a Hookean element of stiffness κ_s. The steady state force is the average force exerted by these elements from 8 to 40 seconds. For each simulation, κ_s was adjusted to ensure that it would always have a similar stretch at steady state: $\kappa_s \propto a(D_m/v_0 kT + 1/f_s)$. **The steady state overlap length** for bivalent motors (Fig. 2.5A) was taken as the final overlap length after 100s of simulated time, while for diffusive motors (Fig. 2.5B), the

average overlap length was calculated from 80 to 200 seconds. **The diffusion rate of crosslinker in overlaps** (Fig. 2.4A) was calculated from the mean squared displacement ($MSD/2t$) of 1000 crosslinkers bound to two microtubules after 1 second of simulated time, in simulations with an infinite capacity lattice. **The expansion speed** (Fig. 2.4C-D) was measured from 15 seconds of simulated time by regression of the distance between microtubule plus ends. **Effective friction of crosslinkers** (Fig. 2.11) was calculated on simulations where a constant force was applied to the microtubule. The effective friction was calculated as the force divided by the sliding speed (obtained by regression of the distance between the microtubule minus ends, from 1 second of simulated time).

5 Discussion

Diffusible crosslinkers have received great attention in the last 15 years, due to their unique biophysical properties, which allow them to selectively crosslink antiparallel microtubules and diffuse on their surface [95, 99]. *In vitro*, such properties make them act like brakes against microtubule sliding, ultimately leading to the formation of overlaps that last for several minutes [22, 114, 211]. These overlaps are reminiscent of the anaphase central spindle, which is composed of interpolar microtubules crosslinked antiparallelly [175]. Importantly, in the central spindle, microtubules are more stable than in metaphase, and are maintained by rescue [21, 10]. This makes *in vitro* overlaps of stabilised microtubules a suitable minimal system to study the central spindle.

In this work, we have developed a theory to explain the formation of stable antiparallel overlaps. We find that their experimental behaviour can be explained by combination of a viscous drag that depends on diffusion rate, stiffness and steric hindrance of crosslinkers on the microtubule lattice. Stable overlaps can form when weak sliding forces are matched by the entropic pressure generated by the confinement of crosslinkers to a limited number of binding sites. However, under stronger forces, stable overlaps only form when all the lattice sites are occupied. In addition, our theory explains how overlaps of constant length can exist while microtubules slide, and that sliding velocity in those is set by microtubule growth speed. We also predict that in such stabilised overlaps, crosslinker unbinding can drive sliding at a speed that is orders of magnitude slower than the motor sliding speed. Our model is consistent with the observed velocities of overlap expansion driven by entropic forces [114]; it explains why sliding in the presence of motors and crosslinkers can be independent of overlap length [22, 180] and it can also describe the sliding by complexes of PRC1 and kinesin-4 [211, 81].

Finally, we have applied our theory to explain the experimental results of an *in vitro* setup in which a combination of crosslinkers, motors and tubulin results in the formation of bundles that resemble the central spindle. Interestingly, these bundles slide at a very slow speed while keeping a constant density of PRC1, which is consistent with crosslinkers reaching total compaction and sliding being driven by crosslinker unbinding.

Crosslinker diffusion rate, stiffness and occupancy determine friction

We have developed a theory to predict the sliding speed produced by combinations of motors and diffusible crosslinkers on pairs of antiparallel microtubules (Fig. 2.1B, D). At steady state, the average speed at which crosslinker heads move in one direction must match the average speed at which the microtubule moves in the opposite direction. Since the movements of crosslinkers on the filament depend on the forces applied to them

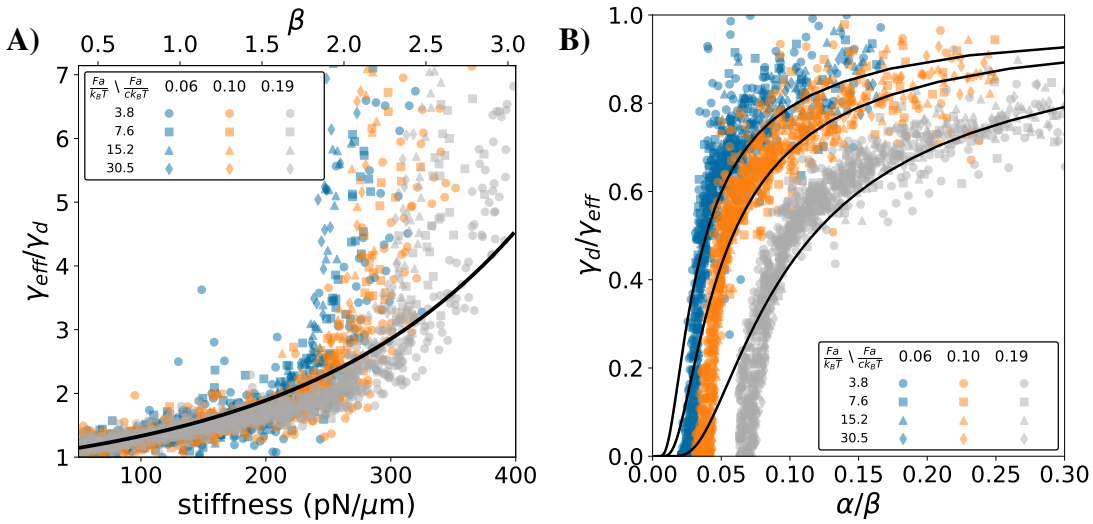

Figure 2.11: Friction generated by diffusible crosslinkers

A) Effective friction per crosslinker defined as $\gamma_{eff} = F/(cv_{\text{fil}})$, in a system composed of a single microtubule under a constant force F with c crosslinker heads bound to it, normalised to the characteristic drag of the crosslinker head γ_d as defined in Table 2.1. Dots represent the results of individual simulations. Force applied to the microtubule is 2 (circles), 4 (squares), 8 (triangles) and 16 (diamonds) pN. Number of crosslinkers depends on the force applied and is 30 pN^{-1} (blue), 20 pN^{-1} (orange), 10 pN^{-1} (grey). In the legend, these values of forces are normalised to the force k_BT/a. Diffusion rate of crosslinkers D_1 was 0.085, 0.04 or 0.02 $\mu\text{m}^2/\text{s}$, but all curves collapse after normalisation. For each condition, 100 simulations are represented in which a random value of stiffness κ was chosen in [50-400] pN/μm. The axis on top shows the value of $\beta = \kappa a^2/2k_BT$. Black line represents model predictions. **B)** Same data as in (A), but represented as a function of α/β, as defined in Equation 2.2. Note that the y axis represents the inverse quantity of (A). Black lines represents model predictions.

(Equation 2.3), this force-velocity relationship eventually determines the filament velocity under a given force. The drag coefficient associated with this force-velocity relationship has been previously called crosslinker friction [114]. This friction is not only determined by the diffusion rate of the crosslinkers D_1, but is also affected by the stiffness of the linker connecting the crosslinker heads κ (Equation 2.2). For low stiffness ($\kappa \leq 100$ pN), we can ignore the contribution of the linker stiffness, and the friction per crosslinker is constant and equal to their characteristic drag $\gamma_d = k_BT/D_1$. This makes it possible to solve steady states analytically, and the predictions fit the stochastic simulations with κ= 100 pN. For higher stiffness, the contribution of the linker cannot be ignored. We can define an effective drag per crosslinker $\gamma_{eff} = F/(cv_{\text{fil}})$, for a filament moving at a speed v_{fil} under a constant force F, with c crosslinkers attached. This effective drag is equal to the characteristic drag γ_d in the continuous limit, but it increases with stiffness (Fig. 2.11A). Unlike in the continuous limit, the effective friction of a crosslinker depends on the force applied to it. Let us suppose we have a filament attached to a given number of crosslinkers under a constant force. If we progressively increase the stiffness of the linker, eventually the force barely biases the diffusion of crosslinkers, since forward and backward rates have very similar values in Equation 2.2 ($k^+ \simeq k^-$ if $\beta \gg \alpha$, equation shown below).

$$k^+ = \frac{\alpha - \beta}{1 - e^{\beta - \alpha}} k_0 \quad \text{and} \quad k^- = \frac{\alpha + \beta}{e^{\alpha + \beta} - 1} k_0,$$
$$\alpha = a\, f_d / k_B T \quad \text{and} \quad \beta = \kappa a^2 / 2 k_B T$$

When $\beta \gg \alpha$, the effective drag increases dramatically (Fig. 2.11B), and the system behaviour qualitatively changes: microtubules adopt positions with their lattices in register, and move by discrete steps of length equal to the lattice unit. This regime generates frictions that increase exponentially with the number of crosslinkers and was recently described in [210]. In the model in [210] and in ours, the value of linker stiffness is a critical parameter. However, the response of real crosslinkers to force might not be Hookean, so measuring κ experimentally might not be simple. In addition, the dependency of forward and backward rates on force is different in this study (Equation 2.2) and [210, 114], but both formulations are theoretically valid. In the future, experimental measurement of the stepping rate of Ase1 or PRC1 in response to force will be important to understand which of the mentioned regimes (continuous, intermediate, exponential) better captures the behaviour of the molecule.

Our model predicts that lattice occupancy also plays an important role in resistance to sliding. Crosslinkers can build up higher tension when lattice occupancy prevents force release through diffusion. This explains why at high occupancies, when the value of entropic forces tends to infinity, overlap expansion speed decreases. This is because the steric hindrance dominates at high densities (Equation 2.10 and Fig. 2.3C).

It was shown previously that simulations with parameters that generated exponential friction reproduced the observed entropic expansion velocities [114]. We found multiple combinations of parameters that could reproduce the experimental results, even in regimes where friction does not increase exponentially with the number of crosslinkers (Fig. 2.4). In the non-exponential regime, the expansion velocity can be calculated analytically (Equation 2.11). Our theory also predicts that under certain parameter conditions, the sliding speed produced by kinesin-14 with Ase1 or kinesin-5 with PRC1 is independent of the overlap length, as observed experimentally [22, 180].

It has been shown experimentally that not all motors are equally affected by diffusible crosslinker braking. Strong motors, like kinesin-5, are barely affected by the presence of crosslinkers, even when these are in great excess [180]. Our theory reproduces this behaviour, given the value of stall force for kinesin-5 (~1 pN), and the unloaded speed (~50 nm/s). This results in a characteristic motor drag of $\gamma_m \simeq 20$ pN s/ µm, significantly higher than the one expected for diffusible crosslinkers, $\gamma_d \simeq 0.5$-0.05 pN s/ µm. With such drag coefficients, we expect the system to slide at the unloaded speed of the motor (Equation 2.6, Fig. 2.2C). The effect is different for diffusive motors, like kinesin-14. Their characteristic drag is mostly determined by the diffusive rate of their non-motor tail, which is in the same order of magnitude as diffusible crosslinkers, therefore ($\gamma_d \simeq \gamma_{tm}$) in Equation 2.9. Additionally, entropic pressure also counteracts sliding by diffusive motors, since they are weak force generators (Equation 2.8). Therefore, our theory agrees with experimental results showing that kinesin-14 sliding is affected by Ase1 [22] and that the diffusive tail of kinesin-14 motors limits their force production [124].

Finally, other modes of braking by diffusible crosslinkers have been observed. When a motile microtubule slides over a fixed microtubule, Ase1 accumulates at overlap edges [22]. Certainly, this braking mode is different from the one generated by a homogeneous

distribution of crosslinkers on the overlap. A similar phenomenon has been observed when measuring the force generated by PRC1 overlaps under different sliding velocities [67]. The experimental results were reproduced with a simulation comparable to the ones used in this work. The authors found that a key parameter to match the experimental behaviour was the rate at which PRC1 heads would hop out of the microtubule by diffusion from their ends. In this scenario, sliding creates an accumulation of PRC1 at the microtubule ends, which slows down sliding. However, the diffusion barrier at the microtubule end is leaky, and molecules can leave the microtubule at its ends at a certain rate, which determines the accumulation of crosslinkers at the edges and sets the sliding speed.

Diffusible crosslinkers form stable overlaps

We have explained how diffusible crosslinkers in combination with motor proteins can form stable overlaps. Our theory also implies that conventional crosslinkers that do not diffuse cannot stabilise overlaps, since sliding speed depends only on the ratio between numbers of motors and crosslinkers (Equation 2.4). On the contrary, overlaps can be stabilised by diffusible crosslinkers, since their density also influences sliding. In presence of weak diffusive motors like kinesin-14, stable overlaps form when sliding forces are counteracted by entropic pressure (Fig. 2.5A), while strong motors can only form stable overlaps when compaction of crosslinkers prevents sliding (Fig. 2.5B). Evidence for such high occupancies producing a traffic jam that stabilises overlaps can be found in previous experiments with pairs of microtubules of fixed length crosslinked by PRC1 and kinesin-4 [211]. In that system, sliding occurs at a constant speed, and abruptly stops, presumably due to jamming at high densities (see Fig. 1.9B, C). In the *in vitro* experiments shown in this study, PRC1 density in final overlaps is independent of motor concentration (Fig. 2.7D). This suggests that these overlaps are not stabilised by an equilibrium of motor forces against entropic pressure, since entropic force depends on density, and we found the same crosslinker density regardless of the concentration of motors. Our interpretation of this results is that overlaps are stalled because crosslinkers are near total compaction. Consistently with this, PRC1 unbinding results in sliding (Fig. 2.6C).

Formation of stable overlaps by strong motors and crosslinkers had been previously addressed in [97]. The authors considered a system with strong kinesin-5 molecules, in which crosslinker stepping rate by diffusion was comparable to the stepping rate of motors. In this regime, crosslinkers are able to sustain motor generated forces, and accumulate at the edges of the overlap, which act as diffusion barriers, allowing for crosslinker pressure to build up. We showed here however that for experimental parameters (stepping rate of crosslinkers is 100 times faster than that of motors), strong kinesin-5 motors drive the system to total compaction.

Crosslinker turnover is important for overlap stabilisation

Because crosslinker density has a role in the formation of stable overlaps, crosslinkers binding and unbinding rates are important parameters of the system. If the timescale of crosslinker unbinding is slower than sliding, overlap shrinkage results in the accumulation of crosslinkers in the overlap, which increases their density and resistance to sliding. This increase in density is not required for the stabilisation of overlaps by weak motors, since overlap shrinkage decreases motor force, but entropic force is constant for a given density, so stable overlaps would form even at high turnovers. However, to form stable overlaps with strong motors, an increase of density is required, otherwise overlaps would slide apart

completely, as observed experimentally [180]. This might be the reason why cell cycle phosphatases target PRC1 and Ase1 specifically at anaphase onset, dephosphorylating them and dramatically decreasing their turnover [60, 10]. During anaphase, maintaining the overlap of microtubules is a key requirement to segregate chromosomes and keep spindle integrity [220, 120]. Interestingly, the properties of diffusible crosslinkers alone might have evolved to promote their retention in overlaps even in absence of regulation. *In vitro* experiments have shown that in compressed overlaps, the turnover of Ase1 is considerably slower than on microtubules that are not under force [114]. This is consistent with reports of Ase1 forming oligomers with low off-rates on microtubule overlaps [99]. Comparable observations have been made for PRC1, where compressed overlaps increased their resistance after sliding was stopped for 20 seconds, and then resumed, presumably because bound PRC1 oligomerised [67]. A similar situation might be ongoing in the *in vitro* experiments presented in this work. We observed no turnover of PRC1 by FRAP, and PRC1 intensity decreased in time during the experiments (Fig. 2.6C). This decrease in intensity was not due to bleaching (see [81]), and we interpreted it as a net unbinding of PRC1. However, at some point the PRC1 level stabilises and so does overlap length, which would mean that PRC1 no longer unbinds. This might be caused by oligomerisation of PRC1 molecules preventing their unbinding.

Diffusible crosslinkers can coordinate growth and sliding

Our theory predicts that motor sliding in the presence of diffusible crosslinkers stops at a given density of crosslinkers, determined either by total compaction or entropic force. Consequently, it follows that if microtubules grow, the density of crosslinkers decreases, allowing for sliding to resume until the critical density is reached again. If microtubules grow at a constant speed, sliding velocity will automatically match growth speed, as long as growth speed remains lower than the maximum sliding velocity (Fig. 2.5C). Coordination of growth and sliding is a landmark of the anaphase central spindle, which elongates while keeping an overlap length at the center. However, for this mechanism to operate, sliding speed at anaphase would have to be growth limited. Whether this is the case or not is unknown for most organisms, since microtubule dynamics in anaphase have not been measured. For fission yeast, it does not seem to be the case, as we observe that sliding speed is constant throughout anaphase regardless of microtubule growth speed (see discussion of chapter 3). This is not necessarily the situation in higher eukaryotes. One of the fundamental differences is that yeast does not have kinesin-4, which in higher eukaryotes suppresses microtubule growth at plus ends in the spindle [16, 224]. From our *in vitro* results, we predict that if kinesin-4 would not completely abolish growth, coordination between growth and sliding would occur. Experiments so far have used combinations of kinesin-4 and PRC1, which ultimately lead to the arrest of growth of microtubules (this work and [16]). However, recent studies have shown that tuning the concentrations of PRC1, kinesin-4 and CLASP can produce sustained growth [126]. In that study, microtubules were fixed at their minus ends, so sustained sliding could not happen. If technically possible, allowing microtubules to slide in such conditions may result in coordinated growth and sliding. Measuring microtubule dynamics during anaphase in higher eukaryotes would also be very informative, but right now it remains a technical challenge.

Future perspectives

Diffusible crosslinkers are required in living cells to form antiparallel overlaps, and for the specific targeting of their binding partners to these overlaps [21, 224]. As discussed above, they might be involved in coordination of growth and sliding in microtubule overlaps that are at total compaction. Nevertheless, it is not clear whether their role as brakes at lower densities is important for any biological function. Depletion of Ase1 in fission yeast does not affect spindle elongation speed [111]. On the other hand, in HeLa, depletion of PRC1 slightly increases elongation velocity and final length of the anaphase spindle. However, this might be an indirect effect due to PRC1 partners being depleted from the midzone [155]. In the future, it will be important to dissect the effects of PRC1. A bona fide example of crosslinker-mediated braking similar to the one observed *in vitro* comes from fission yeast. During interphase, short growing microtubules land on pre-existing long microtubules, are crosslinked antiparallelly by Ase1, and are slid by kinesin-14 Klp2 that localizes at microtubule plus ends. As microtubules grow longer, more Ase1 is recruited, which accumulates at the rear of the moving microtubule, and slows down sliding [22]. This behaviour is very similar to *in vitro* experiments with Ase1 acting like a brake. However, the braking seems to be a side effect of the function of Ase1 in these overlaps, which is promoting the antiparallel orientation of microtubules. In any case, most of the research on diffusible crosslinkers has focused on their roles in mitosis. Considering the interesting properties of these molecules, and the diversity of microtubule-based structures present in living organisms, diffusible crosslinkers most certainly have other functions yet to be discovered, and perhaps those involve their braking properties. It would be important in the future to identify biological models where these roles can be studied to broaden our understanding of this fascinating protein family.

Chapter 3

Microtubule dynamics in fission yeast Anaphase B

Notes about the text

In the text, measured quantities are written as the mean ± standard deviation. Yeast genes are written in lowercase, and protein products begin with an uppercase.

1 Introduction

Cell division requires the segregation of the duplicated genetic material into two daughter cells. This process is orchestrated by the mitotic spindle, a filamentous structure composed of microtubules, motors and MAPs. Defects in mitosis are deleterious and can lead to aneuploidy, developmental errors and are associated with cancer [187, 89]. The spindle plays distinct roles in the different mitotic phases: it is formed in prophase, aligns chromosomes at the cell equator in metaphase, pulls chromosomes to the poles in anaphase A, and pushes the poles apart during anaphase B. A landmark feature of anaphase B are antiparallel bundles of interpolar microtubules that maintain their overlap while being slid by motors. This sliding of interpolar microtubules is the main driver of chromosome segregation during anaphase B across species [220, 60, 202].

Fission yeast has been a popular model to study anaphase because of the available genetic tools. In addition to gene deletion and tagging, it is possible to change the expression levels of proteins by using P81nmt1, P41nmt1 and P1nmt1 promoters [12]. These promoters display increasing levels of transcription and each of them produces a lower expression in presence of thiamine. Another advantage of fission yeast is that the anaphase spindle is simpler than in other eukaryotes, since it lacks poleward flux and dynein pulling forces on astral microtubules [191, 103]. Furthermore, anaphase A and B occur sequentially, unlike in higher eukaryotes, and the start of anaphase B can be easily identified by a sharp increase in the elongation speed of the spindle [143]. Fission yeast spindles have approximately ten microtubules at anaphase onset, and the number of microtubules decreases to 4-5 by the end of anaphase [208]. Despite the number of microtubules being so low, wild type spindles never lose the overlap during anaphase, which suggests microtubule number is tightly regulated.

The main MAPs involved in anaphase B have been identified (Fig. 3.1), but how their activities are coordinated to ensure sustained sliding is not yet clear. The antiparallel specific crosslinker Ase1 (homologue of human PRC1) is required for midzone formation,

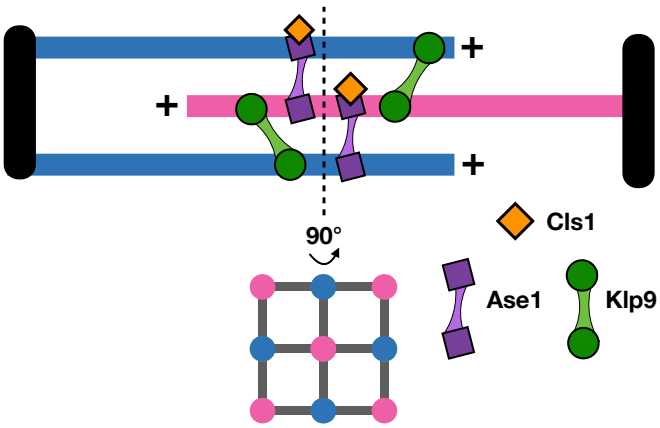

Figure 3.1: Anaphase B in fission yeast
Cartoon depicting the three main players involved in spindle elongation (Klp9, green), midzone organisation (Ase1, purple), and microtubule rescue (Cls1, orange) during anaphase B. Klp9 produces the relative sliding of antiparallel microtubules by walking to their plus ends. Ase1 ensures the formation of a midzone in which the microtubules are organised in an antiparallel square lattice. By allowing microtubules to only be crosslinked to antiparallel neighbours, a square lattice spontaneously forms (see rotated view). Cls1 is recruited to the midzone by Ase1, where it promotes rescues of shrinking microtubules. SPBs are shown as rounded rectangles at spindle poles.

and ase1 deletion results in aberrant spindle organisation and early disassembly [120, 216]. In addition to its structural role, Ase1 recruits its binding partners specifically to the midzone. One of them is the rescue promoter Cls1 (homologue of human CLASP). Cls1 promotes microtubule rescue, and its absence leads to the total depolymerisation of the anaphase spindle due to lack of rescues [21]. These roles of Ase1 and Cls1 are conserved in higher eukaryotes [198, 224, 82, 107, 156]. Finally, the tetrameric kinesin-6 Klp9 drives the sliding of interpolar microtubules to produce pole separation. Deletion of klp9 results in slower spindle elongation, and sliding is presumably taken over by kinesin-5 Cut7 [60].

A fundamental missing part of the picture is microtubule dynamics, which have not been directly measured during anaphase so far, due to technical limitations. Fluorescently labelled tubulin can be used to observe microtubule dynamics in fission yeast spindles, but only at very late anaphase, where the spindle is composed of approximately four microtubules [169]. Nevertheless, indirect methods have been used to infer certain aspects of microtubule dynamics. FRAP experiments showed that no nucleation of microtubules occurs at the SPBs during anaphase, and that microtubule overlaps are maintained through rescues [103]. Since not all microtubules that undergo catastrophe are rescued, the number of microtubules in the spindle decreases during anaphase [51, 208]. In human cells, it was shown recently that the turnover of EB1 decreases with anaphase progression [10]. EB1 is a protein that binds to growing plus ends of microtubules, so this decrease in turnover might reflect a change in microtubule dynamics with anaphase progression. However, direct measurements of microtubule dynamics during anaphase have not been performed yet. In addition, it is currently unknown how anaphase MAPs affect microtubule dynamics, and whether altering microtubule dynamics can in turn have an effect on sliding speed. Interplay between microtubule dynamics and sliding might be important to prevent midzone microtubules from completely sliding apart and causing spindle collapse.

In this work, we combined anaphase B measurements of microtubule number inferred from fluorescently labelled tubulin with microtubule dynamics measured from fluorescently labelled Mal3 (EB1 homologue). We confirmed the previous hypothesis that Ase1 dependent recruitment of Cls1 restricts microtubule rescues to the midzone [21]. Additionally, we showed that, as anaphase progresses, microtubule growth speed decreases, while the amount of Cls1 per microtubule and rescue rate increase. Conversely, increasing Cls1 expression levels decreased microtubule growth speed and promoted rescue, mimicking the effects of anaphase progression. We propose a model in which microtubule loss during anaphase increases Cls1 density on the spindle, which in turn slows down microtubule growth speed and increases rescue rate. We hypothesize that this mechanism is in play to prevent the collapse of late spindles, which have very few microtubules. Finally, we show that increasing cell size or deleting klp9 decrease the rate at which microtubules are lost.

2 Results

Simultaneous measurement of spindle and midzone length allows inference of microtubule number during anaphase B

In order to measure the number of microtubules during anaphase in fission yeast, we used strains tagged with mCherry and 3xGFP in the endogenous loci of atb2 (α-tubulin 2) and cls1 (fission yeast analogue of CLASP, also called peg1) (Fig. 3.2A). In live imaging movies, we could simultaneously measure the spindle length and midzone length from the mCherry-Atb2 and Cls1-3xGFP signals, respectively. As expected, the spindle elongation profile is very stereotypical, with little variance between cells, and allows for the identification of anaphase B onset as the transition from a moderate elongation speed in phase II, which consists of metaphase and anaphase A (0.11±0.03) to a higher speed in anaphase B (0.65±0.07 µm/min, Fig. 3.2B). We found that the midzone length increases from 2.0±0.3 µm at anaphase B onset until a maximum of 3.1±0.3 µm at mid anaphase, and then decreases, vanishing abruptly at spindle disassembly (Fig. 3.2A, C).

It has been shown before that total intensity of fluorescently labelled Atb2 is proportional to the total length of polymerised tubulin in the spindle [119, 208]. We took advantage of this, and used previously published electron microscopy data [208] to infer total polymerised tubulin in the spindle from total mCherry-Atb2 intensity (see Methods). We found good agreement between our calibrated intensity and the electron microscopy data (Fig. 3.2D). In addition, we used the simultaneous measurements of midzone and spindle length to convert total polymer length into number of microtubules. This is described in detail in the Methods section, but in essence we assumed that the midzone is composed only of microtubule overlap, while the rest of the spindle is composed of non-overlapping microtubules. This simplification allowed us to calculate the number of microtubules from total polymer length, midzone length and spindle length. The results are in good agreement with electron microscopy data during anaphase (Fig. 3.2E), but not in metaphase (data not shown in the graph, see Fig. S1). This is because, as seen in electron microscopy tomograms [208, 50], most microtubules do not form antiparallel overlaps in metaphase, while most of anaphase microtubules do. We therefore concluded that our method allows to infer microtubule number and total polymer length during anaphase B from live imaging data. As shown previously [208, 51], we observed that total polymer length reached a plateau during anaphase (Fig. 3.2D), while the number of microtubules continuously decreased (Fig. 3.2E).

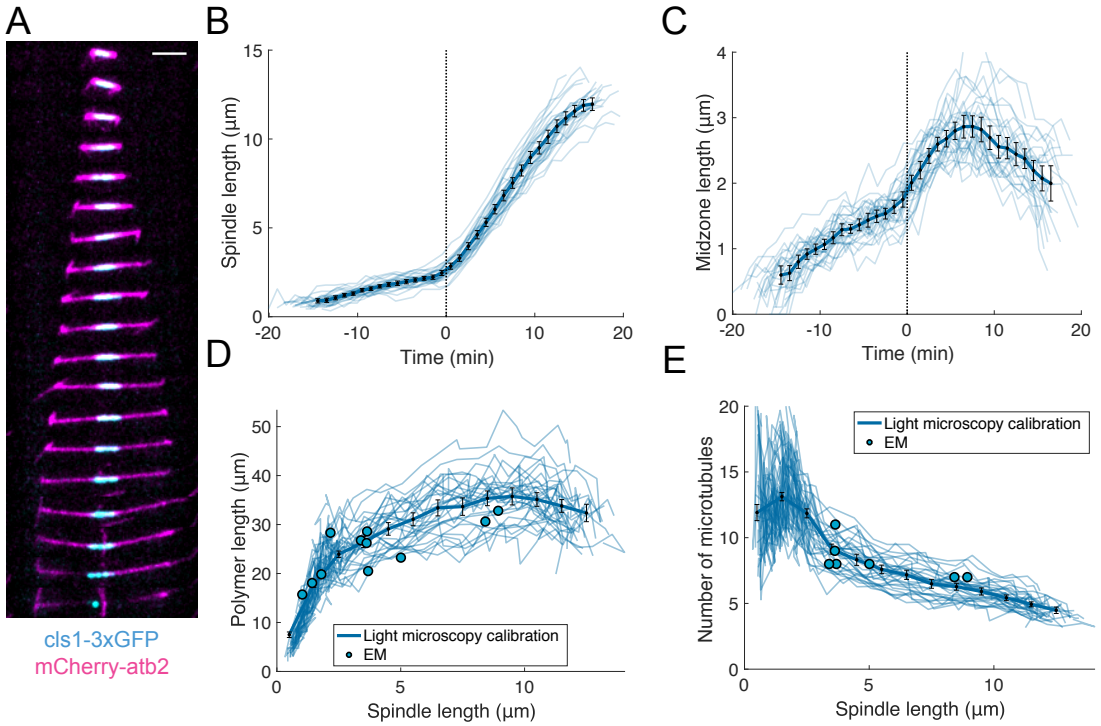

Figure 3.2: Simultaneous measurement of spindle and midzone length allows inference of microtubule number during anaphase B

A) Time-lapse images of the anaphase spindle of a wild type cell expressing mCherry-Atb2 and Cls1-3xGFP. Time between images is 1 minute, scale bar 3 µm. **B)** Spindle length measured from mCherry-Atb2 signal in time, from spindle formation to spindle disassembly. Time is zero at anaphase onset (dotted line) **C)** Overlap length measured from Cls1-3xGFP signal in time, from spindle formation to spindle disassembly. Time is zero at anaphase onset (dotted line). **D)** Calibrated total intensity of tubulin in the spindle as a function of spindle length. Intensity is scaled to fit the values measured by electron microscopy in [208] (dots). **E)** Inferred number of microtubules as a function of spindle length (see Methods). Values measured by electron microscopy in [208] are shown as dots.

Thin lines represent individual trajectories, thick lines represent average of binned data. Error bars represent 95% confidence interval of the mean. Data of 30 cells from 3 independent experiments. Same wild type data as in Fig. 3.8.

Microtubule dynamics change as anaphase progresses

We next used strains expressing GFP-Mal3 (EB1 analogue) under the control of the strong P1nmt1 promoter. This promoter is repressed in our experimental conditions (we use YE5S, which contains thiamine). In the repressed state, the promoter produces an overexpression of GFP-Mal3, but it was shown that this does not affect microtubule dynamics [32]. Mal3/EB1 proteins bind to the GTP-cap of microtubules and therefore track growing microtubule tips [167]. Using Super Resolution Structured Illumination Microscopy (SR-SIM), we produced kymographs in which we could identify spindle poles and resolve individual GFP-Mal3 comets, which correspond to growing plus ends of microtubules (Fig. 3.3A, B). In these kymographs, metaphase to anaphase transition is evidenced by an increase in the speed of separation of the spindle poles, by a change in the distribution of GFP-Mal3 comets, and by the presence of astral microtubules emanating from the poles. During metaphase, individual comets are rarely resolvable, but those we

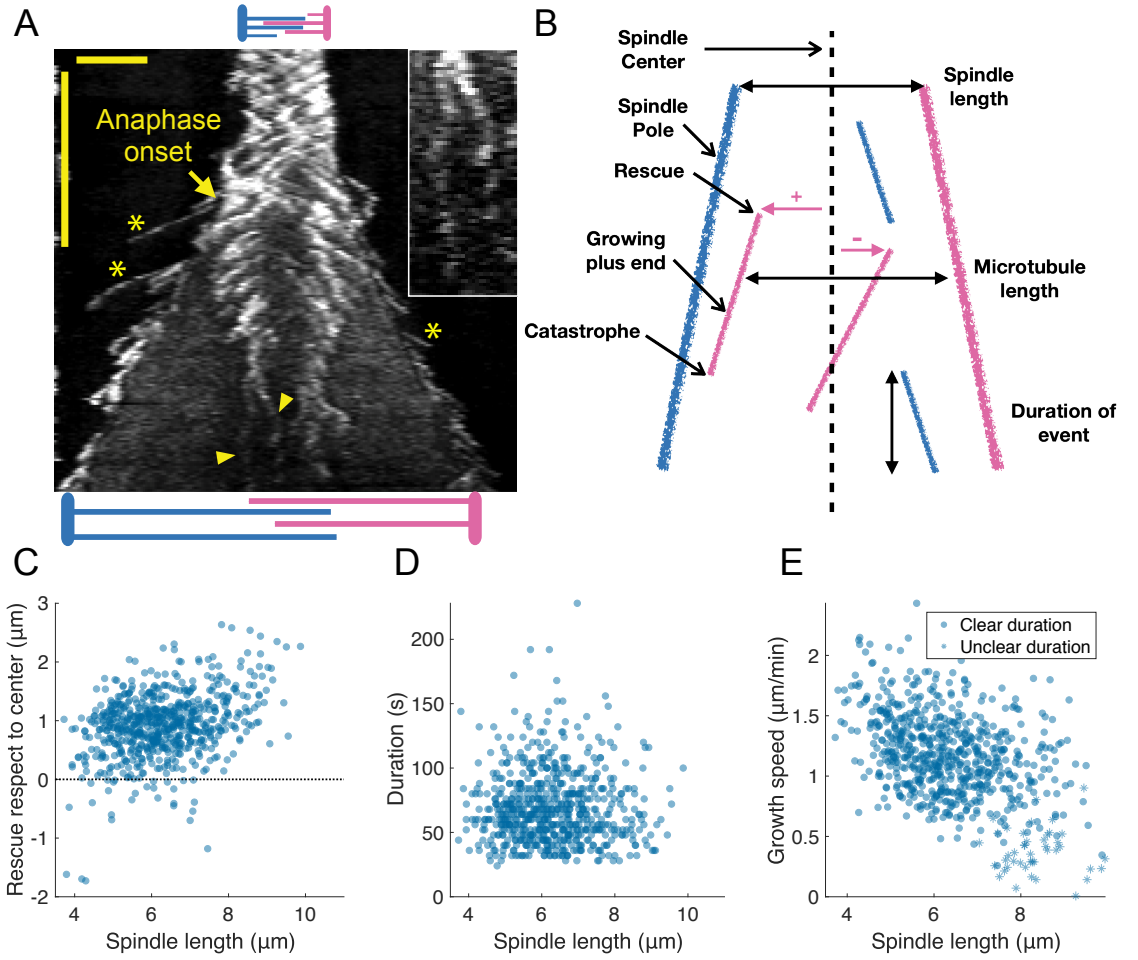

Figure 3.3: Microtubule dynamics change as anaphase progresses

A) Kymograph of the mitotic spindle of a cell expressing GFP-Mal3, in which time is in the vertical axis, and space is in the horizontal axis (see Methods). Arrow marks anaphase onset (note the change in the distribution of GFP-Mal3 comets, the increase in elongation speed of the spindle, and the appearance of astral microtubules, indicated by asterisks). Arrowheads at the bottom mark late anaphase growth events in which the microtubule growth speed is slow and the start and finish cannot be unambiguously determined. Inset at the top-right shows a magnification of those growth events with a higher contrast. Scalebars are 5 minutes (vertical) and 2 µm (horizontal). Schematics of the spindle structure at metaphase (top) and late anaphase (bottom) are provided to facilitate the interpretation of the kymograph. In the scheme, rounded rectangles at the poles represent SPBs and lines represent microtubules. Microtubules are linked to the SPBs at their minus end, and their plus ends interdigitate in the midzone, as in Fig. 3.1. **B)** Scheme depicting the elements that we can identify in a kymograph (left) and the measurements that can be made (right). We define spindle length as the distance between poles, and microtubule length as the distance from the growing plus end to its corresponding pole (pink plus ends have their minus end at the pink pole, and same for blue, see schemes in (A)). We define the duration of a growth event as the time between rescue and catastrophe. To measure the microtubule growth speed, we fit the length vs. time curve of each growth event to a first order polynomial. To measure the position of a rescue, we use the spindle center as a reference (dashed line). For a plus end, we consider positions that are between the spindle center and the minus end as negative, and those between the spindle center and the opposite pole as positive (see pink arrows with plus and minus sign). **C)** Positions of rescues with respect to center as a function of spindle length at rescue. Correlation coefficient 0.35. The fact that the value is almost always bigger than zero (dotted line), with an average of 0.9±0.5 µm, indicates that rescues happen mostly at the edge of the midzone, as seen in (A). **D)** Duration of growth events as a function of spindle length at rescue. Correlation coefficient -0.01. ... (continues next page)

(legend from Fig. 3.3) ... **E)** Microtubule growth speed as a function of spindle length at rescue (or first time point of ambiguous events). Growth events for which the start and finish could be unambiguously determined are shown as round dots, and are the same as in (C) and (D). Other events are shown as stars. Correlation coefficient -0.45. Each dot corresponds to a growth single event. Data from 707 growth events, of which 664 were unambiguous, from 75 cells, in 11 independent experiments. Same wild type data as in Fig. 3.4 and Fig. 3.8.

---

could identify appear at spindle poles, which suggests the start of these microtubule growth events corresponds to nucleation of microtubules at the SPB, as expected [173]. These microtubules grow and sometimes reach the opposite pole (Fig. S2). This is consistent with electron microscopy data, which shows interpolar microtubules spanning the whole spindle during metaphase [208, 51]. After transitioning to anaphase, fewer comets are present, which makes it possible to resolve individual events. During anaphase, comets appear most often at midzone edges (Fig. 3.3A, C), suggesting that the start of these microtubule growth events corresponds to a rescue, and not to nucleation, as expected for anaphase [103, 169]. As spindle elongates, the number of observable comets decreases, consistent with the reported loss of microtubules in time during anaphase [208, 51]. Therefore, our kymographs present multiple known features of metaphase and anaphase spindles.

This method has certain limitations. We cannot resolve all microtubule growth events in a kymograph, since sometimes they are superimposed. This means we cannot count the number of growing microtubules in the spindle. However, for the microtubule growth events we can resolve, we can measure the microtubule growth speed, duration and rescue position (Fig. 3.3B). In addition, for spindles longer than ~8 µm, the intensity of GFP-Mal3 comets decreases, and is no longer possible to unambiguously determine where events of microtubule growth start and finish (Fig. 3.3A, arrowheads and inset). However, the microtubule tip can be followed, and therefore we can measure the growth speed of these events. This lower intensity is not due to photobleaching, since we observe such dim events even when movies start at mid or late anaphase (data not shown). Since not all our kymographs include the metaphase to anaphase transition moment, to study the evolution of these parameters in time during anaphase, we plot them as a function of spindle length, which is a good proxy for anaphase progression (Fig. 3.2B).

We therefore measured growth speed, duration and position of rescues of microtubule growth events in which we could unambiguously determine start and finish of the event, and only microtubule growth speed in those that we could resolve but either start or finish were not clear. We found that most rescues occur at the edges of the midzone (Fig. 3.3C). At early anaphase, we could sometimes observe microtubule growth events starting close to the poles (dots in bottom left corner in Fig. 3.3C), which we interpreted as rare metaphase-like nucleation. Consistent with this interpretation, growth events starting close to spindle poles were not seen at later stages of anaphase. We observed a weak increase in the position of rescues with respect to the spindle center with anaphase progression (correlation coefficient 0.35). This is consistent with our previous measurements, which showed that midzone length increased during anaphase (Fig. 3.2B). Duration of microtubule growth events did not change over time (correlation coefficient -0.01), and events lasted 72±32 seconds (Fig. 3.2D). The distribution of catastrophe times was well described by the gamma function, similarly to *in vitro* data [66], consistent with microtubule catastrophe being a multi-step process (Fig. S3). Surprisingly, we observed a strong decrease in microtubule growth speed with anaphase progression (Fig. 3.3E, correlation coefficient -0.45). This

decrease in microtubule growth speed can be seen within a single kymograph (Fig. 3.3A). Late microtubule growth events with slow growth speeds are longer than early events, but since we could not unambiguously determine their start and finish, we did not include them in Fig. 3.3D. Interestingly, the duration and growth speed of microtubule growth events in anaphase are significantly lower than those observed in interphase microtubules, which grow faster (~2.3 μm/min) for longer times (~3 minutes) [172]. This change in microtubule dynamics had been inferred with indirect techniques before [125, 103], and observed at late anaphase stages [169] but never at early anaphase. We therefore conclude that rescues during anaphase occur mostly at midzone edges, and that microtubule growth speed decreases with anaphase progression.

Ase1 organises spindle rescues and affects microtubule dynamics

Having established methods to measure microtubule number and dynamics during anaphase, we next tested how these were affected by known anaphase MAPs. We started with Ase1, an antiparallel specific crosslinker required for midzone formation [120, 216]. Ase1 not only crosslinks microtubules but also recruits other proteins to the midzone, like Cls1, which is necessary for microtubule rescue. It had been previously hypothesized that since Ase1 recruits Cls1, it would induce rescues specifically at the midzone [21]. Indeed, we observed that cells in which ase1 was deleted, lost the characteristic rescue distribution, and rescues occurred all across the spindle (Fig. 3.4A, B). We unexpectedly found that ase1 deletion also affected microtubule dynamics: growth events were on average ~40% longer (Fig. 3.4C) and microtubule growth speed did not decrease with anaphase progression (Fig. 3.4D, correlation coefficient of -0.45 in wild type vs. 0.14 in ase1Δ).

Since ase1 deletion prevents midzone formation, these changes in microtubule dynamics may result from the loss of spindle structure, and not be direct effects of Ase1. To address this, we imaged cells expressing Ase1 from a weak P81nmt1 promoter (ase1^{off}). Expression of GFP-Ase1 from this promoter results in ~3-4 times lower intensity on the spindle when compared to GFP-Ase1 expressed from the native promoter (Fig. S4D). We found that ~30% (11 out of 35) of ase1^{off} cells presented a disorganised spindle like ase1Δ cells, but the rest showed the characteristic organisation of wild type spindles (Fig. 3.4A, E, Fig. S4A). We analysed only organised spindles, and found that the microtubule growth speed was higher than in wild type (Fig. 3.4G), while the duration of microtubule growth events was not significantly changed (Fig. 3.4F). Interestingly, ase1^{off} spindles which were disorganised showed an increase in the duration of microtubule growth events, similarly to ase1Δ (Fig. S4B). We concluded therefore that Ase1 levels affect microtubule growth speed, and that disruption of the midzone further perturbs microtubule dynamics, increasing duration of growth events significantly.

Cls1 modifies microtubule dynamics in a dose dependent manner

We reasoned that the effects on microtubule growth speed resulting from reducing Ase1 levels could be due to a decreased recruitment of an Ase1 binding partner. Cls1 was a good candidate, since it binds to Ase1 [21], and its homologues have been shown to decrease microtubule growth speed *in vitro* [1, 141] and *in vivo* [136]. Supporting the possible involvement of Cls1, levels of Cls1-3xGFP on the spindle were decreased by approximately half compared to the wild type levels in ase1^{off} cells (Fig. 3.6B).

Cls1 is an essential gene, and cls1 thermosensitive alleles cause complete depolymerisation of the spindles in anaphase due to lack of rescue [21]. We therefore decided to

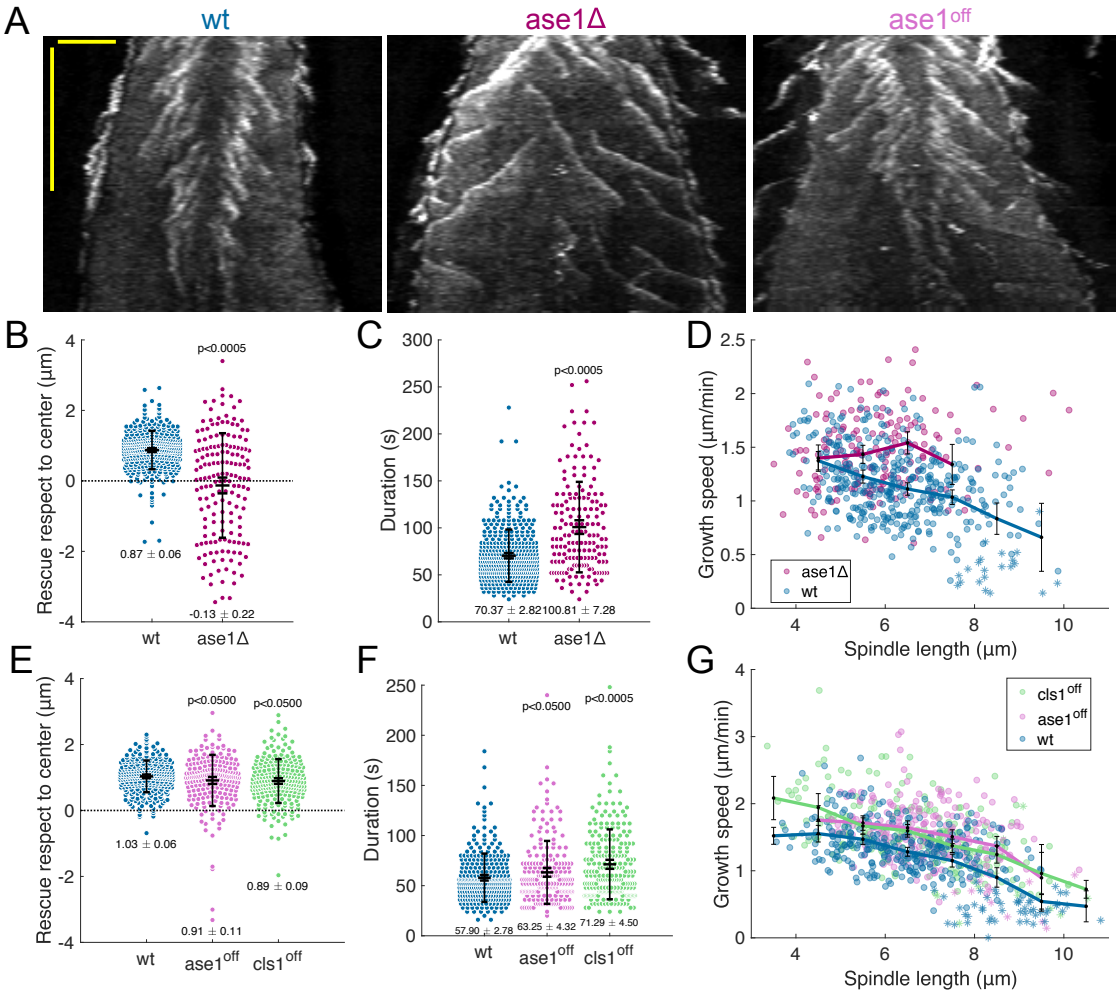

Figure 3.4: Ase1 organises spindle rescues and affects microtubule dynamics

Color code: wild type (blue), ase1Δ (wine), ase1^{off} (pink), cls1^{off}(green) **A)** Kymograph of the mitotic spindle of wild type (wt), ase1Δ and ase1^{off} cells expressing GFP-Mal3. Note that ase1Δ does not show the typical distribution of comets, and growth events are longer. For a kymograph of cls1^{off}, see Fig. 3.5A. Scalebars are 5 minutes (vertical) and 2 µm (horizontal). **B)** Positions of rescues with respect to center in wt and ase1Δ. Note that ase1Δ average rescue position is not significantly different from zero. **C)** Duration of growth events in wt and ase1Δ. **D)** Microtubule growth speed of events as a function of spindle length at rescue (or first time point of ambiguous events) in wt and ase1Δ. Growth events for which the start and finish could be unambiguously determined are shown as round dots, and are the same as in (B) and (C). Other events are shown as stars. Correlation coefficient -0.45 in wt and 0.14 in ase1Δ. **E)** Positions of rescues with respect to center in wt, ase1^{off}, and cls1^{off}. **F)** Duration of growth events in wt, ase1^{off}, and cls1^{off}. **G)** Microtubule growth speed of events as a function of spindle length at rescue (or first time point of ambiguous events) in wt, ase1^{off}, and cls1^{off}. Events for which the start and finish could be unambiguously determined are shown as round dots, and are the same as in (E) and (F). Other events are shown as stars. Correlation coefficient -0.61 in wt, -0.37 in ase1^{off}, and -0.55 in cls1^{off}. Thick lines represent average of binned data, error bars of average lines represent 95% confidence interval of the mean. Error bars in univariate scatter plots represent 95% confidence interval of the mean and standard deviation, text is mean ± 95% confidence interval. ... (continues next page)

(legend from Fig. 3.4) ... Each dot represents a single growth event. Data in C-D comes from 6 independent experiments (396 growth events, of which 375 were unambiguous, from 43 cells in wt; 168 growth events, of which 168 were unambiguous, from 27 cells in ase1Δ). Data in E-G comes from 5 independent experiments (336 growth events, of which 288 were unambiguous, from 43 cells in wt; 214 growth events, of which 203 were unambiguous, from 24 cells in ase1^{off}; 242 growth events, of which 231 were unambiguous, from 27 cells in cls1^{off}).

study the effect of decreasing the levels of Cls1, by expressing it from a weak P81nmt1 promoter (cls1^{off}). Expression of Cls1-3xGFP from this promoter results in ~3 times lower intensity on the spindle when compared to Cls1-3xGFP expressed from the native promoter (Fig. 3.6B). In cls1^{off} cells, microtubule growth speed was faster than in wild type, similarly to ase1^{off} cells with organised spindles (Fig. 3.4G). In addition, we also observed a moderate increase in duration of microtubule growth events, similar to the one in ase1^{off} cells with disorganised spindles (Fig. 3.4F, Fig. S4B). These results suggest that the changes in microtubule dynamics in ase1^{off} might be due to a reduction in Cls1 recruitment to the midzone.

To further confirm that Cls1 levels on the spindle affect microtubule dynamics, we expressed Cls1 from a P1nmt1 promoter in the presence of thiamine, which presumably[1] produces a mild overexpression (cls1^{OE}, see footnote). We also expressed Cls1 from a P41nmt1 promoter in the absence of thiamine (cls1^{OE+}). This produced a stronger overexpression, and cells presented interphase-like stable microtubule bundles that remained in mitosis (Fig. S5). Since these experiments were performed in the absence of thiamine, GFP-Mal3 was expressed from a P41nmt1 promoter in cls1^{OE+} and control strains. Under these conditions, microtubule dynamics in the wild type strain were different than in previous experiments (faster growth speed and shorter duration, Fig. S6A, B), most likely due to the difference in the medium (YE5S in previous experiments, EMM for thiamine depletion), but remained qualitatively similar: we could observe a decrease in microtubule growth speed with anaphase progression (Fig. 3.5C), and rescue distribution was similar (wt in Fig. 3.5A and Fig. S6C). We observed that increasing levels of Cls1 progressively reduced microtubule growth velocity (Fig. 3.5B, C), and increased the duration of microtubule growth events (Fig. 3.5D). In cls1^{OE+} spindles, growth events lasted very long (Fig. 3.5A), but just like in wild type late anaphase microtubule growth events, it was not possible to unambiguously determine their start and finish.

We conclude that Cls1 affects microtubule dynamics during anaphase in a dose dependent manner. Decreasing Cls1 levels at the spindle, either by perturbing its Ase1-mediated recruitment to the midzone or by reducing Cls1 expression, results in a higher microtubule growth speed and a mild increase in event duration. Conversely, increasing Cls1 expression results in lower microtubule growth speed and longer events.

Cls1 density and rescue rate increase with anaphase progression

Given that increasing the Cls1 levels on the spindle has a similar effect on microtubule dynamics as anaphase progression, we next asked whether progressive change in anaphase microtubule dynamics could be caused by a gradual increase of Cls1 levels on the

[1]We still have to confirm that expression of Cls1 is higher from the uninduced P1nmt1 promoter, by expressing a GFP tagged version of Cls1 from this promoter. So far we did not manage to obtain transformants after two tries. However, the tendency of the phenotypes is consistent with P1nmt1 producing higher protein levels than the native promoter.

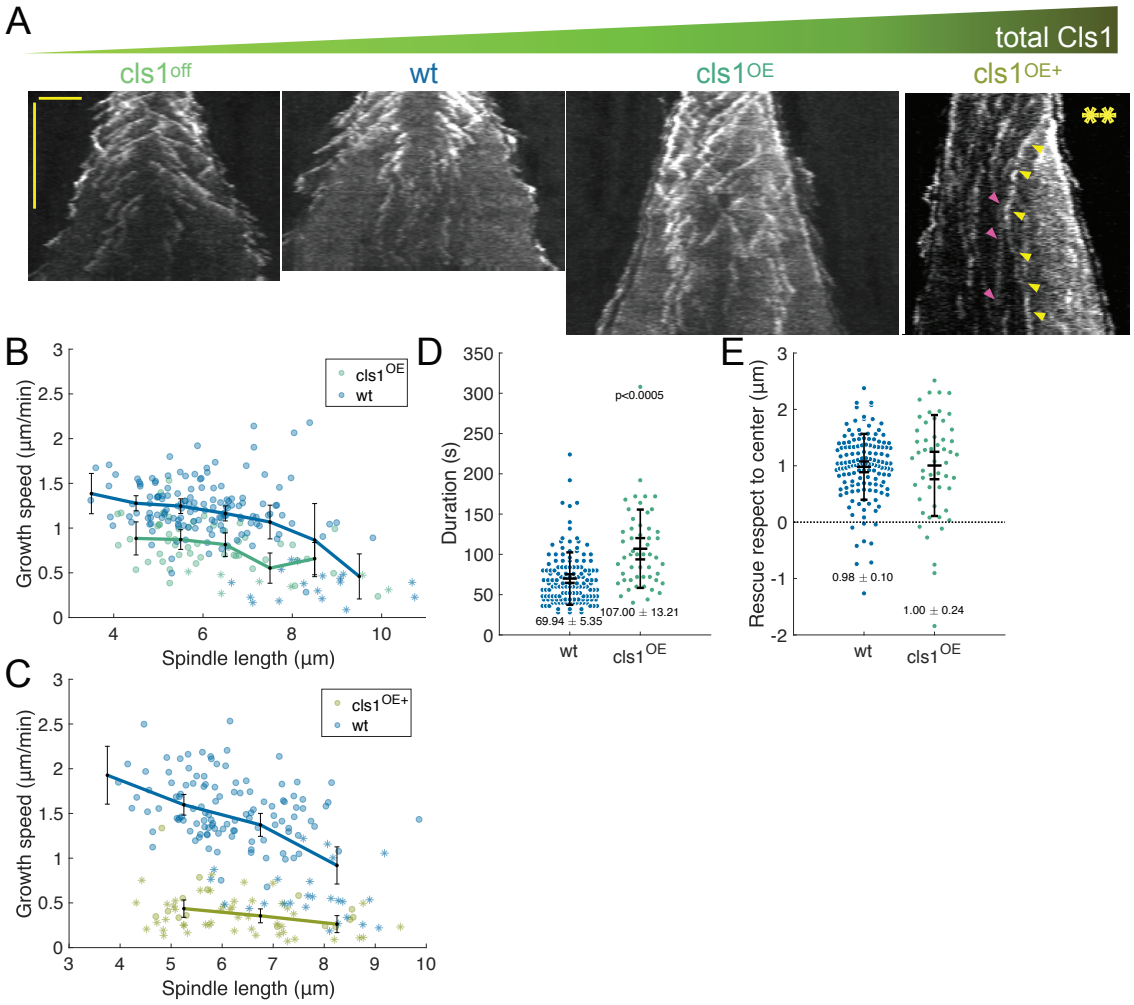

Figure 3.5: Cls1 modifies microtubule dynamics in a dose dependent manner

Color code: cls1^{off} (light green), wild type (blue), cls1^{OE} (teal), cls1^{OE+} (olive) **A)** Kymograph of the mitotic spindle of strains expressing GFP-Mal3 and increasing levels of Cls1: cls1^{off}, wild type, cls1^{OE}, cls1^{OE+}. Scalebars are 5 minutes (vertical) and 2 µm (horizontal). Wild type and cls1^{OE+} kymographs are from experiments in the absence of thiamine, where GFP-Mal3 was expressed from a P41nmt1 promoter. Asterisks on the right indicate that the contrast of the kymograph is different from the others, because intensity of GFP-Mal3 was low in cls1^{OE+}. Arrowheads mark the positions of two long and slow growth events. **B)** Microtubule growth speed of events as a function of spindle length at rescue (or first time point of ambiguous events) in wt and cls1^{OE}. Events for which the start and finish could be unambiguously determined are shown as round dots, and are the same as in (D) and (E). Other events are shown as stars. Correlation coefficient -0.45 in wt and -0.49 in cls1^{OE}. **C)** Same as (B), for wt and cls1^{OE+}. Correlation coefficient -0.52 in wt and -0.41 in cls1^{OE+}. **D)** Duration of growth events in wt and cls1^{OE}. **E)** Positions of rescues with respect to center in wt and cls1^{OE}.

Thick lines represent average of binned data, error bars of average lines represent 95% confidence interval of the mean. Error bars in univariate scatter plots represent 95% confidence interval of the mean and standard deviation, text is mean ± 95% confidence interval. Each dot represents a single growth event. Data in C comes from 4 independent experiments (141 growth events, of which 115 were unambiguous, from 24 cells in wt; 65 growth events, of which 16 were unambiguous, from 7 cells in cls1^{OE+}). Data in B, D, E comes from 3 independent experiments (159 growth events, of which 142 were unambiguous, from 23 cells in wt; 59 growth events, of which 52 were unambiguous, from 11 cells in cls1^{OE}).

spindle. Consistent with this hypothesis, total Cls1 intensity remains roughly constant during anaphase (Fig. 3.6A, B), while the number of microtubules decreases (Fig. 3.6D). Consequently, the density of Cls1 at the midzone increases in time (Fig. 3.6C). This increase in the density of Cls1 could drive the observed gradual change in microtubule dynamics.

So far, we have focused on the effects of Cls1 on microtubule dynamics that could be measured from GFP-Mal3 kymographs (growth speed and duration). However, Cls1 main function during anaphase is to promote microtubule rescue [21]. Consistent with this known role, ase1^{off} and cls1-3xGFP^{off} cells, which recruit less Cls1 to the spindle (Fig. 3.6B), have lower total polymer length for the same spindle length (Fig. 3.6E), and ase1^{off} strains lose microtubules at a higher rate than wild type cells (Fig. 3.6D, we cannot infer the number of microtubules in cls1-3xGFP^{off}, because Cls1-3xGFP levels are too low to determine midzone length). It is therefore possible that the gradual decrease in microtubule growth speed during anaphase, presumably caused by Cls1 accumulation, might be accompanied by an increase in the rescue rate. Since the duration of microtubule growth events does not change in time (Fig. 3.3D), for a given average duration of a growth event τ_d and a probability of being rescued at the midzone P_r, the change in number of microtubules N in time is given by:

$$\frac{dN}{dt} = N\frac{(1-P_r)}{\tau_d} \tag{3.1}$$

If the rescue rate is constant, we can define a characteristic time scale at which microtubules are lost, $\tau = \tau_d/(1-P_r)$, and the number of microtubules in time starting from N_0 microtubules is given by:

$$N(t) = N_0 e^{-t/\tau} \tag{3.2}$$

To test whether rescue rate is constant, we fitted each of our wild type anaphase curves of number of microtubules in time to exponential decays (Equation 3.2), where N_0 and τ were two fit parameters. We found that the best fit curve is systematically above the experimental curve at early anaphase, and below the same curve at later times (Fig. 3.6F, which shows the average fit error as a function of anaphase time). This shows that the data is not well described by a model in which microtubules are lost at a constant rate. Instead, microtubules are lost at a higher rate at early anaphase. Given that the duration of microtubule growth events is constant (Fig. 3.3D), this means that rescue rate is higher at early anaphase.

We conclude that, as anaphase progresses, Cls1 density increases in the midzone, concomitantly with an increase in rescue rate and a decrease in microtubule growth speed of microtubules.

Klp9 deletion increases rescue rate

We next decided to test the effects of kinesin-6 Klp9 on microtubule dynamics. Klp9 is a tetrameric motor involved in microtubule sliding during anaphase. It is dephosphorylated at anaphase onset, which is necessary for its recruitment to the midzone [60]. Deletion of Klp9 reduces sliding speed and significantly increases the duration of anaphase [60]. In this scenario, kinesin-5 Cut7 presumably takes over the role of Klp9 and slides microtubules, since fission yeast has no other tetrameric kinesin.

Previously, we have used spindle length as a proxy for anaphase progression, because not all of our kymographs include the metaphase to anaphase transition. However, since

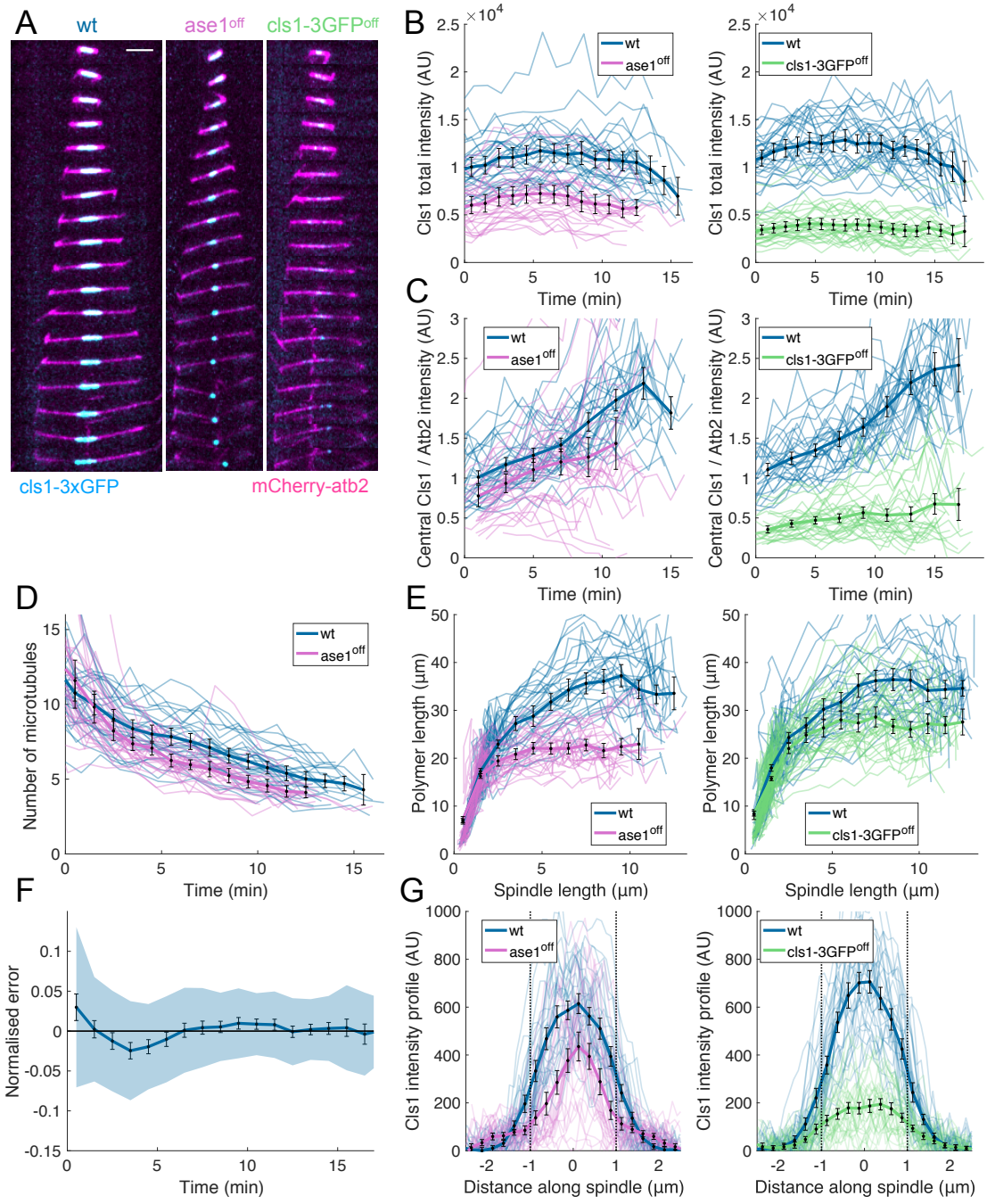

Figure 3.6: Cls1 density and rescue rate increase with anaphase progression

Color code: wild type (blue), ase1^{off} (pink), cls1^{off} (green) **A)** Time-lapse images of anaphase in wt, ase1^{off} and cls1^{off} in cells expressing mCherry-Atb2 and Cls1-3xGFP. Time between images is 1 minute, scale bar 3 µm. **B)** Cls1-3xGFP total intensity on the spindle in wt, ase1^{off} and cls1-3xGFP^{off} cells. **C)** Total intensity of Cls1-3xGFP divided by total intensity of mCherry-Atb2 in a window of 2 µm at the spindle center, see (G). **D)** Inferred number of microtubules (see Methods) as a function of anaphase time for wt and ase1^{off}. This could not be measured for cls1^{off}, since the Cls1-3xGFP signal at the midzone is too dim. **E)** Inferred microtubule polymer length (see methods) in the spindle as a function of spindle length in wt, ase1^{off} and cls1-3xGFP^{off} cells. ... (continues next page)

(legend from Fig. 3.6) ... **F)** For each cell, the curve of inferred number of microtubules in time during anaphase was fitted to an exponential decay (Equation 3.2, $N = N_0 e^{-t/\tau}$, where N is predicted number of microtubules, t is the anaphase time, and N_0, τ are fitting parameters). The difference between each experimental curve and the corresponding fit, divided by the fit's N_0 was calculated, and the average of this value is plotted as a function of anaphase time. Note that the average error is positive at the beginning and then becomes negative, indicating that the rate of microtubule loss decreases in time. **G)** Profile of summed Cls1-3xGFP intensity as a function of the position along the spindle, where zero denotes spindle center, for the time point for which the spindle length was closest to 5 µm. Dotted lines mark the window of 2 µm used for measuring density at the center of the spindle in (C). We used a fixed length because we could not measure the midzone length in cls1-3xGFP^{off}.
Thin lines represent individual trajectories, thick lines represent average of binned data, error bars of average lines represent 95% confidence interval of the mean. Blue patch in (F) represents the standard deviation. Data comparing wt and ase1^{off} comes from 3 independent experiments (30 cells in wt; 29 cells in ase1^{off}). Data comparing wt and cls1-3xGFP^{off} comes from 3 independent experiments (30 cells in wt; 30 cells in cls1-3xGFP^{off}).

klp9 deletion reduces sliding speed, to compare the changes of microtubule dynamics in wt and klp9Δ, we mapped the length of the spindle to anaphase progression. For this, we used a linear fit to the spindle length vs. time data from time lapse movies in which the acquisition rate was slower than those used to make kymographs (Fig. 3.7C). From microtubule growth events in GFP-Mal3 kymographs (Fig. 3.7B), we found that duration of growth events was not different in wild type and klp9Δ (Fig. 3.7D). However, the decrease of microtubule growth speed in time was lower in klp9Δ than in wt (Fig. 3.7E, correlation coefficient of -0.27 vs. -0.41). Interestingly, our tubulin intensity data (Fig. 3.7A) showed that klp9Δ cells lost microtubules at a lower rate than wild type cells (Fig. 3.7F).

Our interpretation of these results is that, in the absence of Klp9, rescue rate is increased by a different mechanism than Cls1 accumulation. This would explain why microtubules are lost at a lower rate in klp9Δ (Fig. 3.7F), while Cls1 levels per microtubule do not increase as much as in wild type (Fig. 3.7G). Conversely, since Cls1 does not accumulate so much, correlation of microtubule growth speed with anaphase progression is weaker (Fig. 3.7E). This phenotype might not be a direct effect of Klp9. It is known that Klp9 function is required for Aurora B and other Chromosome Passenger Complex proteins to transition from the kinetochore to the midzone [133]. It is possible therefore that some downstream effectors involved in microtubule rescue are affected in klp9Δ.

Bigger cells recruit more Cls1 and have higher rescue rates

Motivated by previous work showing that in *C. elegans* and zebrafish microtubule growth speed in metaphase scales with cell size [113, 163], we decided to analyse the effects of cell size on microtubule dynamics in anaphase. In fission yeast, cell size can be increased by a mutation in the cell cycle gene cdc25. Using this mutation (cdc25-22), cell length increases from 14.9±0.8 µm in wild type to 21.5±2.3 µm in cdc25-22, and it has been shown that this increase in cell size results in higher anaphase spindle elongation speed [111]. As previously done with klp9Δ, since anaphase onset length and spindle elongation speed are higher in cdc25-22 than in wild type, we mapped spindle length to anaphase time by using a linear fit (Fig. 3.7C). From microtubule growth events in GFP-Mal3 kymographs (Fig. 3.8A), we measured microtubule growth speed and event duration. We found that

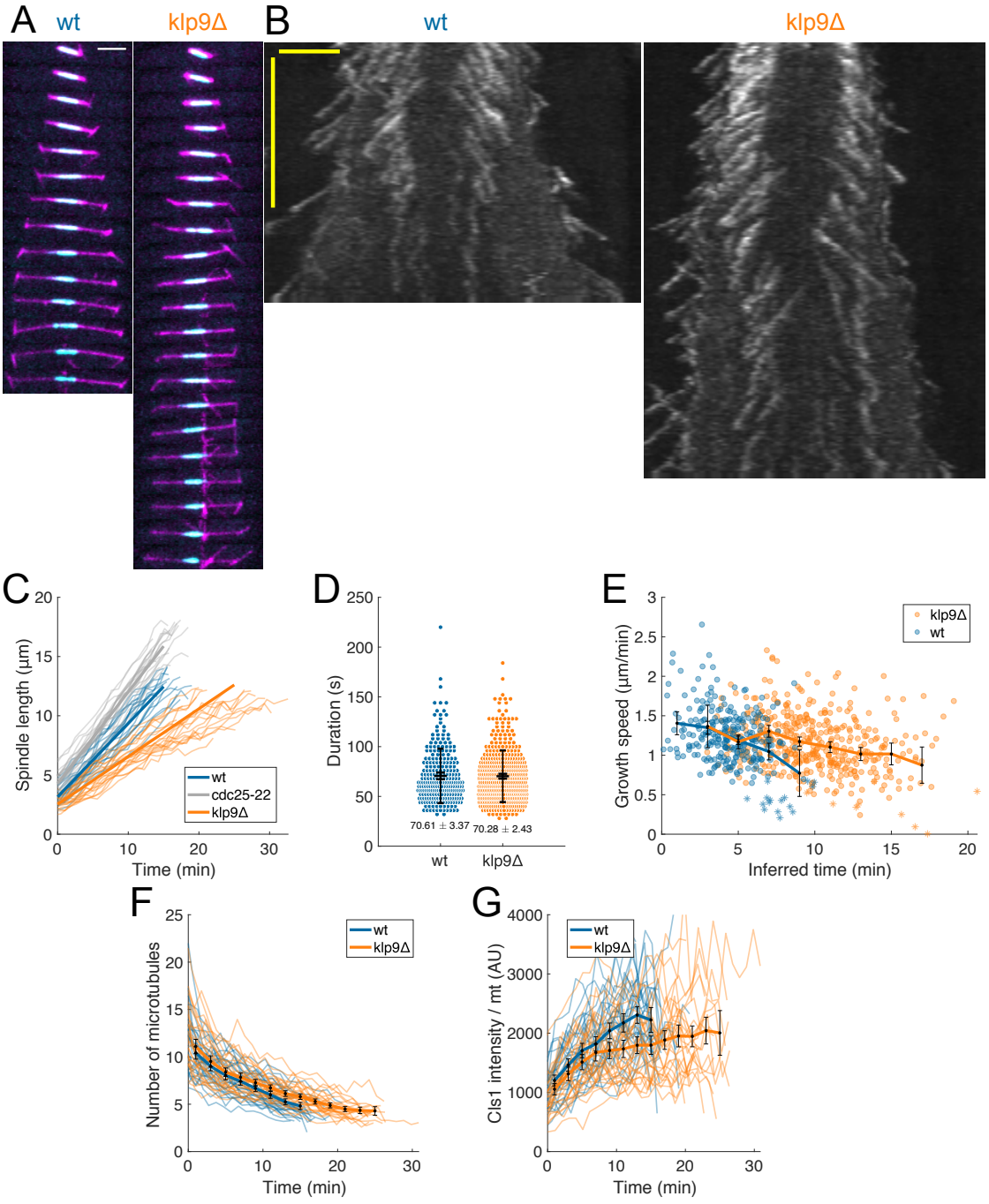

Figure 3.7: Klp9 deletion increases rescue rate

Color code: wild type (blue), klp9Δ (orange), cdc25-22 (grey) **A)** Time-lapse images of anaphase spindles in wt and klp9Δ cells expressing mCherry-Atb2 and Cls1-3xGFP. Time between images is 1 minute, scale bar 3 µm. **B)** Kymograph of the mitotic spindle of wild type (wt) and klp9Δ cells expressing GFP-Mal3. Anaphase in klp9Δ is longer and growth events remain resolvable longer as shown in (E). Scalebars are 5 minutes (vertical) and 2 µm (horizontal). **C)** Spindle length in time during anaphase for wt, klp9Δ and cdc25-22 in GFP-Mal3 movies where the frame rate was lower than in those used for kymographs. Thick lines represent fits to first degree polynomials of all the points in each condition. These fits are used to map spindle length to anaphase progression in (E) and Fig. 3.8C. **D)** Duration of growth events in wt and klp9Δ. **E)** Microtubule growth speed of events as a function of anaphase time at rescue inferred from the linear fits in (C) (or first time point of ambiguous events) in wt and klp9Δ. Events for which the start and finish could be unambiguously determined are shown as round dots, and are the same as in (D). Other events are shown as stars. Correlation coefficient -0.41 in wt and -0.27 in klp9Δ. ... (continues next page)

(legend from Fig. 3.7) ... **F)** Inferred number of microtubules (see Methods) as a function of anaphase time for wt and klp9Δ. **G)** Total intensity of Cls1-3xGFP divided by inferred number of microtubules in wt and klp9Δ. Note that this quantity increases more slowly in klp9Δ.
Thin lines represent individual trajectories, thick lines represent average of binned data, error bars of average lines represent 95% confidence interval of the mean. Error bars in univariate scatter plots represent 95% confidence interval of the mean and standard deviation, text is mean ± 95% confidence interval. Each dot represents a single growth event. Data in C comes from 20 cells for each condition in 2 independent experiments. Data in D-E comes from 6 independent experiments (269 growth events, of which 253 were unambiguous, from 28 cells in wt; 449 growth events, of which 439 were unambiguous, from 35 cells in klp9Δ). Data in F-G comes from from 30 cells for each condition in 3 independent experiments .

---

growth speed decreases with anaphase progression in cdc25-22, similarly to wild type (Fig. 3.8C), but that duration of the events was increased by ~25% (Fig. 3.8D). Our tubulin intensity measurements (Fig. 3.8B) showed that the rate at which microtubules are lost in cdc25-22 cells is slower than in wild type cells (see evolution of normalised number of microtubules in Fig. 3.8F, and Methods). This is consistent with our hypothesis that Cls1 levels on the spindle increase rescue frequency, since the amount of Cls1 per microtubule was higher on cdc25-22 than in wild type across anaphase (Fig. 3.8G). In addition, since microtubule growth events are longer, rescues at the midzone will be tested less often (Equation 3.1), and this will also reduce the rate of microtubule loss.

Therefore, we conclude that cell size does not affect microtubule growth speed in anaphase, but it increases duration of microtubule growth events. Microtubule loss rate is higher in bigger cells, presumably due to a combination of higher rescue by increased levels of Cls1 on the spindle, and longer duration of microtubule growth events.

Progressive increase in microtubule stability prevents spindle collapse

The data we have presented so far is consistent with a model in which progressive accumulation of Cls1 results in a decrease in microtubule growth speed and an increase in rescue rate. In such a model, for a fixed amount of Cls1 on the spindle, microtubules are more stable in spindles that have fewer microtubules. This would not only increase microtubule stability in time with anaphase progression, but would also make spindles that stochastically start anaphase with fewer microtubules more stable. Indeed, we observed that spindles starting anaphase with fewer microtubules, had higher Cls1 levels per microtubule (Fig. 3.9A). From our model, we would expect spindles starting with fewer microtubules and higher Cls1 density to lose microtubules at a lower rate. To test this hypothesis, for each spindle, we fitted the data of number of microtubules in time in the initial 10 minutes of anaphase to an exponential decay (Equation 3.2). We then plotted the deducted initial decay rate as a function of microtubule number at anaphase onset. We observed a positive correlation, indicating that spindles starting with fewer microtubules indeed have higher microtubule stability. Interestingly, we observed these correlations in all conditions tested in this work (Fig. 3.9B). We chose a window of 10 minutes to calculate the initial decay, but the same positive correlation between number of microtubules and decay rate persisted regardless of the time window of the fit (data not shown).

We reasoned that such a mechanism would prevent spindle collapse, since spindles with fewer microtubules would have more rescues. This is particularly important in the fission yeast spindle, where the final number of microtubules is around 4. To test the hypothesis

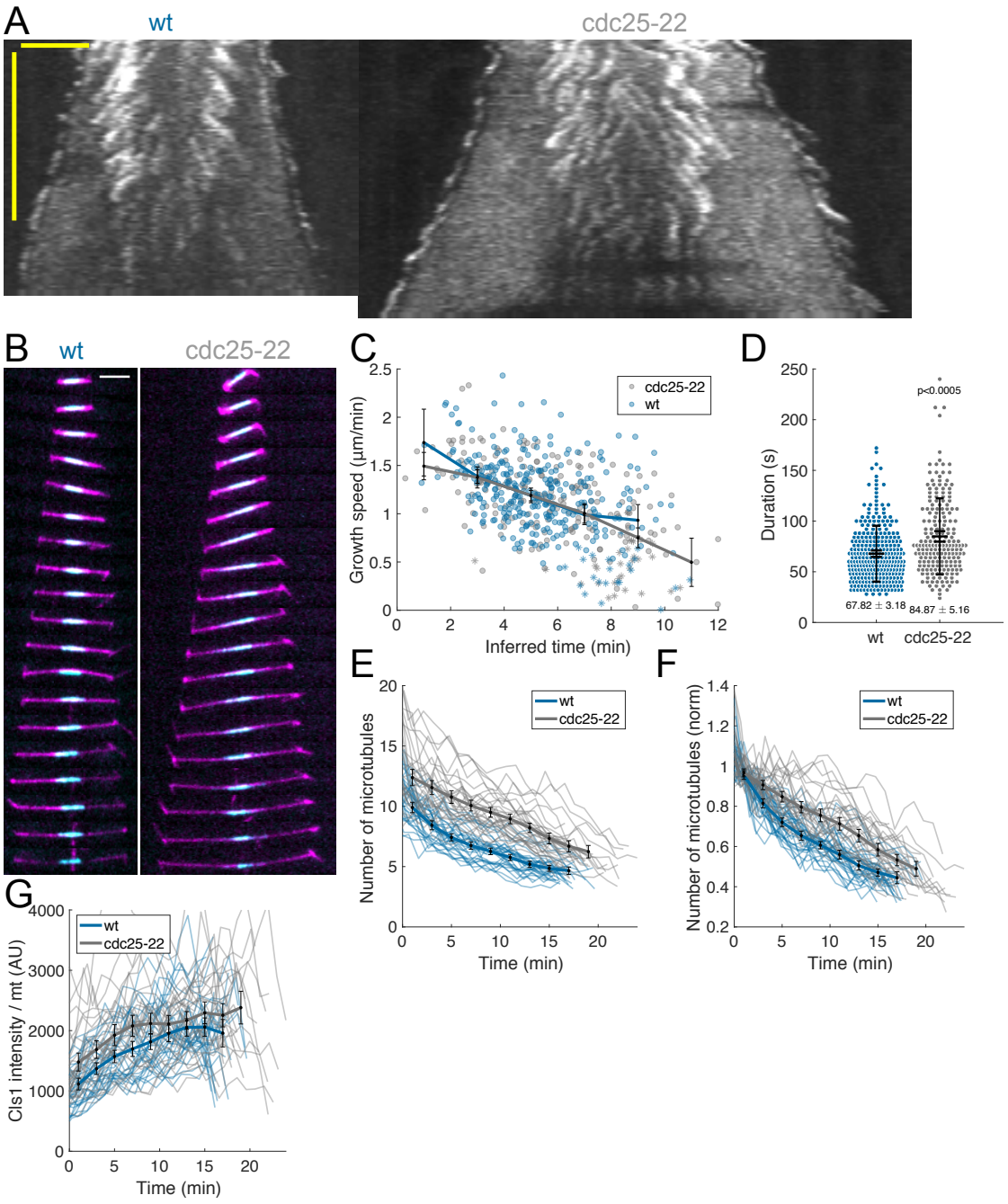

Figure 3.8: Bigger cells recruit more Cls1 and have higher rescue rates

Color code: wild type (blue), cdc25-22 (grey) **A)** Kymograph of the mitotic spindle of wild type (wt) and cdc25-22 cells expressing GFP-Mal3. Scalebars are 5 minutes (vertical) and 2 µm (horizontal). **B)** Time-lapse images of anaphase spindles in wt and cdc25-22 cells expressing mCherry-Atb2 and Cls1-3xGFP. Time between images is 1 minute, scale bar 3 µm. **C)** Microtubule growth speed of events as a function anaphase time at rescue inferred from the linear fits in Fig. 3.7C (or first time point of ambiguous events) in wt and cdc25-22. Events for which the start and finish could be unambiguously determined are shown as round dots, and are the same as in (D). Other events are shown as stars. Correlation coefficient -0.46 in wt and -0.60 in cdc25-22. **D)** Duration of growth events in wt and cdc25-22. **E)** Inferred number of microtubules (see Methods) as a function of anaphase time for wt and cdc25-22. **F)** Same as (E) but inferred microtubules normalised by N_0 from exponential fits as in Fig. 3.6F. This is to show that cdc25-22 spindles lose microtubules at a slower rate than wt. **G)** Total intensity of Cls1-3xGFP divided by inferred number of microtubules in wt and cdc25-22. Note that this quantity increases similarly in both conditions, but is higher in cdc25-22. ... (continues next page)

(legend from Fig. 3.8) ... Thin lines represent individual trajectories, thick lines represent average of binned data, error bars of average lines represent 95% confidence interval of the mean. Error bars in univariate scatter plots represent 95% confidence interval of the mean and standard deviation, text is mean ± 95% confidence interval. Each dot represents a single growth event. Data in C-D comes from 5 independent experiments (311 growth events, of which 289 were unambiguous, from 32 cells in wt; 231 growth events, of which 203 were unambiguous, from 26 cells in cdc25-22). Data in E-G comes from 30 cells for each condition in 3 independent experiments .

---

that a constant rescue rate would produce spindle collapse, we fitted all our wild type data points of microtubule number in time to a single exponential (Fig. 3.9C, see Methods). Then, starting from the empirical distribution of inferred number of microtubules at anaphase onset (Fig. 3.9D), we predicted what the distribution of microtubule number would look like after the average anaphase duration (16.1 minutes), if microtubules were lost at the rate extracted from the fit (see Methods). As expected, the predicted distribution of final microtubule number is wider than the observed one (Fig. 3.9E). In addition, the predicted final distribution shows that approximately 4% of spindles would end with 1 or less microtubules, that is to say, necessarily collapsed. The probability of spindle collapse would be higher, including for example spindles which have lost all microtubules from one of the poles, though the other may contain more than one microtubule.

Our data therefore shows that spindles with fewer microtubules are enriched in Cls1. Consistent with a model in which Cls1 accumulation promotes microtubule rescue, spindles starting with fewer microtubules lose them at a lower rate. In addition, the distribution microtubule number at anaphase end is not compatible with a model in which microtubules are lost stochastically at a constant rate. Furthermore, such constant rate would produce spindle collapse with a probability that is not observed in wild type spindles.

3 Materials and Methods

3.1 Strains and imaging

Production of *S. pombe* mutant strains

All used strains are isogenic to wild-type 972 and were obtained from genetic crosses, selected by random spore germination and replicated on plates with corresponding drugs or supplements. All strains are listed in Table S1. Transformations were made following [102].

Fission yeast culture

All *S. pombe* strains were maintained at 25° in YE5S plates and refreshed every third day. One day before the microscopy experiments, cells were transferred to liquid YE5S culture in the morning, and imaged the next day at exponential growth. For all experiments except for Fig. 3.5C, the cells were grown overnight in YE5S liquid medium at 25°. For experiments in the absence of thiamine (Fig. 3.5C), cells from the liquid YE5S culture were washed three times with deionised water, transferred to EMM supplemented with adenine, leucine and uracil, and incubated 18-22 hours at 25° prior to the microscopy experiment.

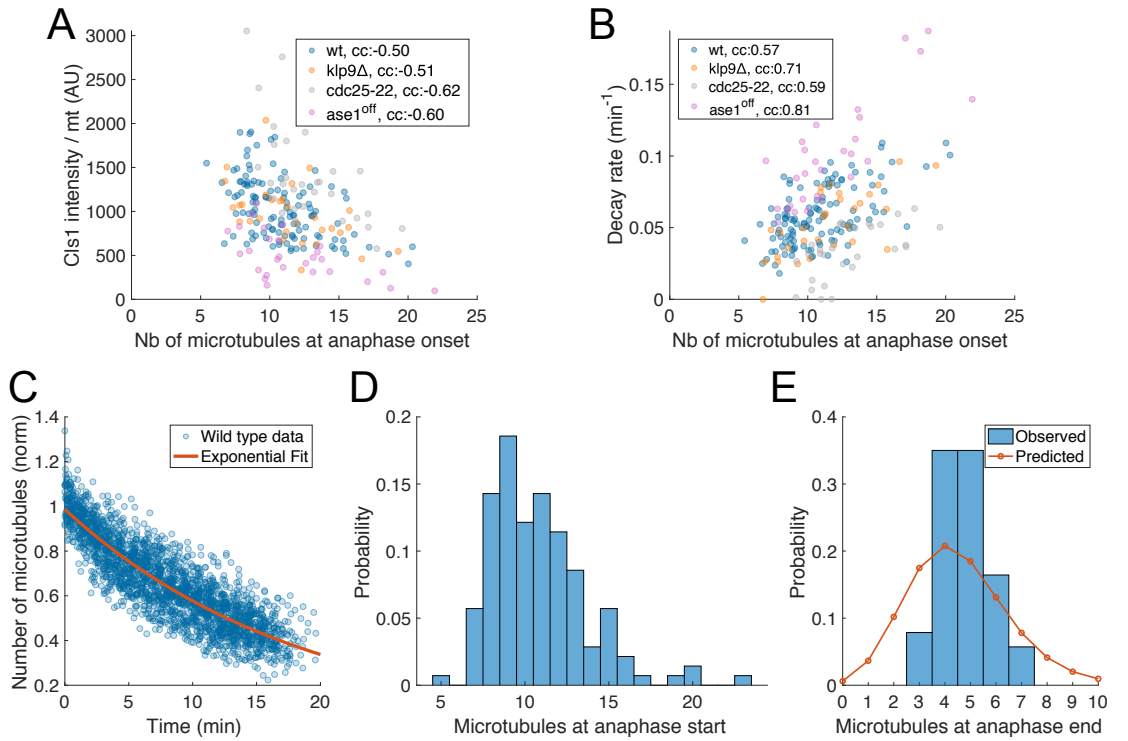

Figure 3.9: Progressive increase in microtubule stability prevents spindle collapse
Color code: wild type (blue), klp9Δ (orange), cdc25-22 (grey), ase1^{off}(pink) **A)** Total intensity of Cls1-3xGFP divided by inferred number of microtubules at anaphase onset as a function of inferred number of microtubules at anaphase onset. The negative correlation indicates that spindles that start with fewer microtubules are enriched in Cls1. **B)** Decay rate resulting from fitting each curve of number of microtubules in time for the first ten minutes to an exponential decay (Equation 3.2,$N = N_0 e^{-t/\tau}$, where N is predicted number of microtubules, t is the anaphase time, and N_0, τ are fitting parameters). The decay rate of each spindle ($1/\tau$) is plotted as a function of the inferred number of microtubules at anaphase onset. The positive correlation indicates that spindles starting with more microtubules lose them at a higher rate. **C)** All wild type observations of normalised inferred number of microtubules (see Methods) as a function of anaphase time plotted as dots, along with a fit of all the data points to an exponential decay (red line). **D)** Distribution of inferred number of microtubules at anaphase onset for all wild type data combined. **E)** Histogram representing the observed distribution of inferred number of microtubules at anaphase end for all wild type data combined. The red line represents the prediction of probabilities in a situation in which we start with the microtubule distribution in (D) and microtubules are lost at a constant rate, given by the fit in (C), for the average duration of anaphase (16.1 minutes).
Data in A, B is all the mCherry-Atb2 cls1-3xGFP from previous figures combined, except for experiments with wt and cls1-3xGFP^{off} in Fig. 3.6, because number of microtubules in cls1-3xGFP^{off} cannot be determined. Data in C-D is all the wild type mCherry-Atb2 cls1-3xGFP from previous figures combined.

Live-cell microscopy

For live-cell imaging, cells were mounted on YE5S agarose pads, containing 4% agarose [193]. Imaging was performed at 27° with an inverted Spinning disk confocal microscope Eclipse Ti-E (Nikon) with Spinning disk CSU-X1 (Yokogawa), equipped with Plan Apochromat 100×/1.4 NA objective lens (Nikon), a PIFOC module (perfect image focus), and sCMOS camera Prime 95B (Photometrics), integrated in Metamorph software by Gataca Systems. Movies used for kymographs were imaged using a Live-SR module (Gataca systems).

For kymographs, stacks of 5 planes spaced 0.5 µm without binning were acquired every 4 seconds during 15 minutes. For mCherry movies, stacks of 11 planes spaced 0.5 µm without binning were acquired every minute during 90 minutes. For GFP-Mal3 movies used for measuring spindle elongation dynamics (Fig. 3.7C), stacks of 7 planes spaced 1 µm without binning were acquired every minute during 90 minutes. Exposure used was always 100 ms.

To minimize the inter-experiment variance, all the data shown within the same plot was acquired during the same experiment, except for Fig. 3.9A-B, and Fig. S6. In the case of movies used for kymographs this meant that samples of the conditions tested were alternated on the microscope. In the case of one minute interval movies, positions corresponding to all conditions were imaged simultaneously.

3.2 Image and data analysis

All feature detections, kymographs and length measurements were done in maximal projections of fluorescence microscopy images. Only intensity measurements were taken from summed projections.

Pre-processing of imaging

All movies of mCherry-Atb2 Cls1-3xGFP, and the movies of GFP-Mal3 used in Fig. 3.7C were initially processed with the Fiji distribution of Imagej (https://imagej.net/Fiji). The plugin *Correct 3D drift* was used to calculate the drift of images from the DIC channel, and the plugin *Trainable Weka Segmentation* was used to generate probability images of each frame in the maximal projection images. Each probability image has the same size as the original maximal projection, and each pixel value goes from 0 to 1. Higher values correspond to higher likelihood of that pixel corresponding to a spindle (in the tubulin channel) or to a midzone (Cls1 channel).

The probability images and the drift were later used in a custom written Matlab program, Pomber, which is publicly available in https://github.com/manulera/Pomber. In essence, the program allows to load the movies, run a semi-automated analysis described in the next sections, inspect the results, and correct them when necessary. Finally, the results can be exported for posterior analysis. The user is required to draw the profile of each analysed cell by hand. Since generally cells do not move between frames, the same profile can be used for all the frames, but it can be changed between frames if necessary.

Analysis of mCherry-Atb2 images

To find the spindles in mCherry-Atb2 images, we use the pixels inside the cell mask in mCherry-Atb2 probability images for which the probability is bigger than 0.8 (This gives a

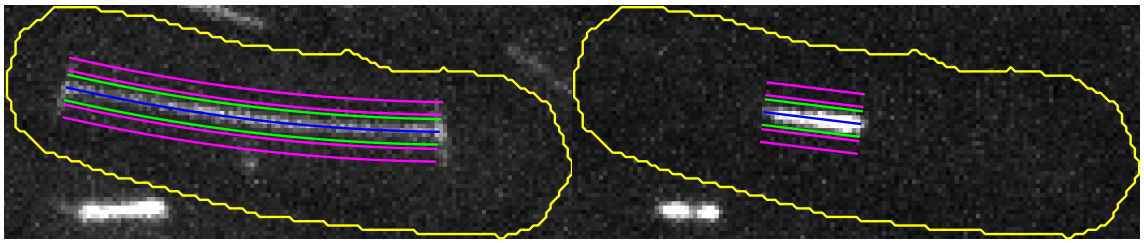

Figure 3.10: Measurements of intensity
Maximal projections of signals of mCherry-Atb2 (left) and Cls1-3xGFP (right), along with the lines used to measure the intensity of the spindle (left) and midzone (right) in the movies (see text). Yellow line, cell outline extracted from the mask. Blue line shows the orthogonal polynomial ($g(x)$) resulting from the fit in Equation 3.4. Magenta lines mark the areas used for calculating the background. Green lines mark the areas used for calculating the signal.

good segmentation of the spindle). They are defined by X_i, Y_i, P_i (position x, position y, probability of pixel i out of N). We find the parameters (X_0,Y_0,θ,α) that maximize F:

$$\begin{bmatrix} x_i \\ y_i \end{bmatrix} = \begin{bmatrix} cos\theta & -sin\theta \\ sin\theta & cos\theta \end{bmatrix} \begin{bmatrix} X_i - X_0 \\ Y_i - Y_0 \end{bmatrix} \tag{3.3}$$

$$F(x_i, y_i, P_i) = \sum_{i=i}^{N} P_i^2 \; exp\left(-\left|\frac{\alpha x_i^2 - y_i}{\lambda}\right|\right) \tag{3.4}$$

Equation 3.3 generates a rotation of angle θ of points centred on point (X_0, Y_0). Equation 3.4 returns a weighted squared probability for each point, where the weight decays exponentially with the distance to a polynomial of grade 2 in the rotated axis $g(x) = \alpha x^2$ (blue line in Fig. 3.10), with a characteristic decay length λ. We find that the orthogonal polynomial $g(x)$ that maximizes F matches well the spindle for λ=0.55 µm. To find the edges of the spindle, we projected all the points of the probability image on the polynomial $g(x)$. The edges were defined as the two points on $g(x)$ that contain all projections with P_i>0.6 between them. We define the length of the spindle as the length of the curve $g(x)$ between these two edges. We fit data in each frame to this function, starting by the first time point. Initially, we set α to zero, until we find a spindle of length greater than 6 µm, since shorter spindles are straight and well described by a line. If the algorithm fails to find the trace of the spindle, the user can draw the spindle by hand. We used the same method to measure the length of spindles in GFP-Mal3 movies used in Fig. 3.7C.

To measure the intensity, we used intensity profiles (matlab *improfile* function) on summed projections along curves in which the sampled points were evenly spaced at a distance of 1 pixel. We used 7 parallel curves, separated by 1 pixel, the central one coinciding with the orthogonal polynomial g(x). The total width corresponds to 0.77 µm in our microscope (green lines in Fig. 3.10), we call this the signal region. As background, we subtracted the median of two parallel regions of 4 pixels width each at the top and bottom of the signal region (magenta lines in Fig. 3.10). The total tubulin intensity was the sum of the intensities of all the points in the signal region after background subtraction.

Analysis of Cls1-3xGFP images

To determine midzone edges, we used a similar method as the one used to determine the spindle edges. The edges were defined as the two points on $g(x)$ (from the spindle fit) that

contained all projections of probabilities of Cls1-3xGFP movies with P_i>0.6 between them. The intensity was measured the same way as for the spindle signal (see Fig. 3.10).

Kymograph analysis

To make kymographs from GFP-Mal3 movies, we followed a similar approach. We used Equation 3.4 but instead of the probability calculated with an ImageJ plugin, we used the intensity (I) of maximal projections:

$$F(x_i, y_i, P_i) = \sum_{i=i}^{N} (I_i - median(I))^2 \, exp\left(-\left|\frac{\alpha x_i^2 - y_i}{\lambda}\right|\right) \tag{3.5}$$

Here the weight is given by the intensity of each pixel minus the median of the pixels inside the cell mask. In addition, we chose the frame from which the value of α would be allowed to be different from zero by visual inspection of each movie.

We used fits to orthogonal polynomials to make the kymographs. For each of the frames in the movie, we made a maximal projection on the orthogonal polynomial of all the points that were at a distance of 3 or less pixels from the orthognal polynomial. This yielded a vector of intensities for each time point. To align the vectors into a kymograph we used the center of mass of the maximal projection in time of the movie as a reference, and we aligned all the vectors such that this point would be at the center of the kymograph. We found that growth events were best identified when kymographs were made from movies that had been pre-processed in ImageJ, correcting the bleaching with the plugin *Adjust/ Bleach Correction* and subsequently applying a Gaussian filter of σ of 1 pixel.

To annotate the kymographs, we wrote a Matlab program, KymoAnalyzer, which is publicly available in https://github.com/manulera/KymoAnalyzer. The user can draw polygonal lines to mark the poles of the spindle and the microtubule growth events. These lines are then linearly, so that they are equally sampled in time (1 point per time point). Like this, we can calculate the length of the spindle and microtubules in every time point. Duration of the growth event was defined as the time between apparition of the comet and its disappearance. To calculate the microtubule growth speed, the length vs. time curve was fitted to a first order polynomial using Matlab's *polyfit*. The spindle center was defined at each time point as the middle point between the poles.

Anaphase onset determination

To determine the onset of anaphase, we fitted the curves of length of spindle in time to the function $G(t)$, with fitting parameters (L_0, t_1, t_2, s_1, s_2, s_3):

$$G(t) = \begin{cases} L_0 + t\ s_1 & \text{if } t \leq t_1 \\ G(t_1) + (t - t_1)\ s_2 & \text{if } t > t_1 \text{ and } t \leq t_2 \\ G(t_2) + (t - t_2)\ s_3 & \text{if } t > t_2 \end{cases} \tag{3.6}$$

$G(t)$ is a series of three linear fits that start at L_0 at $t = 0$. Anaphase onset is determined by t_2, and we use s_2 and s_3 as the velocities of phase II and Anaphase B in the text. In general, fits correctly identified the switch in velocity seen in Fig. 3.2B. In some cases, particularly in klp9Δ, where the anaphase velocity decreases in time, t_2 was fixed manually if the fit gave an obviously wrong result.

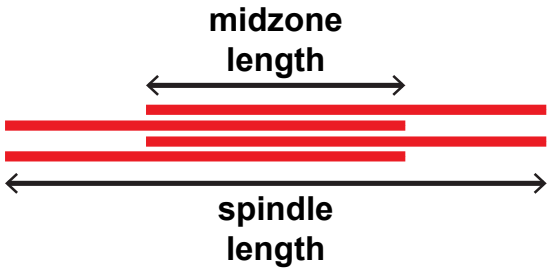

Figure 3.11: Estimating microtubule number from spindle and midzone length
Scheme illustrating the simplifications used to reach Equation 3.7

Calibration of mCherry-Atb2 total intensity to polymer length and number of microtubules

To calibrate total intensity to total polymer length, we used pairs of spindle length and polymer length (S_i,P_i) measured by electron microscopy in [208] and shown in Fig. 3.2D. For each set of experiments, we produced an average curve of total intensity as a function of spindle length for wild type data, similar to the one showed in Fig. 3.2D, with bins evenly spaced 1 µm between them. We used linear interpolation on the average curve to obtain the value of intensity (I_i) at the spindle lengths observed experimentally (S_i). We then found the scaling factor (σ) that minimised the sum of the absolute value of the differences between the total polymer length and the interpolated values $\sum_{i=1}^{N} |\sigma I_i - P_i|$.

If we make a simplification and assume that the midzone is exclusively composed of microtubule overlap, and that outside of it there is no overlap (Fig. 3.11), we can calculate the number of microtubules N from total polymer length P, spindle length S, and midzone length M with:

$$N = \frac{2P}{S + M} \tag{3.7}$$

Although this is an oversimplification, the results fit the experimental data and we can infer the number of microtubules using a single parameter σ to fit the total polymer length to the total intensity of labelled tubulin (Fig. 3.2E).

Statistical tests

Student t-test was used to compare conditions in univariate scatter plots, the p-values are indicated if they are smaller than (0.05, 0.005, 0.0005).

Exponential fits to the inferred number of microtubules in time

For Fig. 3.6C, in each analysed wild type cell, the curve of inferred number of microtubules in time during anaphase was fitted to Equation 3.2 (Equation 3.2, $N = N_0 e^{-t/\tau}$, where N is predicted number of microtubules, t is the anaphase time, and N_0, τ are fitting parameters). For each cell, the difference between the fit error divided by the fit parameter N_0 was calculated, and the average value was plotted as a function of anaphase time in Fig. 3.6.

In Fig. 3.8F, the curves of inferred number of microtubules in time were also fitted to Equation 3.2, and each curve of number of microtubules in time is plotted normalised to N_0 from the corresponding fit.

In Fig. 3.9C, the points from each curve of inferred microtubule number in time from Fig. 3.6C divided by their corresponding N_0 were fitted to a single exponential.

Prediction of the distribution of number of microtubules at anaphase end

To predict the distribution of number of microtubules at anaphase end (Fig. 3.9E), we fitted all wild type data points of normalised microtubule number in time to a single exponential (Fig. 3.9C, see previous section). If we start from a number of microtubules N_0, which can be lost at a constant rate $1/\tau$, after a given time t the number of microtubules (N) is binomally distributed with $p = e^{-t/\tau}$:

$$P(N; N_0, p) = \binom{N_0}{N} p^N (1-p)^{N_0-N} \tag{3.8}$$

To predict the distribution of number microtubules at the end of anaphase, $P(N)$, shown in Fig. 3.9E, we used the empirical distribution of microtubules at anaphase onset, $P(N_0)$ (Fig. 3.9D) and Equation 3.8, then $P(N)$ is given by:

$$P(N) = \sum_{N_0=0}^{N_0=\infty} P(N_0) P(N; N_0, p) \tag{3.9}$$

Public Matlab libraries used in this study

- geom2d - 2D geometry library
- hline-vline - function to draw horizontal and vertical lines
- UnivarScatter - making univariate scatter plots

4 Discussion

Anaphase B is the stage of mitosis where microtubule sliding at the central spindle drives the separation of the segregated chromosome masses into the two daughter cells [175]. Because of its specificity for antiparallel-specific crosslinking, Ase1 only connects interpolar microtubules to neighbours emanating from the opposite pole, generating a characteristic square lattice, which is optimal to produce microtubule sliding (Fig. 3.1) [51, 208, 95]. Therefore, Ase1 localises to the spindle midzone, where it can recruit its binding partners [21]. Importantly, the microtubule overlap in the midzone is maintained during sliding, which requires the coordination of microtubule dynamics and sliding. The functions of the main anaphase B MAPs (Ase1, Klp9, Cls1) have been described individually [120, 216, 60, 21, 133]. However, little is known about how their combined activities result in the coordination of sliding and microtubule growth at the midzone or whether they affect microtubule dynamics. The lack of measurements of microtubule dynamics during anaphase greatly limits our understanding of this process, and is a necessary step towards a complete description of mitosis. Previously, fluorescently labelled tubulin was used to image anaphase microtubules, and individual microtubule dynamics could be observed at late anaphase when only few microtubules were present [169]. We tried this method and found that kymographs where single microtubule dynamics can be

observed at late anaphase are rare, and most kymographs cannot be used. This method is therefore not amenable for a systematic study of microtubule dynamics in the spindle.

In this work, we have showed that SR-SIM imaging of GFP-Mal3 allows to visualize microtubule dynamics during anaphase B (Fig. 3.3). Using this method, we have verified the previous hypothesis that recruitment of Cls1 by Ase1 specifically concentrates rescues at the midzone [21]. We have also observed that ase1 deletion increases both microtubule growth speed and duration of microtubule growth events. This is, at least in part, due to lower recruitment of Cls1 (Fig. 3.4). In addition, we have shown that microtubule dynamics change with anaphase progression: microtubule growth velocity decreases and rescue rate increases. We propose that this is mediated by a progressive enrichment of Cls1 on spindle microtubules, which occurs because Cls1 amounts remain constant during anaphase, while the number of microtubules decreases (Fig. 3.6). Consistent with this, overexpression of Cls1 has a similar effect on microtubule dynamics as anaphase progression, and lowering its expression has the opposite effect (Fig. 3.5). We hypothesize that this progressive increase in microtubule stability prevents spindle collapse at late anaphase (Fig. 3.9). Finally, we have tested the effects of deletion of kinesin-6 klp9 and of cell size on microtubule dynamics (Fig. 3.7 and Fig. 3.8). We have found that klp9 deletion increases rescue rate, and that bigger cells display longer microtubule growth events and lose microtubules at a lower rate.

Duration and growth speed of microtubule growth events are lower in anaphase than in interphase

We have found that during anaphase, the average duration of microtubule growth events is 72±32 seconds (Fig. 3.3E). Microtubule growth speed is around 1.5 µm/min at anaphase onset, and it decreases with anaphase progression (Fig. 3.3D). In contrast, interphase microtubules grow faster (~2.3 µm/min) for longer time (~3 minutes) [172]. Such properties seem convenient for *S. pombe* cells, since microtubules in interphase need to reach a length comparable to half the cell length, in order to deliver growth factors at the cell tips, as well as to push on cell tips to center the nucleus [38, 192] (see subsection 5.1 of introduction). In contrast, microtubule extensions of that length are probably not desirable in anaphase, since this would mean that growing plus ends would push against the opposite spindle pole. A possible reason why microtubule dynamics differ in the nucleus and cytoplasm might be that Tip1/CLIP170 does not localise to spindle microtubules [33, 147]. Tip1/CLIP170 is a MAP that promotes the recruitment of Alp14/XMAP215 in cytoplasmic microtubules and increases duration and speed of microtubule growth events during interphase [33, 147]. In the future, it would be interesting to study the effects of artificially targeting Tip1 and its partners to the spindle microtubules, to see whether this induces cytoplasm-like microtubule dynamics in the spindle.

Ase1 recruitment of Cls1 controls rescue distribution

It had been previously hypothesized that since Ase1 recruits Cls1, this would constrain the occurrence of rescues to the midzone [21]. We verified this in our experiments, where deletion of ase1 resulted in rescues occurring anywhere along the spindle. In contrast, in wild type spindles, rescues occurred mostly at the edge of the midzone (Fig. 3.4B). Additionally, we found that the duration of microtubule growth events increased approximately ~40% in ase1Δ cells (Fig. 3.4C) and that microtubule growth speed did not decrease with anaphase progression, unlike in wild type cells (Fig. 3.4D). We reasoned that

these strong effects might in part be due to the disruption of the midzone in absence of Ase1. Using the shut-off strain ase1^{off}, which expresses lower levels of Ase1 than the wild type strain, we showed that spindles that have a midzone with less Ase1 than wild type spindles, display milder effects on microtubule dynamics than ase1Δ spindles. Despite the Ase1 levels being approximately half of those in wild type (Fig. S4D), duration of microtubule growth events was only slightly longer in ase1^{off} cells with a structured midzone (Fig. 3.5F). Microtubule growth speed decreased with anaphase progression in ase1^{off} spindles, but it was higher than in wild type across anaphase (Fig. 3.5G). In contrast, duration of microtubule growth events in ase1^{off} cells without a midzone was significantly increased (Fig. S4B). This confirms that both Ase1 levels and midzone structure affect microtubule dynamics. It is possible that Ase1 itself affects microtubule dynamics. However, our data favours the hypothesis that the observed changes are mostly due to lower recruitment of its binding partner Cls1 (Fig. 3.6B). Consistent with this possibility, reducing the expression levels of Cls1 had a similar effect to the depletion of Ase1 (Fig. 3.4E-G).

We do not have a clear answer as to why rescues happen specifically at the edges, rather than all along the midzone. Cls1, which is required for microtubule rescues [21], is localised all along the midzone, and not enriched at the edges (Fig. 3.6G), so its localisation cannot explain why rescues occur at the edge. Perhaps some unidentified factor is specifically concentrated at midzone edges. Another possible explanation is that the rescue mechanism is more effective at the edge. One speculative reason why this could be the case is the characteristic ram horn structure of shrinking microtubule ends. *In vivo*, protofilaments of depolymerising microtubules curve outwards as they shrink, resembling the peeling of a banana [132]. The distance between the tip of these curved protofilaments and the axis of the microtubule is comparable to the inter-microtubule distance in the midzone [132, 208]. Therefore, it is possible that when the shrinking microtubule reaches the midzone, steric hindrance on the curved protofilaments promotes their straightening and hence enhances rescue. This curvature would be lost once the shrinkage proceeds further inside the midzone. In the future, it would be interesting to combine Cls1 and Ase1 *in vitro* and see whether in those overlaps rescues also happen at the edges.

The function of interpolar microtubules during anaphase is to maintain the overlap, which is the main mechanical connection between spindle poles, and drives their separation by sliding. Microtubules that only fluctuate in length beyond the midzone edge with frequent rescues seem to be adequate for this task. However, microtubules are still lost as anaphase progresses. Why not rescue them all? The reason for this might be found in the limited amount of tubulin present in yeast cells. Polymerising all the available tubulin would allow a maximal microtubule length of approximately 120 µm [208, 119]. This means that the peak of polymerised tubulin length during anaphase (~35 µm Fig. 3.2D), represents roughly 1/4 to 1/3 of the total tubulin of the cell. If no microtubules were lost, the amount of polymerised tubulin at anaphase end would be more than half of the total tubulin. This would significantly reduce the concentration of soluble tubulin, and perhaps prevent microtubule elongation at the required rate to maintain the overlap.

Microtubule dynamics change in time during anaphase

A recent study in HeLa cells showed that the turnover of EB1 decreases with anaphase progression [10]. Since EB1 binds only to growing microtubules, a decrease in its turnover with anaphase progression might be indicative of a change in microtubule dynamics. We have indeed observed gradual changes of microtubule dynamics in our experiments,

where growth velocity and rescue rate increase with anaphase progression (Fig. 3.3E, Fig. 3.6F). Our data suggests that these changes are caused by a progressive enrichment of Cls1 on microtubules. Since the total amount of Cls1 on the spindle remains roughly constant, and the number of microtubules decreases, the amount of Cls1 per microtubule increases (Fig. 3.6B-D). We believe this enrichment causes the change in microtubule dynamics, because overexpression of Cls1 slows down microtubule growth (Fig. 3.5), mimicking anaphase progression, while reducing the expression levels of Cls1 results in higher microtubule growth speeds, which are characteristic of early anaphase (Fig. 3.4E-G).

We observed that both increasing and reducing the expression of Cls1 resulted in longer microtubule growth events (Fig. 3.4F, Fig. 3.5D). Perhaps the increased duration observed in cls1^{off} only occurs at very low levels of Cls1 that are never observed in the wild type spindle. This is consistent with our observation that Cls1 amounts on the spindle are lower in cls1-3xGFP^{off} cells than in ase1^{off} (Fig. 3.6B). Along these lines, duration of microtubule growth events in ase1^{off} spindles that assemble a midzone is similar to wild type (Fig. 3.4F), but events are longer in ase1^{off} spindles that do not have a midzone, as Cls1 is presumably less recruited to such structures (Fig. S4B).

We believe that the progressive increase in rescue rate prevents the collapse of spindles at late stages of anaphase, where the number of microtubules is low. We showed that, starting from the empirical distribution of number of microtubules at anaphase onset (Fig. 3.9D), if microtubules were lost at the constant rate that best matches the experimental decrease of microtubule number in time (Fig. 3.9C), the distribution of number of microtubules at the end of anaphase would be wider than the observed one, and some spindles would collapse (Fig. 3.9E). This same mechanism also stabilizes spindles which stochastically start anaphase with fewer microtubules (Fig. 3.9A, B).

It is likely that rescues are affected by more than just the average amount of Cls1 per microtubule. In the midzone, microtubules are organised in a square lattice, where internal microtubules are connected to more neighbours than those on the outside [51, 208]. If Cls1 would be uniformly distributed along the antiparallel overlaps, internal microtubules with more neighbours would have more Cls1 bound to them and would be more likely to be rescued. This is consistent with electron microscopy data, in which we see no sign of internal microtubules being lost [208, 51]. Additionally, if rescue rate increased with the number of neighbours, this would promote microtubules to be lost from both spindle poles evenly, since multiple losses of microtubules from the same pole would cause an increased average number of neighbours at that pole compared to the other. In the future, we will be able to test this hypothesis by simulating a bundle of microtubules with molecular motors, crosslinkers and rescue factors.

Microtubule rescue organisation and changes in microtubule dynamics affect spindle function

An important consequence of rescues being restricted to a narrow region in space is that it allows for the decoupling of microtubule growth and sliding. Since microtubule rescues occur mostly at the midzone edge (Fig. 3.3C), the microtubules only fluctuate in length beyond that point (Fig. 3.12). Therefore, the midzone structure will be maintained as long as microtubule growth speed is faster than sliding speed. If microtubule growth speed would be slower than sliding, the overlap at the midzone would shrink. Sliding speed is 0.32±0.03 μm/min (from Fig. 3.2B), so microtubule growth speed is faster until late anaphase (Fig. 3.4E).

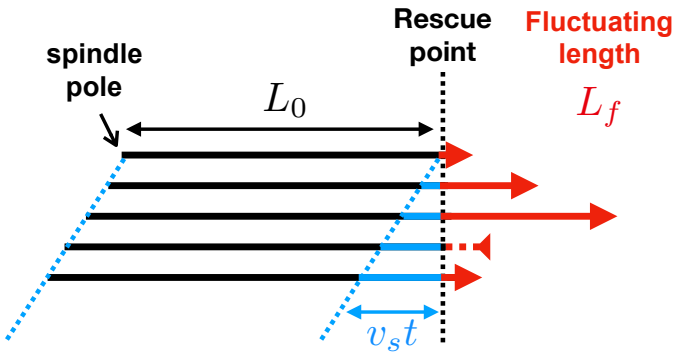

Figure 3.12: Phenomenological model

Illustration depicting the elements of the phenomenological model described in the text. We make the simplifying assumption that all rescues occur at a given point in space (vertical dashed line), that is at distance L_0 from the spindle pole at anaphase onset. It follows that the length to the left of this point is not lost during catastrophe, unless there is no rescue. The length protected from rescue increases in time as microtubules slide at constant speed v_s (blue line). In contrast, the length beyond the rescue point undergoes dynamic instability alternating between growth (red full line) and shrinkage (red dashed line).

We can write a simple phenomenological equation to describe this process, if we make the simplifying assumption that rescues only occur at a point in space for all the microtubules from the same pole (Fig. 3.12). In this scenario, microtubule sliding transports an increasing part of the microtubule beyond the rescue point, away from the fluctuating region, at a constant speed v_s (Fig. 3.12, blue segment). This section will not be depolymerised during the next catastrophe, as long as the microtubule is rescued. The average microtubule length beyond the rescue point L_f is relatively small compared to the length of microtubules (0.6±0.4 µm from the data in Fig. 3.3). For a spindle in which the initial rescue point is at a distance L_0 with respect to the spindle pole (Fig. 3.12), the polymer length (L_p) in time depends on the number of microtubules (N) and is given by:

$$L_p(t) = N(t)\left[L_0 + L_f(t) + v_s t\right] \tag{3.10}$$

This model naturally fits our data, since this equation is equivalent to the one we used to calculate the number of microtubules from polymer length (Equation 3.7), if midzone length does not change in time and $L_f(t)$=0. This formulation highlights that changing microtubule growth velocity only modifies the average fluctuating length, but the extra polymer produced during each microtubule growth event is lost upon catastrophe, since rescues occur at the midzone edge. Therefore, the spatial distribution of rescues generated by the Ase1/ Cls1 system removes the need for cross-talk between microtubule growth and sliding, as long as microtubule growth speed is faster than sliding.

While this model can explain the behaviour of the spindle at early anaphase, at later stages we predominantly observe comets that are almost vertical, meaning that the sliding speed is the same or very close to the microtubule growth speed (see kymographs in Fig. 3.8 and Fig. 3.7). We expect this to be due to the high levels of Cls1 on the spindle at late anaphase. In cls1^{OE+} spindles, which we think are representative of this stage, microtubule growth speed is on average 0.37±0.23 µm/min (Fig. 3.5C), very close to the wild type sliding speed of 0.32±0.03 µm/min. Perhaps this constitutes the lowest limit of microtubule growth speed, and the difference between sliding and microtubule growth

speeds is small enough to keep the overlap. Alternatively, an unknown mechanism could keep microtubule growth speed at the edge of the midzone at the same speed as sliding. This mechanism would probably be different from the coordination of microtubule growth and sliding proposed in chapter 2, because at the time where we start seeing these slow microtubule growth events (around 8 minutes into anaphase, Fig. 3.8C), the sliding speed of the spindle does not change (Fig. 3.7C, see wild type curve), suggesting that sliding occurs at constant speed regardless of microtubule dynamics. In this scenario, it would be sliding speed that set microtubule growth speed, while in the mechanism proposed in chapter 2, it was the other way around.

Our understanding of this is that cells need to lose microtubules during anaphase in order not to deplete their limited pool of tubulin. However, once they have reached a number of around 4 microtubules, they need those to be stable to prevent spindle collapse. A constant amount of Cls1 on the spindle allows for rescue rate to increase in time, but it comes at the price of slowing down the microtubule growth speed. It is known that increasing CLASP concentrations has this effect on rescue and microtubule growth speed from experiments *in vitro* [1, 141] and *in vivo* [21]. We believe therefore that the progressive decrease of microtubule growth speed has no role in itself, but is rather a consequence of higher Cls1 activity per microtubule.

Deletion of kinesin-6 klp9 increases rescue rate

Some mitotic kinesins are involved in the regulation of microtubule dynamics. *In vitro*, kinesin-5 acts like a microtubule polymerase [40], and in fission yeast, it promotes nucleation by binding to γ-tubulin [152]. In higher eukaryotes, kinesin-4 is recruited to the central spindle by PRC1, where it suppresses microtubule dynamics [224, 206, 46] (described in detail in chapter 2). Fission yeast does not have kinesin-4, and our data suggests that it is Cls1 that has a similar effect on microtubule dynamics in the midzone (Fig. 3.5, Fig. 3.4). We tested the effects of the deletion of kinesin-6 klp9, the tetrameric kinesin that drives microtubule sliding during anaphase [60]. We found that in klp9Δ spindles, rescue rate was higher, and microtubule growth velocity decreased at a lower rate with anaphase progression than in wild type (Fig. 3.7E, F). Since the duration of microtubule growth events was the same in wild type and klp9Δ (Fig. 3.7D), any decrease in rate of microtubule loss in klp9Δ must be due to a higher rescue rate. Our interpretation of these results is that in klp9Δ spindles, the rescue rate is increased by a mechanism other than Cls1 enrichment. Consistent with this hypothesis, the amount of Cls1 per microtubule does not increase at the same pace in klp9Δ as in wild type cells, despite the rescue rate being higher (Fig. 3.7G). Conversely, since Cls1 accumulates less on microtubules, the decrease in microtubule growth speed with anaphase progression is lower in klp9Δ than in wild type (Fig. 3.7E).

There are multiple ways by which deletion of klp9 could increase rescue rate. It could be a direct effect of Klp9, which would mean that in wild type, the presence of Klp9 mildly suppresses rescues. Alternatively, less crowding on the midzone in the absence of Klp9 could make microtubule rescues more efficient. Finally, Klp9 is required to translocate the Chromosome Passenger Complex proteins from the kinetochore to the midzone [133]. Aurora B is among them, and it is known to have multiple downstream targets that could be affected by its mislocalisation [133].

Bigger cells have longer microtubule growth events and lose microtubules at a slower rate

Previous data from zebrafish and *C. elegans* showed that microtubule growth speed increases with cell size in metaphase [113, 163]. In contrast, we found that microtubule growth speed in anaphase does not change with cell size in fission yeast (Fig. 3.8C). However, duration of microtubule growth events increased by ~25% in cdc25-22 cells, which are ~50% bigger (Fig. 3.8D). In addition, microtubule loss rate is lower in bigger cells (Fig. 3.8F). This decrease in the microtubule loss rate could be due to a combination of the longer duration of microtubule growth events, which decreases the frequency at which rescues are tested at the midzone (Equation 3.1), and the increased levels of Cls1 per microtubule (Fig. 3.8G). Simulations will be useful to test whether bigger spindles, which start anaphase with more microtubules (Fig. 3.8E), could lose microtubules at a lower rate also because a larger fraction of their microtubules are stabilized by antiparallel neighbours.

Future plans and perspectives

Our study has enabled us to uncover previously unknown features as well as validate some long-standing hypotheses regarding anaphase spindle elongation in fission yeast. In addition, it has also pointed us to other questions that we were not able to address because of time or technological constraints. Due to time limitations, it has not been possible to carry out all the planned experiments and to develop a model of how the rescue rate can increase in time with simulations. Before publishing this work, we want to test whether Cls1 might be antagonised by Alp14/XMAP215, which is a known promoter of microtubule growth. Importantly, our preliminary data (not shown) suggests that microtubule dynamics in alp14Δ appear very similar to cls1^{OE+} (Fig. 3.5A, C). In addition, we want to see whether a milder overexpression of Cls1-3xGFP from P1nmt1 promoters increases rescue rate. We expect this from our GFP-mal3 cls1^{OE} data (Fig. 3.5B, D, E), but we did not obtain P1nmt1-Cls1-3xGFP transformants in our previous attempts, and this remains a key step to fulfil.

In the future, better imaging and image analysis techniques might allow to resolve all comets in kymographs. This would be extremely informative, as it would allow to count the number of growing microtubules in the spindle. Additionally, such improvements might also enable measurements of microtubule dynamics in metaphase, which is not possible in our movies. Studying microtubule dynamics during anaphase in higher eukaryotes more closely related to humans will also be important, specifically those containing kinesin-4, which is absent in yeast. *Xenopus* spindles might be amenable for this, but so far the interest of researchers has focused mostly on metaphase in this system. Additionally, *in vitro* reconstructions with dynamic microtubules, PRC1, CLASP and mitotic kinesins are now technically possible [81, 126], but have not yet produced a system that shows persistent sliding and microtubule dynamics. However, the conditions to reconstitute a minimal system that recapitulates the main features of the anaphase spindle might be found in the near future.

5 Supplementary figures and tables

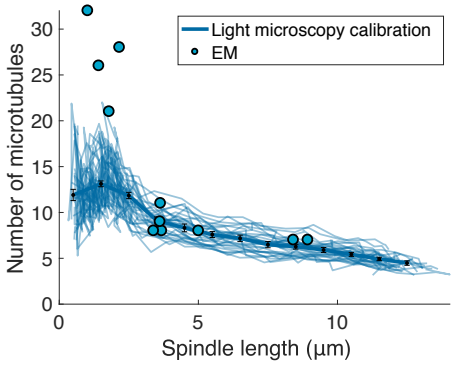

Figure S1: Our method for inferring number of microtubules only works for anaphase
Inferred number of microtubules as a function of spindle length (see Methods). Values measured by electron microscopy in [208] are shown as dots. Note that the values of metaphase (4 values on the top left), where microtubules are not predominantly part of antiparallel overlaps [51, 208], are not correctly inferred.
Thick lines represent average of binned data, error bars of average lines represent 95% confidence interval of the mean. Same data as in Fig. 3.2E.

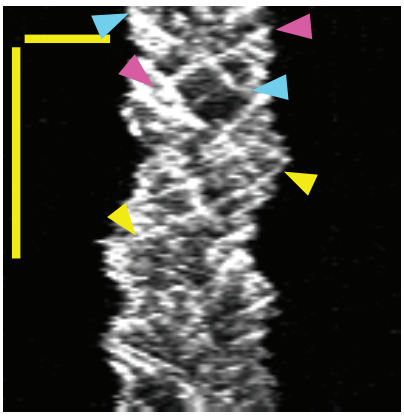

Figure S2: Metaphase kymograph
Kymograph of the mitotic spindle of a cell in metaphase expressing GFP-Mal3, in which time is in the vertical axis, and space is in the horizontal axis (see Methods). Arrowheads of the same color denote the start and finish of microtubule growth events that span the whole length of the spindle. Scalebars are 5 minutes (vertical) and 2 µm (horizontal).

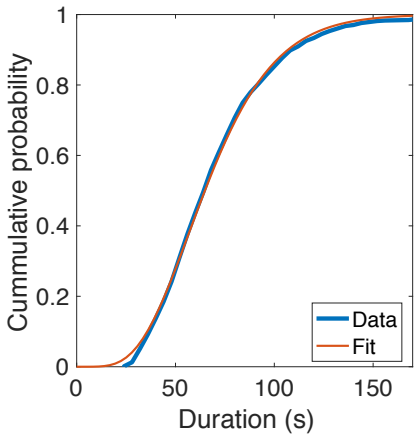

Figure S3: Distribution of the duration of microtubule growth events
Cumulative probability of duration of microtubule growth events. The distribution is well described by a gamma function This is indicative of catastrophe being a multi-step process [66]
Same data as in Fig. 3.3.

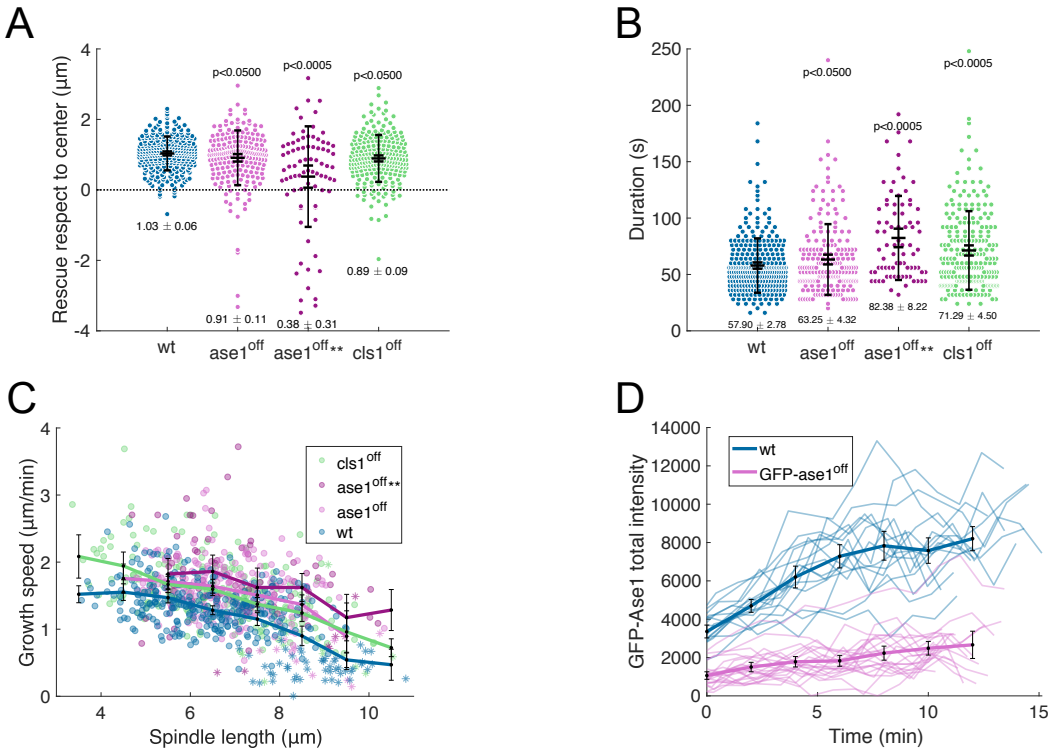

Figure S4: Ase1 organises spindle rescues and affects microtubule dynamics

Color code for A, B, C: wild type (blue), ase1^{off} with midzone (pink), ase1^{off**} without midzone (wine), cls1^{off}(green). Color code for D: wild type (blue), GFP-ase1^{off} (pink) **A)** Positions of rescues with respect to center in wt cells, ase1^{off} cells with midzone, ase1^{off} cells without midzone (ase1^{off**}) , and cls1^{off} cells. **B)** Duration of microtubule growth events in wt cells, ase1^{off} cells with midzone, ase1^{off} cells without midzone (ase1^{off**}) , and cls1^{off} cells. **C)** Growth speed of events as a function of spindle length at rescue (or first time point of ambiguous events) in wt cells, ase1^{off} cells with midzone, ase1^{off} cells without midzone (ase1^{off**}) , and cls1^{off} cells. Events for which the start and finish could be unambiguously determined are shown as round dots, and are the same as in (A) and (B). Other events are shown as stars. **D)** GFP-ase1 total intensity on the spindle in wt, and GFP-ase1^{off} cells, which express GFP-ase1 under the control of the p81nmt1 promoter.
Thin lines represent individual trajectories, thick lines represent average of binned data, error bars of average lines represent 95% confidence interval of the mean. Error bars in univariate scatter plots represent 95% confidence interval of the mean and standard deviation, text is mean ± 95% confidence interval. Each dot represents a single growth event. Data in A-C is the same as in Fig. 3.4E-F, in addition the ase1^{off**} data comes from 86 growth events, of which 79 were unambiguous, from 11 cells. Data in D comes from 2 independent experiments, for 17 cells in wt and 21 cells in GFP-ase1^{off}.

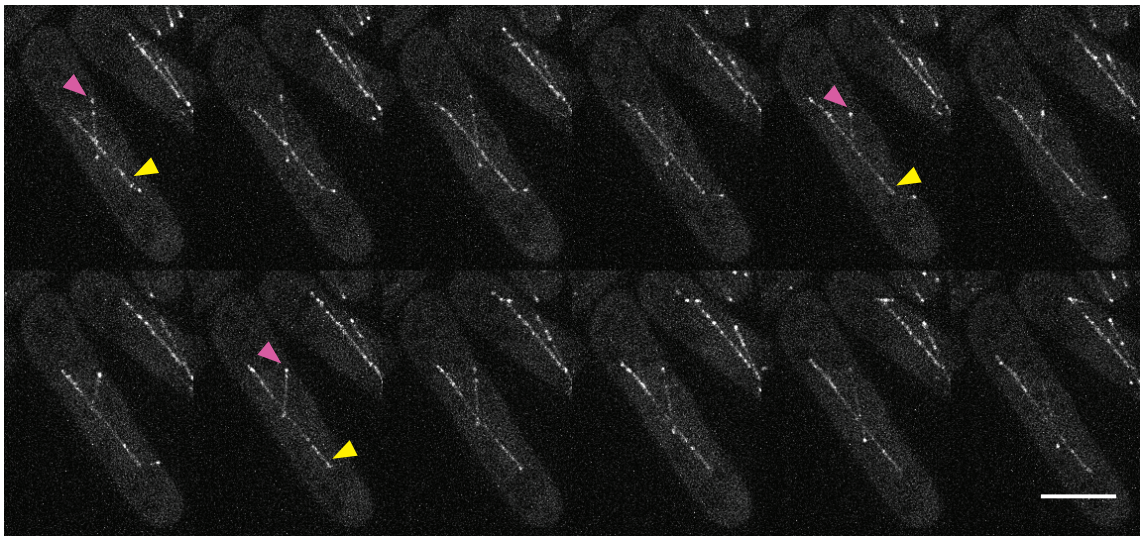

Figure S5: Overexpression of Cls1 from induced P41nmt1 produces ectopic cytoplasmic bundles during mitosis

Time lapse images of a cell in anaphase expressing GFP-Mal3, in which Cls1 is expressed from an induced P41nmt1 promoter. Yellow arrowhead marks the spindle, pink arrowhead marks an ectopic cytoplasmic bundle. Time between images is 16 seconds, scale bar is 5µm.

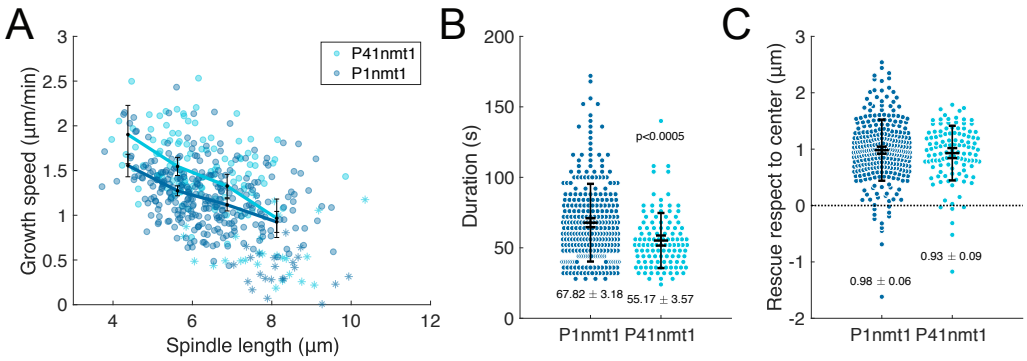

Figure S6: Comparison of microtubule dynamics in cells expressing GFP-mal3 from uninduced P1nmt1 and induced P41nmt1

Color code: cells expressing GFP-Mal3 from the P1nmt1 promoter in YE5S medium with thiamine (P1nmt1, dark blue), cells expressing GFP-Mal3 from the P41nmt1 promoter in EMM medium without thiamine (P41nmt1, light blue). **A)** Growth speed of events as a function of spindle length at rescue (or first time point of ambiguous events) in P1nmt1 and P41nmt1 cells. Events for which the start and finish could be unambiguously determined are shown as round dots, and are the same as in (A) and (B). Other events are shown as stars. **B)** Duration of microtubule growth events in P1nmt1 and P41nmt1 cells. **C)** Positions of rescues with respect to center in P1nmt1 and P41nmt1 cells. Thick lines represent average of binned data, error bars of average lines represent 95% confidence interval of the mean. Error bars in univariate scatter plots represent 95% confidence interval of the mean and standard deviation, text is mean ± 95% confidence interval. Each dot represents a single microtubule growth event. P1nmt1 data comes from 311 growth events, of which 289 were unambiguous, from 32 cells in 5 independent experiments. P41nmt1 data comes from 141 growth events, of which 115 were unambiguous, from 24 cells in 4 independent experiments. P1nmt1 data is the same as wild type from Fig. 3.8, and P41nmt1 data as wild type from Fig. 3.5C. Note that unlike in all other figures, P41nmt1 and P1nmt1 cells from which data of this figure comes from were not imaged simultaneously (see Methods).

Code	Genotype	Source
AP239	cdc25-22 leu1-32 h+	Lab collection
AP241	ade6-M216 ura4-D18 leu1-32 h+	Lab collection
TP1057	h- P1nmt1-GFP-mal3::KanMX	Lab collection
TP1058	h+ P1nmt1-GFPmal3::KanMX	Lab collection
TP1222	h.+ leu1-32 ura4-D18 ase1Δ::Nat	Lab collection
TP2810	h- P81nmt1-ase1::KanMX6 mCherry-atb2::HphMX6 leu1-32 ura4-D18	Lab collection
TP2829	h+ klp9Δ::NatMX6 leu1-32 ura4-D18 ade6-	Lab collection
TP2944	h+ mCherry-atb2::HphMX6 leu1:sid4-GFP leu1-32 ura4-D18 ade6-	Lab collection
TP3121	h- alp14Δ::ura4+ leu1-32 uraD-18	Lab collection
TP3288	h- cls1-3xGFP::KanMX6 mCherry-atb2::HphMX6	Lab collection
TP3293	h+ P1nmt1-cls1::KanMX6 leu1-32 ura4-D18 ade6-	Lab collection
TP4778	h- P81nmt1-ase1::KanMX6 leu1-32 ura4-D18	TP2810XAP241
TP4904	h+ P1nmt1-GFP-mal3::KanMX ase1Δ::Nat	TP1057xTP1222
TP4907	h- P1nmt1-GFP-mal3::KanMX klp9Δ::Nat	TP1057xTP2829
TP4914	h- P1nmt1-GFP-mal3::KanMX cdc25-22	TP1057xAP239
TP4984	h- P81nmt1-ase1::Nat leu1-32 ura4-D18	Marker switch TP4778
TP5017	h- P1nmt1-GFP-mal3::KanMX P81nmt1-ase1::Nat leu1-32 ura4-D18	TP4984xTP1058
TP5143	h+ P1nmt1-cls1::NatMX6 leu1-32 ura4-D18 ade6-	Marker switch TP3293
TP5147	h- cls1-3xGFP::KanMX6 mCherry-atb2::HphMX6 klp9Δ:Nat	TP3288xTP2829
TP5149	h- cls1-3xGFP::KanMX6 mCherry-atb2::HphMX6 cdc25-22	TP3288xAP239
TP5335	h- P41nmt1-cls1:KanMX6 leu1-32 ura4-D18	TP3354xAP241
TP5337	h- Nat::p81nmt1-cls1-3xGFP::KanMX6 mCherry-atb2::HphMX6	TP3288 transformed with pFA6a-NatMX6-Pnmt81 with oligos SR6.78, SR6.79
TP5333	h- P81nmt1-cls1:kanMX6 leu1-32 ura4-D18	TP3352xAP241
TP5355	h+ P41nmt1-GFP-mal3::KanMX ade6-M210 ura4-D18 leu1-32	TP5338xAP241
TP5362	h+ P1nmt1-GFP-mal3::KanMX ura4-D18	TP1057xAP241
TP5369	h+ cls1-3xGFP::KanMX6 mCherry-atb2::HphMX6 ura4-D18	TP3288xAP241
TP5392	h- P81nmt1-cls1::NatMX6 leu1-32 ura4-D18	Marker switch TP5333
TP5394	h- P41nmt1-cls1::NatMX6 leu1-32 ura4-D18	Marker switch TP5335
TP5395	h- P1nmt1-GFP-mal3::KanMX P81nmt1-cls1::NatMX6	TP5392xTP1058
TP5397	h+ P1nmt1-GFP-mal3::KanMX alp14Δ::ura4+ uraD-18	TP5362xTP3121
TP5403	h+ P41nmt1-GFP-mal3::KanMX P41nmt1-cls1::NatMX6 ade6-M210 ura4-D18 leu1-32	TP5355xTP5394
TP5418	h+ cls1-3xGFP::KanMX6 mCherry-atb2::HphMX6 P81nmt1-ase1::Nat	TP5369xTP4984

Table S1: Strain list

This table shows the genotypes of the strains used in this study, the parent strains, and the method used to produce them. For oligonucleotide sequences see Table S2.

Code	Name	Sequence
SR-6.78	5-Pnmt1.Cls1	GCGAGTTTTTAATATTCTCTTCGCAAACAACGCTTCACGTT TCTCTTGTTTCGCTCGTTTCATCAATATATTTGTAATTGGA ATTCGAGCTCGTTTAAAC
SR-6.79	3-Pnmt1.Cls1noTAG	TCAGTATATAGATGAAAGCTTTAGAATTTCATACCATTACT TTTAAGGAACTTTAAAAAATCTTGCGCATCCTTATCCGCCA TGATTTAACAAAGCGACTATA

Table S2: Oligonucleotides
Sequence of oligonucleotides referenced in Table S1

Figure	Code	Name	Panels
Fig. 3.2	TP3288	wt	-
Fig. 3.3	TP1057	wt	-
Fig. 3.4	TP1057	wt	-
	TP4904	ase1Δ	-
	TP5017	ase1^{off}	-
	TP5395	cls1^{off}	-
Fig. 3.5	TP1057	wt	B, D, E
	TP5143	cls1^{OE}	-
	TP5355	wt	A, C
	TP5403	cls1^{OE+}	-
Fig. 3.6	TP3288	wt	-
	TP5418	ase1^{off}	-
	TP5337	cls1-3xGFP^{off}	-
Fig. 3.7	TP3288	wt	A, F, G
	TP5147	klp9Δ	A, F, G
	TP1057	wt	B, C, D, E
	TP4907	klp9Δ	B, C, D, E
	TP4914	cdc25-22	C
Fig. 3.8	TP1057	wt	A, C, D
	TP4914	cdc25-22	A, C, D
	TP3288	wt	B, E, F, G
	TP5149	cdc25-22	B, E, F, G
Fig. 3.9	TP3288	wt	-
	TP5147	klp9Δ	-
	TP5149	cdc25-22	-
	TP5418	ase1^{off}	-

Table S3: Strains in figures
Code of strains used in the different figures, see Table S1 for genotypes.

Chapter 4

Bibliography

Bibliography

[1] A. Aher, M. Kok, A. Sharma, A. Rai, N. Olieric, R. Rodriguez-Garcia, E. A. Katrukha, T. Weinert, V. Olieric, L. C. Kapitein, M. O. Steinmetz, M. Dogterom, and A. Akhmanova. CLASP Suppresses Microtubule Catastrophes through a Single TOG Domain. *Developmental Cell*, 46(1):40–58.e8, jul 2018.

[2] A. Akhmanova and M. O. Steinmetz. Tracking the ends: A dynamic protein network controls the fate of microtubule tips, apr 2008.

[3] B. Akiyoshi, K. K. Sarangapani, A. F. Powers, C. R. Nelson, S. L. Reichow, H. Arellano-santoyo, T. Gonen, J. a. Ranish, C. L. Asbury, and S. Biggins. Tension directly stabilizes reconstituted kinetochore- microtubule attachments. *Nature*, 468(7323):576–579, 2010.

[4] J. Al-bassam and F. Chang. Regulation of microtubule dynamics by TOG-domain proteins XMAP215/Dis1 and CLASP. *Trends in Cell Biology*, 21(10):604–614, 2011.

[5] J. Al-bassam, H. Kim, G. Brouhard, A. V. Oijen, S. C. Harrison, and F. Chang. CLASP Promotes Microtubule Rescue by Recruiting Tubulin Dimers to the Microtubule. *Developmental Cell*, 19(2):245–258, 2010.

[6] J. Al-Bassam, H. Kim, I. Flor-Parra, N. Lal, H. Velji, and F. Chang. Fission yeast Alp14 is a dose-dependent plus end-tracking microtubule polymerase. *Molecular Biology of the Cell*, 23(15):2878–2890, aug 2012.

[7] B. Alberts, A. Johnson, J. Lewis, M. Raff, K. Robert, and P. Walter. *Molecular Biology of the Cell*. 2008.

[8] K. Aoki, Y. Nakaseko, K. Kinoshita, G. Goshima, and M. Yanagida. Cdc2 Phosphorylation of the Fission Yeast Dis1 Ensures Accurate Chromosome Segregation. *Current Biology*, 16(16):1627–1635, aug 2006.

[9] C. L. Asbury. Anaphase a: Disassembling microtubules move chromosomes toward spindle poles, mar 2017.

[10] J. Asthana, N. I. Cade, W. M. Lim, and T. Surrey. PRC1 and EB1 Binding Dynamics Reveal a Solidifying Central Spindle during Anaphase Compaction in Human Cells. *bioRxiv*, page 2020.07.09.195347, jul 2020.

[11] A. C. Badin-Larçon, C. Boscheron, J. M. Soleilhac, M. Piel, C. Mann, E. Denarier, A. Fourest-Lieuvin, L. Lafanechère, M. Bornens, and D. Job. Suppression of nuclear oscillations in Saccharomyces cerevisiae expressing Glu tubulin. *Proceedings of the National Academy of Sciences of the United States of America*, 101(15):5577–5582, apr 2004.

[12] J. Bähler, J. Q. Wu, M. S. Longtine, N. G. Shah, A. McKenzie, A. B. Steever, A. Wach, P. Philippsen, and J. R. Pringle. Heterologous modules for efficient and versatile PCR-based gene targeting in Schizosaccharomyces pombe. *Yeast*, 14(10):943–951, 1998.

[13] R. Behrens and P. Nurse. Roles of fission yeast tea1p in the localization of polarity factors and in organizing the microtubular cytoskeleton. *Journal of Cell Biology*, 157(5):783–793, may 2002.

[14] P. Bieling, S. Kandels-Lewis, I. A. Telley, J. Van Dijk, C. Janke, and T. Surrey. CLIP-170 tracks growing microtubule ends by dynamically recognizing composite EB1/tubulinbinding sites. *Journal of Cell Biology*, 183(7):1223–1233, dec 2008.

[15] P. Bieling, L. Laan, H. Schek, E. L. Munteanu, L. Sandblad, M. Dogterom, D. Brunner, and T. Surrey. Reconstitution of a microtubule plus-end tracking system in vitro. *Nature*, 450(7172):1100–1105, dec 2007.

[16] P. Bieling, I. A. Telley, and T. Surrey. A minimal midzone protein module controls formation and length of antiparallel microtubule overlaps. *Cell*, 142(3):420–432, 2010.

[17] R. Blackwell, C. Edelmaier, O. Sweezy-Schindler, A. Lamson, Z. R. Gergely, E. O'Toole, A. Crapo, L. E. Hough, J. R. McIntosh, M. A. Glaser, and M. D. Betterton. Physical determinants of bipolar mitotic spindle assembly and stability in fission yeast. *Science Advances*, 3(1):e1601603, 2017.

[18] K. A. Blake-Hodek, L. Cassimeris, and T. C. Huffaker. Regulation of microtubule dynamics by Bim1 and Bik1, the budding yeast members of the EB1 and CLIP-170 families of plus-end tracking proteins. *Molecular Biology of the Cell*, 21(12):2013–2023, jun 2010.

[19] I. B. Bouhlel, M. Ohta, A. Mayeux, N. Bordes, F. Dingli, J. Boulanger, G. V. Casquillas, D. Loew, P. T. Tran, M. Sato, and A. Paoletti. Cell cycle control of spindle pole body duplication and splitting by Sfi1 and Cdc31 in fission yeast. *Journal of Cell Science*, 128(8):1481–1493, apr 2015.

[20] H. Bowne-Anderson, M. Zanic, M. Kauer, and J. Howard. Microtubule dynamic instability: A new model with coupled GTP hydrolysis and multistep catastrophe. *BioEssays*, 35(5):452–461, may 2013.

[21] S. V. Bratman and F. Chang. Stabilization of Overlapping Microtubules by Fission Yeast CLASP. *Developmental Cell*, 13(6):812–827, dec 2007.

[22] M. Braun, Z. Lansky, G. Fink, F. Ruhnow, S. Diez, and M. E. Janson. Adaptive braking by Ase1 prevents overlapping microtubules from sliding completely apart. *Nature Cell Biology*, 13(10):1259–1264, sep 2011.

[23] M. Braun, Z. Lansky, A. Szuba, F. W. Schwarz, A. Mitra, M. Gao, A. Lüdecke, P. R. ten Wolde, and S. Diez. Changes in microtubule overlap length regulate kinesin-14-driven microtubule sliding. *Nature Chemical Biology*, 13(12):1245–1252, oct 2017.

[24] A. L. Brittle and H. Ohkura. Mini spindles, the XMAP215 homologue, suppresses pausing of interphase microtubules in Drosophila. *EMBO Journal*, 24(7):1387–1396, apr 2005.

[25] G. J. Brouhard, J. H. Stear, T. L. Noetzel, J. Al-Bassam, K. Kinoshita, S. C. Harrison, J. Howard, and A. A. Hyman. XMAP215 Is a Processive Microtubule Polymerase. *Cell*, 132(1):79–88, jan 2008.

[26] J. Brugués, V. Nuzzo, E. Mazur, and D. J. Needleman. Nucleation and transport organize microtubules in metaphase spindles. *Cell*, 149(3):554–64, apr 2012.

[27] L. Brun, B. Rupp, J. J. Ward, and F. Nédélec. A theory of microtubule catastrophes and their regulation. *Proceedings of the National Academy of Sciences of the United States of America*, 106(50):21173–21178, 2009.

[28] I. Brust-Mascher, G. Civelekoglu-Scholey, M. Kwon, A. Mogilner, and J. M. Scholey. Model for anaphase B: Role of three mitotic motors in a switch from poleward flux to spindle elongation. *Proceedings of the National Academy of Sciences of the United States of America*, 101(45):15938–15943, nov 2004.

[29] I. Brust-Mascher, G. Civelekoglu-Scholey, and J. M. Scholey. Mechanism for anaphase B: Evaluation of "slide-and-cluster" versus "slide-and-flux-or-elongate" models. *Biophysical Journal*, 108(8):2007–2018, apr 2015.

[30] K. S. Burbank, T. J. Mitchison, and D. S. Fisher. Slide-and-Cluster Models for Spindle Assembly. *Current Biology*, 17(16):1373–1383, aug 2007.

[31] R. G. Burns. ALPHA-TUBULIN, BETA-TUBULIN, AND GAMMA-TUBULINS - SEQUENCE COMPARISONS AND STRUCTURAL CONSTRAINTS. *Cell Motility and the Cytoskeleton*, 1991.

[32] K. E. Busch and D. Brunner. The Microtubule Plus End-Tracking Proteins mal3p and tip1p Cooperate for Cell-End Targeting of Interphase Microtubules. *Current Biology*, 14(7):548–559, apr 2004.

[33] K. E. Busch, J. Hayles, P. Nurse, and D. Brunner. Tea2p kinesin is involved in spatial microtubule organization by transporting Tip1p on microtubules. *Developmental Cell*, 6(6):831–843, jun 2004.

[34] P. Carvalho, M. L. Gupta, M. A. Hoyt, and D. Pellman. Cell cycle control of kinesin-mediated transport of Bik1 (CLIP-170) regulates microtubule stability and dynein activation. *Developmental Cell*, 6(6):815–829, jun 2004.

[35] L. Cassimeris, B. Becker, and B. Carney. TOGp regulates microtubule assembly and density during mitosis and contributes to chromosome directional instability. *Cell Motility and the Cytoskeleton*, 66(8):535–545, 2009.

[36] I. Castanon and M. González-Gaitán. Oriented cell division in vertebrate embryogenesis. *Current opinion in cell biology*, 23(6):697–704, dec 2011.

[37] N. Caudron, I. Arnal, E. Buhler, D. Job, and O. Valiron. Microtubule nucleation from stable tubulin oligomers. *Journal of Biological Chemistry*, 2002.

[38] F. Chang and S. G. Martin. Shaping fission yeast with microtubules., jul 2009.

[39] D. K. Cheerambathur, I. Brust-Mascher, G. Civelekoglu-Scholey, and J. M. Scholey. Dynamic partitioning of mitotic kinesin-5 cross-linkers between microtubule-bound and freely diffusing states. *The Journal of cell biology*, 182(3):429–36, aug 2008.

[40] Y. Chen and W. O. Hancock. Kinesin-5 is a microtubule polymerase. *Nature Communications*, 6(1):8160, dec 2015.

[41] D. Chretien, F. Metoz, F. Verde, E. Karsenti, and R. H. Wade. Lattice defects in microtubules: Protofilament numbers vary within individual microtubules. *Journal of Cell Biology*, 1992.

[42] D. Cimini, X. Wan, C. B. Hirel, and E. D. Salmon. Aurora Kinase Promotes Turnover of Kinetochore Microtubules to Reduce Chromosome Segregation Errors. *Current Biology*, 16(17):1711–1718, sep 2006.

[43] G. Civelekoglu-Scholey, D. J. Sharp, A. Mogilner, and J. M. Scholey. Model of chromosome motility in Drosophila embryos: Adaptation of a general mechanism for rapid mitosis. *Biophysical Journal*, 90(11):3966–3982, jun 2006.

[44] T. Courtheoux, G. Gay, Y. Gachet, and S. Tournier. Ase1/Prc1-dependent spindle elongation corrects merotely during anaphase in fission yeast. *Journal of Cell Biology*, 187(3):399–412, 2009.

[45] R. R. Daga, K. G. Lee, S. Bratman, S. Salas-Pino, and F. Chang. Self-organization of microtubule bundles in anucleate fission yeast cells. *Nature Cell Biology*, 8(10):1108–1113, 2006.

[46] P. P. D'Avino, V. Archambault, M. R. Przewloka, W. Zhang, K. S. Lilley, E. Laue, and D. M. Glover. Recruitment of polo kinase to spindle midzone during cytokinesis requires the Feo/Klp3A complex. *PLoS ONE*, 2(6), jun 2007.

[47] C. P. C. De Souza and S. A. Osmani. Mitosis, not just open or closed. *Eukaryotic cell*, 6(9):1521–7, sep 2007.

[48] F. Decker, D. Oriola, B. Dalton, and J. Brugués. Autocatalytic microtubule nucleation determines the size and mass of Xenopus laevis egg extract spindles. *eLife*, 7:e31149, jan 2018.

[49] A. Des Georges, M. Katsuki, D. R. Drummond, M. Osei, R. A. Cross, and L. A. Amos. Mal3, the Schizosaccharomyces pombe homolog of EB1, changes the microtubule lattice. *Nature Structural and Molecular Biology*, 15(10):1102–1108, oct 2008.

[50] D.-q. Q. Ding, Y. Chikashige, T. Haraguchi, and Y. Hiraoka. Oscillatory nuclear movement in fission yeast meiotic prophase is driven by astral microtubules, as revealed by continuous observation of chromosomes and microtubules in living cells. *Journal of cell science*, 111 (Pt 6:701–12, 1998.

[51] R. Ding, K. L. McDonald, and J. R. McIntosh. Three-dimensional reconstruction and analysis of mitotic spindles from the yeast, Schizosaccharomyces pombe. *The Journal of cell biology*, 120(1):141–51, jan 1993.

[52] R. Dixit, B. Barnett, J. E. Lazarus, M. Tokito, Y. E. Goldman, and E. L. Holzbaur. Microtubule plus-end tracking by CLIP-170 requires EB1. *Proceedings of the National Academy of Sciences of the United States of America*, 106(2):492–497, jan 2009.

[53] H. Ebina, L. Ji, and M. Sato. CLASP promotes microtubule bundling in metaphase spindle independently of Ase1/PRC1 in fission yeast. *Biology Open*, 8(10), 2019.

[54] C. J. Edelmaier, A. R. Lamson, Z. R. Gergely, S. Ansari, R. Blackwell, J. Richard McIntosh, M. A. Glaser, and M. D. Betterton. Mechanisms of chromosome biorientation and bipolar spindle assembly analyzed by computational modeling. *eLife*, 9, feb 2020.

[55] L. Evans, T. Mitchison, and M. Kirschner. Influence of the centrosome on the structure of nucleated microtubules. *Journal of Cell Biology*, 1985.

[56] I. Flor-Parra, A. B. Iglesias-Romero, and F. Chang. The XMAP215 Ortholog Alp14 Promotes Microtubule Nucleation in Fission Yeast. *Current Biology*, 28(11):1681–1691.e4, jun 2018.

[57] H. Flyvbjerg, T. E. Holy, and S. Leibler. Stochastic dynamics of microtubules: A model for caps and catastrophes. *Physical Review Letters*, 73(17):2372–2375, oct 1994.

[58] C. S. Fong, M. Sato, and T. Toda. Fission yeast Pcp1 links polo kinase-mediated mitotic entry to γ-tubulin-dependent spindle formation. *The EMBO Journal*, 29(1):120–130, jan 2010.

[59] A. D. Franck, A. F. Powers, D. R. Gestaut, T. Gonen, T. N. Davis, and C. L. Asbury. Tension applied through the Dam1 complex promotes microtubule elongation providing a direct mechanism for length control in mitosis. *Nature Cell Biology*, 9(7):832–837, 2007.

[60] C. Fu, J. J. Ward, I. Loiodice, G. Velve-Casquillas, F. J. Nedelec, and P. T. Tran. Phospho-Regulated Interaction between Kinesin-6 Klp9p and Microtubule Bundler Ase1p Promotes Spindle Elongation. *Developmental Cell*, 17(2):257–267, 2009.

[61] N. J. Ganem and D. A. Compton. Functional roles of poleward microtubule flux during mitosis. *Cell Cycle*, 5(5):481–485, 2006.

[62] N. J. Ganem, K. Upton, and D. A. Compton. Efficient mitosis in human cells lacking poleward microtubule flux. *Current Biology*, 2005.

[63] D. L. Gard, B. E. Becker, and S. Josh Romney. MAPping the eukaryotic tree of life: Structure, function, and evolution of the MAP215/Dis1 family of microtubule-associated proteins. *International Review of Cytology*, 239:179–272, jan 2004.

[64] D. L. Gard and M. W. Kirschner. A microtubule-associated protein from Xenopus eggs that specifically promotes assembly at the plus-end. *Journal of Cell Biology*, 105(5):2203–2215, nov 1987.

[65] M. K. Gardner, D. C. Bouck, L. V. Paliulis, J. B. Meehl, E. T. O'Toole, J. Haase, A. Soubry, A. P. Joglekar, M. Winey, E. D. Salmon, K. Bloom, and D. J. Odde. Chromosome Congression by Kinesin-5 Motor-Mediated Disassembly of Longer Kinetochore Microtubules. *Cell*, 135(5):894–906, 2008.

[66] M. K. Gardner, M. Zanic, C. Gell, V. Bormuth, and J. Howard. Depolymerizing kinesins Kip3 and MCAK shape cellular microtubule architecture by differential control of catastrophe. *Cell*, 147(5):1092–1103, nov 2011.

[67] I. Gaska, M. E. Armstrong, A. Alfieri, and S. Forth. The Mitotic Crosslinking Protein PRC1 Acts Like a Mechanical Dashpot to Resist Microtubule Sliding. *Developmental Cell*, pages 1–12, 2020.

[68] G. Gay, T. Courtheoux, C. Reyes, S. Tournier, and Y. Gachet. A stochastic model of kinetochore-microtubule attachment accurately describes fission yeast chromosome segregation. *Journal of Cell Biology*, 196(6):757–774, mar 2012.

[69] E. A. Geyer, M. P. Miller, C. A. Brautigam, S. Biggins, and L. M. Rice. Design principles of a microtubule polymerase. *eLife*, 7, jun 2018.

[70] M. Giam and G. Rancati. Aneuploidy and chromosomal instability in cancer: A jackpot to chaos, 2015.

[71] F. Gittes, B. Mickey, J. Nettleton, and J. Howard. Flexural rigidity of microtubules and actin filaments measured from thermal fluctuations in shape. *Journal of Cell Biology*, 120(4):923–934, feb 1993.

[72] S. Goldstone, C. Reyes, G. Gay, T. Courthéoux, M. Dubarry, S. Tournier, and Y. Gachet. Tip1/clip-170 protein is required for correct chromosome poleward movement in fission yeast. *PLoS ONE*, 5(5), 2010.

[73] G. Goshima, R. Wollman, N. Stuurman, J. M. Scholey, and R. D. Vale. Length control of the metaphase spindle. *Current Biology*, 15(22):1979–1988, nov 2005.

[74] A. Goupil, M. Nano, G. Letort, S. Gemble, F. Edwards, O. Goundiam, D. Gogendeau, C. Pennetier, and R. Basto. Chromosomes function as a barrier to mitotic spindle bipolarity in polyploid cells. *The Journal of cell biology*, 219(4), apr 2020.

[75] S. M. Gouveia and A. Akhmanova. *Cell and molecular biology of microtubule plus end tracking proteins. End binding proteins and their partners*, volume 285. Elsevier Inc., 1 edition, 2010.

[76] R. A. Green, R. Wollman, and K. B. Kaplan. APC and EB1 function together in mitosis to regulate spindle dynamics and chromosome alignment. *Molecular Biology of the Cell*, 16(10):4609–4622, oct 2005.

[77] J. Gregan, S. Polakova, L. Zhang, I. M. Tolić-Nørrelykke, and D. Cimini. Merotelic kinetochore attachment: Causes and effects, jun 2011.

[78] P. M. Grissom, T. Fiedler, E. L. Grishchuk, D. Nicastro, R. R. West, and J. Richard McIntosh. Kinesin-8 from Fission Yeast: A Heterodimeric, Plus-End–directed Motor that Can Couple Microtubule Depolymerization to Cargo Movement. *Molecular Biology of the Cell*, 20(3):963–972, feb 2009.

[79] A. A. Guerrero, C. Martínez-A, and K. H. van Wely. Merotelic attachments and non-homologous end joining are the basis of chromosomal instability. *Cell Division*, 5(May), 2010.

[80] D. Halpin, P. Kalab, J. Wang, K. Weis, and R. Heald. Mitotic Spindle Assembly around RCC1-Coated Beads in Xenopus Egg Extracts. *PLoS Biology*, 9(12):e1001225, dec 2011.

[81] J. Hannabuss, M. Lera-Ramirez, N. I. Cade, F. J. Fourniol, F. Nédélec, and T. Surrey. Self-Organization of Minimal Anaphase Spindle Midzone Bundles. *Current Biology*, 29(13):2120–2130.e7, 2019.

[82] E. Hannak and R. Heald. Xorbit/CLASP links dynamic microtubules to chromosomes in the Xenopus meiotic spindle. *Journal of Cell Biology*, 172(1):19–25, 2006.

[83] Y. Hara and A. Kimura. Cell-Size-Dependent Spindle Elongation in the Caenorhabditis elegans Early Embryo. *Current Biology*, 19(18):1549–1554, 2009.

[84] R. Heald and A. Khodjakov. Thirty years of search and capture: The complex simplicity of mitotic spindle assembly. *Journal of Cell Biology*, 211(6):1103–1111, 2015.

[85] K. J. Helmke and R. Heald. TPX2 levels modulate meiotic spindle size and architecture in Xenopus egg extracts. *Journal of Cell Biology*, 206(3):385–393, 2014.

[86] C. Hentrich and T. Surrey. Microtubule organization by the antagonistic mitotic motors kinesin-5 and kinesin-14. *Journal of Cell Biology*, 189(3):465–480, may 2010.

[87] A. Hepperla, P. Willey, C. Coombes, B. Schuster, M. Gerami-Nejad, M. McClellan, S. Mukherjee, J. Fox, M. Winey, D. Odde, E. O'Toole, and M. Gardner. Minus-End-Directed Kinesin-14 Motors Align Antiparallel Microtubules to Control Metaphase Spindle Length. *Developmental Cell*, 31(1):61–72, oct 2014.

[88] P. Hinow, V. Rezania, and J. A. Tuszyński. Continuous model for microtubule dynamics with catastrophe, rescue, and nucleation processes. *Physical Review E - Statistical, Nonlinear, and Soft Matter Physics*, 80(3):1–10, 2009.

[89] A. J. Holland and D. W. Cleveland. Boveri revisited: Chromosomal instability, aneuploidy and tumorigenesis, 2009.

[90] S. Honnappa, S. M. Gouveia, A. Weisbrich, F. F. Damberger, N. S. Bhavesh, H. Jawhari, I. Grigoriev, F. J. van Rijssel, R. M. Buey, A. Lawera, I. Jelesarov, F. K. Winkler, K. Wüthrich, A. Akhmanova, and M. O. Steinmetz. An EB1-Binding Motif Acts as a Microtubule Tip Localization Signal. *Cell*, 138(2):366–376, jul 2009.

[91] K. S. Hsu and T. Toda. Ndc80 internal loop interacts with Dis1/TOG to ensure proper kinetochore-spindle attachment in fission yeast. *Current Biology*, 21(3):214–220, feb 2011.

[92] F. Hussmann, D. R. Drummond, D. R. Peet, D. S. Martin, and R. A. Cross. Alp7/TACC-Alp14/TOG generates long-lived, fast-growing MTs by an unconventional mechanism. *Scientific Reports*, 6(1):1–15, feb 2016.

[93] A. A. Hyman, S. Salser, D. N. Drechsel, N. Unwin, and T. J. Mitchison. Role of GTP hydrolysis in microtubule dynamics: Information from a slowly hydrolyzable analogue, GMPCPP. *Molecular Biology of the Cell*, 1992.

[94] M. Jagrić, P. Risteski, J. Martinčić, A. Milas, and I. M. Tolić. Optogenetic control of PRC1 reveals its role in kinetochore alignment at the metaphase plate. *bioRxiv*, page 865394, dec 2019.

[95] M. E. Janson, R. Loughlin, I. Loïodice, C. Fu, D. Brunner, F. J. Nédélec, and P. T. Tran. Crosslinkers and motors organize dynamic microtubules to form stable bipolar arrays in fission yeast. *Cell*, 128(2):357–68, jan 2007.

[96] S. L. Jaspersen and S. Ghosh. Nuclear envelope insertion of spindle pole bodies and nuclear pore complexes. *Nucleus (United States)*, 3(3):226, 2012.

[97] D. Johann, D. Goswami, and K. Kruse. Assembly of bipolar microtubule structures by passive cross-linkers and molecular motors. *Physical Review E*, 93(6):1–12, 2016.

[98] A. W. Jongerius. *Control mechanisms of microtubule overlap regions*. PhD thesis, 2017.

[99] L. C. Kapitein, M. E. Janson, S. M. van den Wildenberg, C. C. Hoogenraad, C. F. Schmidt, and E. J. Peterman. Microtubule-Driven Multimerization Recruits ase1p onto Overlapping Microtubules. *Current Biology*, 18(21):1713–1717, nov 2008.

[100] L. C. Kapitein, E. J. Peterman, B. H. Kwok, J. H. Kim, T. M. Kapoor, and C. F. Schmidt. The bipolar mitotic kinesin Eg5 moves on both microtubules that it crosslinks. *Nature*, 435(7038):114–118, may 2005.

[101] M. Katsuki, D. R. Drummond, M. Osei, and R. A. Cross. Mal3 masks catastrophe events in Schizosaccharomyces pombe microtubules by inhibiting shrinkage and promotingrescue. *Journal of Biological Chemistry*, 284(43):29246–29250, oct 2009.

[102] S. Kawai, W. Hashimoto, and K. Murata. Transformation of Saccharomyces cerevisiae and other fungi: methods and possible underlying mechanism., 2010.

[103] A. Khodjakov, S. La Terra, and F. Chang. Laser Microsurgery in Fission Yeast: Role of the Mitotic Spindle Midzone in Anaphase B. *Current Biology*, 14(15):1330–1340, 2004.

[104] M. Kirschner and T. Mitchison. Beyond self-assembly: From microtubules to morphogenesis. *Cell*, 45(3):329–342, 1986.

[105] M. Kitagawa, S. Y. S. Fung, U. F. S. Hameed, H. Goto, M. Inagaki, and S. H. Lee. Cdk1 coordinates timely activation of MKlp2 kinesin with relocation of the chromosome passenger complex for cytokinesis. *Cell Reports*, 7(1):166–179, oct 2014.

[106] E. Kitamura, K. Tanaka, S. Komoto, Y. Kitamura, C. Antony, and T. U. Tanaka. Kinetochores Generate Microtubules with Distal Plus Ends: Their Roles and Limited Lifetime in Mitosis. *Developmental Cell*, 18(2):248–259, feb 2010.

[107] D. Kitazawa, T. Matsuo, K. Kaizuka, C. Miyauchi, D. Hayashi, and Y. H. Inoue. Orbit/CLASP is required for myosin accumulation at the cleavage furrow in Drosophila male meiosis. *PLoS ONE*, 9(5), may 2014.

[108] A. L. Knowlton, W. Lan, and P. T. Stukenberg. Aurora B Is Enriched at Merotelic Attachment Sites, Where It Regulates MCAK. *Current Biology*, 16(17):1705–1710, sep 2006.

[109] J. M. Kollman, A. Merdes, L. Mourey, and D. A. Agard. Microtubule nucleation by γ-tubulin complexes, nov 2011.

[110] Y. Komarova, C. O. De Groot, I. Grigoriev, S. M. Gouveia, E. L. Munteanu, J. M. Schober, S. Honnappa, R. M. Buey, C. C. Hoogenraad, M. Dogterom, G. G. Borisy, M. O. Steinmetz, and A. Akhmanova. Mammalian end binding proteins control persistent microtubule growth. *Journal of Cell Biology*, 184(5):691–706, mar 2009.

[111] L. K. Krüger, J.-L. Sanchez, A. Paoletti, and P. T. Tran. Kinesin-6 regulates cell-size-dependent spindle elongation velocity to keep mitosis duration constant in fission yeast. *eLife*, 8:1–22, 2019.

[112] D. Kuchnir Fygenson, H. Flyvbjerg, K. Sneppen, A. Libchaber, and S. Leibler. Spontaneous nucleation of microtubules, 1995.

[113] B. Lacroix, G. Letort, L. Pitayu, J. Sallé, M. Stefanutti, G. Maton, A. M. Ladouceur, J. C. Canman, P. S. Maddox, A. S. Maddox, N. Minc, F. Nédélec, and J. Dumont. Microtubule Dynamics Scale with Cell Size to Set Spindle Length and Assembly Timing. *Developmental Cell*, 45(4):496–511.e6, may 2018.

[114] Z. Lansky, M. Braun, A. Lüdecke, M. Schlierf, P. R. Ten Wolde, M. E. Janson, and S. Diez. Diffusible crosslinkers generate directed forces in microtubule networks. *Cell*, 160(6):1159–1168, 2015.

[115] A. Leary, S. Sim, E. Nazarova, K. Shulist, R. Genthial, S. K. Yang, K. H. Bui, P. Francois, and J. Vogel. Successive Kinesin-5 Microtubule Crosslinking and Sliding Promote Fast, Irreversible Formation of a Stereotyped Bipolar Spindle. *Current biology : CB*, pages 1–13, 2019.

[116] C. L. Lemos, P. Sampaio, H. Maiato, M. Costa, L. V. Omel'yanchuk, V. Liberal, and C. E. Sunkel. Mast, a conserved microtubule-associated protein required for bipolar mitotic spindle organization. *EMBO Journal*, 19(14):3668–3682, 2000.

[117] M. Lera-Ramirez and F. J. Nédélec. Theory of antiparallel microtubule overlap stabilization by motors and diffusible crosslinkers. *Cytoskeleton*, 76(11-12):600–610, 2019.

[118] J. Liu, Z. Wang, K. Jiang, L. Zhang, L. Zhao, S. Hua, F. Yan, Y. Yang, D. Wang, C. Fu, X. Ding, Z. Guo, and X. Yao. PRC1 cooperates with CLASP1 to organize central spindle plasticity in mitosis. *The Journal of biological chemistry*, 284(34):23059–71, aug 2009.

[119] I. Loiodice, M. E. Janson, P. Tavormina, S. Schaub, D. Bhatt, R. Cochran, J. Czupryna, C. Fu, and P. T. Tran. Quantifying tubulin concentration and microtubule number throughout the fission yeast cell cycle. *Biomolecules*, 9(3):1–14, 2019.

[120] I. Loïodice, J. Staub, T. G. Setty, N.-P. T. Nguyen, A. Paoletti, and P. T. Tran. Ase1p Organizes Antiparallel Microtubule Arrays during Interphase and Mitosis in Fission Yeast. *Molecular Biology of the Cell*, 16(4):1756–1768, apr 2005.

[121] A. Loncar, S. A. Rincon, M. L. Ramirez, A. Paoletti, and P. T. Tran. Kinesin-14 family proteins and microtubule dynamics define S. pombe mitotic and meiotic spindle assembly, and elongation. *Journal of Cell Science*, 133(11), 2020.

[122] R. Loughlin, R. Heald, and F. Nédélec. A computational model predicts Xenopus meiotic spindle organization. *Journal of Cell Biology*, 191(7):1239–1249, 2010.

[123] R. Loughlin, J. D. Wilbur, F. J. McNally, F. J. Nédélec, and R. Heald. Katanin contributes to interspecies spindle length scaling in xenopus. *Cell*, 147(6):1397–1407, 2011.

[124] A. Lüdecke, A.-M. Seidel, M. Braun, Z. Lansky, and S. Diez. Diffusive tail anchorage determines velocity and force produced by kinesin-14 between crosslinked microtubules. *Nature Communications*, 9(1):2214, dec 2018.

[125] A. Mallavarapu, K. Sawin, and T. Mitchison. A switch in microtubule dynamics at the onset of anaphase B in the mitotic spindle of Schizosaccharomyces pombe. 1999.

[126] N. Mani, S. Jiang, and R. Subramanian. Differential Regulation of Single Microtubules and Cross-linked Bundles by a Minimal Three-Protein Module. *bioRxiv*, (i):2020.03.05.979864, 2020.

[127] H. Mary, J. Fouchard, G. Gay, C. Reyes, T. Gauthier, C. Gruget, J. Pécréaux, S. Tournier, and Y. Gachet. Fission yeast kinesin-8 controls chromosome congression independently of oscillations. *Journal of Cell Science*, 128(20):3720–3730, 2015.

[128] D. N. Mastronarde, K. L. McDonald, R. Ding, and J. R. McIntosh. Interpolar spindle microtubules in PTK cells. *Journal of Cell Biology*, 123(6 I):1475–1489, 1993.

[129] J. Mata and P. Nurse. tea1 and the microtubular cytoskeleton are important for generating global spatial order within the fission yeast cell. *Cell*, 89(6):939–949, jun 1997.

[130] A. Mathur, S. R. Correia, S. Dmitrieff, R. Gibeaux, I. Kalinina, T. Quidwai, J. Ries, and F. Nedelec. Cytoskeleton mechanics determine resting size and activation dynamics of platelets. *bioRxiv*, page 413377, sep 2018.

[131] Y. Matsuo, S. P. Maurer, M. Yukawa, S. Zakian, M. R. Singleton, T. Surrey, and T. Toda. An unconventional interaction between Dis1/TOG and Mal3/EB1 in fission yeast promotes the fidelity of chromosome segregation. *J Cell Sci*, 129(24):4592–4606, dec 2016.

[132] J. R. McIntosh, E. L. Grishchuk, M. K. Morphew, A. K. Efremov, K. Zhudenkov, V. A. Volkov, I. M. Cheeseman, A. Desai, D. N. Mastronarde, and F. I. Ataullakhanov. Fibrils Connect Microtubule Tips with Kinetochores: A Mechanism to Couple Tubulin Dynamics to Chromosome Motion. *Cell*, 135(2):322–333, oct 2008.

[133] J. C. Meadows, T. C. Lancaster, G. J. Buttrick, A. M. Sochaj, L. J. Messin, M. del Mar Mora-Santos, K. G. Hardwick, and J. B. Millar. Identification of a Sgo2-Dependent but Mad2-Independent Pathway Controlling Anaphase Onset in Fission Yeast. *Cell Reports*, 18(6):1422–1433, feb 2017.

[134] J. C. Meadows, L. J. Messin, A. Kamnev, T. C. Lancaster, M. K. Balasubramanian, R. A. Cross, and J. B. Millar. Opposing kinesin complexes queue at plus tips to ensure microtubule catastrophe at cell ends. *EMBO reports*, 19(11):1–12, 2018.

[135] E. Meyhöfer and J. Howard. The force generated by a single kinesin molecule against an elastic load. *Proceedings of the National Academy of Sciences of the United States of America*, 92(January):574–578, 1995.

[136] Y. Mimori-Kiyosue, I. Grigoriev, G. Lansbergen, H. Sasaki, C. Matsui, F. Severin, N. Galjart, F. Grosveld, I. Vorobjev, S. Tsukita, and A. Akhmanova. CLASP1 and CLASP2 bind to EB1 and regulate microtubule plus-end dynamics at the cell cortex. *Journal of Cell Biology*, 168(1):141–153, jan 2005.

[137] T. Mitchison and M. Kirschner. Dynamic instability of microtubule growth. *Nature*, 1984.

[138] D. T. Miyamoto, Z. E. Perlman, K. S. Burbank, A. C. Groen, and T. J. Mitchison. The kinesin Eg5 drives poleward microtubule flux in Xenopus laevis egg extract spindles. *Journal of Cell Biology*, 167(5):813–818, dec 2004.

[139] C. Mollinari, J. P. Kleman, W. Jiang, G. Schoehn, T. Hunter, and R. L. Margolis. PRC1 is a microtubule binding and bundling protein essential to maintain the mitotic spindle midzone. *Journal of Cell Biology*, 157(7):1175–1186, 2002.

[140] J. K. Moore, M. D. Stuchell-Brereton, and J. A. Cooper. Function of dynein in budding yeast: Mitotic spindle positioning in a polarized cell. *Cell Motility and the Cytoskeleton*, 66(8):546–555, 2009.

[141] T. Moriwaki and G. Goshima. Five factors can reconstitute all three phases of microtubule polymerization dynamics, nov 2016.

[142] A. Musacchio and E. D. Salmon. The spindle-assembly checkpoint in space and time, may 2007.

[143] K. Nabeshima, T. Nakagawa, A. F. Straight, A. Murray, Y. Chikashige, Y. M. Yamashita, Y. Hiraoka, and M. Yanagida. Dynamics of centromeres during metaphase-anaphase transition in fission yeast: Dis1 is implicated in force balance in metaphase bipolar spindle. *Molecular Biology of the Cell*, 9(11):3211–3225, oct 1998.

[144] F. Nédélec. Computer simulations reveal motor properties generating stable antiparallel microtubule interactions. *Journal of Cell Biology*, 158(6):1005–1015, sep 2002.

[145] F. Nedelec and D. Foethke. Collective Langevin dynamics of flexible cytoskeletal fibers. *New Journal of Physics*, 9(11):427–427, nov 2007.

[146] P. A. Nguyen, C. M. Field, and T. J. Mitchison. Prc1E and Kif4A control microtubule organization within and between large Xenopus egg asters. *Molecular Biology of the Cell*, 29(3):304–316, feb 2018.

[147] X. Niu, F. Zheng, and C. Fu. The concerted actions of Tip1/CLIP-170, Klp5/Kinesin-8, and Alp14/XMAP215 regulate microtubule catastrophe at the cell end. *Journal of molecular cell biology*, 11(11):956–966, 2019.

[148] E. Nogales, M. Whittaker, R. A. Milligan, and K. H. Downing. High-resolution model of the microtubule. *Cell*, 1999.

[149] E. Nogales, S. G. Wolf, and K. H. Downing. Structure of the $\alpha\beta$ tubulin dimer by electron crystallography. *Nature*, 1998.

[150] S. R. Norris, S. Jung, P. Singh, C. E. Strothman, A. L. Erwin, M. D. Ohi, M. Zanic, and R. Ohi. Microtubule minus-end aster organization is driven by processive HSET-tubulin clusters. *Nature Communications*, 9(1):1–14, 2018.

[151] R. Nunes Bastos, S. R. Gandhi, R. D. Baron, U. Gruneberg, E. A. Nigg, and F. A. Barr. Aurora B suppresses microtubule dynamics and limits central spindle size by locally activating KIF4A. *The Journal of cell biology*, 202(4):605–21, aug 2013.

[152] Z. T. Olmsted, A. G. Colliver, T. D. Riehlman, and J. L. Paluh. Kinesin-14 and kinesin-5 antagonistically regulate microtubule nucleation by γ-TuRC in yeast and human cells. *Nature Communications*, 5:5339, oct 2014.

[153] Y. Ovechkina and L. Wordeman. Unconventional Motoring: An Overview of the Kin C and Kin I Kinesins. *Traffic*, 4(6):367–375, jun 2003.

[154] R. Padinhateeri, A. B. Kolomeisky, and D. Lacoste. Random hydrolysis controls the dynamic instability of microtubules. *Biophysical Journal*, 102(6):1274–1283, 2012.

[155] M. C. Pamula, L. Carlini, S. Forth, P. Verma, S. Suresh, W. R. Legant, A. Khodjakov, E. Betzig, and T. M. Kapoor. High-resolution imaging reveals how the spindle midzone impacts chromosome movement. *The Journal of cell biology*, 218(8):2529–2544, 2019.

[156] A. L. Pereira, A. J. Pereira, A. R. Maia, K. Drabek, C. L. Sayas, P. J. Hergert, M. Lince-Faria, I. Matos, C. Duque, T. Stepanova, C. L. Rieder, W. C. Earnshaw, N. Galjart, and H. Maiato. Mammalian CLASP1 and CLASP2 cooperate to ensure mitotic fidelity by regulating spindle and kinetochore function. *Molecular Biology of the Cell*, 17(10):4526–4542, oct 2006.

[157] J. M. Peters. The anaphase promoting complex/cyclosome: A machine designed to destroy, 2006.

[158] M. Piel and P. T. Tran. Cell Shape and Cell Division in Fission Yeast, sep 2009.

[159] B. Polak, P. Risteski, S. Lesjak, and I. M. Tolić. PRC1-labeled microtubule bundles and kinetochore pairs show one-to-one association in metaphase. *EMBO reports*, 18(2):217–230, 2017.

[160] D. Portran, M. Zoccoler, J. Gaillard, V. Stoppin-Mellet, E. Neumann, I. Arnal, J. L. Martiel, and M. Vantard. MAP65/Ase1 promote microtubule flexibility. *Molecular Biology of the Cell*, 24(12):1964–1973, 2013.

[161] S. B. Reber, J. Baumgart, P. O. Widlund, A. Pozniakovsky, J. Howard, A. A. Hyman, and F. Jülicher. XMAP215 activity sets spindle length by controlling the total mass of spindle microtubules. *Nature Cell Biology*, 15(9):1116–1122, 2013.

[162] M. Rehberg and R. Gräf. Dictyostelium EB1 is a genuine centrosomal component required for proper spindle formation. *Molecular Biology of the Cell*, 2002.

[163] E. Rieckhoff, F. Berndt, S. Golfier, F. Decker, M. Elsner, K. Ishihara, and J. Brugues. Spindle scaling is governed by cell boundary regulation of microtubule nucleation. *bioRxiv*, page 2020.06.15.136937, jun 2020.

[164] S. A. Rincon, A. Lamson, R. Blackwell, V. Syrovatkina, V. Fraisier, A. Paoletti, M. D. Betterton, and P. T. Tran. Kinesin-5-independent mitotic spindle assembly requires the antiparallel microtubule crosslinker Ase1 in fission yeast. *Nature Communications*, 8:15286, may 2017.

[165] S. L. Rogers, G. C. Rogers, D. J. Sharp, and R. D. Vale. Drosophila EB1 is important for proper assembly, dynamics, and positioning of the mitotic spindle. *Journal of Cell Biology*, 2002.

[166] J. Roostalu, E. Schiebel, and A. Khmelinskii. Cell cycle control of spindle elongation. *Cell Cycle*, 9(6):1084–1090, 2010.

[167] J. Roostalu, C. Thomas, N. I. Cade, S. Kunzelmann, I. A. Taylor, and T. Surrey. The speed of GTP hydrolysis determines GTP cap size and controls microtubule stability. *eLife*, 9, feb 2020.

[168] H. Roque, J. J. Ward, L. Murrells, D. Brunner, and C. Antony. The fission yeast XMAP215 homolog dis1p is involved in microtubule bundle organization. *PLoS ONE*, 5(12), 2010.

[169] M. J. Sagolla, S. Uzawa, and W. Z. Cande. Individual microtubule dynamics contribute to the function of mitotic and cytoplasmic arrays in fission yeast. *Journal of cell science*, 116(Pt 24):4891–903, dec 2003.

[170] W. Saunders, V. Lengyel, and M. A. Hoyt. Mitotic spindle function in Saccharomyces cerevisiae requires a balance between different types of kinesin-related motors. *Molecular Biology of the Cell*, 8(6):1025–1033, 1997.

[171] W. S. Saunders and M. A. Hoyt. Kinesin-related proteins required for structural integrity of the mitotic spindle. *Cell*, 70(3):451–458, aug 1992.

[172] K. Scheffler, P. Recouvreux, A. Paoletti, and P. T. Tran. Oscillatory AAA+ ATPase Knk1 constitutes a novel morphogenetic pathway in fission yeast. *Proceedings of the National Academy of Sciences of the United States of America*, 111(50):17899–17904, 2014.

[173] E. Schiebel. γ-tubulin complexes: Binding to the centrosome, regulation and microtubule nucleation, feb 2000.

[174] M. Schliwa and G. Woehlke. Molecular motors, apr 2003.

[175] J. Scholey, G. Civelekoglu-Scholey, I. Brust-Mascher, J. M. Scholey, G. Civelekoglu-Scholey, and I. Brust-Mascher. Anaphase B. *Biology*, 5(4):51, dec 2016.

[176] S. C. Schuyler, J. Y. Liu, and D. Pellman. The molecular function of Ase1p: Evidence for a MAP-dependent midzone-specific spindle matrix. *Journal of Cell Biology*, 160(4):517–528, 2003.

[177] Y. Shimamoto, S. Forth, and T. M. Kapoor. Measuring Pushing and Braking Forces Generated by Ensembles of Kinesin-5 Crosslinking Two Microtubules. *Developmental cell*, 34(6):669–81, sep 2015.

[178] A. Sousa, R. Reis, P. Sampaio, and C. E. Sunkel. The Drosophila CLASP homologue, mast/orbit regulates the dynamic behaviour of interphase microtubules by promoting the pause state. *Cell Motility and the Cytoskeleton*, 64(8):605–620, 2007.

[179] R. Subramanian, S. C. Ti, L. Tan, S. A. Darst, and T. M. Kapoor. Marking and measuring single microtubules by PRC1 and kinesin-4. *Cell*, 154(2):377–390, 2013.

[180] R. Subramanian, E. M. Wilson-Kubalek, C. P. Arthur, M. J. Bick, E. A. Campbell, S. A. Darst, R. A. Milligan, and T. M. Kapoor. Insights into Antiparallel Microtubule Crosslinking by PRC1, a Conserved Nonmotor Microtubule Binding Protein. *Cell*, 142(3):433–443, aug 2010.

[181] V. Syrovatkina, C. Fu, and P. T. Tran. Antagonistic Spindle Motors and MAPs Regulate Metaphase Spindle Length and Chromosome Segregation. 2013.

[182] T. U. Tanaka, N. Rachidi, C. Janke, G. Pereira, M. Galova, E. Schiebel, M. J. Stark, and K. Nasmyth. Evidence that the Ipl1-Sli15 (Aurora Kinase-INCENP) complex promotes chromosome bi-orientation by altering kinetochore-spindle pole connections. *Cell*, 108(3):317–329, feb 2002.

[183] M. E. Tanenbaum and R. H. Medema. Mechanisms of Centrosome Separation and Bipolar Spindle Assembly, 2010.

[184] N. H. Tang, H. Takada, K. S. Hsu, and T. Toda. The internal loop of fission yeast Ndc80 binds Alp7/TACC-Alp14/TOG and ensures proper chromosome attachment. *Molecular Biology of the Cell*, 24(8):1122–1133, apr 2013.

[185] N. H. Tang and T. Toda. Alp7/TACC recruits kinesin-8-PP1 to the Ndc80 kinetochore protein for timely mitotic progression and chromosome movement. *Journal of Cell Science*, 128(2):354–363, jan 2015.

[186] A. Thawani, R. S. Kadzik, and S. Petry. XMAP215 is a microtubule nucleation factor that functions synergistically with the γ-tubulin ring complex. *Nature Cell Biology*, 20(5):575–585, may 2018.

[187] S. L. Thompson, S. F. Bakhoum, and D. A. Compton. Mechanisms of Chromosomal Instability, 2010.

[188] L. G. Tilney. How microtubule patterns are generated: The relative importance of nucleation and bridging of microtubules in the formation of the axoneme of raphidiophrys. *Journal of Cell Biology*, 51(3):837–854, 1971.

[189] M. M. Tirado and J. García De La Torre. Translational friction coefficients of rigid, symmetric top macromolecules. Application to circular cylinders. *The Journal of Chemical Physics*, 71(6):2581–2587, 1979.

[190] C. Tischer, D. Brunner, and M. Dogterom. Force- and kinesin-8-dependent effects in the spatial regulation of fission yeast microtubule dynamics. *Molecular Systems Biology*, 5(250):1–10, 2009.

[191] I. M. Tolić-Nørrelykke, L. Sacconi, G. Thon, and F. S. Pavone. Positioning and Elongation of the Fission Yeast Spindle by Microtubule-Based Pushing. 2004.

[192] P. T. Tran, L. Marsh, V. Doye, S. Inoué, and F. Chang. A mechanism for nuclear positioning in fission yeast based on microtubule pushing. *Journal of Cell Biology*, 153(2):397–411, apr 2001.

[193] P. T. Tran, A. Paoletti, and F. Chang. Imaging green fluorescent protein fusions in living fission yeast cells. *Methods*, 33(3):220–225, jul 2004.

[194] M. Uteng, C. Hentrich, K. Miura, P. Bieling, and T. Surrey. Poleward transport of Eg5 by dynein-dynactin in Xenopus laevis egg extract spindles. *Journal of Cell Biology*, 182(4):715–726, aug 2008.

[195] R. D. Vale and R. J. Fletterick. THE DESIGN PLAN OF KINESIN MOTORS. *Annual Review of Cell and Developmental Biology*, 1997.

[196] R. D. Vale, F. Malik, and D. Brown. Directional instability of microtubule transport in the presence of kinesin and dynein, two opposite polarity motor proteins. *Journal of Cell Biology*, 119(6):1589–1596, 1992.

[197] K. J. Verhey and J. W. Hammond. Traffic control: Regulation of kinesin motors. *Nature Reviews Molecular Cell Biology*, 10(11):765–777, 2009.

[198] F. Vernì, M. P. Somma, K. C. Gunsalus, S. Bonaccorsi, G. Belloni, M. L. Goldberg, and M. Gatti. Feo, the Drosophila homolog of PRC1, is required for central-spindle formation and cytokinesis. *Current Biology*, 14(17):1569–1575, sep 2004.

[199] B. Vitre, F. M. Coquelle, C. Heichette, C. Garnier, D. Chrétien, and I. Arnal. EB1 regulates microtubule dynamics and tubulin sheet closure in vitro. *Nature Cell Biology*, 10(4):415–421, mar 2008.

[200] O. Von Loeffelholz, N. A. Venables, D. R. Drummond, M. Katsuki, R. Cross, and C. A. Moores. Nucleotide- and Mal3-dependent changes in fission yeast microtubules suggest a structural plasticity view of dynamics. *Nature Communications*, 8(1):1–13, dec 2017.

[201] W. A. Voter, E. T. O'Brien, and H. P. Erickson. Dilution-induced disassembly of microtubules: Relation to dynamic instability and the GTP cap. *Cell Motility and the Cytoskeleton*, 1991.

[202] K. Vukušić, R. Buđa, I. Ponjavić, P. Risteski, and I. M. Tolić. Mitotic spindle elongation is driven by joint microtubule sliding action of kinesins KIF4A and EG5. *bioRxiv*, page 863381, 2019.

[203] R. A. Walker, S. Inoue, and E. D. Salmon. Asymmetric behavior of severed microtubule ends after ultraviolet-microbeam irradiation of individual microtubules in vitro. *Journal of Cell Biology*, 1989.

[204] R. A. Walker, E. T. O'Brien, N. K. Pryer, M. F. Soboeiro, W. A. Voter, H. P. Erickson, and E. D. Salmon. Dynamic instability of individual microtubules analyzed by video light microscopy: rate constants and transition frequencies. *The Journal of cell biology*, 1988.

[205] R. A. Walker, N. K. Pryer, and E. D. Salmon. Dilution of individual microtubules observed in real time in vitro: Evidence that cap size is small and independent of elongation rate. *Journal of Cell Biology*, 1991.

[206] H. Wang, I. Brust-Mascher, and J. M. Scholey. The microtubule cross-linker Feo controls the midzone stability, motor composition, and elongation of the anaphase B spindle in Drosophila embryos. *Molecular Biology of the Cell*, 26(8):1452–1462, apr 2015.

[207] H. WANG, C. S. PESKIN, and T. C. ELSTON. A Robust Numerical Algorithm for Studying Biomolecular Transport Processes. *Journal of Theoretical Biology*, 221(4):491–511, 2003.

[208] J. J. Ward, H. Roque, C. Antony, and F. J. Nedelec. Mechanical design principles of a mitotic spindle. *eLife*, 3(December):1–28, 2014.

[209] K. L. Wendell, L. Wilson, and M. A. Jordan. Mitotic block in HeLa cells by vinblastine: Ultrastructural changes in kinetochore-mcirotubule attachment and in centrosomes. *Journal of Cell Science*, 104(2):261–274, 1993.

[210] H. Wierenga and P. R. ten Wolde. Diffusible crosslinkers cause superexponential friction forces. *Physical Review Letters*, 125(7):78101, 2019.

[211] S. Wijeratne and R. Subramanian. Geometry of antiparallel microtubule bundles regulates relative sliding and stalling by PRC1 and kif4A. *eLife*, 7, oct 2018.

[212] M. Winey, C. L. Mamay, E. T. O'Toole, D. N. Mastronarde, T. H. Giddings, K. L. McDonald, and J. R. McIntosh. Three-dimensional ultrastructural analysis of the Saccharomyces cerevisiae mitotic spindle. *Journal of Cell Biology*, 129(6):1601–1615, jun 1995.

[213] R. Wollman, G. Civelekoglu-Scholey, J. M. Scholey, and A. Mogilner. Reverse engineering of force integration during mitosis in the Drosophila embryo. *Molecular Systems Biology*, 4(1):195, jan 2008.

[214] R. Wollman, E. N. Cytrynbaum, J. T. Jones, T. Meyer, J. M. Scholey, and A. Mogilner. Efficient chromosome capture requires a bias in the 'search-and-capture' process during mitotic-spindle assembly. *Current Biology*, 15(9):828–832, may 2005.

[215] M. J. Wolyniak, K. Blake-Hodek, K. Kosco, E. Hwang, L. You, and T. C. Huffaker. The regulation of microtubule dynamics in Saccharomyces cerevisiae by three interacting plus-end tracking proteins. *Molecular Biology of the Cell*, 17(6):2789–2798, jun 2006.

[216] A. Yamashita, M. Sato, A. Fujita, M. Yamamoto, and T. Toda. The Roles of Fission Yeast Ase1 in Mitotic Cell Division, Meiotic Nuclear Oscillation, and Cytokinesis Checkpoint Signaling. *Molecular biology of the cell*, 16(1):1–13, 2005.

[217] G. Yang, L. A. Cameron, P. S. Maddox, E. D. Salmon, and G. Danuser. Regional variation of microtubule flux reveals microtubule organization in the metaphase meiotic spindle. *Journal of Cell Biology*, 182(4):631–639, aug 2008.

[218] K. W. Yau, P. Schatzle, E. Tortosa, S. Pages, A. Holtmaat, L. C. Kapitein, and C. C. Hoogenraad. Dendrites In Vitro and In Vivo Contain Microtubules of Opposite Polarity and Axon Formation Correlates with Uniform Plus-End-Out Microtubule Orientation. *Journal of Neuroscience*, 36(4):1071–1085, jan 2016.

[219] A. Yildiz, M. Tomishige, R. D. Vale, and P. R. Selvin. Kinesin Walks Hand-Over-Hand. *Science*, 303(5658):676–678, 2004.

[220] C. H. Yu, S. Redemann, H. Y. Wu, R. Kiewisz, T. Y. Yoo, W. Conway, R. Farhadifar, T. Müller-Reichert, and D. Needleman. Central-spindle microtubules are strongly coupled to chromosomes during both anaphase A and anaphase B. *Molecular Biology of the Cell*, 30(19):2503–2514, 2019.

[221] M. Yukawa, C. Ikebe, and T. Toda. The Msd1-Wdr8-Pkl1 complex anchors microtubule minus ends to fission yeast spindle pole bodies. *Journal of Cell Biology*, 209(4):549–562, 2015.

[222] M. Yukawa, T. Kawakami, C. Pinder, and T. Toda. Two XMAP215/TOG microtubule polymerases, Alp14 and dis1, play non-exchangeable, distinct roles in microtubule organisation in fission yeast. *International Journal of Molecular Sciences*, 20(20), 2019.

[223] F. Zheng, T. Li, M. Cheung, V. Syrovatkina, and C. Fu. Mcp1p tracks microtubule plus ends to destabilize microtubules at cell tips. *FEBS Letters*, 588(6):859–865, mar 2014.

[224] C. Zhu and W. Jiang. Cell cycle-dependent translocation of PRC1 on the spindle by Kif4 is essential for midzone formation and cytokinesis. *Proceedings of the National Academy of Sciences of the United States of America*, 102(2):343–8, jan 2005.

[225] C. Zhu, E. Lau, R. Schwarzenbacher, E. Bossy-Wetzel, and W. Jiang. Spatiotemporal control of spindle midzone formation by PRC1 in human cells. *Proceedings of the National Academy of Sciences*, 103(16):6196–6201, 2006.